Geoscience BC

Summary of Activities 2019

Energy and Water

GEOSCIENCE BC
SUMMARY OF ACTIVITIES 2019:
ENERGY AND WATER

Geoscience BC Report 2020-02

This publication is also available, free of charge, as colour digital files in Adobe Acrobat® PDF format from the Geoscience BC website: http://www.geosciencebc.com/s/SummaryofActivities.asp.

When using information from this publication in other publications or presentations, due acknowledgment should be given to Geoscience BC. The recommended reference is included on the title page of each paper. The complete volume should be referenced as follows:

Geoscience BC (2020): Geoscience BC Summary of Activities 2019: Energy and Water; Geoscience BC, Report 2020-02, 160 p.

Summary of Activities: Energy and Water (Geoscience BC)
Annual publication

ISSN 2562-2757 (Print)
ISSN 2562-2765 (Online)

Geoscience BC
1101–750 West Pender Street
Vancouver, British Columbia V6C 2T7
Canada

Front cover photo and credit: Helicopter transporting University of Alberta magnetotelluric researchers from extensive pyroclastic tuff–lapillistone field on Devastator Peak (Mount Meager), southwestern British Columbia (C.J. Salas, 2019).

Back cover photo and credit: R. Bryant laying out magnetotelluric sensors along a ridge on Mount Meager, southwestern British Columbia, to help image geothermal reservoirs in the subsurface (S.E. Grasby, 2019).

Foreword

Geoscience BC is pleased to once again present results from our ongoing projects and scholarship winners in our annual *Summary of Activities* publication. Papers are published in two separate volumes: *Minerals*, and this volume, *Energy and Water*. Both volumes are available in print and online via www.geosciencebc.com.

Summary of Activities 2019: Energy and Water

This volume, *Summary of Activities 2019: Energy and Water*, contains 15 papers from Geoscience BC–funded projects or scholarship recipients that are within Geoscience BC's strategic focus areas of energy (including oil and gas, and geothermal) and water. The papers are divided into four sections, based on Geoscience BC's strategic objectives of

1) Facilitating Responsible Natural Resource Development,
2) Advancing Science and Innovative Geoscience Technologies,
3) Enabling Clean Energy, and
4) Understanding Water.

The five papers in the 'Facilitating Responsible Natural Resource Development' section focus on induced seismicity in northeastern British Columbia (BC). Monahan et al. present interim results from work done in the Fort St. John–Dawson Creek area to map the potential for near-surface geological materials to amplify seismic waves. Babaie Mahani assesses the results of earthquake monitoring in the area to identify source mechanisms and the regional stress field. Wozniakowska and Eaton use machine learning to begin to identify factors affecting the occurrence of induced seismicity using existing data, while Bustin et al. deployed accelerographs to provide additional monitoring data for seismicity. Roth et al. use tomographic double-difference analysis to look at pore pressure increase as a potential contributor to induced seismicity.

In the 'Advancing Science and Innovative Geoscience Technologies' section, Chalmers et al. discuss the results of their ongoing research into the distribution of hydrogen sulphide in the Montney Formation, while González et al. assess the depositional setting of the Lower Montney Formation using drillcore, thin-section analysis and wireline data. Silva and Bustin present the results of sampling to assess the thermal history of the Doig Formation by determining the kerogen activation energy of samples.

Under 'Enabling Clean Energy', Whiticar and Evans present the results of a multiyear project to compile publicly available information and generate additional data on gas chemistry and gas-isotope chemistry, in order to generate geochemical signatures for natural gases in northeastern BC; and Whiticar et al. detail the use of drone-mounted scientific equipment to assess methane leakage at a variety of sites in Alberta during a field trial.

Also under 'Enabling Clean Energy' are three papers that address geothermal potential and settings in the province. Grasby et al. detail the monitoring and data-collection program that was initiated in the Mount Meager area during the summer of 2019, while Van Acken and Gleeson present preliminary results from a geological, structural and hot-spring mapping exercise as the first steps in understanding the geothermal regime in the Sloquet Hot Springs area. Finley et al. completed an assessment of geothermal resources in southeastern BC, looking at kinematic influences on a regional scale to help focus future geothermal investigations in the area.

The final two papers, in the 'Understanding Water' section, describe work conducted in northeastern BC. Ladd et al. present the details of several field campaigns that were undertaken to install a network of 29 groundwater monitoring wells in the Peace Region for the purpose of monitoring methane in groundwater, while Cahill et al. show the preliminary results from a field investigation conducted to observe the effects and migration of natural gas in a shallow confined aquifer.

Geoscience BC Energy and Water Publications 2019

In addition to the two *Summary of Activities* volumes, Geoscience BC releases interim and final products from our projects as Geoscience BC reports. The following five Energy and Water reports and maps were published in 2019:

- Thirteen technical papers in the *Geoscience BC Summary of Activities 2018: Energy and Water* volume (Geoscience BC Report 2019-02)
- **Mapping the Susceptibility to Amplification of Seismic Ground Motions in the Montney Play Area of Northeast British Columbia**, by P.A. Monahan, V.M. Levson, B.J. Hayes, K. Dorey, Y. Mykula, R. Brenner, J. Clarke, B. Calambos, C. Candy, C. Krumbiegel and E. Calderwood (Geoscience BC Report 2018-16)

- **Quantification of the Gas and Liquids in Place and Flow Characteristics of Shale and Other Fine-Grained Facies in Western Canada,** by R.M. Bustin, A.A.M. Bustin, S. Hazel, A. Hosseinian, M. LeMessiuer, E.A. Letham, M. Longobardi, E. Munson, J. Owen, T. Wilson and P.L. Silva (Geoscience BC Report 2019-06)
- **South Meager Geothermal Project: New Perspectives from Recently Unearthed Data**, by J. Witter (Geoscience BC Report 2019-07)
- **Clarke Lake Geothermal Pre-Feasibility Study**, by Associated Engineering (Geoscience BC Report 2019-11)

All releases of Geoscience BC reports, maps and data are published on our website and are announced through our website and e-mail updates. Most final reports and data can also be viewed or accessed through our Earth Science Viewer at https://gis.geosciencebc.com/esv/?viewer=esv.

Acknowledgments

Geoscience BC would like to thank all authors and reviewers of the *Summary of Activities* for their contributions to this volume. RnD Technical is also acknowledged for its work in editing and assembling both volumes. As well, Geoscience BC would like to acknowledge the Province of British Columbia and our project funding partners for their ongoing support of public geoscience, and express our appreciation for the leaders and volunteers in British Columbia's mineral exploration, mining and energy sectors who support our organization through their guidance, use and recognition of the information that we collect and distribute.

Laura Wytrykush
Manager, Energy and Water
Geoscience BC
www.geosciencebc.com

Carlos Salas
Executive Vice President & Chief Scientific Officer
Geoscience BC

Contents

Facilitating Responsible Natural Resource Development

Advancing Science and Innovative Geoscience Technologies

Enabling Clean Energy

Understanding Water

Amplification of Seismic Ground Motion in the Fort St. John–Dawson Creek Area, Northeastern British Columbia (NTS 093P, 094A)

P.A. Monahan, Monahan Petroleum Consulting, Victoria, British Columbia, pmonahan@shaw.ca

B.J. Hayes, Petrel Robertson Consulting Ltd., Calgary, Alberta

M. Perra, Petrel Robertson Consulting Ltd., Calgary, Alberta

Y. Mykula, Petrel Robertson Consulting Ltd., Calgary, Alberta

J. Clarke, Petrel Robertson Consulting Ltd., Calgary, Alberta

B. Galambos, Frontier Geosciences Inc., North Vancouver, British Columbia

D. Griffiths, Frontier Geosciences Inc., North Vancouver, British Columbia

O. Bayarsaikhan, Frontier Geosciences Inc., North Vancouver, British Columbia

U. Oki, Northern Geo Testing and Engineering, Fort St. John, British Columbia

Monahan, P.A., Hayes, B.J., Perra, M., Mykula, Y., Clarke, J., Galambos, B., Griffiths, D., Bayarsaikhan, O. and Oki, U. (2020): Amplification of seismic ground motion in the Fort St. John–Dawson Creek area, northeastern British Columbia (NTS 093P, 094A); *in* Geoscience BC Summary of Activities 2019: Energy and Water, Geoscience BC, Report 2020-02, p. 1–12.

Introduction

Seismicity in northeastern British Columbia (BC) has increased significantly recently due to hydraulic fracturing and water disposal by the petroleum industry (Atkinson et al., 2016; Kao et al., 2018). Most of these events are small, but rare events up to magnitude (M) 4.6 have occurred (Babaie Mahani et al., 2017a, b, 2019). Ground motions for the largest of these events are at the lower bound of possible damage, in the range of modified Mercalli intensity (MMI) VI (Worden et al., 2012; Babaie Mahani and Kao, 2018; Babaie Mahani et al., 2019), and minor damage has been reported or is suspected. These events occur at very shallow depths, 1 to 3 km, and partly because of this, events as low as M 0.8 have been felt by residents of the region.

Monahan et al. (2019) recently completed a regional assessment of the potential for amplification of seismic ground motions due to local differences in near-surface geological materials in the Montney play area, currently the most active oil and gas play in BC. Their mapping was based on existing surficial geological maps, generally at a scale of 1:250 000 (e.g., Mathews, 1978; Reimchen, 1980), and they noted a number of inconsistencies between amplifications from instrumentally recorded events and those predicted by the mapping. Consequently, a follow-up study was initiated in the Fort St. John–Dawson Creek area, which is the most heavily populated part of the Montney play area, and where a M 4.6 event occurred in November 2018 (Babaie Mahani et al., 2019). The objectives of this study are to refine the surficial geological mapping, generate a map more representative of shallow subsurface conditions by collecting additional subsurface geological data, and obtain additional shear-wave velocity (V_S) data to better understand the distribution of geological materials susceptible to amplification. The new mapping will be done at a scale of 1:100 000. The purpose of this paper is to present some of the initial results of this investigation: surface geological investigations, subsurface geological data acquisition, the summary of newly acquired V_S data, and interviews with residents who have experienced frequent seismic events.

Ground-Motion Amplification

Ground-motion amplification due to shallow geological conditions can be estimated by the average V_S in the upper 30 m (V_{S30}; Kramer, 1996; Finn and Wightman, 2003). The National Earthquake Hazards Reduction Program (NEHRP) in the United States has defined five Site classes (A to E) based on V_{S30} and these have been adopted by the National Building Code of Canada (Table 1; Building Seismic Safety Council, 2003; National Research Council, 2015).

The V_{S30} is the time-averaged V_S in the upper 30 m (i.e., harmonic mean) and is calculated using the following formula:

$$V_{S30} = \Sigma h / \Sigma t$$

This publication is also available, free of charge, as colour digital files in Adobe Acrobat® PDF format from the Geoscience BC website: http://www.geosciencebc.com/updates/summary-of-activities/.

where h = each measured interval thickness, where Σh = 30 m, and t = the measured interval travel time; $t = h/V_S$ for each interval.

Moderate to high amplification of seismic ground motions can occur in Site classes D and E.

Amplification can also be due to resonance, where the dominant period of the ground motions is the same as the dominant site period. The dominant site period (T) is calculated by the quarter wavelength rule (Kramer, 1996; Finn and Wightman, 2003):

$$T = 4H/V_S$$

where H = thickness of the low velocity layer, and V_S = the average shear-wave velocity of the low velocity layer.

Amplification due to resonance was also suspected in the region by Monahan et al. (2019).

Regional Geology

The project area extends from Fort St. John to Dawson Creek and from the Alberta border west to the Pine and Moberly rivers (Figure 1), in the western part of the Alberta Plateau (Holland, 1976). Hilltops in the western part are up to 900 m in elevation, with up to 200 m of local relief, and the topography becomes more subdued toward the east, where hilltops are up to 700 m in elevation and local relief is 50 m. The <250 m deep valleys of the Peace River and its major tributaries, the Kiskatinaw, Pine, Moberly and Beatton rivers, are the result of the incision by the rivers into this plateau surface.

Bedrock consists of gently easterly dipping, relatively soft Cretaceous sedimentary rocks (Irish, 1958; Stott, 1982; McMechan, 1994). The principal geological units exposed from northwest to southeast across the project area are, in ascending order: the Shaftesbury Formation, which consists of marine shale; the Dunvegan Formation, which consists of interbedded sandstone, conglomerate and shale; the Kaskapau Formation, which consists of marine shale; and the Cardium Formation, which consists of interbedded sandstone, conglomerate and shale. The upper 10 to 20 m of bedrock is commonly weathered to clay, particularly the shale intervals, and the upper surface is commonly observed to be glaciotectonized in outcrop (e.g., Monahan et al., 2019).

At least three glaciations occurred during the Quaternary in this area (Mathews, 1978; Hartman and Clague, 2008; Hickin et al., 2016a). Deposits of the last two glacial and adjoining nonglacial periods show a repetitive pattern of fluvial incision and deposition during nonglacial intervals, followed by deposition of glaciolacustrine silt as drainageways were blocked by advancing Laurentide ice, and finally, by till during the glacial maximum. Fluvial incision cut deeper following each glaciation, so that modern valleys of the Peace River and its major tributaries are incised through the older Quaternary deposits into bedrock.

Deposits of the latest glaciation, which is Late Wisconsinan in age, are the best known. Both Cordilleran and Laurentide ice extended into the area, but the maximum extents of each appear to have been out of sync. West of the project area, Cordilleran till has been reported interbedded with advance-phase glaciolacustrine deposits (Hartman et al., 2018). The advance-phase glaciolacustrine deposits are overlain by clay-rich and clast-poor till deposited by Laurentide ice. The ice sheets appear to have coalesced, but in the latter stages, the Laurentide till appears to have been overridden by Cordilleran ice (Hickin et al., 2015). As Laurentide ice retreated, drainage was again blocked, resulting in widespread deposition of glaciolacustrine silt, clay, and very fine sand in glacial Lake Peace (Mathews, 1978, 1980; Hartman and Clague, 2008; Hickin et al., 2016a, b).

Sediments older than the last glacial maximum are restricted to Quaternary river valleys (paleovalleys) and are exposed only in the valley walls of the Peace River and other major rivers. Elsewhere, only till and retreat-phase deposits of the most recent glaciation and Holocene sediments can be mapped at the surface. Surficial units have characteristic geomorphic expressions (Mathews, 1978; Hartman and Clague, 2008; Hickin et al., 2015; Monahan et al., 2019). Rolling uplands are underlain mainly by clay till with a veneer of glaciolacustrine silt and clay. Topography in the upland areas is largely controlled by bedrock, which is locally exposed and generally within a few metres of the surface in the western parts of the project area. However, in the upland areas of more subdued relief in the eastern part of the project area, till forms a blanket locally up to 30 m thick. Low relief platforms and terraces, between the uplands and deeply incised major valleys, are underlain by retreat-phase glaciolacustrine and related deposits. Terraces on the walls of major valleys are underlain by late stage gla-

Table 1. National Earthquake Hazards Reduction Program (NEHRP) Site classes (Building Seismic Safety Council, 2003). Susceptibility ratings from Hollingshead and Watts (1994).

Site Class	General description	Definition by V_{S30} (m/s)
A	Hard rock	$V_{S30}>1500$
B	Rock	$760<V_{S30}<1500$
C	Very dense soils and soft rock	$360<V_{S30}<760$
D	Stiff soils	$180<V_{S30}<360$
E	Soft soils, or soil profile with >3 m soft silt or clay	$V_{S30}<180$, or >3 m silt and clay with plasticity index >20, moisture content >40%, and undrained shear strength <25 kPa

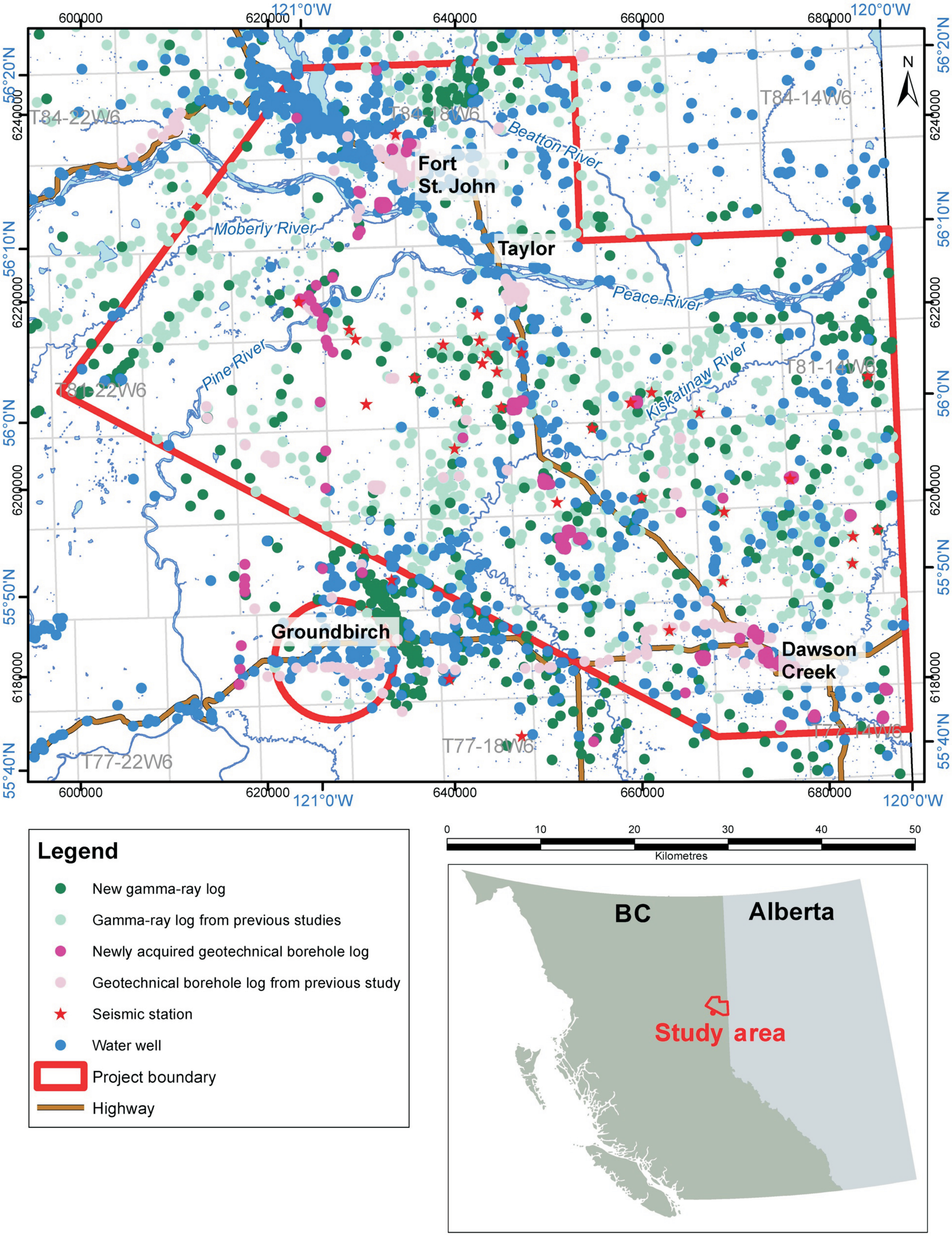

Figure 1. Map of the study area showing the location of subsurface geological database sites. Previous studies are those by Petrel Robertson Consulting Ltd. (2016; gamma-ray logs) and Monahan et al. (2019; gamma-ray logs, geotechnical borehole logs). All co-ordinates are in UTM Zone 10N, NAD83.

ciofluvial sand and gravel representing the earliest phases of postglacial fluvial incision. Modern fluvial sand and gravel occupy river valley bottoms.

Within the upland areas, the valleys of minor streams have gently sloping floors and are underlain by glaciolacustrine sediments, into which the modern streams have now incised. The degree of incision increases markedly as these streams approach the major valleys. Boundaries between the upland areas and adjacent glaciolacustrine terraces, platforms and valley bottoms are commonly marked by distinct breaks in slope. However, these breaks in slope are not as clear in the areas of subdued topography in the east.

Surficial Geology Mapping

Detailed topographic mapping at a 5 m contour interval and slope mapping have been computed from a Natural Resources Canada digital elevation model (Natural Resources Canada, 2015). These enable more reliable definition of the breaks in slope that mark the boundaries of the glaciolacustrine platforms with the adjoining uplands and with the deeply incised river valleys than shown on existing surficial geological maps (Mathews, 1978; Reimchen, 1980).

An eight-day field program was also conducted in August 2019 to spot check the interpretations, observe landforms and note the topographic setting of sites with subsurface geological data and seismograph stations established by government and industry to monitor induced seismic activity.

Subsurface Geological Database

As with the previous study, three sources of subsurface geological data are being employed: cased-hole gamma-ray logs from petroleum wells, water well logs and geotechnical borehole logs.

Gamma-ray logs run through surface casing to (near) surface are required for petroleum well sites drilled in BC and are available in public databases. Top of bedrock can be picked with reasonable confidence where stratigraphic markers in Cretaceous strata are truncated and overlain by Quaternary sediments, particularly where bedrock consists of marine shale, in which abundant markers can be traced over tens of kilometres (Hayes et al., 2016; Petrel Robertson Consulting Ltd., 2016; Monahan et al., 2019). For the studies by Petrel Robertson Consulting Ltd. (2016) and Monahan et al. (2019), logs from 918 wells in and adjacent to the project area were normalized to remove surface casing effects (documented by Quartero et al., 2014). These data are being used for the current study. An additional 458 gamma-ray logs, which represent all those remaining in the area, have been added to this dataset (Figure 1). Even though gamma-ray log data are highly repeatable, each log curve provides only limited lithological information. Furthermore, not all logs have been run continuously to surface and, in many places, attenuation of the gamma-ray signal by the conductor pipe obscures the lithological signature in the upper 10 to 30 m. Where the bedrock top is shallow and lies above the top of the logged interval, all that can be reported is a maximum depth to bedrock. Nonetheless, cased-hole gamma-ray logs provide important constraints on thickness and lithology of the Quaternary section, particularly when combined with other subsurface geological data.

An edited database of depth to bedrock values in northeastern BC water wells was prepared by Hickin (2013), primarily from the BC Ministry of Environment and Climate Change Strategy's GWELLS database (https://apps.nrs.gov.bc.ca/gwells/). This dataset has been updated from those used in previous studies, and includes 1282 wells in and adjacent to the project area (Figure 1). Although it includes an enormous amount of useful information, it has been generated from water well records prepared with large variations in accuracy of lithological descriptions and unit depths, and well locations are in some cases suspect.

Geotechnical borehole logs provide the best data for Quaternary geological studies, because they are consistently described by professionals, reliably located and include repeatable quantitative measurements that can be correlated to physical properties. The latter include standard penetration test (SPT) blowcount (N) values and moisture content, which are useful stratigraphic indices. The SPT N value is the number of hammer blows required to drive a sample tube 305 mm (1 ft.) into the material at the bottom of the hole under standardized conditions. If after 50 blows, penetration has not reached 305 mm, the test is usually terminated; this upper limit is termed refusal, and indicates a material very resistant to penetration. The principal disadvantage of these borehole data is that they are generally drilled to very shallow depths, a few tens of metres at most. Furthermore, they are proprietary and so laborious to compile. Monahan et al. (2019) obtained 582 borehole logs at 107 sites in and adjacent to the current project area and these are being used in the current study. To supplement these, an additional 592 borehole logs at 99 sites have been obtained to date, and data collection is ongoing (Figure 1). Of the 206 sites represented, 143 have data deeper than 10 m.

Acquisition of V_S Data and Initial Results

New V_S data have been obtained by downhole logging using the vertical seismic profiling (VSP) method, and by multichannel analysis of surface waves (MASW), a non-invasive surface technique that generates a V_S profile along a 100 m transect. These two methods are described by Arsenault et al. (2012) and Phillips and Sol (2012), respectively.

Monahan et al. (2019) acquired V_S data at 14 sites in and adjacent to the project area (Figure 2). These included six

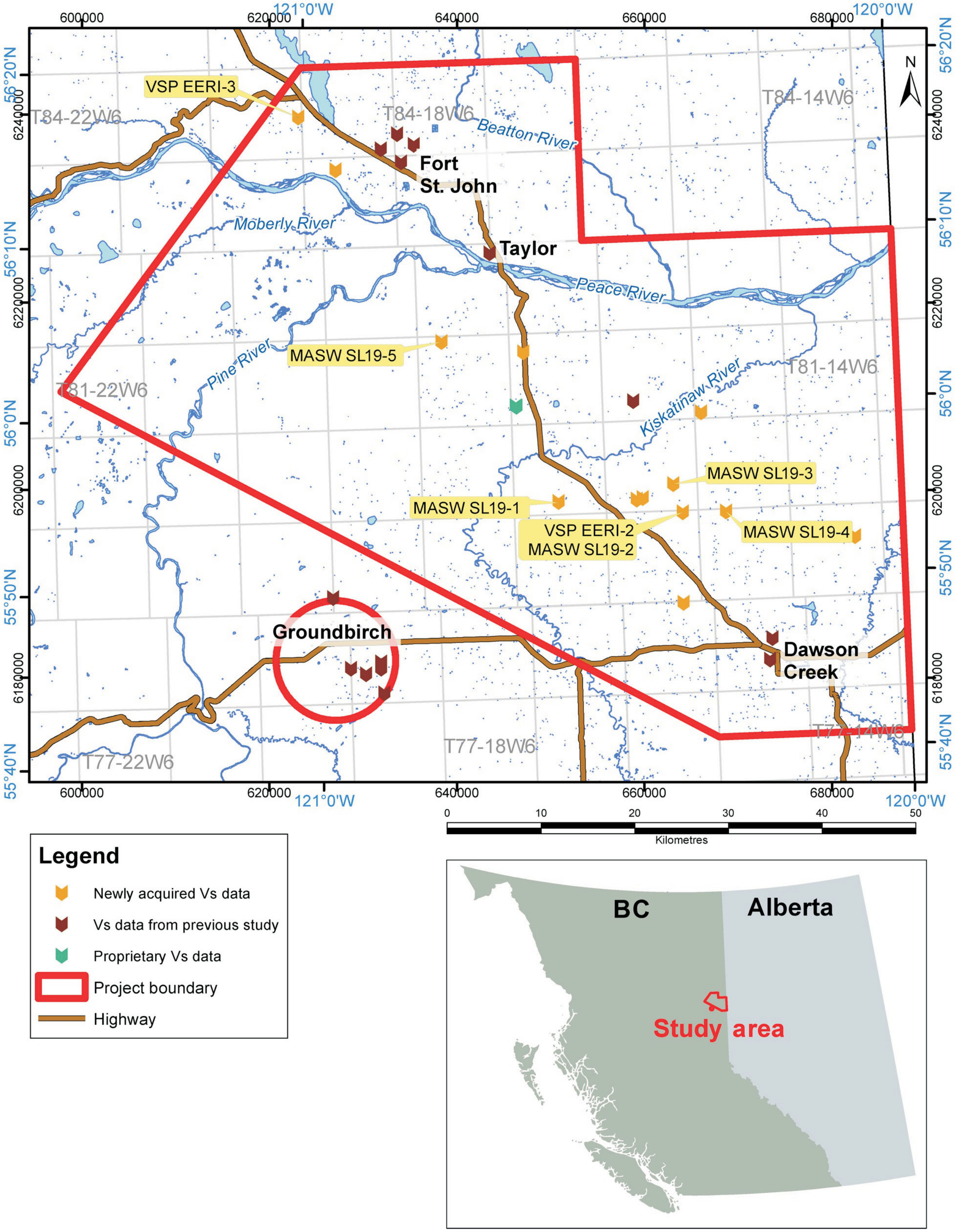

Figure 2. Spatial distribution of shear-wave velocity (V_S) data. Sites identified are those shown in Table 2. Previous study is that by Monahan et al. (2019). All co-ordinates are in UTM Zone 10N, NAD83. Abbreviations: MASW, multichannel analysis of surface waves; VSP, vertical seismic profiling.

downhole logs in pre-existing cased boreholes acquired by the VSP method at Groundbirch, south of the project area, and eight MASW profiles. The latter were concentrated in a few areas – four in Fort St John, two in Dawson Creek, one at Taylor, and only one in the rural areas south of the Peace River, which constitute most of the current project area.

To date, an additional four downhole logs in pre-existing boreholes and 10 new MASW profiles have been acquired (Figure 2). Two of the boreholes were drilled by the Energy and Environment Research Initiative (EERI) as part of a regional groundwater monitoring project by The University of British Columbia (Cahill et al., 2019), and the other two are Province of BC groundwater observation wells. In addition to V_S data, P-wave velocity (V_P) and gamma-ray data were acquired. Most of the MASW tests were done at seismograph stations, in order to correct seismic records for site effects and to understand the seismic responses at these stations. An additional two downhole logs in existing boreholes and 10 to 12 MASW tests are being planned. Proprietary V_S data have also been obtained at one site.

At the time of writing, V_S data have been received for the first two boreholes, EERI-2 and-3 (Figures 3, 4), and the first five MASW tests (Figures 5–7). The results are summarized in Table 2. To estimate the site period, the depth of the low-velocity surface layer was determined from the most abrupt V_S change on the downhole logs, and the main inflection below the surface layer on the MASW profiles, at the profile midpoint. Stations MONT 1 (MASW SL19-1) and MONT 8 (MASW SL19-5) are part of a network established by the BC Oil and Gas Commission and Natural Resources Canada, and station MG05 (MASW SL19-4) is part of a network established for the McGill University Dawson-Septimus induced seismicity study. An MASW test was conducted adjacent to borehole EERI-2 (MASW SL19-2) to compare the results of the two techniques.

Some observations can be made, and conclusions drawn, from the new data. All the new V_S sites are in Site Class D, with V_{S30} ranging from 228 to 345 m/s. These sites occupy a range of geomorphic settings, from a valley bottom site, where the low velocity layer corresponds to glaciolacustrine clay (MASW SL19-1; Figures 2, 5, Table 2) and Site

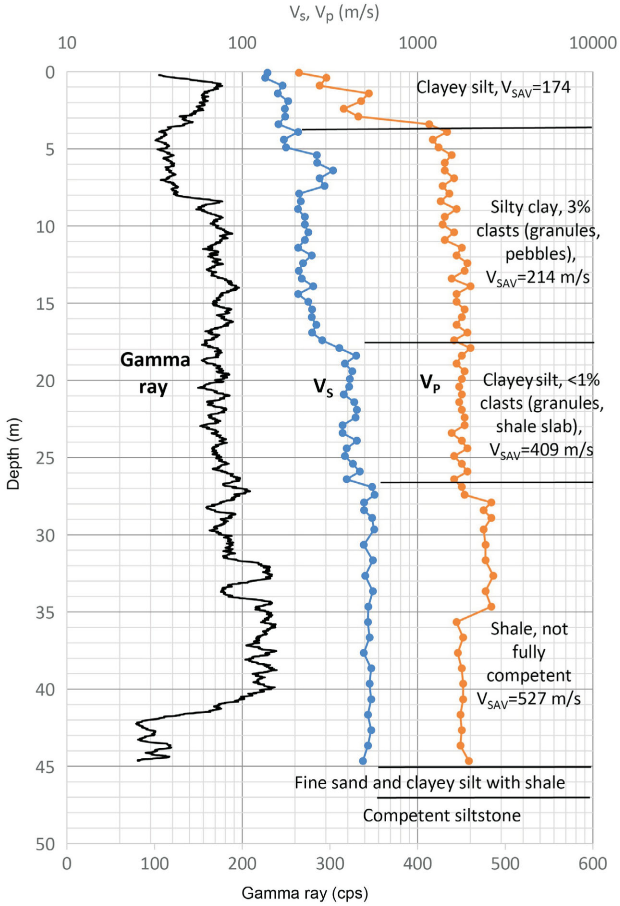

Figure 3. Borehole log for EERI-2. Gamma-ray, shear-wave velocity (V_S) and P-wave velocity (V_P) data. Lithological log and descriptions adapted from that of M. Goetz (Cahill et al., 2019). Note gamma-ray scale at bottom. Abbreviations: cps, counts per second; V_{SAV}, interval average of shear-wave velocity.

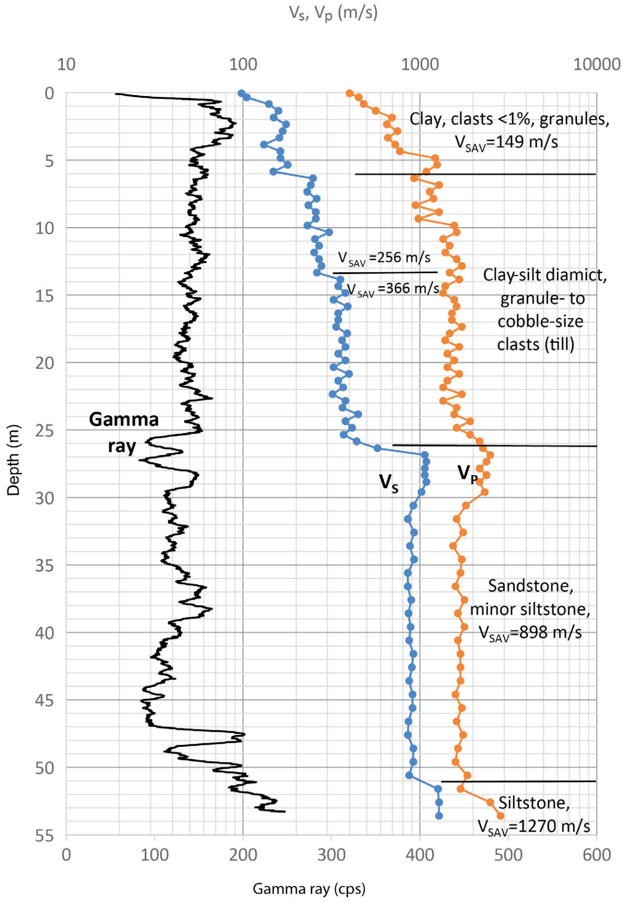

Figure 4. Borehole log for EERI-3. Gamma-ray, shear-wave velocity (V_S) and P-wave velocity (V_P) data. Lithological log and descriptions adapted from that of M. Goetz (Cahill et al., 2019). Note gamma-ray scale at bottom. Abbreviations: cps, counts per second; V_{SAV}, interval average of shear-wave velocity.

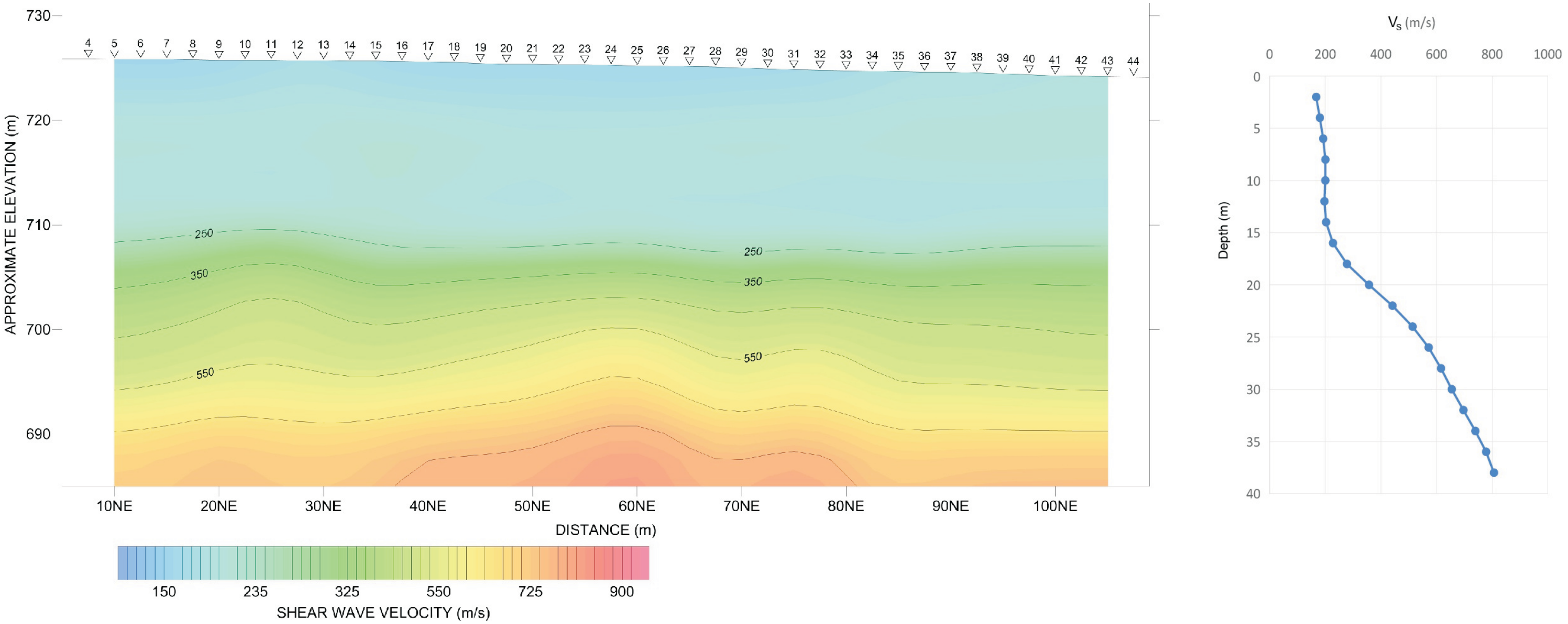

Figure 5. Multichannel analysis of surface waves at MASW SL19-1 (station MONT 1), valley bottom location; left panel, profile; right panel, shear-wave velocity (V_S) trace in middle of profile. Numbers along the top of the profile are geophone locations. Abbreviation: NE, to the northeast.

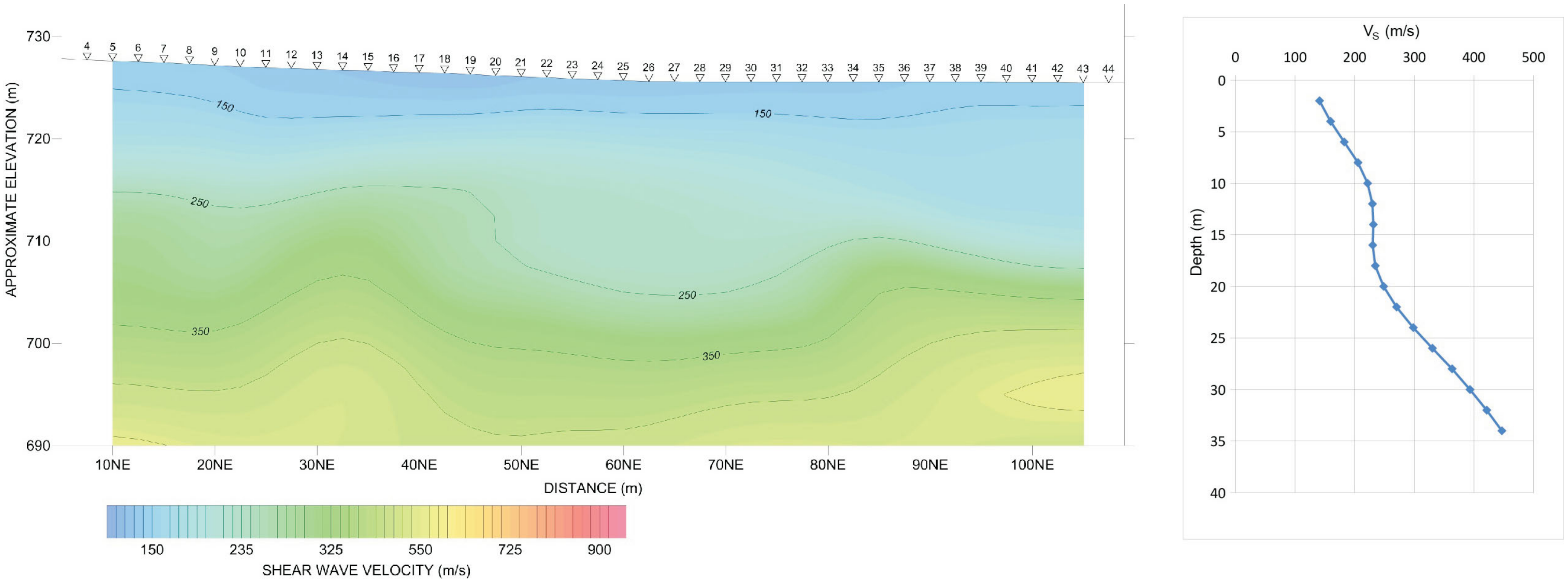

Figure 6. Multichannel analysis of surface waves at MASW SL19-2, adjacent to the site of borehole EERI-2 (Figure 3), on gently sloping hillside; left panel, profile; right panel, shear-wave velocity (V_S) trace in middle of profile. Numbers along the top of the profile are geophone locations. Abbreviation: NE, to the northeast.

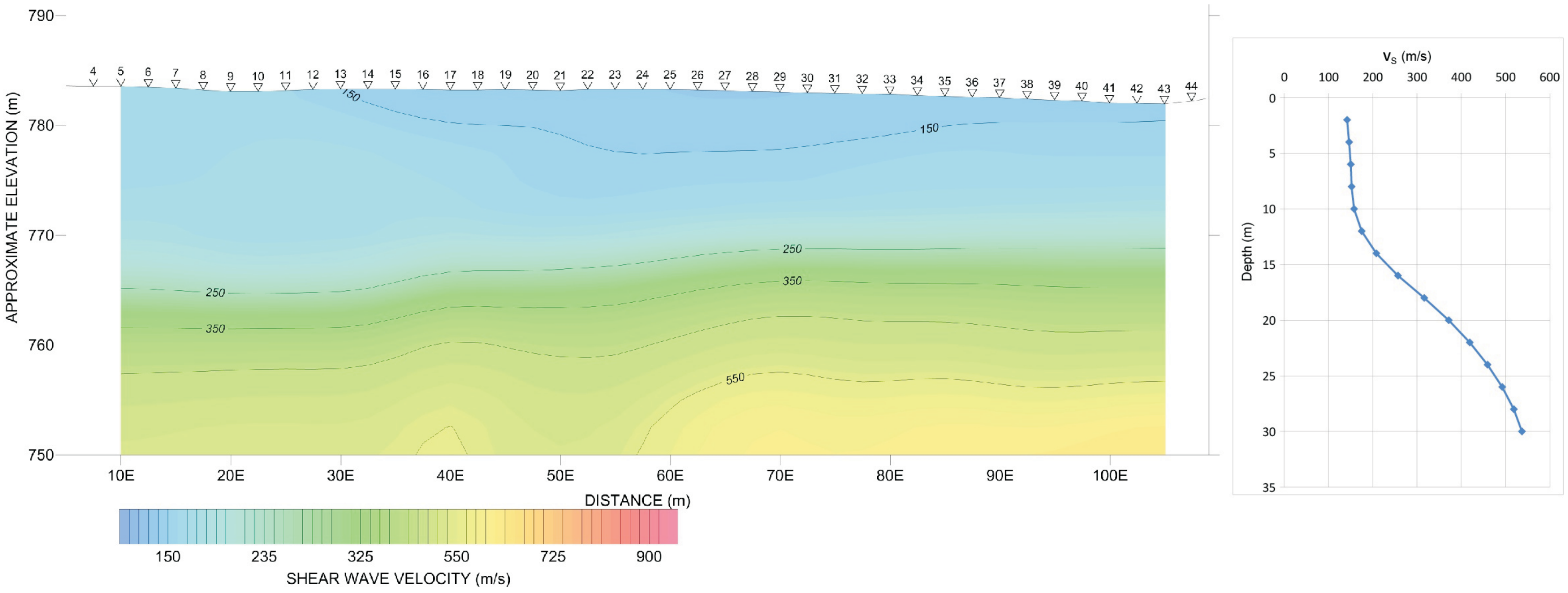

Figure 7. Multichannel analysis of surface waves at MASW SL19-4 (station MG05) at 16-32-79-15W6 (L.S. 16, Sec. 32, Twp. 79, Rge. 15, W 6th Mer.) well site, on a hilltop; left panel, profile; right panel, shear-wave velocity (V_S) trace in middle of profile. Numbers along the top of the profile are geophone locations. Abbreviation: E, to the east.

Table 2. Summary of new shear-wave velocity (V_S) data acquisition and results. These test sites are identified on Figure 2. All co-ordinates are in UTM Zone 10N, NAD83.

Number	Location/ borehole/ station number	Easting (m)	Northing (m)	Depth (m)	V_{S30} (m/s)	Site Class	Low velocity layer Thickness (m)	Low velocity layer V_{SAV} (m/s)	Site period (s)	Setting
VSP EERI-2	EERI-2	664116	6197620	45	270	D	17.7	214	0.33	Gently sloping hillside
VSP EERI-3	EERI-3	623071	6239713	55	278	D	26.1	250	0.42	Minor valley bottom in hilly terrain
MASW SL19-1	Station MONT 1	650843	6198718	38	253 ±4	D	15	189	0.31	Valley bottom, 7 m clay in dugout
MASW SL19-2	EERI-2	664116	6197620	34	228 ±7	D	19	194	0.39	Gently sloping hillside
MASW SL19-3	Industry station 11-11-80-16W6[1]	663081	6200617	36	345 ±14	D	13	280	0.19	Steep hillside
MASW SL19-4	Station MG05, 16-32-79-15W6	668703	6197693	30	233 ±13	D	12	151	0.32	Hilltop
MASW SL19-5	Station MONT 8	638356	6215783	36	246 ±16	D	19	189	0.40	Gently sloping hillside

[1] L.S. 11, Sec. 11, Twp. 80, Rge. 16, W 6th Mer.

Class D is expected, to upland sites, where surficial deposits are primarily till and Site Class C had been previously assigned (Monahan et al., 2019). These data demonstrate that the low blowcount (N=15 to 50) till recognized in many of the geotechnical boreholes obtained for this study is characterized by low V_S (150–300 m/s), and that in the upland areas where topography is more subdued in the central and eastern parts of the study area, geotechnical borehole data show that till forms a blanket 10 to 30 m thick. An example is the hilltop MASW site (MASW SL19-4; Figures 2, 7, Table 2), where the low velocity layer correlates with till in a nearby borehole (M. Goetz and B. Ladd, pers. comm., 2019). Consequently, Site Class D occurs commonly within the upland hillsides and hilltops.

However, Site Class C conditions have also been documented in upland areas, both where bedrock is shallow (<7 m), and where the till section is dominated by high-blowcount (N>50) and high-V_S (>400 m/s) intervals (Monahan et al., 2019). These intervals generally occur stratigraphically below low-blowcount, low-V_S till. An example of the latter is provided by the VSP log from EERI-3, where V_S in the till interval increases abruptly from 256 to 366 m/s at 13.5 m (Figure 4). The V_S increase does not reflect a change in lithology (Cahill et al., 2019), but increased glacial compaction. In this case, the thickness of low-V_S till keeps this site in Site Class D. Consequently, Site classes C and D both occur in upland areas, and further integration of the borehole, V_S and topographic data will be necessary to determine areas dominated by each Site Class. In addition, the authors acknowledge that blowcount data in till must be interpreted carefully, as high blowcounts can also occur in low-V_S till where the SPT is performed directly on a large clast.

The V_{S30} calculated from the MASW test (MASW SL19-2) conducted adjacent to borehole EERI-2 is 228 m/s, which is significantly lower than that in the VSP log for EERI-2, V_{S30} of 270 m/s (Table 2, Figures 2, 3, 6). This discrepancy will be investigated further. However, the V_S of bedrock above 47 m in the VSP log is 527 m/s, which is low compared to other bedrock intervals (Monahan et al., 2019), and it is described as not fully competent and is underlain by beds of silt and fine sand (Cahill et al., 2019; Monahan et al., 2019). This suggests it may be a glaciotectonized or glacially transported block in which extensive fracturing has reduced the V_S relative to undisturbed bedrock. Consistent with this, V_S in the lower part of the MASW profile is variable, suggesting a disrupted stratigraphic succession. The larger volume of material investigated by MASW may include a larger number of Quaternary interbeds and fractures, resulting in lower V_S than in the VSP log.

Interviews with Residents

Residents at 12 households, ranging from near Dawson Creek to the Pine River, have been interviewed to date to record their experiences with induced earthquakes. A common experience is hearing a loud thump or rumbling, like a train, truck or cow coming through the house, loud enough to wake people at night. Others describe rattling of windows and dishes. These observations are consistent with modified Mercalli intensity IV. The differences in experiences may correlate with differences in geological and topographic setting. Some residents report several events in a single day during ongoing hydraulic fracturing operations. Acquisition of MASW profiles is planned to determine the V_{S30} and V_S structure at five of these residences and additional interviews will be conducted.

Conclusions

The initial results of this project demonstrate that Site Class D conditions are widespread. They occur not only in areas underlain by glaciolacustrine silt and clay, as previously recognized, but also in the upland slopes and hilltops, where Site Class C had been assigned previously. This is due to the common occurrence of low–shear-wave velocity till, locally up to 30 m thick.

Further integration of subsurface geological datasets with shear-wave velocity and topographic data is required to determine which areas are dominated by Site Class D rather than Site Class C conditions. These will be compared with instrumental earthquake records and residents' reports to determine where induced seismic events are more strongly felt.

Acknowledgments

The authors gratefully thank the following organizations and individuals:

- Geoscience BC for providing project funding;
- for assistance in acquiring geotechnical borehole data: Northern Geo Testing and Engineering; Urban Systems; City of Fort St. John; City of Dawson Creek; District of Taylor; Peace River Regional District; School Board 60: Peace River North; BC Hydro; BC Oil and Gas Commission; Shell Canada Limited; ARC Resources Ltd; Crew Energy Inc.; Encana Corporation; Canadian Natural Resources Ltd.; and The University of British Columbia's (UBC) Energy and Environment Research Initiative (EERI) Program; particular thanks to B. Rodowski, B. Ladd and J. Cegnar;
- for access to field sites: UBC EERI Program, BC Ministry of Forests, Lands, Natural Resource Operations and Rural Development, McGill University Dawson-Septimus induced seismicity project, BC Oil and Gas Commission, Tourmaline Oil Corp., Northern Lights College, ARC Resources Ltd., Crew Energy Inc., Canadian Natural Resources Ltd., Encana Corporation, Shell Canada Limited; particular thanks to L. Hurrell, M. Goetz, G. Langston, A. Babaie Mahani, K. Evers, R. Nakamoto, D. McHarg and several residents who granted access to their lands;
- for helpful discussions: S. Venables, J. Johnson, A.S. Hickin and A. Babaie Mahani;
- K. Hadavi and J. Cegnar of BC Hydro for arranging a tour of Site C;
- L. Sears for assembling the manuscript;
- an anonymous reviewer for reviewing the manuscript and suggesting many helpful changes;
- and to several residents of the region for providing information and detailed accounts of their experiences.

References

Arsenault, J.-L., Hunter, J.A. and Crow, H.L. (2012): Shear wave velocity logs from vertical seismic profiles; *in* Shear Wave Velocity Measurement Guidelines for Canadian Seismic Site Characterization in Soil and Rock, J.A. Hunter and H.L. Crow (ed.), Geological Survey of Canada, Open File 7078, p. 123–138.

Atkinson, G.M., Eaton, D.W., Ghofrani, H., Walker, D., Cheadle, B., Schultz, R., Shcherbakov, R., Tiampo, K., Gu, J., Harrington, R.M., Liu, Y., van der Baan, M. and Kao, H. (2016): Hydraulic fracturing and seismicity in the Western Canada Sedimentary Basin; Seismological Research Letters, v. 87, no. 3, p. 1–17.

Babaie Mahani, A. and Kao, H. (2018): Ground motion from M 1.5 to 3.8 induced earthquakes at hypocentral distance <45 km in the Montney play of northeast British Columbia, Canada; Seismological Research Letters, v. 89, no. 1, p. 22–34.

Babaie Mahani, A., Kao, H., Atkinson, G.M., Assatourians, K., Addo, K. and Liu, Y. (2019): Ground-motion characteristics of the 30 November 2018 injection-induced earthquake sequence in northeast British Columbia, Canada; Seismological Research Letters, v. 90, no. 4, p. 1457–1467, URL <https://doi.org/10.1785/0220190040> [July 2019].

Babaie Mahani, A., Kao, H., Johnson, J. and Salas, C. (2017a): Ground motion from the August 17, 2015, moment magnitude 4.6 earthquake induced by hydraulic fracturing in northeastern British Columbia; *in* Geoscience BC Summary of Activities 2016, Geoscience BC, Report 2017-01, p. 9–14, URL <http://www.geosciencebc.com/i/pdf/SummaryofActivities2016/SoA2016_BabaieMahani.pdf> [October 2017].

Babaie Mahani, A., Schultz, R., Kao, H., Walker, D., Johnson, J. and Salas, C. (2017b): Fluid injection and seismic activity in the northern Montney Play, British Columbia, Canada, with special reference to the 17 August 2015 Mw 4.6 induced earthquake; Bulletin of the Seismological Society of America, v. 107, p. 542–552.

Building Seismic Safety Council (2003): NEHRP recommended provisions for seismic regulations for new buildings and other structures (FEMA 450), part 1: provisions (2003 edition); prepared for the Federal Emergency Management Agency, 338 p., URL <http://www.nehrp.gov/pdf/fema450provisions.pdf> [October 2017].

Cahill, A.G., Beckie, R.D., Goetz, M., Allen, A., Ladd, B., Welch, L., Kirste, D., Mayer, B. and van Geloven, C. (2019): Characterizing dissolved methane in groundwater in the Peace region, northeastern British Columbia, using a regional, dedicated, groundwater monitoring well network; *in* Geoscience BC Summary of Activities 2018: Energy and Water, Geoscience BC, Report 2019-02, p. 105–122, URL <http://cdn.geosciencebc.com/pdf/SummaryofActivities2018/EW/2017-002_SoA2018_EW_Cahill_DissolvedMethane.pdf> [November 2019].

Finn, W.D.L. and Wightman, A. (2003): Ground motion amplification factors for the proposed 2005 edition of the National

Building Code of Canada; Canadian Journal of Civil Engineering, v. 30, p. 272–278.

Hartman, G.M.D. and Clague, J.J. (2008): Quaternary stratigraphy and glacial history of the Peace River valley, northeast British Columbia; Canadian Journal of Earth Sciences, v. 45, p. 549–564.

Hartman, G.M.D., Clague, J.J., Barendregt, R.W. and Reyes, A.V. (2018): Late Wisconsinan Cordilleran and Laurentide glaciation of the Peace River Valley east of the Rocky Mountains, British Columbia; Canadian Journal of Earth Sciences, v. 55, no. 12, p. 1324–1338.

Hayes, B.J.R., Levson, V., Carey, J. and Mykula, Y. (2016): Interpretation of Quaternary sediments and depth to bedrock, Peace Project area, northeastern British Columbia: project update; *in* Geoscience BC Summary of Activities 2015, Geoscience BC, Report 2016-01, p. 61–68, URL <http://www.geosciencebc.com/i/pdf/SummaryofActivities2015/SoA2015_Hayes.pdf> [October 2017].

Hickin, A.S. (2013): Late Quaternary to Holocene geology, geomorphology and glacial history of Dawson Creek and surrounding area, northeast British Columbia, Canada; Ph.D. thesis, University of Victoria, 369 p.

Hickin, A.S., Best, M.E. and Pugin, A. (2016a): Geometry and valley-fill stratigraphic framework for aquifers in the Groundbirch paleovalley assessed through shallow seismic and ground-based electromagnetic surveys; BC Ministry of Energy, Mines and Petroleum Resources, BC Geological Survey, Open File 2016-5, 46 p.

Hickin, A.S., Lian, O.B. and Levson, V.M. (2016b): Coalescence of late Wisconsinan Cordilleran and Laurentide ice sheets east of the Rocky Mountain Foothills in the Dawson Creek region, northeast British Columbia, Canada; Quaternary Research, v. 85, p. 409–429.

Hickin, A.S., Lian, O.B., Levson, V.M. and Cui, Y. (2015): Pattern and chronology of glacial Lake Peace shorelines and implications for isostacy and ice-sheet configuration in northeastern British Columbia, Canada; Boreas, v. 44, p. 288–304.

Holland, S.S. (1976): Landforms of British Columbia – a physiographic outline (second edition); BC Ministry of Energy, Mines and Petroleum Resources, Bulletin 48, 138 p.

Hollingshead, S. and Watts, B.D. (1994): Preliminary seismic microzonation assessment for British Columbia; prepared for Resources Inventory Committee, Earth Sciences Task Force, 109 p.

Irish, E.J.W. (1958): Charlie Lake, West of Sixth Meridian, British Columbia; Geological Survey of Canada, Preliminary Map 17-1958, scale 1:253 440, 1 sheet.

Kao, H., Hyndman, R., Jiang, Y., Visser, R., Smith, B., Babaie Mahani, A., Leonard, L., Ghofrani, H. and He, J. (2018): Induced seismicity in western Canada linked to tectonic strain rate: implications for regional seismic hazard; Geophysical Research Letters, v. 45, 12 p., URL <https://doi.org/10.1029/2018GL079288> [November 2018].

Kramer, S.L. (1996): Geotechnical Earthquake Engineering; Prentice-Hall, Inc., Upper Saddle River, New Jersey, 653 p.

Mathews, W.H. (1978): Quaternary stratigraphy and geomorphology of the Charlie Lake (94A) map-area, British Columbia; Geological Survey of Canada, Paper 76-20, 25 p., includes Map 1460A, scale 1:250 000.

Mathews, W.H. (1980): Retreat of the last ice sheets in northeastern British Columbia and adjacent Alberta; Geological Survey of Canada, Bulletin 331, 22 p.

McMechan, M.E. (1994): Geology and structure cross section, Dawson Creek, British Columbia; Geological Survey of Canada, Map 1858A, scale 1:250 000.

Monahan, P.A., Levson, V.M., Hayes, B.J., Dorey, K., Mykula, Y., Brenner, R., Clarke, J., Galambos, B., Candy, C., Krumbiegel, C. and Calderwood, E. (2019): Mapping the susceptibility to amplification of seismic ground motions in the Montney play area of northeastern British Columbia; Geoscience BC Report 2018-16, 65 p., URL <http://cdn.geosciencebc.com/project_data/GBCR2018-16/GBCR2018-16-NEBC_Amplification_Report.pdf> [November 2019].

National Research Council (2015): National Building Code of Canada; National Research Council, Ottawa, v. 1, 708 p.

Natural Resources Canada (2015): Canadian Digital Elevation Model; Natural Resources Canada, URL <https://open.canada.ca/data/en/dataset/7f245e4d-76c2-4caa-951a-45d1d2051333> [May 2019].

Petrel Robertson Consulting Ltd. (2016): Interpretation of Quaternary sediments and depth to bedrock, Peace Project area, northeastern British Columbia; Geoscience BC, Report 2016-04, URL <http://www.geosciencebc.com/reports/gbcr-2016-04/> [October 2017].

Phillips, C. and Sol, S. (2012): Multichannel analysis of surface waves (MASW) technique for hazard studies; *in* Shear Wave Velocity Measurement Guidelines for Canadian Seismic Site Characterization in Soil and Rock, J.A. Hunter and H.L. Crow (ed.), Geological Survey of Canada, Open File 7078, p. 62–66.

Quartero, E.M., Bechtel, D., Leier, A.J. and Bentley, L.R. (2014): Gamma-ray normalization of shallow well-log data with applications to the Paleocene Paskapoo Formation, Alberta; Canadian Journal of Earth Sciences, v. 51, p. 452–465.

Reimchen, T.H.F. (1980): Surficial geology, Dawson Creek, West of the Sixth Meridian, British Columbia; Geological Survey of Canada, Map 1467A, scale 1:250 000.

Stott, D.F. (1982): Lower Cretaceous Fort St. John Group and Upper Cretaceous Dunvegan Formation of the foothills and plains of Alberta, British Columbia, and District of Mackenzie and Yukon Territory; Geological Survey of Canada, Bulletin 328, 124 p.

Worden, C.B., Gerstenberger, M.C., Rhoades, D.A. and Wald, D.J. (2012): Probabilistic relationships between ground-motion parameters and modified Mercalli intensity in California; Bulletin of the Seismological Society of America, v. 102, p. 204–221.

Systematic Study of Earthquake Source Mechanism and Regional Stress Field in the Southern Montney Unconventional Play of Northeastern British Columbia (NTS 093P/09, 10, 15, 16, 094A/01, 02, 07, 08)

A. Babaie Mahani, Geoscience BC, Vancouver, British Columbia, ali.mahani@mahangeo.com

Babaie Mahani, A. (2020): Systematic study of earthquake source mechanism and regional stress field in the southern Montney unconventional play of northeastern British Columbia (NTS 093P/09, 10, 15, 16, 094A/01, 02, 07, 08); *in* Geoscience BC Summary of Activities 2019: Energy and Water, Geoscience BC, Report 2020-02, p. 13–18.

Introduction

The Western Canada Sedimentary Basin (WCSB) has experienced a significant increase in both the number and magnitude of earthquakes in the past decade due to fluid injection associated with hydraulic fracturing operations (Schultz et al., 2014; Rubinstein and Babaie Mahani, 2015; Atkinson et al., 2016; Bao and Eaton, 2016; Babaie Mahani et al., 2017; Kao et al., 2018). As a result, continuous improvements in earthquake detection have been made within the unconventional resources of the Montney and Duvernay formations, in northeastern British Columbia (BC) and western Alberta, through densification of seismographic networks (Salas et al., 2013; Salas and Walker, 2014; Schultz et al., 2015; Babaie Mahani et al., 2016). The addition of new seismographic stations, at close distances from injection sites, have provided the required data for detailed analysis of seismic activity, especially with regard to small-magnitude earthquakes (as low as 1.5) for which sufficient data had not been available.

The source mechanisms of induced earthquakes in the WCSB have been analyzed by several researchers using moment tensor inversion and P-wave first motions (Eaton and Babaie Mahani, 2015; Wang et al., 2016, 2017, 2018; Zhang et al., 2016). Overall, focal mechanisms show a combination of strike-slip and reverse faulting for the events occurring within the Montney and Duvernay formations and along the Rocky Mountain fold and thrust belt (RMFTB) in northeastern BC and western Alberta (Ristau et al., 2007; Babaie Mahani et al., 2017; Kao et al., 2018; Zhang et al., 2019).

In this study, data from local and regional seismographic stations were used to obtain focal mechanisms and parameters of the stress field for 66 earthquakes, which occurred between April 2018 and May 2019, in the southern Montney unconventional play of northeastern BC. These events occurred in an area to the south of Fort St. John and north of Dawson Creek, where multistage hydraulic fracturing operations have been conducted for several years (Figure 1; Babaie Mahani et al., 2016; Babaie Mahani and Kao, 2018). Residents in the area have felt events with small magnitudes (M) ranging from 1 to 2. Moreover, large peak ground accelerations (PGA) have been recorded at close hypocentral distances (<5 km) from events as small as M 3 (e.g., PGA of >0.1 g with 1 g = 9.8 m/s^2; Atkinson and Assatourians, 2017; Babaie Mahani and Kao, 2018).

Tectonic Setting

The main tectonic structure in the study area is the Fort St. John graben (FSJG), which is the predominant graben in the Dawson Creek graben complex. The FSJG was formed during the Carboniferous–Permian period by localized subsidence of the Peace River arch. The Golata, Kiskatinaw and Taylor Flat formations, of the Stoddart Group, successively infilled FSJG, all of them overlying the Debolt Formation. This succession was later overlain with the Permian Belloy and Triassic Montney, Doig, Halfway, Charlie Lake and Baldonnel formations (O'Connell, 1994; Petrel Robertson Consulting Inc., 2015).

Although grabens are associated with normal faulting, the subsidence of the Peace River arch and the formation of FSJG were coupled with strike-slip motion and related compressional and rotational movement during the graben's development (Barclay et al., 1990). The complex tectonic history of FSJG, including the Laramide orogenic phase, resulted in development of normal, strike-slip and reverse faults, which influenced the Carboniferous Debolt to the Triassic Doig formations (Berger et al., 2009; Dixon, 2011; Petrel Robertson Consulting Inc., 2015; Davies et al., 2018).

Dataset

Due to the increase in seismicity rate and occurrence of several felt events, the BC Oil and Gas Commission (BCOGC) implemented requirements for ground-motion monitoring based on PGA. The initial PGA reporting threshold of 0.02 g introduced in June 2016 was refined to 0.008 g in January 2018. In May 2018, BCOGC instituted the Kiskati-

---

This publication is also available, free of charge, as colour digital files in Adobe Acrobat® PDF format from the Geoscience BC website: http://www.geosciencebc.com/updates/summary-of-activities/.

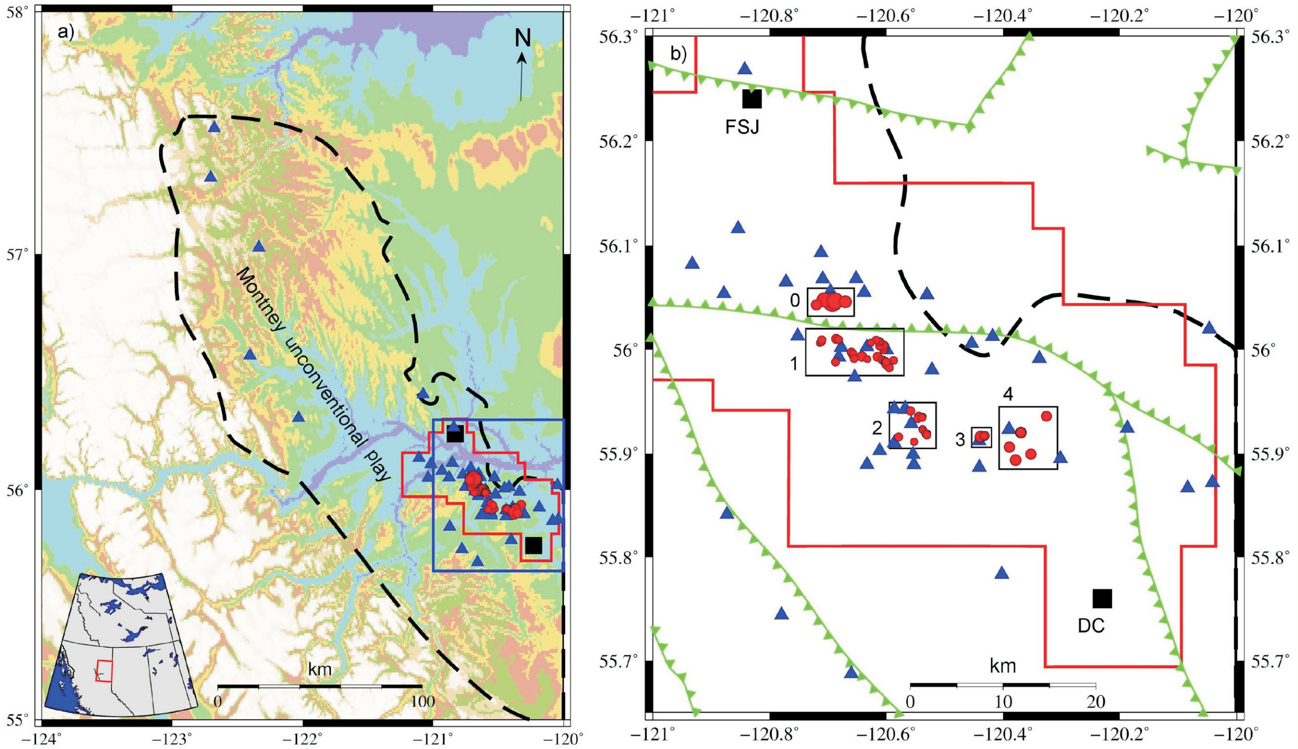

Figure 1. a) The Montney unconventional play (outlined with black dashed line) in northeastern British Columbia. Background image from Linquist et al. (2004) shows the topography. The study area is outlined with a solid blue line. The red line shows the outline of the Kiskatinaw Seismic Monitoring and Mitigation Area. Black solid squares indicate the major cities (FSJ, Fort St. John; DC, Dawson Creek). Earthquakes and seismographic stations are shown with circles and triangles, respectively. Inset map shows the geographic location of the study area with respect to western Canada. **b)** Study area with the areas of the five clusters outlined with solid black lines. Solid green lines show the normal faults associated with the Dawson Creek graben complex (from Davies et al., 2018). Triangles on fault lines depict the hanging wall.

naw Seismic Monitoring and Mitigation Area (KSMMA; Figure 1). Permit holders operating within KSMMA must report to BCOGC any felt event or ground motion equal to or above the assigned threshold in the form of a catalogue containing event parameters such as location, magnitude and ground motion values. Moreover, waveforms from seismographic stations that recorded the higher-than-threshold PGA must be submitted to BCOGC, which are made available to the public via BCOGC's eLibrary. Most of the events analyzed in this study are small in magnitude (M <2), therefore were only clearly recorded by local seismographic stations within 20 to 30 km of the epicentres. The largest event is the November 30, 2018, hydraulic fracturing–induced earthquake with moment magnitude of 4.6.

Although focal depths reported in earthquake catalogues are usually associated with large uncertainties, induced events within KSMMA mostly have depths in the range of 3 to 4 km, located within the lower Montney, Belloy and Debolt formations (Babaie Mahani and Kao, 2018). Figure 1 shows the distribution of 66 events for which focal mechanisms were obtained and the location of seismographic stations used in this study. These events were grouped into five clusters (0 to 4) based on the proximity of their locations.

Focal Mechanisms

In this study, focal mechanisms were obtained from the P-wave first motions using the vertical components of waveforms that were filtered by a 4th order Butterworth bandpass filter with corner frequencies of 1 and 3 Hz. The 1 Hz high-pass corner frequency was chosen to eliminate prominent long-period trends observed on the majority of seismograms, whereas the 3 Hz low-pass corner frequency was selected to obtain relatively simple waveforms suitable for phase picking. For the purpose of this study, the velocity model and the methodology described by Eaton and Babaie Mahani (2015) were followed to determine focal mechanisms. Near the surface, the velocity model incorporates two sedimentary layers totalling 4.5 km in thickness underlain by a 35 km thick crystalized basement. The crystalized basement is characterized by a linear velocity gradient with $V_0 = 6$ km/sec and gradient $k = 0.0229$ sec^{-1}. Takeoff angles were determined using this velocity model and ray-tracing results (Eaton and Babaie Mahani, 2015). For all of the solutions obtained here, a source depth of 5 km was assumed, which is situated 500 m below the base of the sedimentary basin. Although, based on the information provided from some hydraulic fracturing wells, depth to the basement can be less than 4.5 km in this area. Figure 2 shows that the

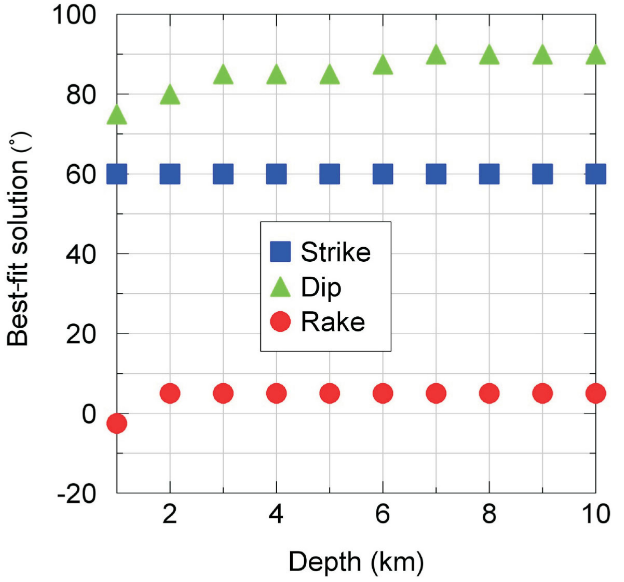

Figure 2. The effect of different depth assumptions on the results of the best-fit solution of focal mechanisms.

solutions are relatively insensitive to focal depth within a focal depth range of 2 to 10 km.

To ensure the reliability of focal mechanisms, only events with at least 10 P-wave polarities were considered. Following this criterion, focal mechanisms for 66 earthquakes were obtained. For each event, the parameters of the best fitting plane were calculated from the average and standard deviation of strike, dip and rake values of the trial focal mechanisms with the minimum associated error (Eaton and Babaie Mahani, 2015).

Overall, fault plane solutions show that the prevailing mechanism in all clusters (Figure 1b) is strike-slip with strike of the best fitting plane mostly ~60º in clusters 0, 1 and 2. For clusters 3 and 4, however, there is a wider range of strike directions. Moreover, dip angles of the best fitting plane are >20º with most planes having dip angles >60º. As an example, Figure 3 shows the focal mechanisms in cluster 1, which includes more earthquakes than the other clusters. In Figure 4, the compression (P) and extension (T) axes are shown for the focal mechanisms in each cluster based on the best fitting nodal plane. Although there is scatter in data points, the P and T axes mostly have low plunges with the trends of northeast-southwest and northwest-southeast, respectively. Similar results were obtained using the auxiliary nodal plane. The trends of the P and T axes are consistent with other studies for earthquakes in the WCSB and along the RMFTB (Ristau et al., 2007).

Stress Tensor Inversion

Focal mechanisms determined from the P-wave first motions or moment tensor inversion can be used to invert the stress tensor of a regional stress field (Michael, 1987). An important factor in stress inversion is to decide which nodal plane is the actual causative fault. Aftershock distribution or robust constraint on earthquake locations are usually

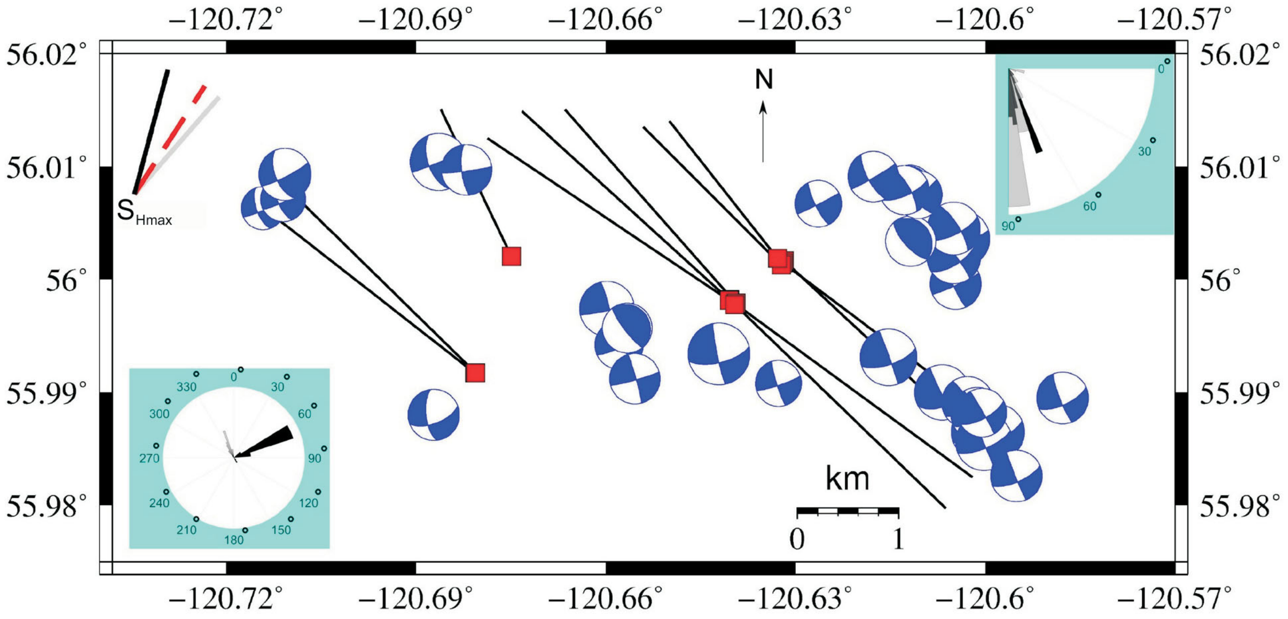

Figure 3. Focal mechanisms derived from P-wave first motions for events in cluster 1 (Figure 1b). The three lines in the upper left corner show the orientation of maximum horizontal stress from the World Stress Map (grey solid line; Heidbach et al., 2016) and from stress inversion results of this study using the best fitting (red dashed line) and auxiliary (solid black line) planes. Polar diagrams show the dip and strike distributions for the best fitting (black) and auxiliary (grey) nodal planes. Dark grey shows overlapping values. Squares show the location of the surface hole of the hydraulic fracturing wells in the area with black solid lines showing the surface projection of the horizontal extent of these wells.

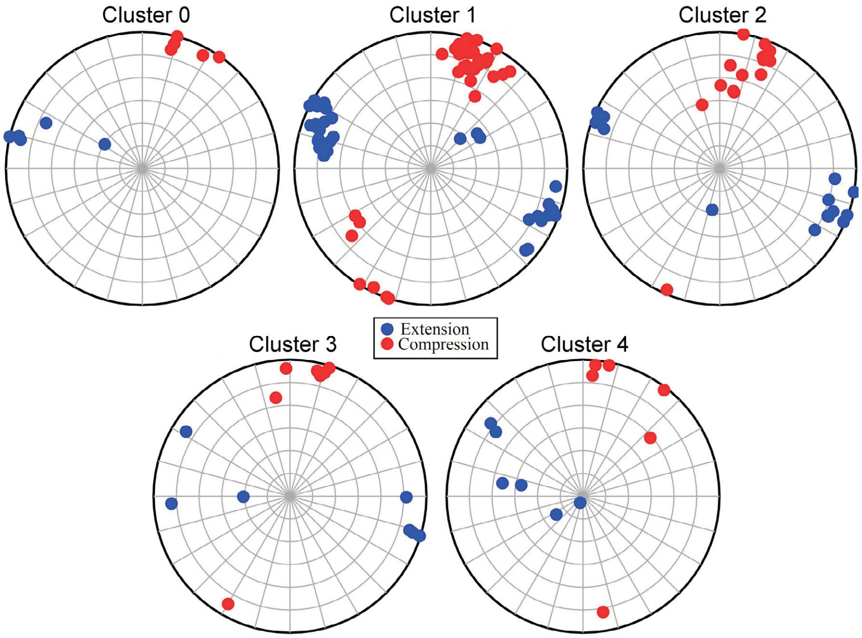

Figure 4. Orientation of the compression (P) and extension (T) axes for all the events in each cluster (Figure 1b). Results are shown for the best fitting nodal plane of the focal mechanisms.

good sources of information for this purpose. In this study, however, most events are small and there are statistically not enough events to unambiguously identify the fault orientation in each cluster. Here, the stress inversion is applied for both nodal planes and the results are compared with values from the World Stress Map (WSM; Heidbach et al., 2016).

Usually four parameters are calculated for the stress field using focal mechanisms; the orientation of three principal compressive stresses ($S_1>S_2>S_3$) and a relative measure of the magnitude of the intermediate principal stress (R; Etchecopar et al., 1981; Gephart and Forsyth, 1984; Lund and Townend, 2007) as

$$R = (S_1–S_2) / (S_1–S_3) \qquad (1)$$

The relative stress magnitude (R) quantifies whether the magnitude of the intermediate (S_2) principal stress is closer to the magnitude of the most (S_1) compressive principal stress or the least (S_3) compressive principal stress. Whereas small values of R imply that S_1 and S_2 are close in magnitude, large values of R imply that S_1 and S_3 have similar magnitudes.

Martinez-Garzon et al. (2014) provided a MATLAB package for stress inversion from earthquake focal mechanisms. Their inversion provides the orientation of S_1, S_2 and S_3 and R, thus suitable for the purpose of this study. Using the focal mechanism parameters (dip direction, dip and rake) in each cluster, stress inversion was applied in each cluster. Table 1 shows the trend and plunge of the best solutions for the three principal stresses and R in each cluster using both

Table 1. Results of stress inversion for each cluster based on the Martinez-Garzon et al. (2014) inversion module using both the best fitting (in bold) and the auxiliary nodal planes of focal mechanisms. The three principal compressive stresses are S_1, S_2 and S_3 and the relative stress magnitude is R. The trend of maximum horizontal stress (S_{Hmax}) is based on the relationships provided in Lund and Townend (2007). Trends are clockwise from north.

Cluster ID	Trend S_1 (°)	Plunge S_1 (°)	Trend S_2 (°)	Plunge S_2 (°)	Trend S_3 (°)	Plunge S_3 (°)	R	S_{Hmax} (°)
0	**33**	**3**	**310**	**68**	**122**	**22**	**0.8**	**32**
1	**34**	**2**	**307**	**56**	**122**	**33**	**0.8**	**33**
2	**26**	**3**	**290**	**63**	**118**	**27**	**0.6**	**30**
3	**21**	**1**	**289**	**56**	**112**	**34**	**0.8**	**22**
4	**22**	**2**	**290**	**40**	**115**	**50**	**0.9**	**22**
0	21	7	179	82	291	3	0.8	18
1	19	7	186	83	289	2	0.6	15
2	13	13	181	77	283	3	0.6	10
3	14	9	179	81	284	2	0.7	11
4	15	12	141	69	282	16	0.6	5

the best fitting and auxiliary nodal planes of focal mechanisms.

The best solution for S_1 has an average plunge of 2º and an average trend of 27º over all clusters using the best fitting nodal planes. On the other hand, average values of 10º and 17º were obtained for the plunge and trend of S_1 for the auxiliary nodal planes. The plunge of the best solution for S_3 is quite different between using the best fitting and the auxiliary planes of focal mechanisms. S_3 increases from 22º to 50º from cluster 0 to 4 with an average trend of 118º over all clusters when using the best fitting nodal plane. On the other hand, S_3 remains fairly horizontal for clusters 0, 1, 2 and 3 and increases to 16º in cluster 4 with an average trend of 286º using the auxiliary plane. As expected, the plunge of S_2 follows the opposite direction to S_3 and decreases from cluster 0 to 4 but remains closer to vertical for the case when the auxiliary plane was used in the stress tensor inversion.

Although, prior to stress inversion, the actual causative fault was not clear, the results from stress inversion are consistent between the best fitting and auxiliary nodal planes suggesting a major strike-slip component and a minor reverse mechanism for the earthquakes in this area. This can also be observed from the relative stress magnitude (R) in Table 1, suggesting a strike-slip/reverse faulting regime. Since S_1 and S_3 are not perfectly horizontal and S_2 is not vertical, the trend of S_1 is not exactly the same as the maximum horizontal stress (S_{Hmax}). In Table 1, the trend of S_{Hmax} is shown using the relationships provided by Lund and Townend (2007). In Figure 3, the trend of S_{Hmax} is plotted and compared with the value from WSM, which is from two borehole breakout measurements in the study area. The trend of S_{Hmax} from the best fitting nodal plane is close to the average trend value of 41º from WSM (Heidbach et al., 2016). The trend in the study area varies from 22º to 33º for the best fitting nodal plane and varies from 5º to 18º for the auxiliary nodal plane.

Conclusion

Focal mechanisms for several induced earthquakes caused by hydraulic fracturing within the Montney unconventional play of northeastern British Columbia were determined for this study. Using the polarities of the first P-wave motion, focal mechanisms for 66 events, for which there were at least 10 recordings each, were obtained. Magnitudes of these events were between 1.5 and 4.6 and were distributed in five clusters based on the proximity of epicentres. Results show that strike-slip movement is the prevailing source mechanism for the events in this area, although reverse faulting was also observed for a few earthquakes. The best fitting nodal plane mostly strikes at ~60º with most events having dip angles of >60º. For each cluster, the orientation of the three principal compressive stresses (S_1>S_2>S_3) and the relative intermediate principal stress magnitude (R) were calculated. Assuming the best fitting nodal plane to be the causative fault, the plunge of S_1 varies between 1º to 3º with its trend varying between 21º to 34º across the clusters. On the other hand, the plunge of S_3 varies between 22º and 50º with its trend varying between 112º and 122º. The relative stress magnitude shows values between 0.6 and 0.9 suggesting that the magnitude of the intermediate (S_2) and the least compressive stress (S_3) are similar, which is consistent with a strike-slip/reverse faulting regime. The trend of maximum horizontal stress (S_{Hmax}) was estimated from the four parameters (S_1, S_2, S_3, R) obtained during stress inversion. The trend of S_{Hmax} varies from 22º to 33º, using the best fitting nodal plane, which is slightly lower than the average trend of S_{Hmax} from the World Stress Map (41º).

Acknowledgments

The author thanks A. Gamp for his constructive comments on this manuscript. The author also appreciates P. Martinez-Garzon for her consultation on stress inversion. The Seismological Research Letters' editor in chief, A. Bent, and two anonymous reviewers are thanked for their thorough review of this paper. This work was partially supported by the BC Seismic Research Consortium (Geoscience BC, BC Oil and Gas Research and Innovation Society, Canadian Association of Petroleum Producers, BC Oil and Gas Commission and Yukon Geological Survey), the Natural Sciences and Engineering Research Council of Canada, and the Environmental Geoscience Program of Natural Resources Canada.

References

Atkinson, G.M. and Assatourians, K. (2017): Are ground-motion models derived from natural events applicable to the estimation of expected motions for induced earthquakes?; Seismological Research Letters, v. 88, p. 430–441.

Atkinson, G.M., Eaton, D., Ghofrani, H., Walker, D., Cheadle, B., Schultz, R., Scherbakov, R., Tiampo, K., Gu, Y.J., Harrington, R.M., Liu, Y., van der Baan, M. and Kao, H. (2016): Hydraulic fracturing and seismicity in the Western Canada Sedimentary Basin; Seismological Research Letters, v. 87, p. 631–647.

Babaie Mahani, A. and Kao, H. (2018): Ground motion from M 1.5 to 3.8 induced earthquakes at hypocentral distance <45 km in the Montney play of northeast British Columbia, Canada; Seismological Research Letters, v. 89, p. 22–34.

Babaie Mahani, A., Kao, H., Walker, D., Johnson, J. and Salas, C. (2016): Performance evaluation of the regional seismograph network in northeast British Columbia, Canada, for monitoring of induced seismicity; Seismological Research Letters, v. 87, p. 648–660.

Babaie Mahani, A., Schultz, R., Kao, H., Walker, D., Johnson, J. and Salas, C. (2017): Fluid injection and seismic activity in the northern Montney play, British Columbia, Canada, with special reference to the 17 August 2015 Mw 4.6 induced earthquake; Bulletin of Seismological Society of America, v. 107, p. 542–552.

Bao, X. and Eaton, D.W. (2016): Fault activation by hydraulic fracturing in western Canada; Science, v. 354, p. 1406–1409.

Barclay, J.E., Krause, F.F., Campbell, R.I. and Utting, J. (1990): Dynamic casting and growth faulting: Dawson Creek Graben Complex, Carboniferous-Permian Peace River Embayment, western Canada; Bulletin of Canadian Petroleum Geology, v. 38A, p. 115–145.

Berger, Z., Beast, M. and Mushayandebvu, M. (2009): The contribution of integrated HRAM studies to exploration and exploitation of unconventional plays in North America, part 2: basement structures control on the development of the Peace River Arch's Montney/Doig resource plays; The Reservoir, v. 36, p. 40–45.

Davies, G., Watson, N., Moslow, T. and MacEachern, J. (2018): Regional subdivisions, sequences, correlations, and facies relationships of the Lower Triassic Montney Formation, west-central Alberta to northeastern British Columbia, Canada, with emphasis on role of paleostructure; Bulletin of Canadian Petroleum Geology, v. 66, p. 23–92.

Dixon, J. (2011): A review of the character and interpreted origins of thick, mudstone-encased sandstone bodies in the Middle Triassic Doig Formation of western Canada; Bulletin of Canadian Petroleum Geology, v. 59, p. 261–276.

Eaton, D.W. and Babaie Mahani, A. (2015): Focal mechanisms of some inferred induced earthquakes in Alberta, Canada; Seismological Research Letters, v. 86, p. 1078–1085.

Etchecopar, A., Vasseur, G. and Daignieres, M. (1981): An inverse problem in microtectonics for the determination of stress tensors from fault striation analysis; Journal of Structural Geology, v. 3, p. 51–65.

Gephart, J.W. and Forsyth, D.W. (1984): An improved method for determining the regional stress tensor using earthquake focal mechanism data: application to the San Fernando earthquake sequence; Journal of Geophysical Research, v. 89, p. 9305–9320.

Heidbach, O., Rajabi, M., Reiter, K., Ziegler, M. and WSM Team (2016): World Stress Map, database release 2016, ver. 1.1; GFZ Data Services, URL <https://doi.org/10.5880/WSM.2016.001> [October 2019].

Kao, H., Hyndman, R.D., Jiang, Y., Visser, R., Smith, B., Babaie Mahani, A., Leonard, L., Ghofrani, H. and He, J. (2018): Induced seismicity in western Canada linked to tectonic strain rate: implications for regional seismic hazard; Geophysical Research Letters, v. 45, p. 11 104–11 115.

Lindquist, K.G., Engle, K., Stahlke, D. and Price, E. (2004): Global topography and bathymetry grid improves research efforts; Eos, Transactions, American Geophysical Union, v. 85, no. 19, p. 186, URL <http://onlinelibrary.wiley.com/doi/10.1029/2004EO190003/full> [November 2019].

Lund, B. and Townend, J. (2007): Calculating horizontal stress orientations with full or partial knowledge of the tectonic stress tensor; Geophysical Journal International, v. 170, p. 1328–1335.

Martinez-Garzon, P., Kwiatek, G., Ickrath, M. and Bohnhoff, M. (2014): MSATSI: a MATLAB package for stress inversion combining solid classic methodology, a new simplified user-handling, and a visualization tool; Seismological Research Letters, v. 85, p. 896–904.

Michael, A.J. (1987): Use of focal mechanisms to determine stress: a control study; Journal of Geophysical Research, v. 92, p. 357–368.

O'Connell, S.C. (1994): Geological history of the Peace River Arch; *in* Geological Atlas of the Western Canada Sedimentary Basin, G.D. Mossop and I. Shetsen (comp.), Canadian Society of Petroleum Geologists, Calgary, Alberta, and Alberta Research Council, Edmonton, Alberta, p. 431–438, URL <https://ags.aer.ca/reports/atlas-of-the-western-canada-sedimentary-basin.htm> [October 2019].

Petrel Robertson Consulting Inc. (2015): Characterization of Belloy and Debolt water disposal zones in the Montney play fairway, northeast B.C.; Geoscience BC, Report 2015-03, 45 p., URL <http://www.geosciencebc.com/reports/gbcr-2015-03/> [October 2019].

Ristau, J., Rogers, G.C. and Cassidy, J.F. (2007): Stress in western Canada from regional moment tensor analysis; Canadian Journal of Earth Sciences, v. 44, p. 127–148.

Rubinstein, J.L. and Babaie Mahani, A. (2015): Myths and facts on wastewater injection, hydraulic fracturing, enhanced oil recovery, and induced seismicity; Seismological Research Letters, v. 86, p. 1060–1067.

Salas, C.J. and Walker, D. (2014): Update on regional seismograph network in northeastern British Columbia (NTS 094C, G, I, O, P); *in* Geoscience BC Summary of Activities 2013, Geoscience BC, Report 2014-01, p. 123–126, URL <http://cdn.geosciencebc.com/pdf/SummaryofActivities2013/SoA2013_SalasWalker.pdf> [October 2019].

Salas, C.J., Walker, D. and Kao, H. (2013): Creating a regional seismograph network in northeastern British Columbia to study the effect of induced seismicity from unconventional gas completions (NTS 094C, G, I, O, P); *in* Geoscience BC Summary of Activities 2012, Geoscience BC, Report 2013-01, p. 131–134, URL <http://cdn.geosciencebc.com/pdf/SummaryofActivities2012/SoA2012_Salas_Seismograph_Network.pdf> [October 2019].

Schultz, R., Stern, V. and Gu, Y.J. (2014): An investigation of seismicity clustered near the Cordel Field, west central Alberta, and its relation to a nearby disposal well; Journal of Geophysical Research, v. 119, p. 3410–3423.

Schultz, R., Stern, V., Gu, Y.J. and Eaton, D. (2015): Detection threshold and location resolution of the Alberta Geological Survey earthquake catalogue; Seismological Research Letters, v. 86, p. 385–397.

Wang, R., Gu, Y.J., Schultz, R. and Chen, Y. (2018): Faults and non-double-couple components for induced earthquakes; Geophysical Research Letters, v. 45, p. 8966–8975.

Wang, R., Gu, Y.J., Schultz, R., Kim, A. and Atkinson, G. (2016): Source analysis of a potential hydraulic-fracturing-induced earthquake near Fox Creek, Alberta; Geophysical Research Letters, v. 43, p. 564–573.

Wang, R., Gu, Y.J., Schultz, R., Zhang, M. and Kim, A. (2017): Source characteristics and geological implications of the January 2016 induced earthquake swarm near Crooked Lake, Alberta; Geophysical Journal International, v. 210, p. 979–988.

Zhang, H., Eaton, D.W., Li, G., Liu, Y. and Harrington, R.M. (2016): Discriminating induced seismicity from natural earthquakes using moment tensors and source spectra; Journal of Geophysical Research, v. 121, p. 972–993.

Zhang, H., Eaton, D.W., Rodriguez, G. and Jia, S.Q. (2019): Source mechanism analysis and stress inversion for hydraulic-fracturing-induced event sequences near Fox Creek, Alberta; Bulletin of Seismological Society of America, v. 109, p. 636–651.

Determination of Factors Controlling Geological Susceptibility to Induced Seismicity in the Montney Formation, Northeastern British Columbia and Northwestern Alberta, Based on a Machine-Learning Approach

P. Wozniakowska[1], **Department of Geoscience, University of Calgary, Calgary, Alberta, paulina.wozniakowska@ucalgary.ca**

D.W. Eaton, Department of Geoscience, University of Calgary, Calgary, Alberta

Wozniakowska, P. and Eaton, D.W. (2020): Determination of factors controlling geological susceptibility to induced seismicity in the Montney Formation, northeastern British Columbia and northwestern Alberta, based on a machine-learning approach; *in* Geoscience BC Summary of Activities 2019: Energy and Water, Geoscience BC, Report 2020-02, p. 19–26.

Introduction

A significant increase in the seismicity rate in western Canada in recent years has been associated with the development of unconventional oil and gas reserves, including hydraulic fracturing (Bao and Eaton, 2016) and saltwater disposal (Schultz et al., 2014). Because of incomplete understanding of the underlying spatial-temporal distribution, induced seismicity is a subject of extensive academic research (Baranova et al., 1999; Ellsworth, 2013; Gugliemi et al., 2015). Incomplete information and lack of continuous data hinder a full understanding of the distribution of seismic events, which is potentially linked to seismic hazard in the Western Canadian Sedimentary Basin (WCSB; Ghofrani et al., 2019). Therefore, understanding the mechanisms controlling the geological susceptibility to induced earthquakes is crucial for both seismic-hazard assessment and seismic-risk mitigation. Additionally, it is still not well understood why most hydraulic-fracturing and wastewater-disposal operations are not triggering higher magnitude earthquakes (Ellsworth, 2013). The goal of this project is to identify the most important factors controlling the occurrence of induced earthquakes in the Montney Formation, in northeastern British Columbia (BC) and northwestern Alberta. This will provide a source of additional information, which could help manage more effectively the seismicity induced by oil- and gas-production activities.

Monitoring of induced seismicity can significantly enhance the quality of hydraulic-fracturing stimulation, providing valuable information about the created fracture network and the reservoir mechanics (Eaton, 2018). Large volumes of data, in conjunction with the complex relations between different geological, physical and geomechanical characteristics, significantly hamper the correct interpretation of the phenomena observed in the subsurface. Due to its ability to discover hidden patterns, machine learning has proven to be a helpful tool for geoscientists and its popularity is growing. The focus of this paper was to assess the importance of properties controlling seismic activity during hydraulic-fracturing operations in the Montney Formation. Current knowledge was combined with existing technological advancements to test the common hypotheses about the nucleation of induced seismic events. An analysis was performed using decision-tree and random-forest algorithms, both of which are examples of supervised machine learning.

Methodology

Understanding the occurrence of induced seismic events requires a broad comprehension of the mechanisms in the subsurface and characteristics of the study area. In this study, geological, geomechanical and tectonic indicators were analyzed to estimate the influence of each characteristic on seismogenic potential for the analyzed wells. Parameters were extracted from the collection of compiled characteristics, including, among others, distance from the Rocky Mountain fold-and-thrust belt, distance from known lineaments, distribution of reservoir overpressures and vertical distance to the Debolt Formation (see below).

Overall, more than 6300 hydraulically fractured horizontal wells drilled into the Montney Formation were analyzed in this study. Wells were investigated in terms of their geological characteristics and whether seismicity occurred during or shortly after hydraulic fracturing. Ultimately, the final number of wells was determined by the quality and availability of data (see below).

The project consisted of the following steps:

1) Data collection and preparation:
   a) compilation of data from publicly available sources
   b) data preprocessing (data interpolation, incorrect data identification and removal)

---

[1] *The lead author is a 2019 Geoscience BC Scholarship recipient.*

This publication is also available, free of charge, as colour digital files in Adobe Acrobat® PDF format from the Geoscience BC website: http://www.geosciencebc.com/updates/summary-of-activities/.

   c) labelling wells as seismogenic/nonseismogenic (binary classification)
2) Algorithm development
3) Feature importance analysis

Data Collection and Preparation

Output Values (Target) Determination

To implement the supervised machine-learning algorithm, it was necessary to decide on the appropriate output values. In this project, induced seismicity was considered as a binary-classification problem with respect to the observed seismic activity correlated in time and space with the coinciding hydraulic-fracturing operations. A similar methodology was introduced by Pawley et al. (2018), who investigated the potential for induced seismicity in the Duvernay Formation in Alberta caused by hydraulic fracturing and wastewater disposal. Their research revealed that seismogenic potential in the Duvernay Formation is controlled primarily by the vertical distance to the Precambrian basement, the state of stress in the formation (specifically, overpressure) and the value of the minimum horizontal stress. Due to significant differences in geological setting in the case of the Montney Formation and limited data availability, a similar study was performed using a slightly different set of input features in the analysis. Moreover, only horizontal wells were considered, as they are more likely to cause a change in the stress state and pore pressure near the faults (Atkinson et al., 2016), and are therefore more likely to result in higher magnitude induced earthquakes. Similarly, as in the study by Pawley et al. (2018), wells were flagged as seismogenic, when at least one seismic event of magnitude (M) >2.5 was located closer than 5 km from the well. This condition was valid only when the date of the injection preceded the occurrence of the seismic event and occurred no later than three months after the hydraulic-fracturing operation was completed. Wells which had no observable seismic activity near the hydraulic-fracturing operations were considered as nonseismogenic.

Input Values (Parameters) Preparation

Data used in this study were compiled from publicly available sources, which included geoSCOUT (geoLOGIC systems Ltd., 2019), BC Oil and Gas Commission (BC Oil and Gas Commission, 2019) and Alberta Energy Regulator (AER; Mossop and Shetsen, 1994) databases, as well as the Composite Alberta Seismicity Catalogue (Fereidoni and Cui, 2015). In total, 6315 oil- and gas-producing horizontal wells drilled into the Montney in BC and Alberta were analyzed. Earthquake data were sourced from the Canadian Induced Seismicity Collaboration (2019) website and included the seismic events registered before April 27, 2019. It is worth noting that the analyzed dataset does not include all the Montney horizontal wells, only those with complete (and validated) information.

Pressure Data

Previous literature examples demonstrate the relationship between the formation pressure and occurrence of seismic events (Eaton and Schultz, 2018). Here, pressure data were gathered using the geoSCOUT database and complemented with data published on the BCOGC website. Due to data sparsity and the limited number of measurements, the pressure-gradient values have been estimated using a radial basis function (RBF) interpolation method with linear kernel, which is included in the scipy interpolation Python module (Jones et al., 2001; van Rossum and Drake, 2003). A total of 2376 pressure measurements were used to calculate the pressure gradient; obtained pressure gradients ranged from 0.6 to about 20.6 kPa/m. Previous studies (e.g., Eaton and Schultz, 2018) have revealed that reservoir overpressure (areas where the pressure gradient exceeds a hydrostatic gradient value of 10 kPa/m) has the potential to influence the overall susceptibility to induced seismicity.

Regional Stress Regime

In addition to reservoir pore pressure, information about maximum horizontal-stress (S_{Hmax}) direction was another parameter characterizing the stress regime of the analyzed area. In some cases, fault orientation seems to be conformable with the regional stress field (Snee and Zoback, 2016), whereas examination of other studies suggests the potential for fault activation irrespective of their geometry (Zoback and Zoback, 1989). This implies that the regional stress direction may have a strong impact on the seismicity observed in the given area. The direction of S_{Hmax} has been investigated based on the values of S_{Hmax} azimuths from the World Stress Map (Heidbach et al., 2016), an open-access public database. These values were limited to the vicinity of the Montney Formation subcrop region and interpolated using RBF with linear kernel. Overall, 133 data points were used in the calculation, relying on stress-state variations instead of absolute values as the major factor. The difference between the S_{Hmax} direction and the average value of the S_{Hmax} azimuth observed in the WCSB (estimated to be about 45°) was used in the calculation.

Tectonic Data

Tectonically, the presence of pre-existing conductive thrust faults in the Precambrian crystalline basement (Zhang et al., 2013) as well as proximity to the Precambrian basement (Skoumal et al., 2018) are believed to influence the occurrence of natural and induced earthquakes. Within the WCSB, most of the seismic events tend to be concentrated within a band stretching between the eastern margin of the Cordilleran foreland thrust-and-fold belt and so-called undisturbed WCSB, which represent the margins of the regional seismicity. It was previously observed that the induced seismicity was most common in the vicinity of disturbed belt for two reasons: the high concentration of deep, critically stressed, pre-existing faults that are more likely to be reactivated near the treatment wells (BC Oil and Gas Commission, 2014) and the role of the tectonic-strain rate, which is surmised to have a long-term impact on seismic potential (Kao et al., 2018). To address these hypotheses, distance from the disturbed belt was included into the analysis, together with the distance to minor lineaments indicating the potential locations of minor faults.

Stratigraphic Data

In previous studies, it was suggested that the risk of induced seismicity increased where hydraulic-fracturing operations in the Montney were performed at close distance to the crystalline basement (Skoumal et al., 2015). By also taking into consideration the Debolt Formation, which could represent a geomechanical basement, the impact of those two formations on the overall seismic-activity potential can be compared. Information about the tops of the Debolt Formation and Precambrian basement was implemented as the vertical distance between the hydraulic-fracturing operations (defined by the true vertical depth [TVD] of the well) and upper boundaries of both stratigraphic units. The Montney Formation tops were incorporated into the analysis indirectly, as one of the components of the depth factor described in detail below. Montney and Debolt formation tops were compiled from the geoSCOUT and BCOGC databases, whereas Precambrian basement-top information was sourced from the isopach and structure surface grid data collection available on the AER website. As in the case of the pressure gradient, the linear kernel variant of the RBF interpolation method was used to estimate the depths to the stratigraphic tops of the Montney and Debolt formations, and Precambrian basement.

Depth Factor

Due to the discrepancy between the levels of seismicity observed for hydraulic-fracturing operations performed in the upper, middle and lower units of the Montney Formation, establishing a possible relationship between the phenomena and the depth of injection could help further investigate any potential correlation between the induced seismicity and respective zones. In general, the lower Montney is characterized by higher induced seismic susceptibility; however, some significant seismicity is still observed in both the upper and middle units of the formation (BC Oil and Gas Commission, 2014). One possible explanation is the smaller vertical distance separating the lower unit from the underlying formations compared to the upper and middle Montney units rich in natural fractures (Nieto et al., 2018). In this study, a simple depth factor was implemented to provide a simplified way to divide the Montney into upper, middle and lower units, assuming the vertical division of the formation into three equal layers. Depth factor 'd' was calculated using the following equation:

$$d = (Z_w - Z_t) / Z_{th} \tag{1}$$

where Z_w is the TVD of the well, Z_t is the top of the Montney Formation at the location of the well, and Z_{th} is the thickness of the Montney at the location of the well.

Interpolation may carry the risk of incorrect estimation of the interpolated values. Parameter 'd' was implemented to detect the wells not matching the physical scenarios and guarantee the maximal correctness of the input data. Considering only wells drilled into the Montney interval, the depth factor should range between values 0 and 1. Values <0 indicate that the well was drilled above the top of the Montney Formation, whereas values >1 indicate that the well was drilled below the Montney. Therefore, 'd' values beyond the established range (0–1) suggest errors were made in measuring the formation top, thickness and/or well TVD. Such wells were excluded from further analysis, resulting in the final dataset consisting of 6315 wells. The depth factor was included into the models as a numerical value; however, further investigation revealed additional information about the analyzed wells.

Supposing the division of the Montney into three equal parts, it is possible to use the depth factor to differentiate between the Montney units associated with each well. According to this approach

- a 'd' value in the range of <0 to <0.34 corresponds here to the upper Montney;
- a 'd' value in the range of ≤0.34 to <0.67 corresponds here to the middle Montney; and
- a 'd' value in the range of ≤0.67 to <1 corresponds here to the lower Montney.

Table 1 presents the number of wells assigned to each specific unit of the Montney Formation using the described method.

It can be observed that the percentage of high-magnitude (M >2.5) events induced by hydraulic-fracturing operations is the highest for the wells drilled in the lower Montney, which is consistent with the hypothesis that this unit is more prone to seismic activity. At the same time, it has the fewest number of wells drilled, most of the wells having been drilled into the upper Montney unit.

Assigning Features to the Wells and Preprocessing

The value of each feature characterizing the corresponding wells was assigned using the NNjoin plugin (Tveite, 2019)

Table 1. Numbers and percentages of seismogenic and nonseismogenic wells corresponding to each of the Montney Formation units associated with M >2.5 induced seismic events.

Montney unit	Seismogenic wells		Nonseismogenic wells	
	Number	%	Number	%
upper	23	0.68	3354	99.32
middle	12	0.5	2408	99.5
lower	5	0.97	513	99.03

in QGIS, an open-source geographic information system (QGIS Development Team, 2019). The plugin allows the user to join two points from corresponding layers using the nearest neighbour method (i.e., linking points with the shortest distance). Collected features required preprocessing, which included missing-data identification and handling. For the wells that did not have data determined directly (such as formation tops, pressure and S_{Hmax} values), it was necessary to assign and use the interpolated values. In the next step, quality-control measures helped to determine only those wells that could assure the most reliable results. Due to the high number of wells with interpolated values, some of the interpolated values did not match realistic values. Data were analyzed in terms of the sequence of stratigraphic tops (Montney top – Debolt top – Precambrian top) and well TVD, with respect to the depth of the Montney top.

Algorithm Development

Determination of seismogenic potential related to the geological and geomechanical conditions in the subsurface was defined as a binary-classification problem, in which the algorithm assigns the labels according to the predicted classes (seismogenic/nonseismogenic). Two supervised learning techniques were analyzed with respect to their ability to determine the feature importance when predicting the class: decision-tree and random-forest classifiers (these are examples of tree-based methods).

In general, a decision-tree algorithm constructs the classification (or regression) tree composed of the leaves (estimated attributes) and nodes that split the data according to given conditions (Usuelli, 2014). The algorithm chooses the most important features and separates the samples into two groups until it satisfies the required conditions. Decision trees are expected to give better results than classical methods, such as linear regression, when nonlinear and complex relationships between the data are analyzed (James et al., 2013). Moreover, decision trees can be presented graphically, which makes them easier and more intuitive to interpret.

The random-forest classifier (similar to bagging and boosting machine-learning methods) is an improved and more powerful version of decision-tree algorithms (James et al., 2013) and uses sets of multiple trees to build the predictive models instead of only one. When building a random forest, small, randomly chosen collections of features are considered for splitting the nodes instead of a whole set of predictors. As a result, the feature used for splitting each node is chosen from among a limited number of available characteristics. This approach guarantees a decrease of variance between the single trees, which is desirable when building the machine-learning models.

One of the attributes of the analyzed dataset was the disproportionate size of the two classes. In other words, only a small percentage of the wells were associated with induced seismicity. To overcome this problem (which might lead to biased analysis), stratified random sampling was implemented. Stratified random sampling requires the division of the whole dataset into smaller subgroups (stratas) so that each subgroup corresponds to its class. In the next step, a random sample was drawn independently from each subgroup (Cochran, 2007).

Both models were built using Scikit-learn, a Python library for machine learning (Pedregosa et al., 2011), and trained on the number of 100 randomly shuffled stratified splits, with the training set accounting for 75% of the whole dataset and 25% for the test set. Figure 1 presents the feature importance indicated by both classification algorithms.

Discussion

Based on the decision-tree algorithm, the most important features were determined to be the distance to lineaments and the disturbed belt, the depth factor, the vertical distance to the Debolt Formation, and the vertical distance to the Precambrian basement. The results confirm the currently existing hypotheses about the influence of the tectonic setting of the wells, both in terms of distance to the faulted disturbed belt as well as known lineaments. The high importance of the depth factor potentially indicates the higher seismic risk in the lower Montney; however, this feature should be analyzed further. In contrast, the variation of the S_{Hmax} with respect to the regional stress state does not seem to influence the seismogenic potential. Surprisingly, the pressure gradient was indicated as the least important of all analyzed features, which contradicts the idea proposed by Eaton and Schultz (2018). However, this result could be biased as there were insufficient measurements of pore pressure. A different distribution of the important features might be observed for a dataset containing more exact pressure values. Comparing these results to those obtained using the second algorithm, the random-forest classifier identifies the same set of features as those with the most influence on the seismogenic potential, with similar feature-importance values. At the same time, the random-forest classifier showed a significant decrease in the error rate, which suggests a higher accuracy of the results.

It is worth noting that the machine-learning models are dependent on the quality (and quantity) of the input data. Therefore, the next step of this project is to perform extensive research and include additional parameters that may have an impact on the distribution of induced seismicity. The analysis in this study was limited to publicly available datasets only and some assumptions (e.g., the ratio between Montney intervals) were introduced. Additionally, several of the input parameters (formation tops and pressure, S_{Hmax} azimuths) were interpolated, which might mean they could

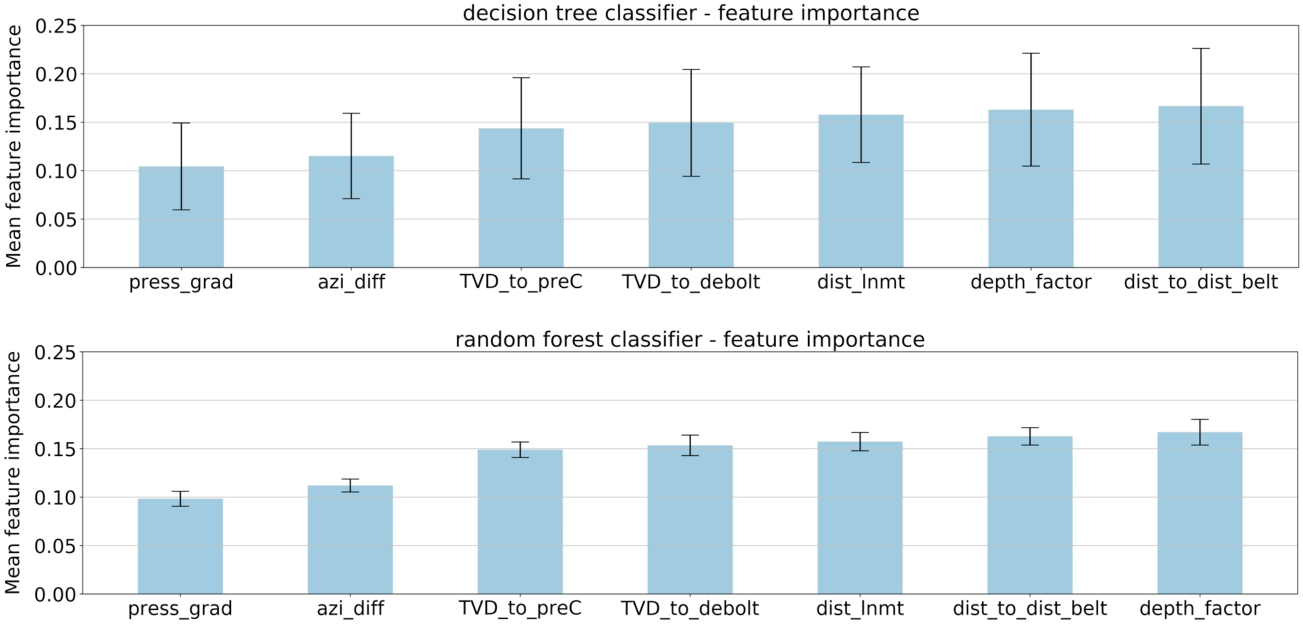

Figure 1. Feature importance calculated using decision-tree (**top**) and random-forest (**bottom**) classification algorithms. Results are presented in ascending order toward the right: pressure gradient (press_grad); maximum horizontal-stress azimuth variance (azi_diff); vertical distance from the well to the Precambrian basement and Debolt Formation (TVD_to_preC and TVD_to_debolt, respectively); distance to lineaments (dstm_lnmt); distance to the disturbed thrust-and-fold belt (dist_to_dist); and depth factor. Abbreviation: TVD, true vertical depth.

vary from the real values. Another problem is the incompleteness of data that cannot be interpolated, such as the location of unknown faults (especially strike-slip faults, which are undetectable using seismic methods). Incorporating more detailed information as well as new attributes into the algorithm will provide more accurate estimates of the geological susceptibility to induced seismicity.

Conclusions

This analysis revealed that three types of features are controlling the geological susceptibility to induced seismicity in the Montney Formation:

- the tectonic setting (specifically the distance from the disturbed belt and lineaments)
- the stratigraphy (vertical distance from the Debolt and Precambrian basement)
- the depth of the injection relative to the Montney Formation top, which correlates with the specific Montney unit (upper, middle and lower) stimulated during hydraulic fracturing.

Observations confirmed the current hypotheses about the factors controlling the induced seismicity. Pore-pressure gradient as well as variance of the S_{Hmax} from the average value were interpreted as less significant in the overall prediction of the induced seismicity for a given dataset. Moreover, a newly introduced parameter, the depth factor, confirms the current hypothesis about the higher susceptibility to induced seismicity in the lower Montney, compared to the upper and middle units. Overall, tree-based methods performed well and helped to address currently established conclusions about the factors controlling the occurrence of induced seismicity during hydraulic-fracturing operations. Including more detailed characteristics and additional features will increase the confidence level of the results and can provide information about the mechanisms responsible for the occurrence of induced seismicity.

Acknowledgments

The authors thank Geoscience BC and the Microseismic Industry Consortium for their financial support. They thank M. Hayes for his help in compiling the pressure data from the BC Oil and Gas Commission database. The authors also thank R. Weir for his comments that helped to improve this manuscript.

References

Atkinson, G.M., Eaton, D.W., Ghofrani, H., Walker, D., Cheadle, B., Schultz, R., Shcherbakov, R., Tiampo, K., Gu, J., Harrington, R.M. and Liu, Y. (2016): Hydraulic fracturing and seismicity in the western Canada sedimentary basin; Seismological Research Letters, v. 87, no. 3, p. 631–647, URL <https://pubs.geoscienceworld.org/ssa/srl/article/87/3/631/315665/Hydraulic-Fracturing-and-Seismicity-in-the-Western> [March 2016].

Bao, X. and Eaton, D. W. (2016): Fault activation by hydraulic fracturing in western Canada; Science, v. 354, no. 6318, p. 1406–1409, URL <https://science.sciencemag.org/content/354/6318/1406.full> [December 2016].

Baranova, V., Mustaqeem, A. and Bell, S. (1999): A model for induced seismicity caused by hydrocarbon production in the Western Canada Sedimentary Basin; Canadian Journal of Earth Sciences, v. 36, no. 1, p. 47–64, URL <https://www.nrcresearchpress.com/doi/10.1139/e98-080#.XaUv9fd7nV8> [January 1999].

BC Oil and Gas Commission (2014): Investigation of observed seismicity in the Montney Trend; BC Oil and Gas Commission, Technical Report, 32 p., URL <https://www.bcogc.ca/investigation-observed-seismicity-montney-trend> [December 2014].

BC Oil and Gas Commission (2019): BC Oil and Gas open data portal; data download web application, URL <https://data-bcogc.opendata.arcgis.com/> [July 2019].

Canadian Induced Seismicity Collaboration (2019), Catalogues website, URL <https://www.inducedseismicity.ca/catalogues/> [June 2019].

Cochran, W.G. (2007): Sampling Techniques (3rd edition); John Wiley and Sons, Inc., New York, New York, 442 p.

Eaton, D.W. (2018): Passive Seismic Monitoring of Induced Seismicity: Fundamental Principles and Application to Energy Technologies; Cambridge University Press, Cambridge, United Kingdom, 360 p.

Eaton, D. W. and Schultz, R. (2018): Increased likelihood of induced seismicity in highly overpressured shale formations; Geophysical Journal International, v. 214, no. 1, p. 751–757, URL <https://academic.oup.com/gji/article/214/1/751/4995198> [May 2018].

Ellsworth, W. L. (2013): Injection-induced earthquakes; Science, v. 341, no. 6142, 7 p., URL <https://science.sciencemag.org/content/341/6142/1225942.full> [July 2013].

Fereidoni, A. and Cui, L. (2015): Composite Alberta Seismicity Catalog: CASC2014-x: URL <https://www.inducedseismicity.ca/wp-content/uploads/2015/01/Composite-Alberta-Seismicity-Catalog3.pdf> [June 2019].

geoLOGIC systems ltd. (2019): geoSCOUT version 8.12; geoLOGIC systems ltd., mapping, data management and analysis software, URL <https://www.geologic.com/products/geoscout/> [August 2019].

Ghofrani, H., Atkinson, G.M., Schultz, R. and Assatourians, K. (2019): Short-term hindcasts of seismic hazard in the western Canada sedimentary basin caused by induced and natural earthquakes; Seismological Research Letters, v. 90, no. 3, p. 1420–1435, URL <https://pubs.geoscienceworld.org/ssa/srl/article/90/3/1420/530744/Short-Term-Hindcasts-of-Seismic-Hazard-in-the> [April 2019].

Guglielmi, Y., Cappa, F., Avouac, J.P., Henry, P. and Elsworth, D. (2015): Seismicity triggered by fluid injection–induced aseismic slip; Science, v. 348, no. 6240, p. 1224–1226, URL <https://science.sciencemag.org/content/348/6240/1224> [June 2015].

Heidbach, O., Rajabi, M., Cui, X., Fuchs, K., Müller, B., Reinecker, J., Reiter, K., Tingay, M., Wenzel, F., Xie, F., Ziegler, M.O., Zoback, M.-L. and Zoback, M.D. (2018): The World Stress Map database release 2016: Crustal stress pattern across scales; Tectonophysics, v. 744, p. 484–498, URL <https://doi.org/10.1016/j.tecto.2018.07.007> [June 2019].

James, G., Witten, D., Hastie, T. and Tibshirani, R. (2013): An Introduction to Statistical Learning – with Applications in R; Springer-Verlag, New York, New York, 426 p.

Jones, E., Oliphant, T. and Peterson, P. (2016): SciPy: Open source scientific tools for Python; SciPy Developers, URL <http://www.scipy.org/> [August 2019].

Kao, H., Hyndman, R., Jiang, Y., Visser, R., Smith, B., Babaie Mahani, A., Leonard, L., Ghofrani, H. and He, J. (2018): Induced seismicity in western Canada linked to tectonic strain rate: implications for regional seismic hazard; Geophysical Research Letters, v. 45, no. 20, p. 11–104, URL <https://agupubs.onlinelibrary.wiley.com/doi/full/10.1029/2018GL079288> [October 2018].

Mossop, G.D. and Shetsen, I., compilers (1994): Precambrian structure from back model grid, elevation (m); in Geological Atlas of the Western Canada Sedimentary Basin, G.D. Mossop and I. Shetsen (comp.), Canadian Society of Petroleum Geologists and Alberta Research Council, isopach and structure surface grid data, URL <https://ags.aer.ca/publications/isopach-and-structure-surface-grid-data.htm> [July 2019].

Nieto, J., Bialowas, B., Batlai, B. and Janega, G. (2018): Managing induced seismicity in Canbriam's Altares field in the Montney Formation, N.E. British Columbia – an update; Canadian Society of Exploration Geophysicists, Recorder, v. 43, no. 7, URL <https://csegrecorder.com/articles/view/managing-induced-seismicity-in-canbriams-altares-field-in-the-montney-fm> [December 2018].

Pawley, S., Schultz, R., Playter, T., Corlett, H., Shipman, T., Lyster S. and Hauck, T. (2018): The geological susceptibility of induced earthquakes in the Duvernay play; Geophysical Research Letters, v. 45, no. 4, p. 1786–1793, URL <https://agupubs.onlinelibrary.wiley.com/doi/full/10.1002/2017GL076100> [February 2018].

Pedregosa, F., Varoquaux, G., Gramfort, A., Michel, V., Thirion, B., Grisel, O., Blondel, M., Prettenhofer, P., Weiss, R., Dubourg, V. and Vanderplas, J. (2011): Scikit-learn: machine learning in Python; Journal of Machine Learning Research, v. 12, p. 2825–2830, URL <http://www.jmlr.org/papers/v12/pedregosa11a> [August 2019].

QGIS Development Team (2019): QGIS Geographic Information System; Open Source Geospatial Foundation Project, URL <http://qgis.osgeo.org> [August 2019].

Schultz, R., Stern, V. and Gu, Y. J. (2014): An investigation of seismicity clustered near the Cordel Field, west central Alberta, and its relation to a nearby disposal well; Journal of Geophysical Research – Solid Earth, v. 119, no. 4, p. 3410–3423, URL <https://agupubs.onlinelibrary.wiley.com/doi/full/10.1002/2013JB010836> [April 2014].

Skoumal, R.J., Brudzinski, M.R. and Currie, B.S. (2015): Earthquakes induced by hydraulic fracturing in Poland Township, Ohio; Seismological Society of America, Bulletin, v. 105, no. 1, p. 189–197, URL <https://pubs.geoscienceworld.org/ssa/bssa/article/105/1/189/323441/Earthquakes-Induced-by-Hydraulic-Fracturing-in> [January 2015].

Skoumal, R.J., Brudzinski, M.R. and Currie, B.S. (2018): Proximity of Precambrian basement affects the likelihood of induced seismicity in the Appalachian, Illinois, and Williston Basins, central and eastern United States; Geosphere, v. 14, no. 3, p. 1365–1379, URL <https://pubs.geoscienceworld.org/gsa/geosphere/article/14/3/1365/530435/Proximity-of-Precambrian-basement-affects-the> [April 2018].

Snee, J.E.L. and Zoback, M.D. (2016): State of stress in Texas: implications for induced seismicity; Geophysical Research Letters, v. 43, no. 19, p. 10–208, URL <https://

agupubs.onlinelibrary.wiley.com/doi/full/10.1002/2016GL070974> [December 2016].Tveite, H. (2019): NNJoin QGIS Plugin, version 1.3.3; NNJoin 3.3.3 documentation, URL <http://arken.nmbu.no/~havatv/gis/qgisplugins/NNJoin> [August 2019]

Usuelli, M. (2014): R Machine Learning Essentials; Packt Publishing Limited, Birmingham, United Kingdom, 218 p.

van Rossum, G. and Drake, F.L. (2001): Python reference manual; PythonLabs, release 2.0.1, URL <https://docs.python.org/2.0/ref/ref.html> [November 2019].

Zhang, Y., Person, M., Rupp, J., Ellett, K., Celia, M.A., Gable, C.W., Bowen, B., Evans, J., Bandilla, K., Mozley, P. and Dewers, T. (2013): Hydrogeologic controls on induced seismicity in crystalline basement rocks due to fluid injection into basal reservoirs; Groundwater, v. 51, no. 4, p. 525–538, URL <https://ngwa.onlinelibrary.wiley.com/doi/full/10.1111/gwat.12071> [June 2013].

Zoback, M.L. and Zoback, M.D. (1989): Tectonic stress field of the continental United States; *in* Geophysical Framework of the Continental United States, L.C. Pakiser and W.D. Mooney (ed.), Geological Society of America, Memoir 172, p. 523–539, URL <https://izaks.people.stanford.edu/sites/g/files/sbiybj2961/f/Zoback_Zoback_1989_Tectonic_stress_field_of_the_continental_United_States.pdf> [January 1989].

Monitoring Induced Seismicity in the Montney Play, Northeastern British Columbia

A.M.M. Bustin, The University of British Columbia, Vancouver, British Columbia, abustin@eos.ubc.ca

D.J. Jones, The University of British Columbia, Vancouver, British Columbia

J. Ou, The University of British Columbia, Vancouver, British Columbia

G.R.L. Chalmers, The University of British Columbia, Vancouver, British Columbia

---

Bustin, A.M.M., Jones, D.J., Ou. J. and Chalmers, G.R.L. (2020): Monitoring induced seismicity in the Montney play, northeastern British Columbia; *in* Geoscience BC Summary of Activities 2019: Energy and Water, Geoscience BC, Report 2020-02, p. 27–32.

Introduction

The limited availability of monitoring data to researchers is one of the greatest challenges limiting the advancement of the understanding of induced seismicity in northeastern British Columbia (BC) and, hence, the development of proactive mitigation schemes and frameworks for hazard assessment. Many of the recommendations regarding induced seismicity from the *Scientific Review of Hydraulic Fracturing in British Columbia* (Scientific Hydraulic Fracturing Review Panel, 2019) directly (6 of 18) or indirectly (4 of 18) refer to the need for increased monitoring and data sharing. While the regional broadband network in the Montney play is sufficient for larger events (M > ~1.8), a more complete catalogue is required for detailed modelling studies and proactive mitigation. Additionally, the coverage of accelerometers remains inadequate to understand whether events will be felt or cause damage. To address the data gap, an array of paired accelerographs plus geophone stations has been developed to densely monitor hydraulic-fracturing operations.

Three-component (3C) accelerographs are currently deployed at 15 sites in western Canada, 11 of which are telemetered and providing real-time data to an online interactive platform, Portae Terra (www.portaeterra.ca). In the past year (November 2018 to November 2019), two hydraulic-fracturing operations were monitored in the Montney play. Two stations, deployed within ~1 km of each other, recorded 33 of the 34 events with M > 1.5 that were induced by the two hydraulic-fracturing operations. Fourteen events with M < 1.5 were also recorded; however, ground-motion parameters for these events are of little use without event information for comparisons; such information is not available for these smaller events. Five of the 10 earthquakes that were not caused by the two fracturing operations being monitored by this project—but occurred within ~30 km of the aforementioned two stations and were reported by Natural Resources Canada (NRCan) with local magnitude (M_L) ranging from 1.4 to 2.6—were also recorded. The site-corrected, peak ground acceleration (PGA) of the geometric mean of the horizontal components ranged from 0.360 to 60.9 cm/s^2 (0.037–6.2% g) for events with M_L values of 1.57 to 4.5 and hypocentral distances of 2.46 to 17.8 km.

In order to obtain event information for smaller magnitude events, the stations have been upgraded to include 4.5 Hz, high-precision 3C geophones. The first paired station was deployed at one of the sites for the second of the project's monitoring operations. Data analysis is ongoing but, to date, in addition to recording all events with M > 1.5 during the hydraulic-fracturing operation, another 60 events were found from a quick visual inspection of the data. Portae Terra is currently being upgraded to provide real-time access to the geophone data and calculated automatic event information for smaller events. In addition, Portae Terra will provide access to public data from broadband stations in regional networks near the monitoring areas and calculated automatic event magnitudes and locations for larger events.

Dataset

Since 2017, accelerographs deployed at 29 sites across western Canada have been used to monitor seven hydraulic-fracturing operations, three disposal wells and a gas-storage facility. Five stations are currently deployed in the Montney play in BC: a telemetered, long-term accelerograph monitoring a disposal well; two long-term accelerographs in the Kiskatinaw Seismic Monitoring and Mitigation Area (KSMMA), one of which is telemetered; a temporary paired station in KSMMA; and a long-term accelerograph at Penalty Ranch.

During the past year, two hydraulic-fracturing completions were monitored in the Montney play. Two accelerographs were deployed within ~1 km of each other to monitor the first completion. For the second completion, one of the accelerographs was upgraded to a paired station with both

---

This publication is also available, free of charge, as colour digital files in Adobe Acrobat® PDF format from the Geoscience BC website: http://www.geosciencebc.com/updates/summary-of-activities/.

an accelerometer and a geophone. The accelerometers recorded 33 of the 34 events detected by the local, operator-deployed array with moment magnitude (M_w) > 1.5 that were induced by the two hydraulic-fracturing operations. The event that was missed by the sensors is the smallest of the events. Fourteen additional events, presumably with M_w < 1.5, were recorded by the accelerometers during the operations; however, ground-motion parameters for these events are of little use without event information for comparisons; such information is not available for these smaller events. Seven of the events detected by the local array were reported by NRCan. NRCan reported 10 additional events, with M_L ranging from 1.4 to 2.6, within 35 km of the two stations in the past year. The accelerometers detected 5 of the 10 events. The largest of the events was missed by the accelerometers; however, smaller events at greater hypocentral distances were detected. In total, 53 events were recorded during the past year by the accelerometers, with pre–site-corrected PGAs (for geometric mean of horizontal components) ranging from 0.030% g to 8.1% g. The measured PGAs were corrected for each event to a reference site-class with a time-averaged shear-wave velocity over the top 30 m (V_{s30}) of 760 m/s, following the procedure outlined in Bustin et al. (2019). The site-corrected PGAs range from 0.037% g to 6.2% g for events with magnitudes of 1.57–4.5 and hypocentral distances of 2.46–17.8 km.

In addition to these two accelerometers, the first of the project's geophones was deployed for the second of the monitoring operations. Data analysis is ongoing but, to date, in addition to recording all events with M > 1.5 during the hydraulic-fracturing operation, another 60 events were found from a quick visual inspection of the data.

Attenuation

The site-corrected PGAs versus hypocentral distances for events recorded by the stations were overlain on the data and predictive model presented for the South Montney play by Babaie Mahani and Kao (2017). The results, which are plotted in Figure 1, show that the datasets are consistent. However, the PGAs for many of the magnitude 2–2.5 events are higher than predicted by the ground-motion prediction equation (GMPE). This may be a result of the simple method used for correcting site effects (i.e., amplification), the combination of local and regional solutions being used, or the effects of radiation patterns resulting from the source mechanisms. The plot also shows the minimum threshold for detection as a result of digital noise. The MEMS sensors that are currently being deployed allow detection of events with PGA > ~0.03% g.

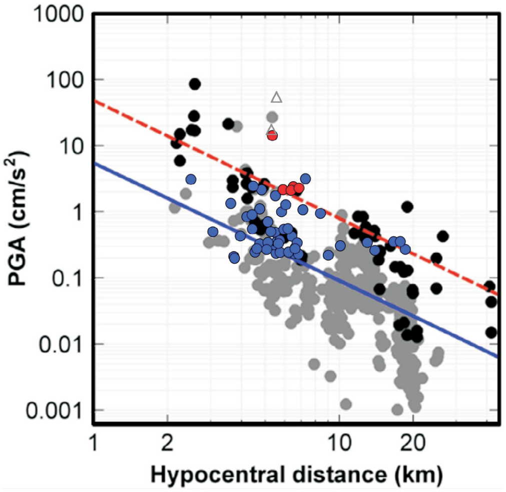

Figure 1. Site-corrected PGA versus hypocentral distance for events recorded by the project's array, with 1.5 < M < 2.5 events plotted as blue dots, 2.5 < M < 3.5 events plotted as red dots and M > 3.5 events plotted as grey triangles on GMPE and data from Babaie Mahani and Kao (2017).

Magnitude of Completeness

To investigate the magnitude of completeness for the sensors, magnitude versus hypocentral distance has been plotted for events that were detected by one or more of the stations (blue dots in Figure 2) and events that were not (grey dots). The results indicate that M > 1.55 events are consistently detected within ~7 km and M > 2 events within ~18 km of the stations. Events with M < 1.5 are being detected, but access to information for these events is not available because the local, operator-deployed array does not provide sufficient solutions for smaller events. Based on its magnitude and hypocentral distance, the M_L 2.6 event on January 19, 2019, reported by NRCan, should have had sufficient ground motions to be detected by the sensors.

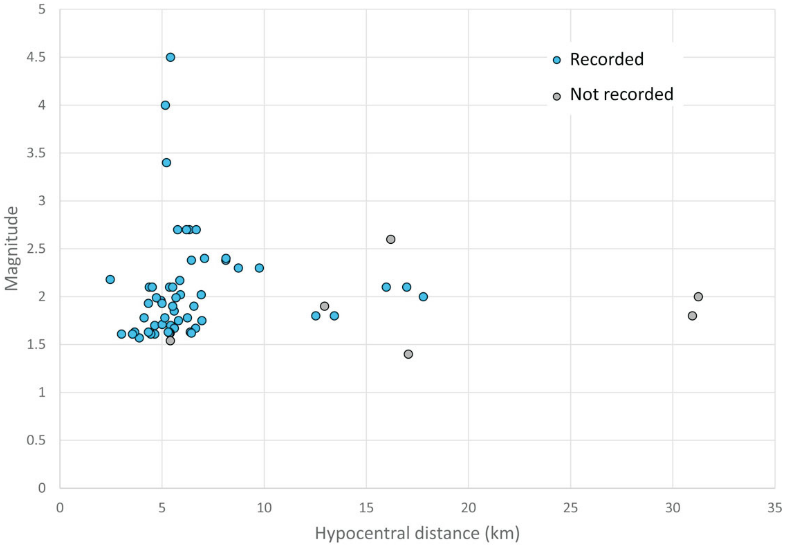

Figure 2. Magnitude versus hypocentral distance for events that were detected (blue) and were not detected (grey) on the study's stations.

The data recorded from one of the stations at the time of the event, showing the usual digital noise, is shown in Figure 3. For comparison, the data recorded from the same station for the M_L 2.1 event on January 27, 2019, reported by NRCan, is also shown. Although the events have similar hypocentral distances (16.0 km for M_L 2.1 versus 16.2 km for M_L 2.6), the smaller event shows clear P- and S-wave arrivals and the larger event does not. A denser array of accelerometers would have been required to understand why this event was not recorded. A possible explanation is that the M_L 2.6 event has a source that radiated asymmetrically with a minimum axis in the direction of the study's stations.

Depth of Burial

To investigate any possible impacts that depth of burial of the sensors might have on recorded ground motions, four sensors were installed at different depths (30, 60, 90, and 120 cm) at a single site in a seismically active area for a 3-month period. The sensors were a maximum of 5 m apart, with the 30 and 90 cm sensors and the 60 and 120 cm sensors within 1 m of each other. Eighteen events were recorded by the four sensors, with no correlation observed between sensor depth and PGA.

Portae Terra

The telemetered stations are providing real-time data to an online interactive platform, Portae Terra (www.portaeterra.ca). When new data are received by the study's server and an alert has been triggered, the raw data are automatically transferred to Portae Terra. Proprietary data are selectively available to operators through a unique passcode to access Portae Terra. Passcode '111111' provides open ac-

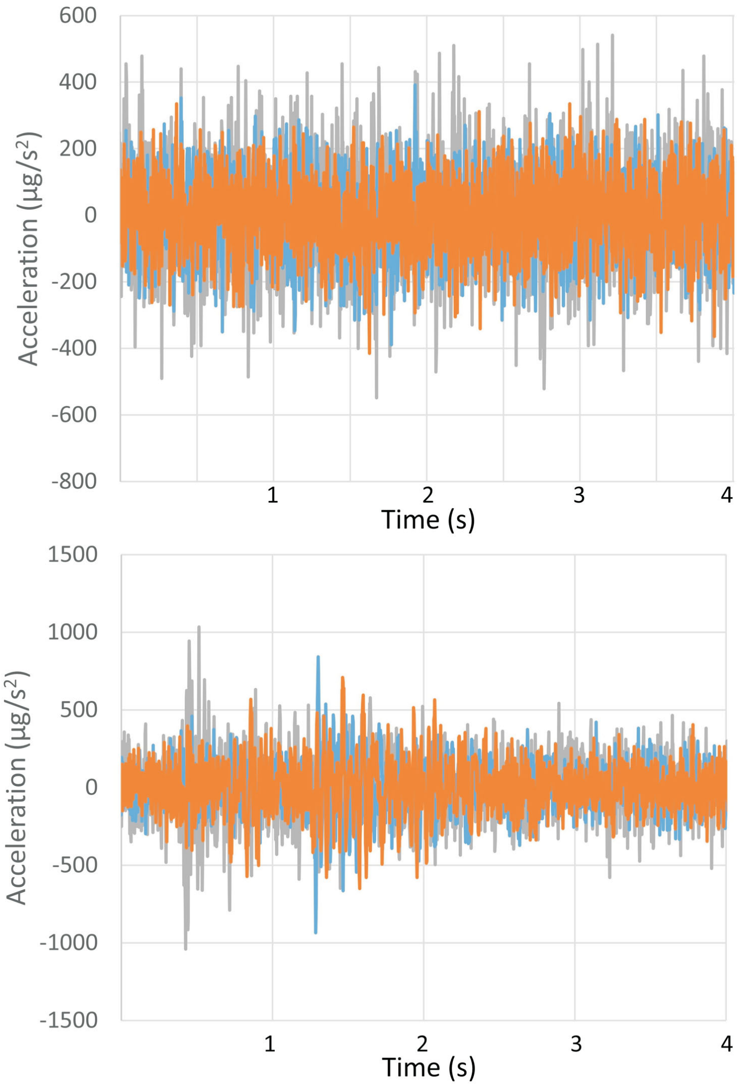

Figure 3. Data recorded on one of the study's accelerometers from the M_L 2.6 event reported by NRCan on January 19, 2019 **(top)**, compared to data recorded on the same station from the M_L 2.1 event reported by NRCan on January 27, 2019 **(bottom)**.

cess to data from the telemetered stations on public land as well as other public stations. Upon entering the site, a map is provided showing the location of all stations available for the specific passcode. Stations with new data since the last login appear with a different icon marker. To view the data from a specific event, the desired station is first chosen by either clicking the station on the map or choosing the station name from the drop-down list. The data file can then be chosen based on date and time from the drop-down list. The data with removed instrument response are then plotted with the event time and calculated ground-motion parameters printed below and next to the plot. A sample screenshot from Portae Terra is included in Figure 4. Waveforms for up to six events can be viewed at once. If the download button is selected, a zipped folder can be downloaded containing CSV files with the data in µg and cm/s^2, the calculated ground-motion parameters and the calculated response spectral accelerations (PSA) at periods of 0.05, 0.1, 0.3, 0.5, 1.0, 2.0 and 3.0 s. The zipped folder also contains the raw data in miniSEED format and dataless SEED volume for the station.

Ongoing Upgrades and Future Work

Systems are being set up for automatic solutions for small-magnitude events using the study's geophone data and for large-magnitude events using data from regional broadband networks available through Incorporated Research Institutions for Seismology (IRIS; https://www.iris.edu/hq/). Earthworm is being used to process the data from the geophone arrays, whereas the procedure of the BC Oil and Gas Commission (BCOGC) for automatic solution using Seiscomp3 is being mimicked for the data from the regional broadband stations. The regional stations for which real-time data are currently being received from IRIS can be viewed on Portae Terra by choosing 'All Stations'. The data from the study's geophone stations and the regional broadband stations in the areas being monitored by the study will be available to view and download through Portae Terra. The automatic solutions calculated by the system will also be plotted on the map. A module is also being prepared for real-time monitoring of hydraulic-fracturing operations through frequency-magnitude, probability and 3D event distributions, and temporal variations in b-value, number of events and maximum magnitude. The upper-limit maximum magnitude estimated from the methods of Shapiro et al. (2010) and van der Elst et al. (2016) will be included on the plot of maximum magnitude versus time, to enable comparisons. A module including basic information on induced seismicity, a glossary and links to sites for additional information is also being prepared.

Once the upgrade of the current accelerographs to paired stations with 3C 4.5 Hz geophones has been completed, up to five hydraulic-fracturing operations in the Montney play can be monitored to obtain a more comprehensive catalogue of events, complete with ground-motion parameters. The recorded monitoring data will be investigated to better understand frequency-magnitude and spatiotemporal distribution, and how they can be used to forecast maximum magnitude, aid in the development of proactive mitigation plans and map seismic susceptibility. In addition, the ground-motion data from the dense monitoring will be investigated to better understand whether ground motions will be felt or pose a risk to critical infrastructure or well-

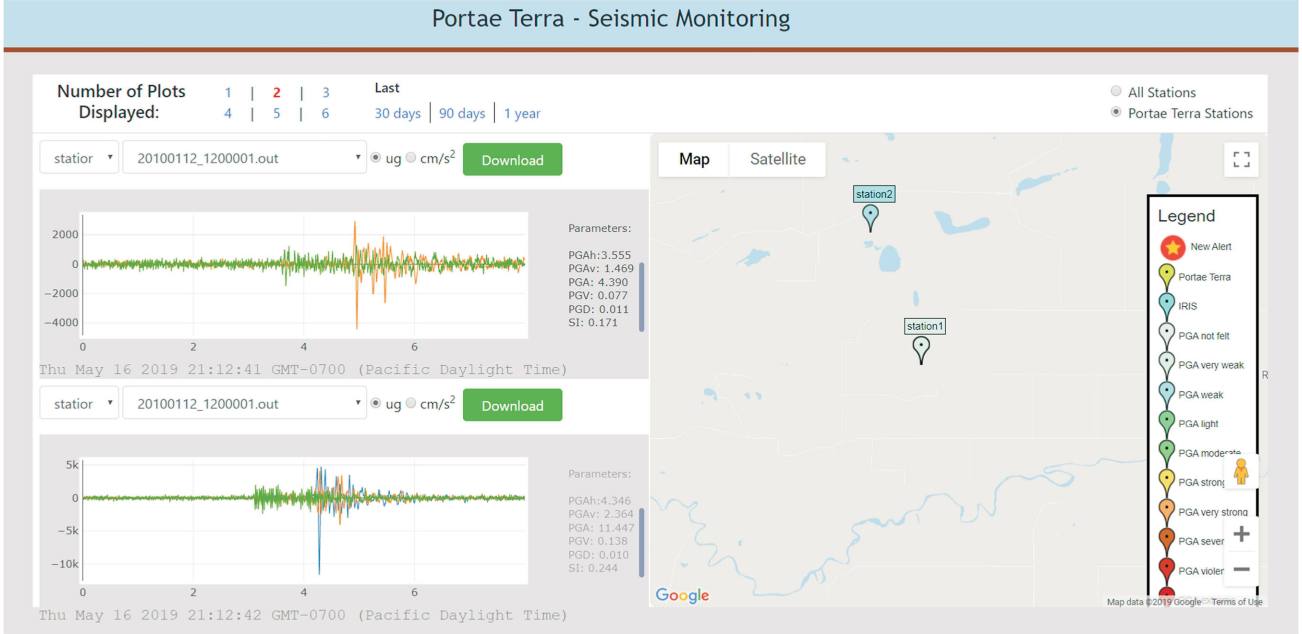

Parameters:

PGAh:3.555
PGAv: 1.469
PGA: 4.390
PGV: 0.077
PGD: 0.011
SI: 0.171

Thu May 16 2019 21:12:41 GMT-0700 (Pacific Daylight Time)

Parameters:

PGAh:4.346
PGAv: 2.364
PGA: 11.447
PGV: 0.138
PGD: 0.010
SI: 0.244

Thu May 16 2019 21:12:42 GMT-0700 (Pacific Daylight Time)

Figure 4. Example of an event recorded on two stations viewed on Portae Terra (www.portaeterra.ca).

bore integrity, to reduce the variability in ground-motion prediction equations due to radiation patterns, and to compare approaches for quantifying their hazard/risks. Finally, the data will be integrated into 3D Earth models to quantitatively rank mitigation strategies and better understand the processes and parameters controlling anomalous induced events.

Summary

The study's accelerographs, which are now providing real-time data to an online interactive dashboard (Portae Terra), were deployed to monitor two hydraulic-fracturing operations during the past year. Fifty-three events were recorded, with site-corrected PGAs for the geometric mean of the horizontal components ranging from 0.037% g to 6.2% g for events with magnitudes of 1.57 to 4.5 and hypocentral distances of 2.46 to 17.8 km. The values obtained are consistent with the data and prediction models previously presented for the south Montney play. The first paired station with both a 3C accelerometer and a 3C geophone was deployed for the second hydraulic-fracturing operation and recorded 60 events not detected by the accelerometers. A system is currently being developing for automatic solutions for smaller events from the geophone data and larger events from regional broadband networks. The data and automatic event information will also be made available through Portae Terra.

Acknowledgments

Geoscience BC is thanked for their support and funding for this study. Thanks also go to K. Johansen and C. Ventura for their help with the design and construction of the sensors and R.M. Bustin for his review of this manuscript.

References

Babaie Mahani, A. and Kao, H. (2017). Ground motion from M1.5 to 3.8 induced earthquakes at hypocentral distance <45 km in the Montney play of northeast British Columbia, Canada; Seismological Research Letters, v. 89, p. 22–34, URL <https://doi.org/10.1785/0220170119> [November 2019].

Bustin, A.M.M., Munson, E., Jones, D. and Chalmers, G. (2019). Ground-motion data from seismicity in the southern Montney Formation, northeastern British Columbia; in Geoscience BC Summary of Activities 2018: Energy, Geoscience BC, Report 2019-02, p. 55-62, URL <http://cdn.geosciencebc.com/pdf/SummaryofActivities2018/EW/2015-031_SoA2018_EW_Bustin.pdf> [November 2019].

Scientific Hydraulic Fracturing Review Panel (2019): Scientific review of hydraulic fracturing in British Columbia; BC Ministry of Energy, Mines and Petroleum Resources, 236 p., URL <https://www2.gov.bc.ca/assets/gov/farming-natural-resources-and-industry/natural-gas-oil/responsible-oil-gas-development/scientific_hydraulic_fracturing_review_panel_final_report.pdf> [November 2019].

Shapiro, S.A., Dinske, C., Langenbruch, C. and Wenzel, F. (2010): Seismogenic index and magnitude probability of earthquakes induced during reservoir fluid stimulations; Leading Edge, v. 29, p. 304–309, URL <https://library.seg.org/doi/10.1190/1.3353727> [November 2019].

van der Elst, N.J., Page, M.T., Weiser, D.A., Goebel, T.H.W. and Hosseini, S.M. (2016): Induced earthquake magnitudes are as large as (statistically) expected; Journal of Geophysical Research: Solid Earth, v. 121, p. 4575–4590, URL <https://doi.org/10.1002/2016JB012818> [November 2019].

Geoscience BC

Velocity-Structure Imaging Based on Seismological Observations Close to Hydraulic Fracturing Sites near Dawson Creek, Northeastern British Columbia (Parts of NTS 093P, 094A)

M.P. Roth[1], **Ruhr University Bochum, Germany, marco.roth@rub.de**

R.M. Harrington, Ruhr University Bochum, Germany

Y. Liu, McGill University, Montréal, Quebec

Roth, M.P., Harrington, R.M. and Liu, Y. (2020): Velocity-structure imaging based on seismological observations close to hydraulic fracturing sites near Dawson Creek, northeastern British Columbia (parts of NTS 093P, 094A); *in* Geoscience BC Summary of Activities 2019: Energy and Water, Geoscience BC, Report 2020-02, p. 33–40.

Introduction

Hydraulic-fracturing (HF) operations for hydrocarbon exploration have been associated with an increasing number of induced earthquakes in North America in the last decade (e.g., Ellsworth, 2013; Atkinson et al., 2016). In contrast to induced earthquakes in the United States being attributed to the high volume of co-produced wastewater being injected, induced earthquakes in the Western Canada Sedimentary Basin (WCSB) are often attributed to the HF operations themselves (e.g., Atkinson et al., 2016; Mahani et al., 2017). Although the majority of induced earthquakes are beneath the threshold to be felt (Ellsworth, 2013), some recent events exceeded a magnitude of M4+, including an M_W 4.6 on 17-Aug-2015 near Fort St. John (Mahani et al., 2017) and an M_L 4.5 on 30-Nov-2018 near Dawson Creek (Mahani et al., 2019).

This paper focuses on the fluid migration after a single HF operation to investigate the role of pore-pressure increase as a potential source of induced earthquakes (Ellsworth, 2013). Double-difference–based tomography inversion and an earthquake sequence close to Dawson Creek in January 2019 were chosen to image fluid accumulation. This sequence is characterized by 190 earthquakes (Figure 1, red circles), detected on 15 stations with hypocentral distances between 5 and 50 km (Figure 1). The station network includes nine broadband stations operated by McGill University (Figure 1, blue triangles) and six broadband stations operated by the Pacific Geoscience Centre of the Geological Survey of Canada (PGC), two of which (NBC4, NBC7) are permanent stations (Figure 1, brown triangles). Green circles show all events detected with this station network, beginning in June 2017 (Figure 1).

Methods

This study was based on seismological observations taken between 04-Jan-2019 and 11-Jan-2019 in a localized area close to an HF well (Figure 1, turquoise diamond), which was operating during this time period. Injection parameters provided by the British Columbia Oil and Gas Commission (BCOGC; last assessed on August 10, 2019) show a total injected volume of ~26 000 m³ of fluids among all horizontal wells (Figure 1, turquoise lines) at the hypocentral depths of most of the seismicity. Fluid accumulation was investigated using a double-difference–tomography approach, based on differential arrival times calculated by cross-correlation lag times to invert for a 3D distribution of seismic P- to S-wave speed ratio (υ_P/υ_S) .

Impact of Fluids on the υ_P/υ_S Ratio

Areas of fluid accumulation were detected using an approach based on seismological observations, which derives from the impacts of fluids on the velocities of both body waves (i.e., compressional [P] and shear [S]). Inversion was carried out for the velocity of both types of wave, followed by calculation of their ratio.

The compressional-wave velocity (υ_P), which moves along the direction of propagation, is characterized by

$$v_{\mathsf{P}} = [(\lambda + 2\mu)/\rho]^{1/2} = [(K + 4\,\mu/3)/\rho]^{1/2}, \tag{1}$$

and is thus dependent on the Lame’s constant (λ), the rigidity (μ), the rock density (ρ) and, alternatively, the bulk modulus (K). Unlike the compressional wave, the shear-wave velocity (υ_S), which produces a displacement perpendicular to the direction of propagation, is defined by

$$v_{\mathsf{S}} = (\mu/\rho)^{1/2}. \tag{2}$$

Thereby, the presence of fluids plays a role in influencing the velocities. On one hand, the mere substitution of non-filled cavities (i.e., porosity) with a fluid of higher density, such as water, will increase υ_P while υ_S stays rather constant as the bulk modulus increases, whereas the shear modulus

---

[1] *The lead author is a 2019 Geoscience BC Scholarship recipient.*

This publication is also available, free of charge, as colour digital files in Adobe Acrobat® PDF format from the Geoscience BC website: http://www.geosciencebc.com/s/SummaryofActivities.asp.

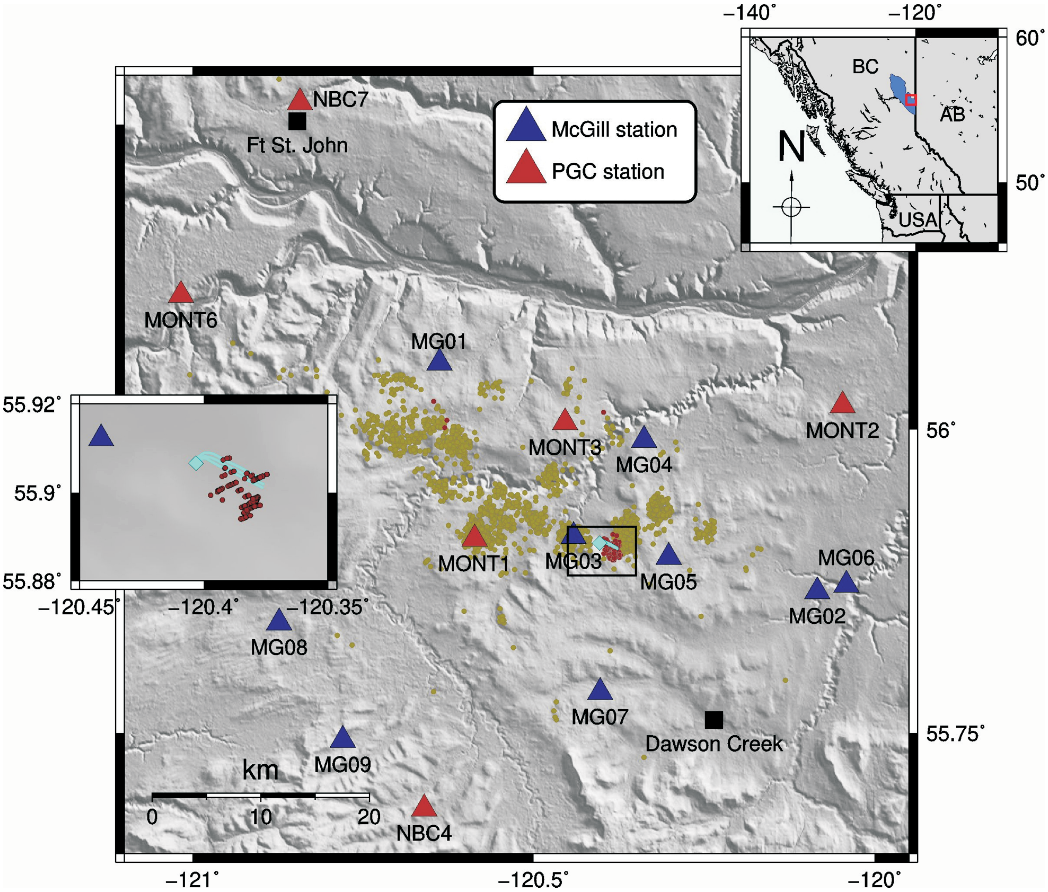

Figure 1. Study area in northeastern of British Columbia. McGill and PGC stations are denoted by blue and orange triangles, respectively. All detected earthquakes between 01-Jul-2017 and 11-Jan-2019 are shown as green dots, while the sequence of interest is highlighted in red. The HF well operating in the same time period as seismicity occurred is shown as a turquoise diamond. The inset map highlights the relative relocations of the chosen sequence.

remains constant (Han and Batzle, 2004). On the other hand, an increase in pore pressure at a constant confining pressure will decrease the seismic velocities significantly. This effect is even stronger on the shear-wave velocity (Christensen, 1984). This being said, zones of high υ_P/υ_S ratio possibly indicate high pore-fluid pressures (i.e., fluid accumulations along pre-existing faults or fractures due to pumping; Shelly et al., 2006).

Double-Difference Tomography

Seismic tomography describes the process of imaging the subsurface of the Earth with the help of seismic waves (i.e., earthquakes of every kind). By using measured travel times and calculated ray paths, one creates an inverse problem, looking for a velocity model. Zhang and Thurber (2003) developed the seismic-tomography method ‘tomoDD’ based on double differences (Waldhauser and Ellsworth, 2000) to solve for this velocity model. The tomoDD software minimizes the misfit between observed and predicted arrival times, which are linearly related to the perturbations in the hypocentre and velocity-structure parameters, by applying the LSQR algorithm (Paige and Saunders, 1982) to the least-square problem (Zhang and Thurber, 2003). The predicted travel times are calculated with a pseudo-bending raytracing algorithm (Um and Thurber, 1987).

This study employs this approach on an earthquake sequence close by Dawson Creek, presumably induced by hydraulic fracturing, that occurred between 04-Jan-2019 and 11-Jan-2019. During this time period, 190 events were detected using an STA/LTA approach with a dense array of 15 broadband stations at hypocentral distances of 5 to 50 km (Figure 1). The velocity inversion is based on a 1-D homogeneous layered velocity model based on Crust1.0 (Laske et al., 2013) for depth shallower than 1 km and on Mahani et al. (2017) for the deeper layers (Figure 2).

Grid-Size Estimation and Quality Control

Resolution of the determined velocity structures is dependent on the initial grid spacing. A localized area (i.e., 5×5 km^2 from the earthquake cluster centroid) was considered in this study, so the velocity grid spacing was in the order of hundreds of metres and was based on the minimum size of ground perturbations that cause changes in the

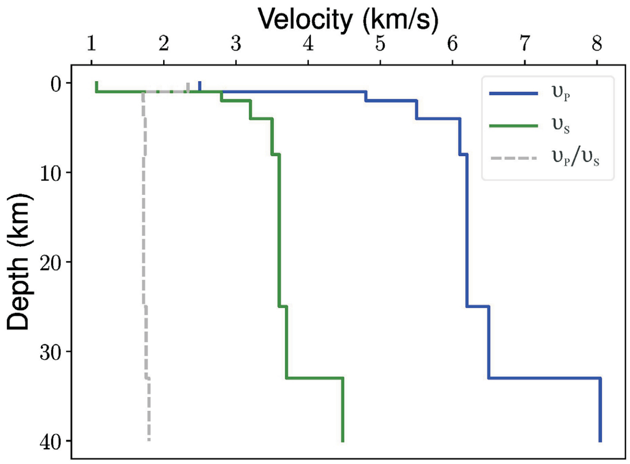

Figure 2. Homogeneous layered, 1-D velocity model, based on Crust1.0 for depth shallower than 1 km and Mahani et al. (2017) for deeper layers. The blue and green lines indicate P- and S-wave velocity, respectively. The grey dashed line shows the υ_P/υ_S ratio.

waveform. As an estimate, the grid spacing was calculated based on the maximum radius of the first Fresnel zone

$$b_{\max} = \frac{\sqrt{\lambda D}}{2}, \tag{3}$$

with wavelength (λ) ranging from 10 to 30 m and signal-station distance of 5 to 50 km. With this approach, the minimum size of structures influencing the recorded waveforms lies between 100 and 600 m. The starting point was a horizontal grid spacing of 200 m to stay in the estimated range. To evaluate the reliability of the results, a checkerboard test (Figure 3) was carried out and the derivative-weight sum (DWS), which quantifies the ray-path density around each grid point, was plotted from the real-velocity inversion (Figure 4). A checkerboard input model was created, with velocities changing by ±10% of the initial velocity model (Figure 2), and 600 × 600 m structures were generated (Figure 3a). The P-wave (Figure 4a) and S-wave (Figure 4b) arrivals were differentiated for the DWS distribution.

Velocity-Structure Imaging

Similar to hypoDD by Waldhauser (2001), tomoDD uses initial locations combined with cross-correlation time shifts between different events observed at the same station as double-difference equations. In addition, tomoDD uses absolute travel-time data for the calculation of the ray paths. Cross-correlations in the present study are based on 2.5 s long recordings, starting 1 s before pick arrival time and ending 1.5 s after pick arrival time, with a bandpass filter between 2 and 15 Hz applied. Only event pairs that exceed a threshold of a cross-correlation coefficient of 0.6 were used and the cross-correlation coefficient was used as a weighting factor. Iteration was carried out ten times using cross-correlation data only. The velocity-model joint inversion was applied in every second iteration step to already relocated event pairs.

The resulting υ_P/υ_S ratios were calculated at a depth corresponding with the horizontal wells and plotted in map view in Figure 5a–d. Figure 5e–f shows cross-sections along the profiles in Figure 5a–d, with one parallel and one perpen-

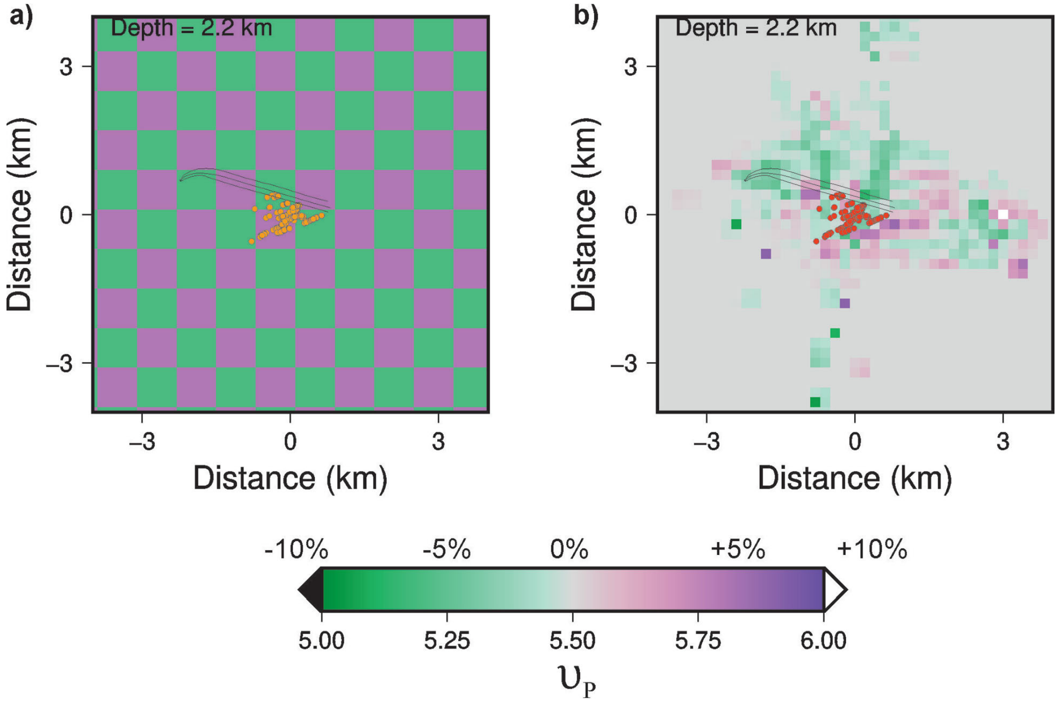

Figure 3. Checkerboard test of **a)** the input-velocity model with a synthetic checkerboard structure; and **b)** the results of the joint inversion based on the synthetic input from (a). Green and purple colours show zones of velocity decrease and increase by up to 10%, respectively.

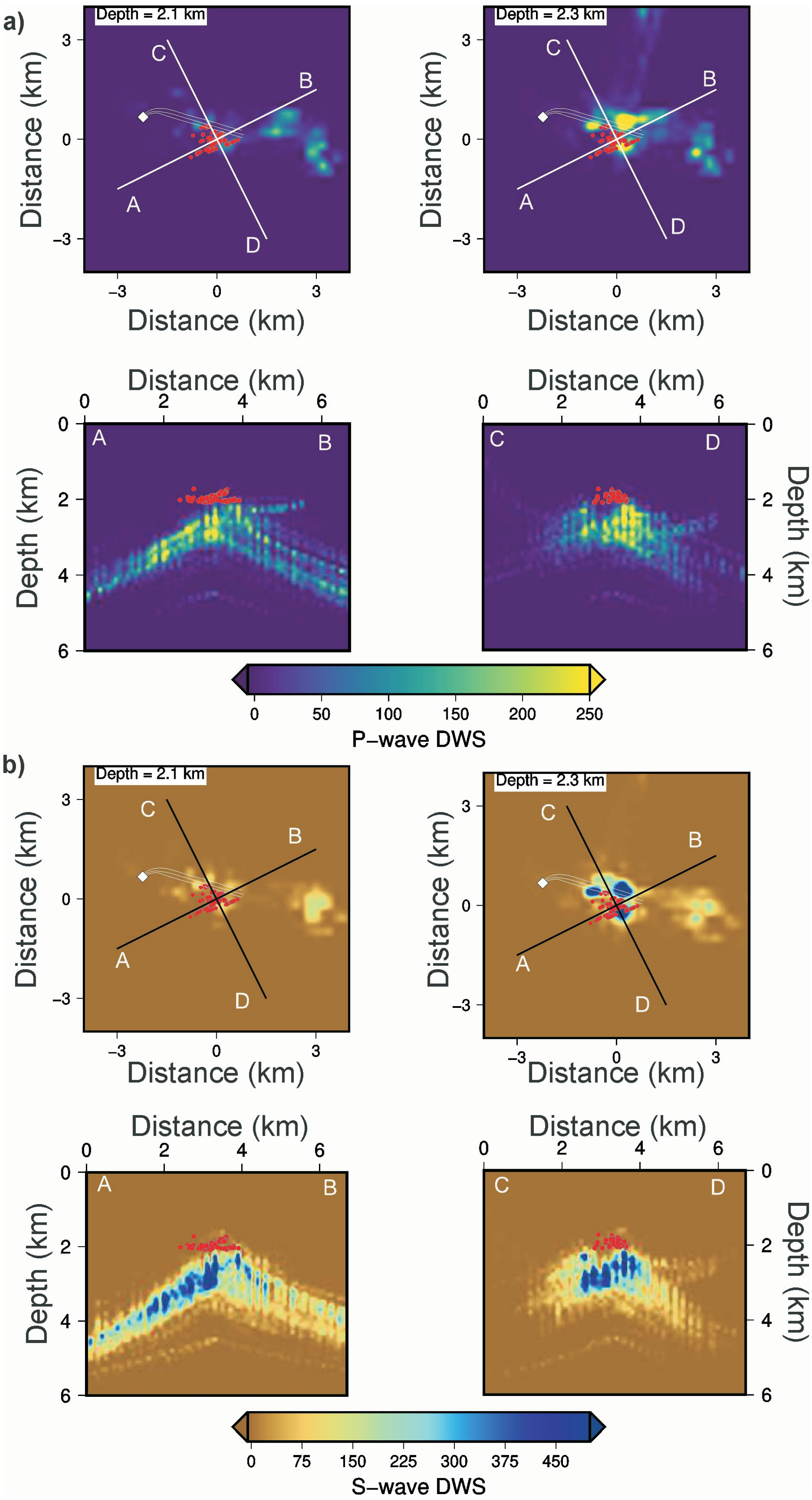
a)
Depth = 2.1 km
Depth = 2.3 km
A
B
C
D
3
0
–3
Distance (km)
Distance (km)
0
2
4
6
Depth (km)
0
50
100
150
200
250
P–wave DWS
b)
Depth = 2.1 km
Depth = 2.3 km
0
75
150
225
300
375
450
S–wave DWS

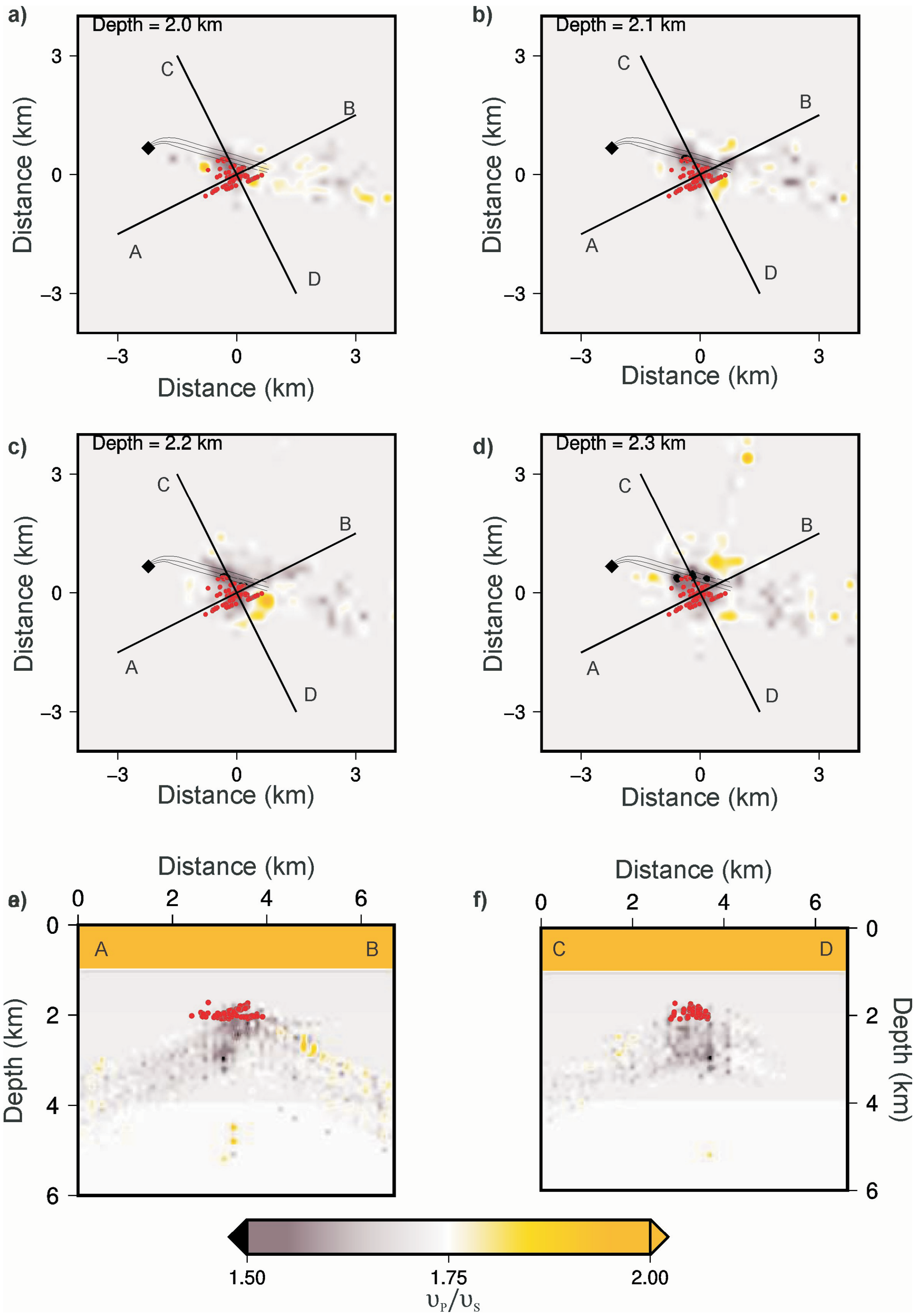

Figure 4. DWS plot of the velocity-structure inversion using the observed data, showing the results for **a)** P-wave arrival times, and **b)** S-wave arrival times.

Figure 5. Velocity-structure imaging based on seismological observations taken between 04-Jan-2019 and 11-Jan-2019: **a–d)** map views at a depth of 2 to 2.3 km; **e–f)** cross-sections along profile lines shown in a–d.

dicular to the alignment of the events. Yellow colours indicate an increase in υ_P/υ_S ratio, while darker shades indicate a decrease.

Results

The inset map in Figure 1 shows the relative relocations. The events align along several parallel northeast-trending structures. All event hypocentres are relocated in close proximity to horizontal wells.

Using the checkerboard test, it was possible to solve for velocity perturbations in the right order of magnitude: low-velocity zones with a decrease in velocity of 10% (Figure 3b; green shows a velocity of 5 km/h) and high-velocity zones with an increase in velocity of 10% (Figure 3b; purple shows a velocity of 6 km/h). The checkerboard test was not capable of spatially resolving the structure that was set in the input model (Figure 3).

The DWS distribution analysis in Figure 4 shows, for both P- and S-wave–based inversions, areas of more dense ray coverage very close to the centroid of hypocentres (~250 crossing ray paths per grid node with P-wave arrivals and 500 crossing ray paths per grid node with S-wave arrivals). No crossing ray paths were observed in the surrounding area.

Figure 5a–c shows changes in the υ_P/υ_S ratio in the direction of the horizontal well orientation, while Figure 5d shows also a perpendicular feature. Figure 5a suggests that patches of υ_P/υ_S increase along the horizontal well orientation, while Figure 5b–d shows, as well, υ_P/υ_S increase perpendicular to it. The cross-sections in Figure 5e–f show changes in υ_P/υ_S ratio concentrated deeper than the earthquake hypocentres, but the shape is dictated largely by the DWS distribution.

Discussion and Conclusion

According to the quality-control criteria in Figures 3 and 4, there are limitations in applying the tomoDD software to the setting. On one hand, the checkerboard test (Figure 3) was able to image the amplitude of the velocity contrast from the input model but, on the other hand, the spatial distribution of structures that were given as an input has not been resolved. The plot of DWS values (Figure 4) shows limitations in the ray coverage, as the densest area covers only a radius of roughly 1 km around the events. Particularly the cross sections show that the DWS might image ray paths only from station MG03 to the west and station MG05 to the east.

Nevertheless, the observed increase in υ_P/υ_S ratio seems convincing with respect to the ambient stress field (i.e., S_H striking 43.7° and $S_H > S_h > S_v$; Bell and Grasby, 2012), as the fluids would follow structures along the horizontal wells, perpendicular to S_H. This might indicate faults or zones of weakness along S_H. In addition, the small increases of υ_P/υ_S ratio parallel to S_H suggest a second orientation of fluid accumulations.

In conclusion, the tomoDD software was applied to an earthquake sequence in January 2019 to image fluid accumulations. Two possible fault orientations were observed: parallel and perpendicular to the largest principal stress. As the seismicity is occurring only in time windows of days and is very localized, the entire area is not well covered by ray paths, which limits the significance of these results.

Acknowledgments

This project is partially funded by Deutsche Forschungsgemeinschaft (DFG) and Ruhr University Bochum (RUB) New Faculty Start-Up Funds. The authors acknowledge H. Kao and PGC, as well as G. Langston from McGill University, for help in station deployment; S. Venables and the BCOGC for providing well data; and K.D. Fischer from RUB Seismological Observatory for help in data acquisition and processing. The lead author received support through a Geoscience BC scholarship. A. Verdecchia provided a review that improved the quality of the manuscript.

References

Atkinson, G.M., Eaton, D.W., Ghofrani, H., Walker, D., Cheadle, B., Schultz. R., Shcherbakov, R., Tiampo, K., Gu, J., Harrington, R.M., Liu, Y., van der Baan, M. and Kao, H. (2016): Hydraulic fracturing and seismicity in the Western Canada Sedimentary Basin; Seismological Research Letters, v. 87, no. 3, p. 631–647.

Bell, J.S. and Grasby, S.E. (2012): The stress regime of the Western Canadian Sedimentary Basin; Geofluids, v. 12, no. 2, p. 150–165.

Christensen, N.I. (1984): Pore pressure and oceanic crustal seismic structure; Geophysical Journal International, v. 79, no. 2, p. 411–423.

Ellsworth, W.L. (2013): Injection-induced earthquakes; Science, v. 341, no. 6142, p. 142.

Han, D. and Batzle, M.L. (2004): Gassmann's equation and fluid-saturation effects on seismic velocities; Geophysics, v. 69, no. 2, p. 398–405.

Laske, G., Masters, G., Ma, Z. and Pasyanos, M. (2013): Update on CRUST1.0 – a 1-degree global model of Earth's crust; Geophysical Research Abstracts, v. 15, EGU2013-2658.

Mahani, A.B., Kao, H., Atkinson, G.M., Assatourians, K., Addo, K. and Liu, Y. (2019): Ground-motion characteristics of the 30 November 2018 injection-induced earthquake sequence in northeast British Columbia, Canada; Seismological Research Letters, v. 90, no. 4, p. 1457–1467.

Mahani, A.B., Schultz, R., Kao, H., Walker, D., Johnson, J. and Salas, C. (2017): Fluid injection and seismic activity in the northern Montney play, British Columbia, Canada, with special reference to the 17 August 2015 Mw 4.6 induced earthquake; Bulletin of the Seismological Society of America, v. 107, no. 2, p. 542–552.

Paige, C.C. and Saunders, M.A. (1982): LSQR: an algorithm for sparse linear equations and sparse least squares.; ACM Transactions on Mathematical Software (TOMS), v. 8, no. 1, p. 43–71.

Shelly, D.R., Beroza, G.C., Ide S. and Nakamula, S. (2006): Low-frequency earthquakes in Shikoku, Japan, and their relationship to episodic tremor and slip; Nature, v. 442, p. 188–191.

Um, J. and Thurber, C. (1987): A fast algorithm for two-point seismic ray tracing; Bulletin of the Seismological Society of America, v. 77, no. 3, p. 972–986.

Waldhauser, F. (2001): hypoDD: a computer program to compute double-difference hypocenter locations; U.S. Geological Survey, Open File Report 01-113, p. 1–25.

Waldhauser, F. and Ellsworth, W.L. (2000): A double-difference earthquake location algorithm: method and application to the northern Hayward fault, California; Bulletin of the Seismological Society of America, v. 90, no. 6, p. 1353–1368.

Zhang, H. and Thurber, C.H. (2003): Double-difference tomography: the method and its application to the Hayward fault, California; Bulletin of the Seismological Society of America, v. 93, no. 5, p. 1875–1889.

Hydrogen Sulphide within the Triassic Montney Formation, Northeastern British Columbia and Northwestern Alberta (NTS 083K–N, 084C–F, 093I, J, O, P, 094A, B, G, H)

G.R.L. Chalmers, The University of British Columbia, Vancouver, British Columbia, garethchalmers@gmail.com

R.M. Bustin, The University of British Columbia, Vancouver, British Columbia

A.A. Bustin, The University of British Columbia, Vancouver, British Columbia

Chalmers, G.R.L., Bustin, R.M. and Bustin, A.A. (2020): Hydrogen sulphide within the Triassic Montney Formation, northeastern British Columbia and northwestern Alberta (NTS 083K–N, 084C–F, 093I, J, O, P, 094A, B, G, H); *in* Geoscience BC Summary of Activities 2019: Energy and Water, Geoscience BC, Report 2020-02, p. 41–52.

Introduction

The Triassic Montney Formation is a large unconventional gas play in western Canada and contributed a significant proportion (34%) of natural gas to the total Canadian gas production in 2017 (National Energy Board, 2018). The Montney Formation is a tight liquids-rich gas reservoir in northeastern British Columbia (BC) with a gas-in-place estimate of 55 642 billion cubic metres (1965 tcf; BC Oil and Gas Commission, 2015). As development expands, a greater proportion of the Montney Formation is found to contain nonhydrocarbon gases such as hydrogen sulphide (H_2S) and carbon dioxide (CO_2). The authors currently estimate 27% of the Montney Formation producing wells have tested or produced greater than 100 ppm of H_2S gas. Hydrogen sulphide gas impacts the economics of the development of this hydrocarbon play as well as poses a risk to the environment and the health and safety of the populace. Hydrogen sulphide in produced gas, even in trace amounts (i.e., ppm), impacts the economics of drilling, production, treatment, and marketing of gas and associated liquids. The occurrence of H_2S in produced fluids is also one of the most serious environmental hazards and risks to gas resource development.

The stratigraphic and lateral variation in H_2S changes across the Montney gas play areas in BC. The distribution, in some areas, can be inexplicable and there are multiple reasons for the presence of H_2S in some Montney Formation producing wells. Hydrogen sulphide in petroleum systems comes from mixed sources, which include: 1) bacterial sulphate reduction; 2) thermal sulphate reduction; 3) kerogen cracking; and 4) sulphide oxidation and/or decomposition of surfactants used for well completions. Understanding H_2S distribution is further complicated by the fact that H_2S can be produced in situ within the Montney reservoir or may have migrated either from above or below through more permeable beds or fracture networks.

To reduce the uncertainty associated with H_2S production from the Montney reservoir, the source and processes that generate H_2S need to be understood, which will require: a) mapping lateral and stratigraphic distributions of H_2S and b) determining the sulphur isotopic composition of H_2S gas, as well as the potential sulphur sources (kerogen, pyrite, anhydrite).

Results

The Montney Formation is over 200 m thick within the study area (Figure 1) and the authors have informally subdivided the formation into the upper, middle and lower Montney members (Figure 2). These subdivisions are based on the sequence-stratigraphic–based boundaries of Davies et al. (2018). The thickness of the informal upper, middle and lower Montney members have been mapped across the study area (Figures 3–5). Using geoLOGIC systems ltd.'s geoSCOUT version 8.8 (geoLOGIC systems ltd., 2019) GIS software, well search criteria were set to identify Montney producers that have tested or produced sour gas (presence of H_2S). The H_2S distribution within the Montney play area of BC and Alberta has been mapped using the thickness data from the geological models (Figures 6–8) in combination with the fluid analysis data from geoSCOUT.

Thickness Maps of the Upper, Middle and Lower Members of the Montney Formation

A total of 200 well tops were used to map the thickness (isochore) variation for the informal upper Montney (Figure 3), middle Montney (Figure 4) and lower Montney (Figure 5) members of the Montney Formation. The thickness of the upper Montney member increases toward the

---

This publication is also available, free of charge, as colour digital files in Adobe Acrobat® PDF format from the Geoscience BC website: http://www.geosciencebc.com/updates/summary-of-activities/.

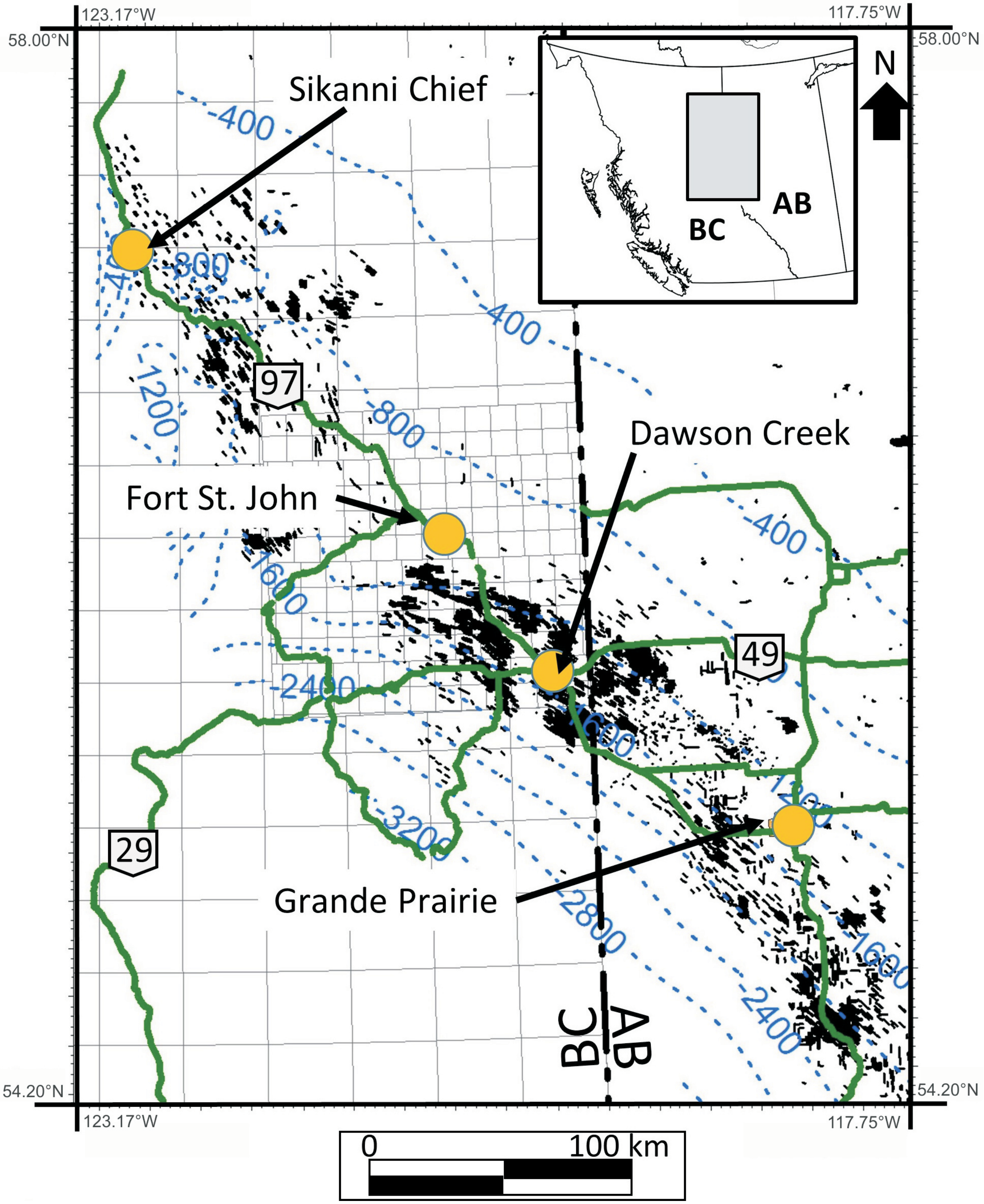

Figure 1. Location of the study area (grey box) within northeastern British Columbia and northwestern Alberta. The depth to the top of the Montney Formation is shown as blue dashed lines and is measured as subsea total vertical depth (metres). The black well traces are for all Montney Formation producing, tested or produced wells. Orange circles represent major population centres in the region and the dark grey lines are the primary roads. Data sourced from geoLOGIC systems ltd. (2019).

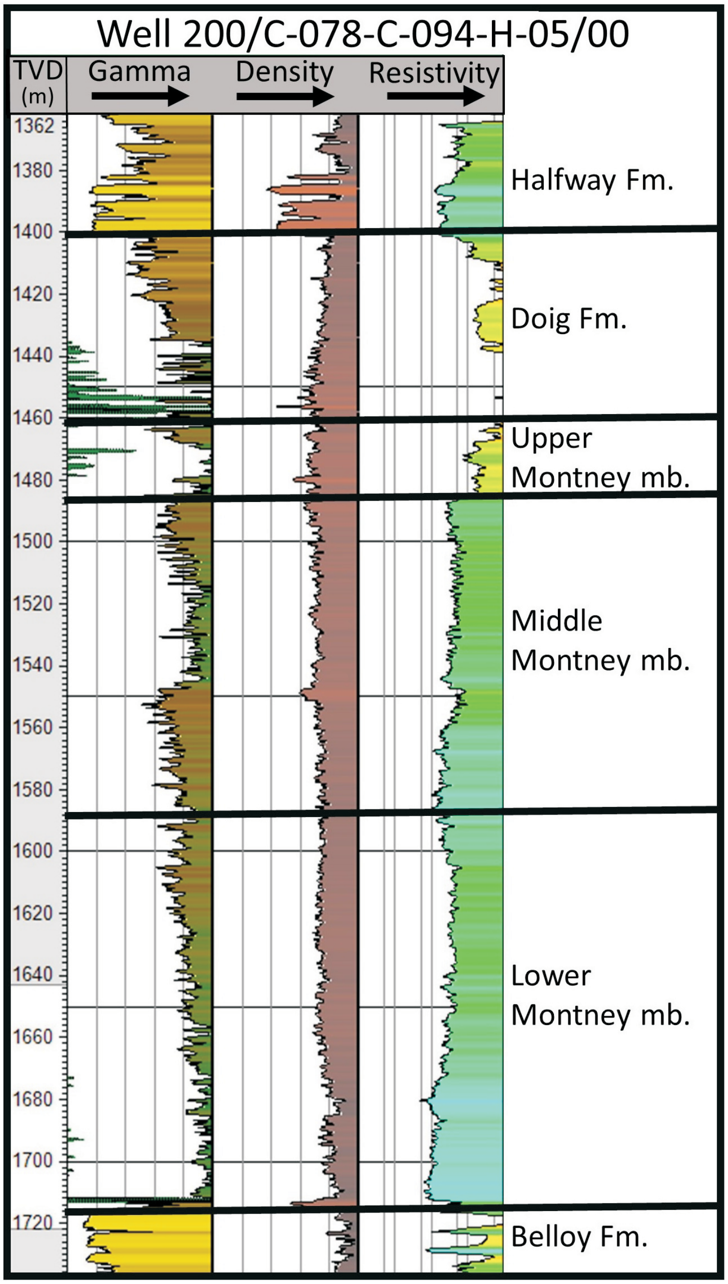

Figure 2. Stratigraphy and log response of the Halfway, Doig, Montney and Belloy formations in well 200/C-078-C-094-H-05/00 (geoLOGIC systems ltd., 2019). The Montney Formation is informally subdivided into the upper, middle and lower Montney members based on a sequence stratigraphic model of Davies et al. (2018). Abbreviation: TVD, total vertical depth.

southwest, from approximately 2 m thick in the eastern part of the study area to over 330 m adjacent to the deformation front along the western margin of the study area (Figure 3). The middle Montney member shows similar distribution as the upper Montney member but remains consistently thicker (i.e., >100 m) across the majority of BC and west-central Alberta (Figure 4). The lower Montney member is the thinnest member of the Montney Formation and is less than 90 m thick across the majority of the study area with the greatest thicknesses of over 120 m along the western margin of the study area (Figure 5).

Hydrogen Sulphide Distribution within the Montney Formation

A total of 2813 wells have been identified that either tested for, produced or currently produce sour gas within the study area (Figures 6–8; geoLOGIC systems ltd., 2019). The H_2S concentrations vary widely across the study area and range from 212 500 ppm (21.25%) to <100 ppm. There are more sour Montney Formation wells in Alberta and they also span a greater geographic area than in BC. The presence of H_2S also varies stratigraphically, with the majority of sour horizontal wells being drilled in the informal upper and middle Montney members of the Montney Formation in BC (Figures 6, 7). The majority of sour wells in Alberta are within the middle and lower Montney members of the Montney Formation (Figures 7, 8). The upper Montney member thins to 1–2 m within Alberta, which is the reason for the low number of upper Montney member sour wells in Alberta. Comparing the Montney members, most sour wells are located within the middle Montney member, which also covers the largest geographic area in both Alberta and BC. There are also more sour wells drilled within the lower Montney member compared to the upper Montney member (Figures 6, 8).

Distribution of Hydrogen Sulphide Above and Below the Montney Formation

Hydrogen sulphide in the Montney Formation can be generated in two ways: 1) via sourcing elemental sulphur from within the reservoir as either sulphate, sulphide or organic sulphur, or 2) from migration of hydrogen sulphide from either above or below the reservoir through conduits like natural fractures, faults or permeable beds. Elemental sulphur within the Montney Formation can either be formed in situ from Triassic seawater or postdepositionally from migration of sulphate in solution.

The major sources of sulphate occur above the Montney Formation in the Triassic Charlie Lake Formation and below in the Permian, Mississippian and Devonian rocks (i.e., Belloy, Debolt, Slave Point, Muskeg formations). Using geoSCOUT version 8.8, fluid analysis module, the sour wells that have either tested for, produced or are producing H_2S gas from both above (Figure 9) and below (Figure 10) the Montney Formation have been mapped to understand the potential risk of producing sour gas within the Montney Formation. A stronger overlap occurs

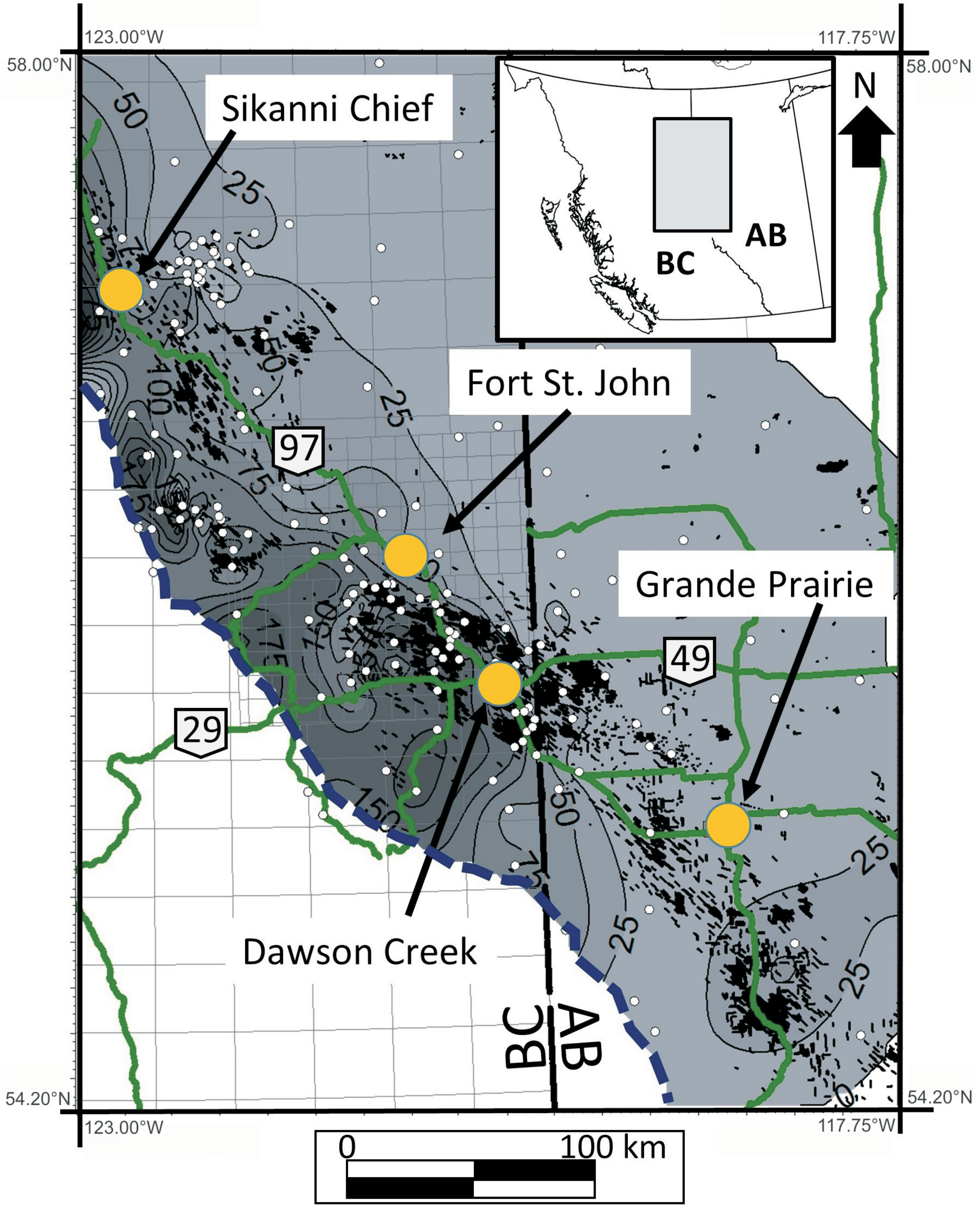

Figure 3. Thickness variation of the informal upper Montney member of the Montney Formation across the regional gas play in northeastern British Columbia and northwestern Alberta. The thickness varies from 338 m in the northwestern part of the study area to less than 2 m in the eastern part of the study area. White filled circles are the well control for thickness contours. Contour interval is 25 m. The black well traces are for all Montney Formation producing, tested or produced wells. Orange circles represent major population centres in the region and the green lines are the primary roads. Blue dashed line is the deformation front (approximate location). Data sourced from geoLOGIC systems ltd. (2019).

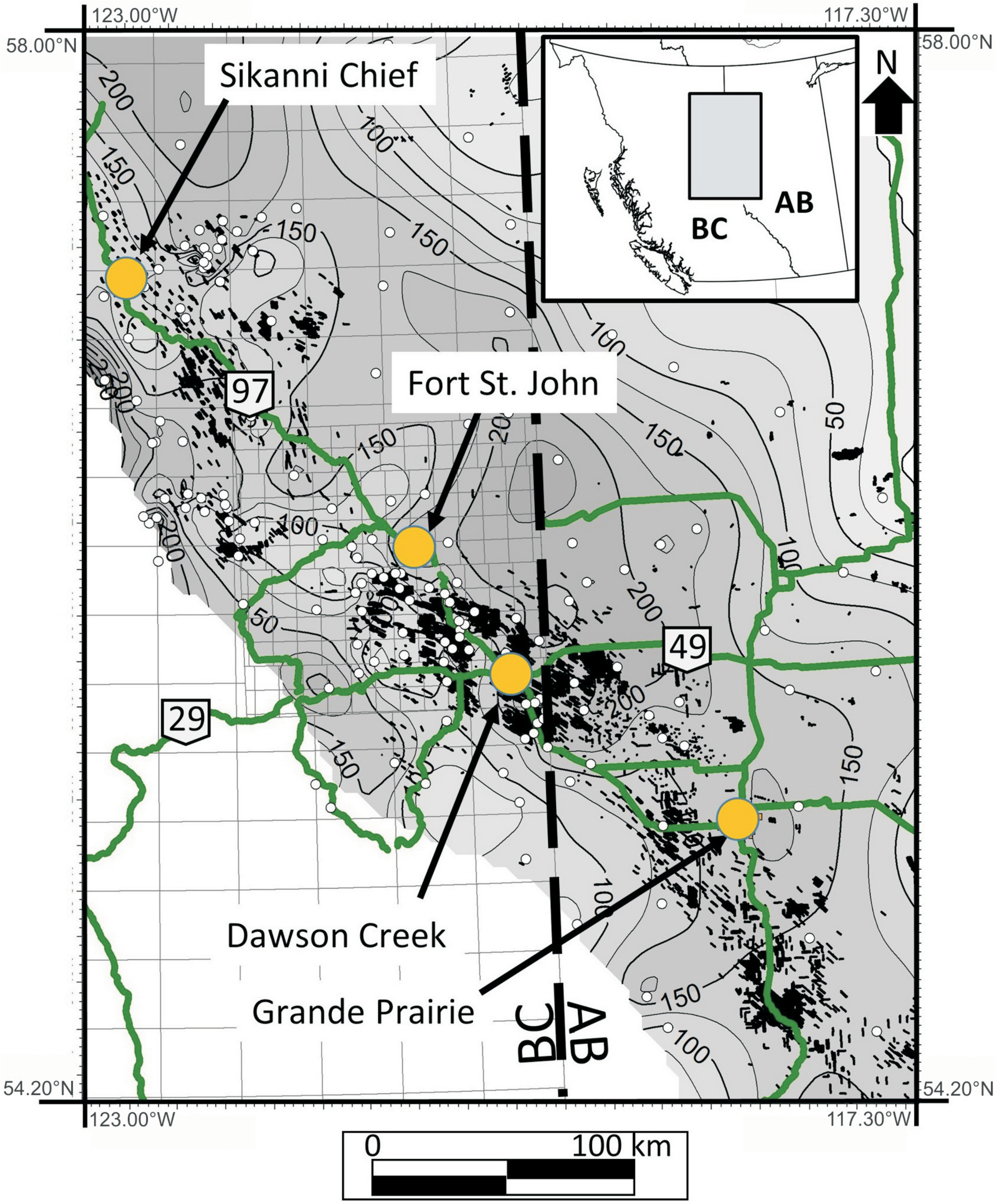

Figure 4. Thickness variation of the informal middle Montney member of the Montney Formation across the regional gas play in northeastern British Columbia and northwestern Alberta. The thickness varies from 300 m in the northwestern part of the study area to less than 11 m in the eastern part of the study area. White filled circles are the well control for thickness contours. Contour interval is 25 m. The black well traces are for all Montney Formation producing, tested or produced wells. Orange circles represent major population centres in the region and the green lines are the primary roads. Data sourced from geoLOGIC systems ltd. (2019).

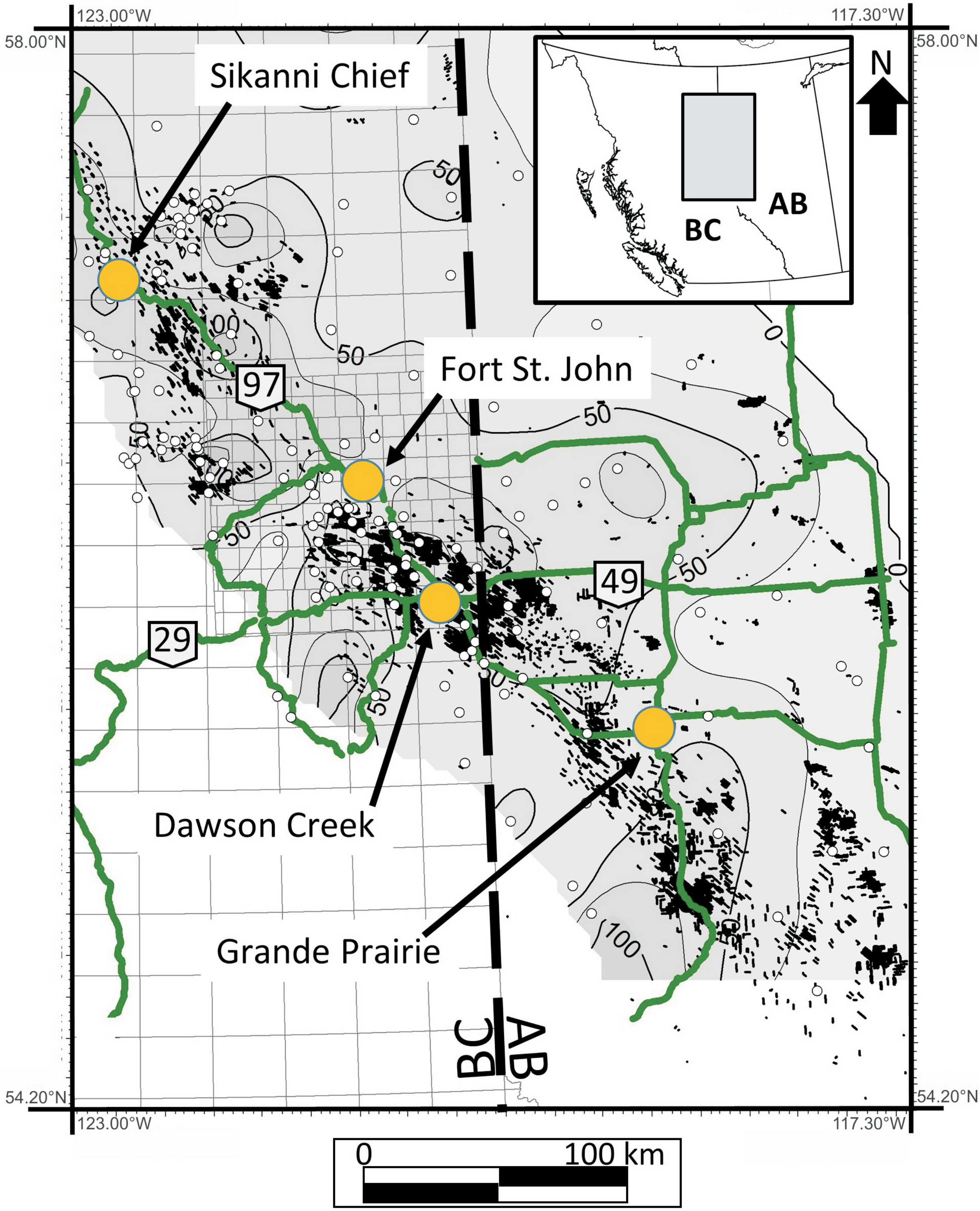

Figure 5. Thickness variation of the informal lower Montney member of the Montney Formation across the regional gas play in northeastern British Columbia and northwestern Alberta. The thickness varies from 229 m in the northwestern part of the study area to less than 10 m in the eastern part of the study area. White filled circles are the well control for thickness contours. Contour interval is 25 m. The black well traces are for all Montney Formation producing, tested or produced wells. Orange circles represent major population centres in the region and the green lines are the primary roads. Data sourced from geoLOGIC systems ltd. (2019).

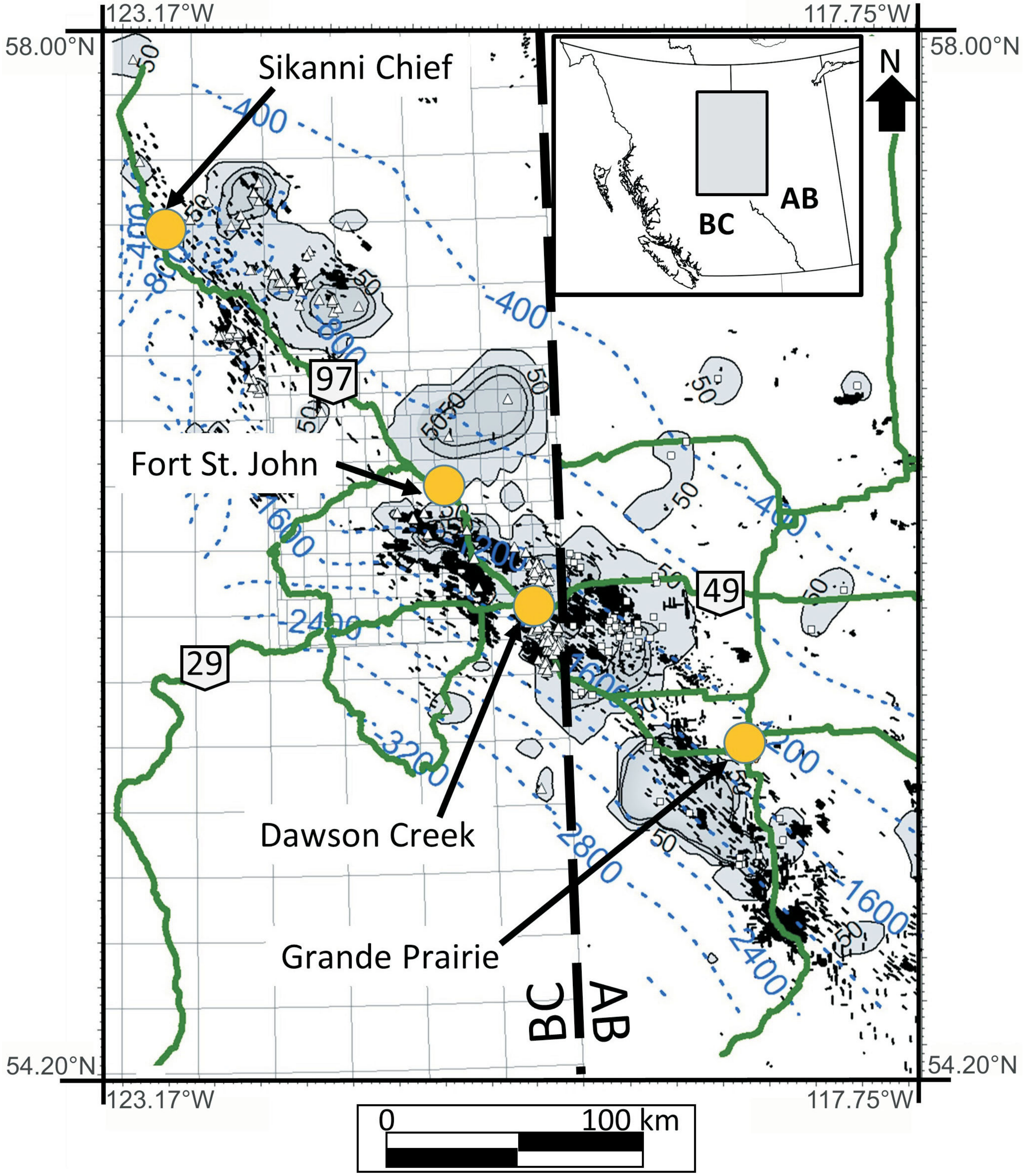

Figure 6. Sour gas distribution within the informal upper Montney member of the Montney Formation across the regional gas play in northeastern British Columbia and northwestern Alberta. The H_2S concentration is in parts per million (ppm) and the contour interval (solid black lines) is 5000 ppm. The H_2S concentrations vary between 100 and 116 000 ppm (0.01–11.6%). The depth contours (blue dashed lines) are to the top of the upper Montney member and are measured in subsea total vertical depth (SSTVD; metres). White triangles represent sour wells in British Columbia and white squares represent sour wells in Alberta. Orange circles represent major population centres in the region and the green lines are the primary roads. Data sourced from geoLOGIC systems ltd. (2019).

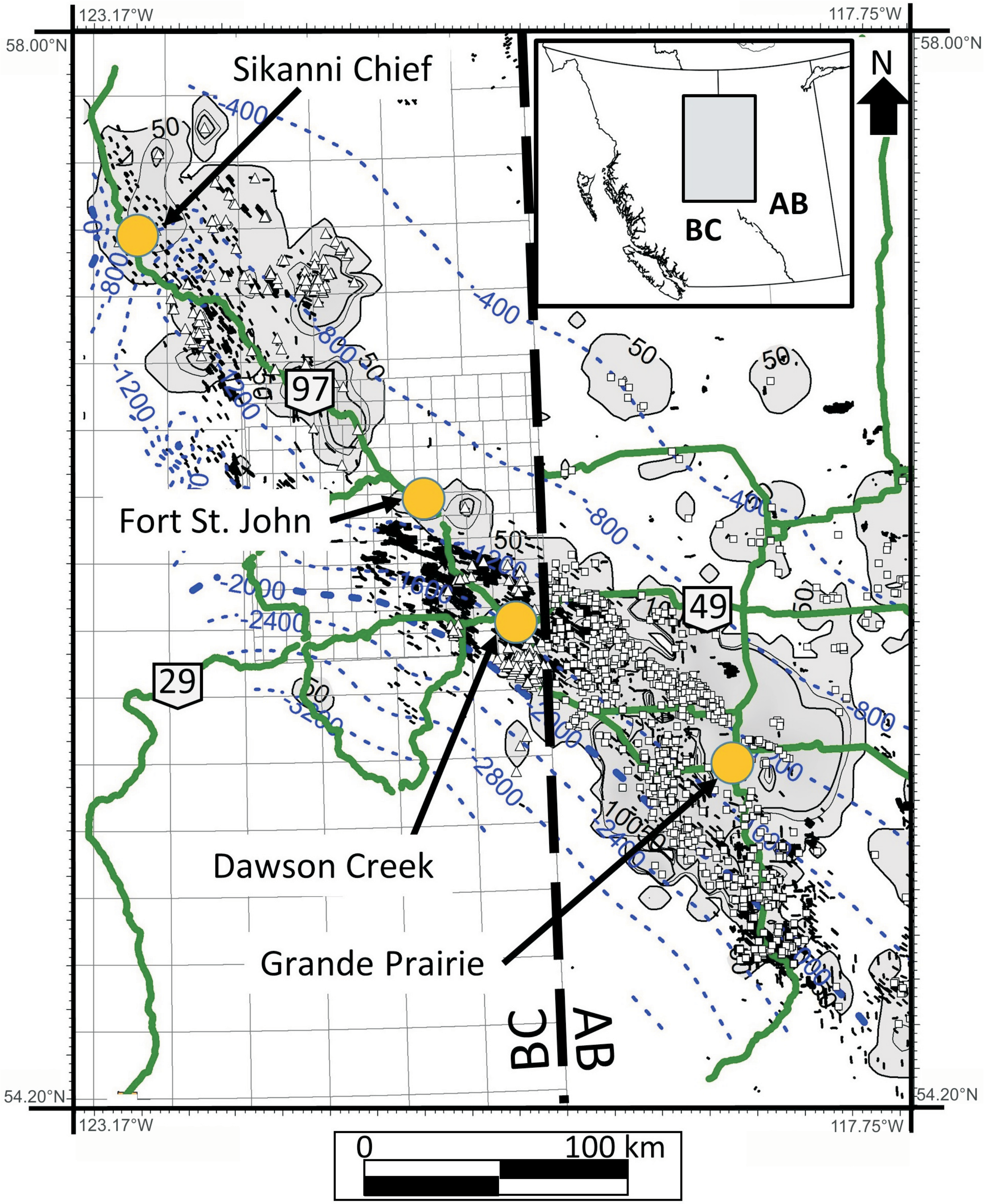

Figure 7. Sour gas distribution within the informal middle Montney member of the Montney Formation across the regional gas play in northeastern British Columbia and northwestern Alberta. The H_2S concentration is in parts per million (ppm) and the contour interval (solid black lines) is5000 ppm. The H_2S concentrations vary between 100 and 212 500 ppm (0.01–21.25%). The depth contours (blue dashed lines) are to the top of the middle Montney member and are measured in subsea total vertical depth (SSTVD; metres). White triangles represent sour wells in British Columbia and white squares represent sour wells in Alberta. Orange circles represent major population centres in the region and the green lines are the primary roads. Data sourced from geoLOGIC systems ltd. (2019).

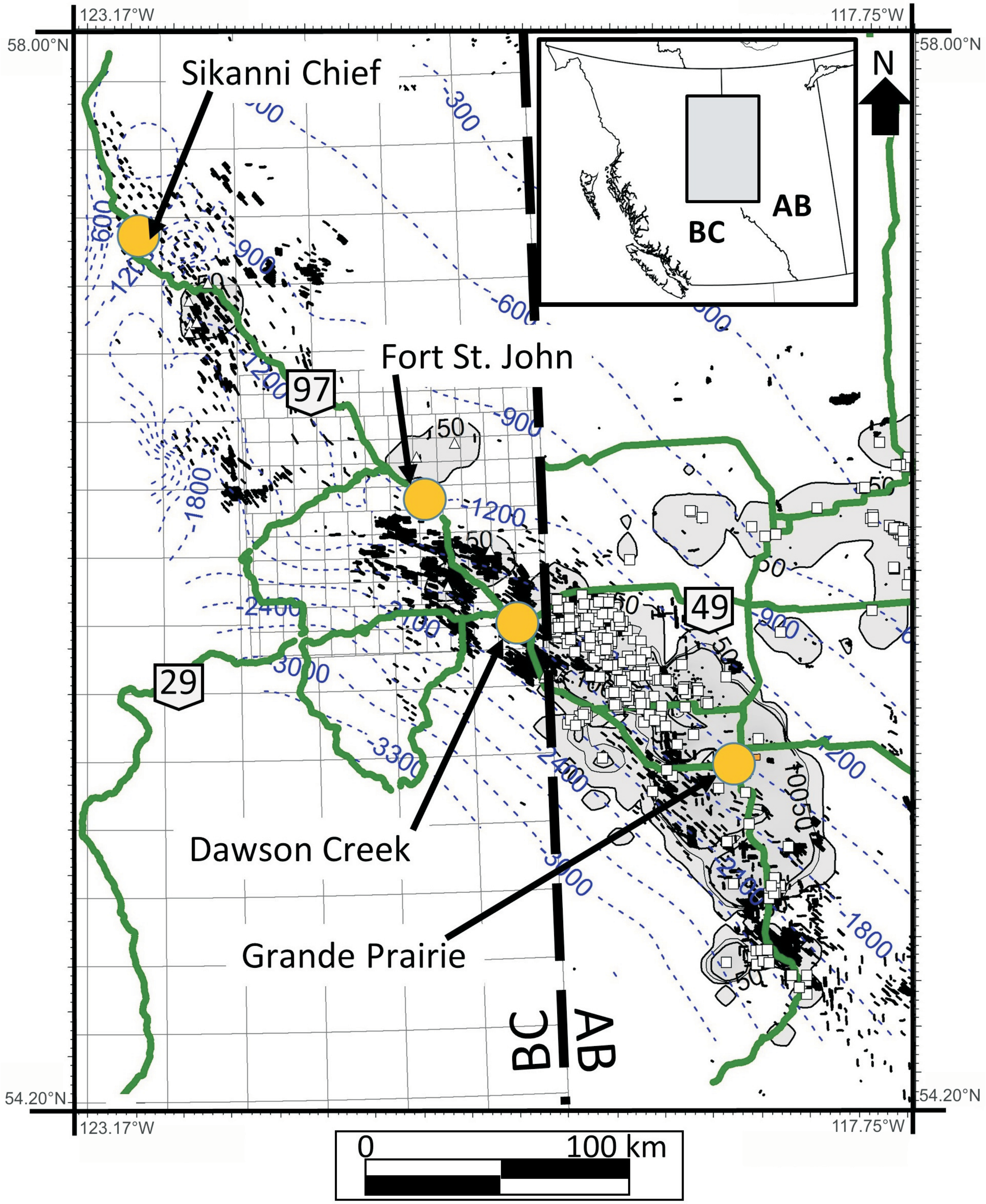

Figure 8. Sour gas distribution within the informal lower Montney member of the Montney Formation across the regional gas play in northeastern British Columbia and northwestern Alberta. The H_2S concentration is in parts per million (ppm) and the contour interval (solid black lines) is 5000 ppm. The H_2S concentrations vary between 100 and 137 000 ppm (0.01-13.7%). The depth contours (blue dashed lines) are to the top of the lower Montney member and are measured in subsea total vertical depth (SSTVD; metres). White triangles represent sour wells in British Columbia and white squares represent sour wells in Alberta. Orange circles represent major population centres in the region and the green lines are the primary roads. Data sourced from geoLOGIC systems ltd. (2019).

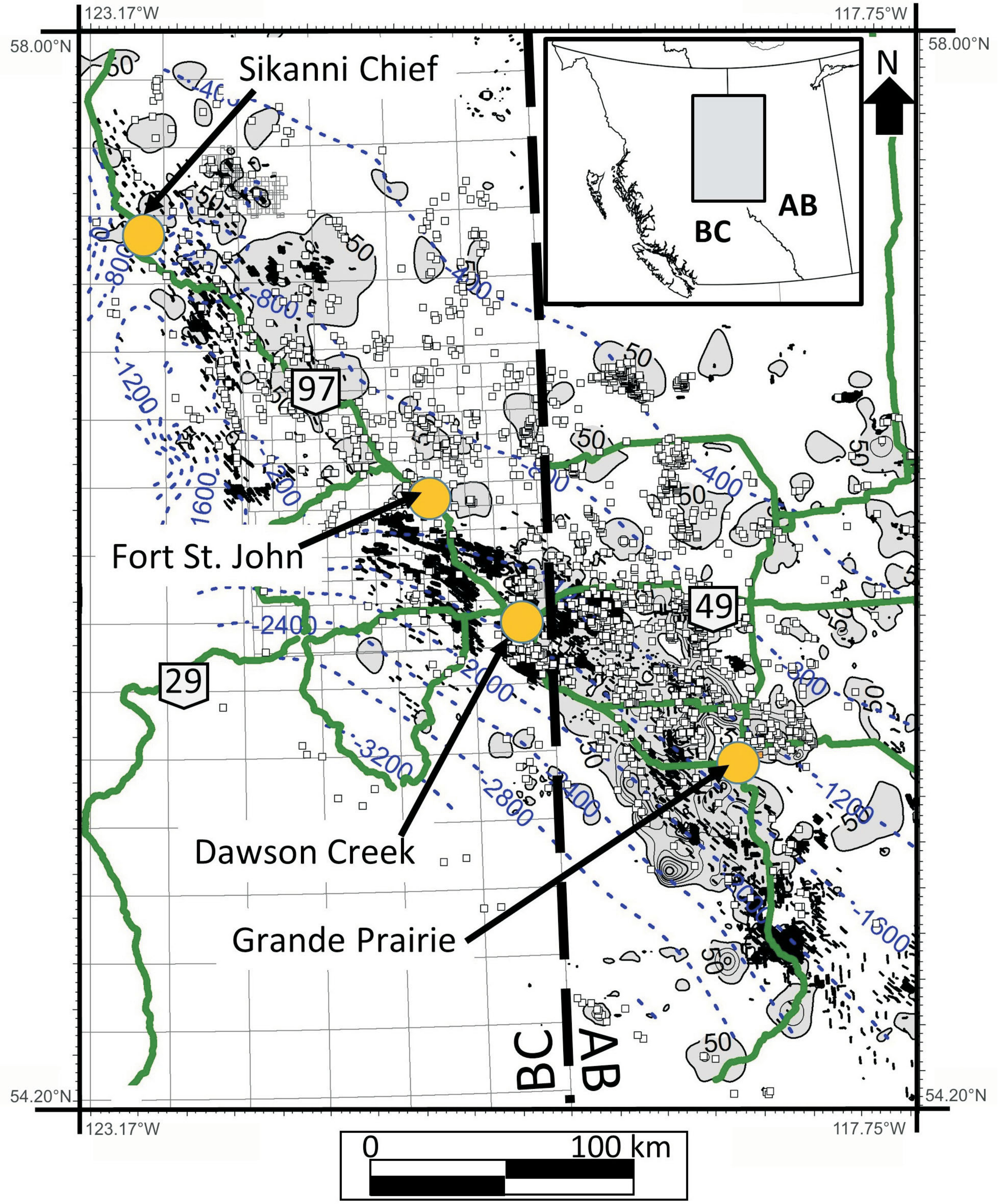

Figure 9. Hydrogen sulphide distribution in the Montney Formation along with sour wells in the overlying Doig and Charlie Lake formations (white squares). The depth contours (blue dashed lines) are to the top of the Montney Formation, measured in subsea total vertical depth (SSTVD; metres). Contour interval is 5000 ppm for the H_2S concentrations and 400 m for the depth contours. Orange circles represent major population centres in the region and the green lines are the primary roads. Data sourced from geoLOGIC systems ltd. (2019).

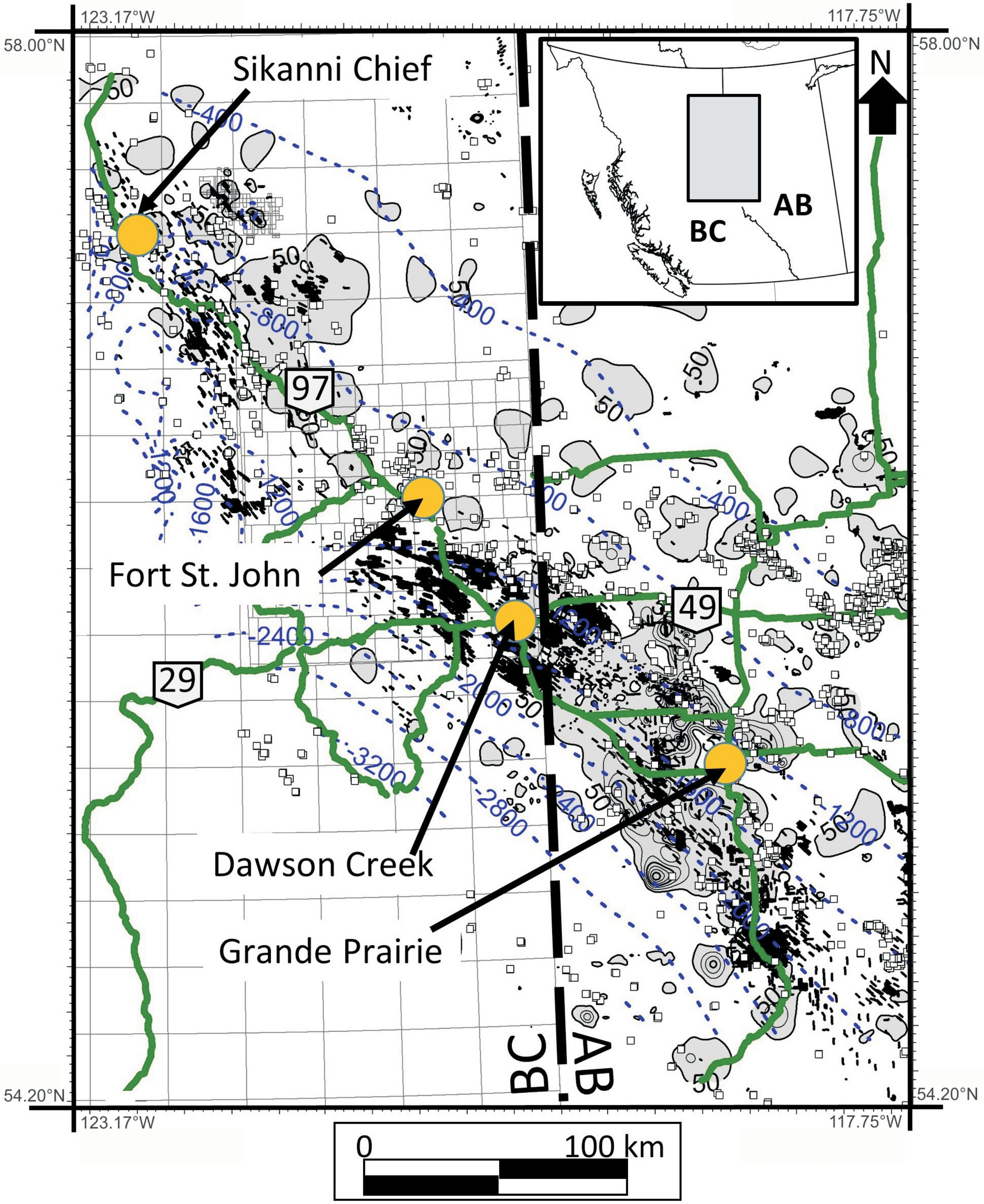

Figure 10. Hydrogen sulphide distribution in the Montney Formation along with sour wells in the underlying Permian, Mississippian and Devonian formations (white squares). The depth contours (blue dashed lines) are to the top of the Montney Formation, measured in subsea total vertical depth (SSTVD; metres). Contour interval is 5000 ppm for the H_2S concentrations and 400 m for the depth contours. Orange circles represent major population centres in the region and the green lines are the primary roads. Data sourced from geoLOGIC systems ltd. (2019).

between overlying sour wells (Doig and Charlie Lake formations) and the sour Montney Formation producers (Figure 9) compared to the underlying sour wells (i.e., Permian, Mississippian and Devonian rocks) and the sour Montney Formation producers (Figure 10). These trends illustrate that a connection may exist between overlying sour pools and areas with higher probability of Montney Formation producing souring within a play area. The connection that exists will be through local fracture systems or fractures associated with regional structures like the Fort St. John graben complex. Sharma (1969) observed anhydrite-filled fractures within the Halfway Formation where the anhydrite had migrated from the Charlie Lake Formation through groundwater circulation. This sulphate-rich water circulated through the Triassic system via fracture networks during early burial and no overpressuring existed as this was prior to any hydrocarbon migration. The anhydrite cementation then healed fractures and allowed a pressure differential to establish between the Charlie Lake and Halfway formations as the depth of burial increased. The same geological model may explain the souring of the Doig and Montney formations with fractures persisting through from the Charlie Lake to the Halfway, Doig and Montney formations. The fractures would allow anhydrite or H_2S gas (or a combination of both) to migrate into the Montney Formation. A predictive framework for sour Montney Formation production would include understanding the distribution of the overlying sour pools in the Doig, Halfway and Charlie Lake formations as well as understanding the fracture network system on regional and gas play scales.

Future Work

Sulphur isotopic data is currently being analyzed and compiled in order to test the geological model proposed above—that sour gas contributions are either from the migration of anhydrite or from H_2S gas from overlying sour pools in the Charlie Lake, Halfway and/or Doig formations. Sulphur isotopes are being analyzed from H_2S gas being produced in the Montney Formation, as well as from anhydrite, pyrite and organic matter concentrates from bulk rock samples of the Montney Formation. Anhydrite is also being analyzed from Triassic to Devonian rocks. This geological model will provide the information companies need to incorporate into their development plans, allowing them to reduce economic, health and environmental risks.

Conclusions

The study of the lateral and stratigraphic H_2S distribution within the Montney Formation in British Columbia (BC) indicates that the upper and middle portions of the Montney Formation in BC are at a higher risk of souring compared to wells that are placed in the lower portions (i.e., informal lower Montney member). However, there are fewer wells currently being drilled in the lower portions of the Montney Formation in BC, which may bias this interpretation. It appears all of the Montney Formation is at risk of souring in the gas play of Alberta. Mapping the sour wells above and below the Montney Formation indicates that souring of the Montney Formation may be linked with the overlying sour pools in the Doig and Charlie Lake formations, particularly in BC, and not linked to the underlying Permian, Mississippian or Devonian sour pools as initially thought. Isotopic analyses of sulphur from the H_2S gas and its sources (i.e., minerals or organic matter) will provide further clarity on the geological processes involved in souring of the Montney Formation.

Acknowledgments

The authors would like to thank P. Lacerda Silva for reviewing this paper. The authors would like to thank the industry partners Saguaro Resources Ltd., Crew Energy Inc., Encana Corporation, Chevron Corporation and Canbriam Energy Inc. for their support of this project. The authors would also like to acknowledge geoLOGIC systems ltd. for the use of geoSCOUT GIS program to search and analyze the well data for this study. This project was supported through a grant from Geoscience BC.

References

BC Oil and Gas Commission (2015): British Columbia's oil and gas reserves and production report, 2015; BC Oil and Gas Commission, 35 p., URL <https://www.bcogc.ca/node/13607/download> [October 2018].

Davies, G., Watson, N., Moslow, T. and MacEacher, J. (2018): Regional subdivisions, sequences, correlations and facies relationships of the Lower Triassic Montney Formation, west-central Alberta to northeastern British Columbia, Canada — with emphasis on role of paleostructure; Bulletin of Canadian Petroleum Geology, v. 66, p. 23–92, URL <https://pubs.geoscienceworld.org/cspg/bcpg/article/66/1/23/538508/regional-subdivisions-sequences-correlations-and> [October 2018].

geoLOGIC systems ltd. (2019): geoSCOUT version 8.8; geoLOGIC systems ltd., mapping, data management and analysis software, URL <https://www.geologic.com/products/geoscout/> [August 2019].

National Energy Board (2018): Canada's energy future 2018 supplement: natural gas production; National Energy Board, 12 p.

Sharma, G. (1969): Paragenetic evolution in Peejay field, British Columbia, Canada; Mineral Deposita, v. 4, issue 4, p. 346–354.

Facies Analysis and Depositional Setting of the Lower Triassic Montney Formation in Northeastern British Columbia, Western Canada Sedimentary Basin

P.D. González[1], **Ichnology Research Group, University of Alberta, Edmonton, Alberta, pdgonzal@ualberta.ca**

C.M. Furlong, Ichnology Research Group, University of Alberta, Edmonton, Alberta

M.K. Gingras, Ichnology Research Group, University of Alberta, Edmonton, Alberta

J.-P. Zonneveld, Ichnology Research Group, University of Alberta, Edmonton, Alberta

González, P.D., Furlong, C.M., Gingras, M.K. and Zonneveld, J.-P. (2020): Facies analysis and depositional setting of the Lower Triassic Montney Formation in northeastern British Columbia, Western Canada Sedimentary Basin; *in* Geoscience BC Summary of Activities 2019: Energy and Water, Geoscience BC, Report 2020-02, p. 53–64.

Introduction

The Lower Triassic Montney Formation in the Western Canada Sedimentary Basin has been a target for oil and gas exploration since the 1950s, containing well-known conventional plays, and more extensive and complex unconventional plays. The Montney Formation marketable unconventional-gas resource is one of the largest in the world and most of it is located in British Columbia (BC; National Energy Board et al., 2013). Overall, the Montney Formation is expected to contain 449 tcf of marketable natural gas, 14.521 million barrels of marketable natural-gas liquids and 1.125 million barrels of marketable oil (BC Oil and Gas Commission, 2012; National Energy Board et al., 2013). The Montney Formation is characterized by small-scale heterogeneities associated with minimal grain-size variations and diminutive biogenic structures; this, added to the extensive lateral-facies variability and the presence of local unconformities of varying nature, increases the stratigraphic complexity of the formation.

Detailed sedimentological and stratigraphic analyses are the key to understanding the complex internal architecture of the Montney Formation and to better understanding the facies-related variables controlling reservoir quality. This study focuses on analyzing facies distribution within the Montney Formation in northeastern BC, to interpret the depositional setting of the Montney Formation and significant stratigraphic surfaces. The identification of stratigraphic surfaces and discontinuities across the study area aids in formulating a sequence-stratigraphic framework across the basin.

Geological Framework

The Montney Formation is a westward-thickening wedge of siliciclastic and mixed carbonate-siliciclastic sediment that records deposition between the offshore and shoreface environments; a variety of subenvironments have been recognized and include turbidite deposits, deltaic units and shallow-water bioclastic sediments (Moslow and Davies, 1996, 1997; Davies et al., 1997; Kendall et al., 1998; Kendall, 1999; Moslow, 2000, 2001; Zonneveld et al., 2010a, b; Zonneveld and Moslow, 2014, 2017, 2018). The base of the Montney Formation is typically placed at an erosional unconformity on top of the Permian Belloy Formation, and the top of the Montney Formation is associated with a *Glossifungites*-demarcated surface and/or a phosphatic conglomerate lag overlain by the Middle Triassic Sunset Prairie or Doig formations (Figure 1; Gibson and Edwards, 1990; Edwards et al., 1994; Furlong et al., 2018a, b).

Deposition of the Montney Formation took place along the arid northwest coast of the North American craton (Davies et al., 1997) and was influenced by the effects of the end-Permian mass extinction, associated with a severe global-warming event, and resulting in anoxia and acidification of the world's oceans (Hallam, 1994; Wignall and Twitchett, 2002; Winguth et al., 2015). This resulted in restricted infaunal communities and typically small biogenic structures within Lower Triassic sediments (Hallam, 1994; Isozaki, 1994; Beatty et al., 2008; Abdolmaleki and Tavakoli, 2016).

Study Area and Methods

The study area focuses on the region known as the 'Northern Montney Field' (BC Oil and Gas Commission, 2017), between Townships 81 to 104 and Ranges 14 to 25 west of the 6th meridian, and NTS map areas 094A, B, G and H (Figure 2). According to recent stratigraphic nomenclature (Zonneveld and Moslow, 2018), the study interval includes the following members: Lower Montney, Pocketknife, Middle Montney, Altares and Upper Montney. A total of 38

---

[1] The lead author is a 2019 Geoscience BC Scholarship recipient.

This publication is also available, free of charge, as colour digital files in Adobe Acrobat® PDF format from the Geoscience BC website: http://www.geosciencebc.com/updates/summary-of-activities/.

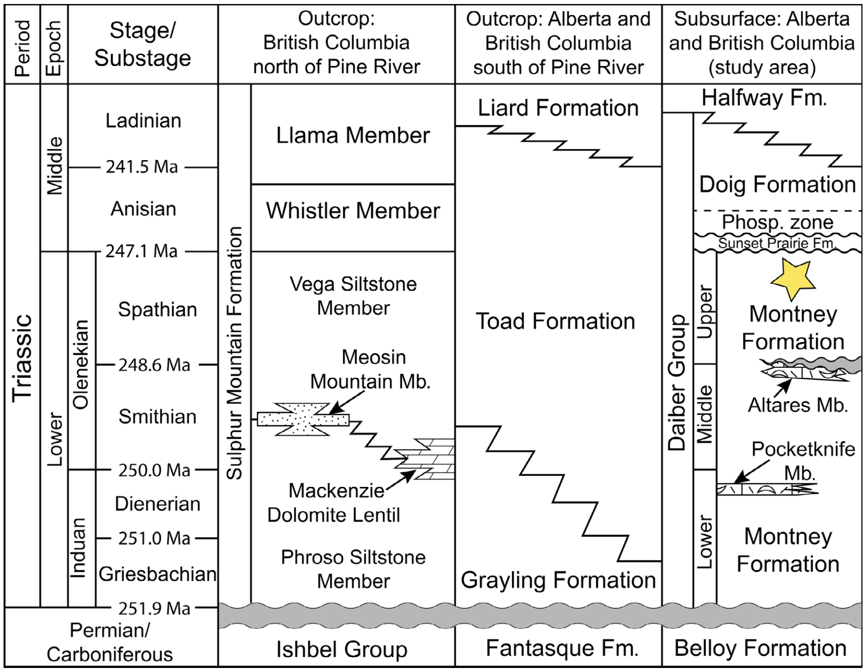

Figure 1. Lithostratigraphic nomenclature for the study interval (yellow star) and equivalent strata across western Canada (modified from Edwards et al., 1994, Furlong et al., 2018a, b and Zonneveld and Moslow, 2018). Abbreviations: Fm., formation; Mb., member; Phosp., phosphate.

drillcores were examined and detailed description of lithology, physical and biogenic sedimentary structures, bioturbation intensity and fossil content were recorded. Twelve lithofacies, summarized in Table 1, and three recurring facies associations were identified and interpreted from this dataset. Additionally, 56 thin sections from four cored wells (Tallisman Graham c-006-L/94-B-08, PC Kobes c-74-G/94-B-09, Suncor PC HZ Kobes d-048-A/94-B-09 and Progress Kobes d-067-J/94-B-09; Figure 2) were analyzed, using standard petrographic techniques on a polarizing microscope, to characterize the texture, composition and diagenetic features of the different facies. Samples were stained to differentiate between different mineral varieties; feldspar stains yellow when using sodium cobaltinitrate; and both alizarin red-S and potassium ferrocyanide stain calcite red, ferroan-dolomite blue/turquoise and ferroan-calcite purple. Additionally, detailed core descriptions were correlated with their corresponding petrophysical data (e.g., gamma-ray, resistivity logs) to properly identify stratigraphic surfaces and facies associations in well-log patterns. These correlations are useful for predicting facies in areas where core has not been obtained.

Results

Lithofacies

Twelve sedimentary facies were recognized in the study area, which occur within three recurring facies associations and are summarized in Table 1. From thin-section analysis, the mineralogical composition of the facies is overall dominated by quartz (detrital and authigenic), feldspar, calcite and dolomite, with smaller amounts of clay, muscovite, pyrite, apatite and chlorite (Figure 3a–c); phosphate is found as cement within thin lenses and laminae (Figure 3d) or as fish remains. Detrital grains are subangular, moderately well sorted and range in size between fine silt (7–30 µm) and coarse silt (31–60 µm), with rare, very fine grained sand (up to 89 µm). Bioclastic grains observed include fish teeth, calcispheres (Figure 3e), bivalves (Figure 3f), brachiopods and gastropods. Calcite and dolomite are present as cement in both ferroan and nonferroan varieties (Figure 3a, b). Quartz was observed as both detrital and authigenic mineral grains; authigenic quartz is most commonly found as overgrowths around detrital quartz grains, euhedral quartz crystals and as replacement of carbonate bioclasts.

Facies Associations

Three recurring facies associations are interpreted within the Montney Formation in northeastern BC. Overall, the facies associations identified in the study area represent distinct distal offshore to lower shoreface settings, with both retrogradational and progradational stacking patterns.

Facies Association A

Facies association A (Figure 4) comprises the predominantly fine-grained siltstone beds of facies 1, 2 and 9, and the calcisphere-rich siltstone beds of facies 5. The predominant sedimentary structures include horizontal planar-parallel laminae and, less commonly, starved ripples, suggest-

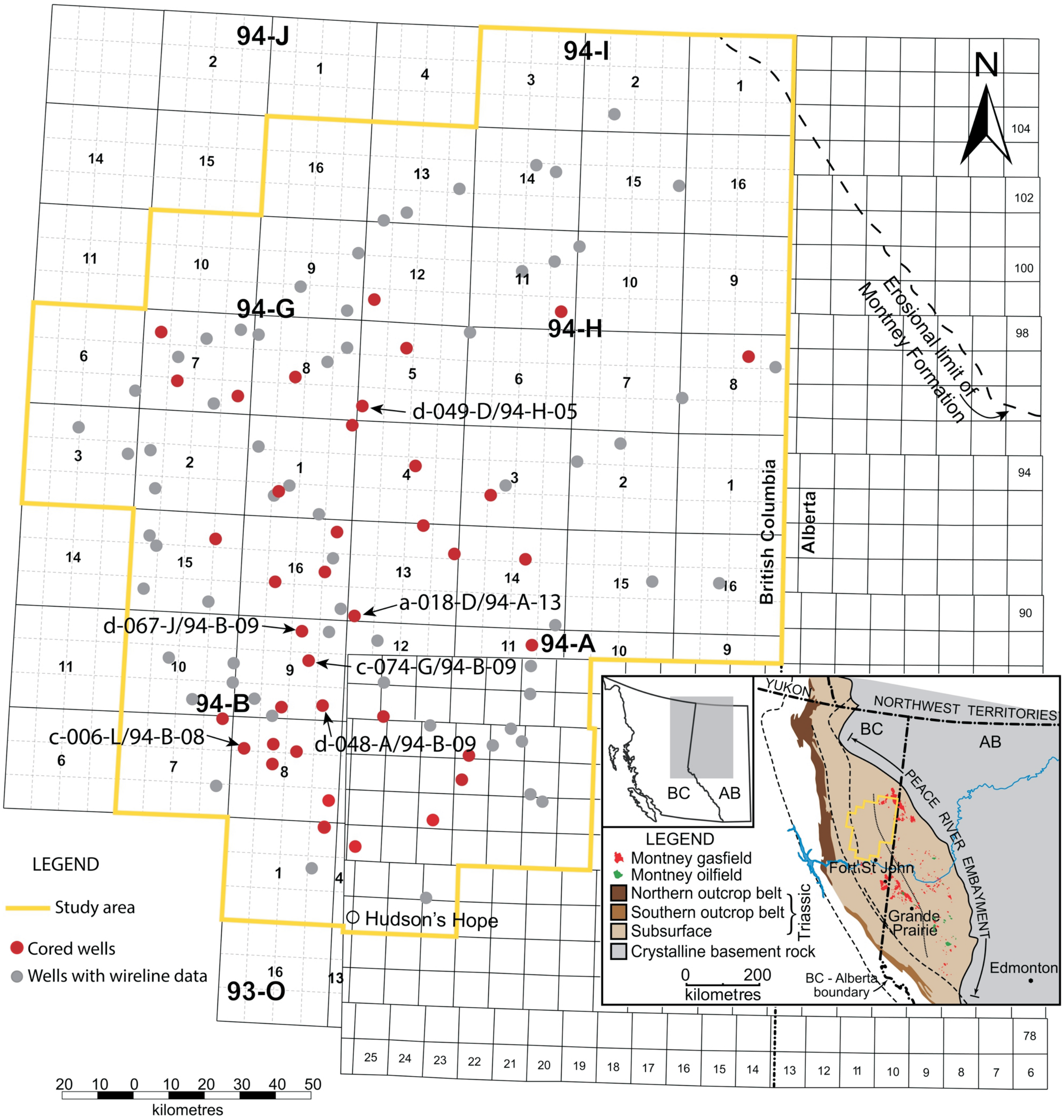

Figure 2. Location map of study area showing cored-well locations used for facies descriptions and petrographic analysis, northeastern British Columbia.

ing the predominant process of deposition was sedimentation from suspension. Phosphate lenses and nodules are common within facies 1 and 9, and are interpreted as deposition within an offshore setting, in association with upwelling processes. Calcispheres are abundant in facies 5 and have been interpreted as planktonic algal blooms associated with coastal upwelling (Chau and Henderson, 2010; Moslow et al., 2018; Zonneveld and Moslow, 2018). Bioturbation, expressed as a bioturbation index (BI), is very rare (BI = 0–1) except in facies 9, where it can be pervasive (BI = 4–6). Trace fossils present in facies association A include *Helminthopsis*, *Phycosiphon*, *Planolites*, *Teichichnus* and, less commonly, *Zoophycos*, overall indicative of a distal *Cruziana* Ichnofacies. This facies association consists of a fining-upward succession of facies, interpreted as a retrogradational sequence from a distal offshore transition setting (facies 9), to a distal offshore setting (facies 1), intermittently influenced by upwelling processes. Phos-

Table 1. Summary of sedimentary-facies characteristics in the Lower Triassic Montney Formation, northeastern British Columbia.

	Description	Physical sedimentary structures	Biogenic structures and fossils	Inferred process of deposition	Interpreted depositional setting
	Facies 1: Phosphate-rich fine-grained siltstone	Horizontal planar-parallel laminae; mm-thick phosphate-rich lenses and laminae. Rare layers of phosphatic sand to pebble-sized clasts	Small phosphatic fish debris	Deposition from suspension. Upwelling (?)	Distal offshore setting
	Facies 2: Dark grey fine-grained siltstone	Pinstripe laminae, very thin horizontal planar-parallel laminae. Rare laterally restricted starved ripples	Rare shell and bone fragments, ammonoid/fish-scale impressions along bedding planes. Calcispheres. Rare isolated traces of *Planolites* (BI = 0-2)	Predominantly deposition from suspension, influenced by infrequent/weak storms	Proximal offshore setting
Facies 3	**Facies 3A:** Predominantly dark grey fine-grained siltstone interbedded with coarse-grained siltstone	Horizontal planar-parallel laminae with subordinate wavy parallel laminae and current/starved ripples. Small-scale soft-sediment deformation; convolute bedding. Disseminated phosphatic sand/gravel	Small shell and bone fragments, fish bones, ammonoid/bivalve impressions along bedding planes	Predominantly deposition from suspension influenced by waves and currents, above storm wave base	Distal offshore transition setting (storm weather)
	Facies 3B: Bioturbated predominantly dark grey fine-grained siltstone interbedded with coarse-grained siltstone	Horizontal plana- parallel laminae with subordinate wavy parallel laminae and current/starved ripples. Small-scale soft-sediment deformation; convolute bedding. Disseminated phosphatic sand/gravel	Small shell/bone fragments, ammonoid/bivalve impressions along bedding planes. *Bergaueria, Conichnus, Planolites, Palaeophycus,* fugichnia (BI = 1-4)	Predominantly deposition from suspension influenced by waves and currents, above storm wave base	Distal offshore transition setting (fair weather) Stressed *Cruziana* ichnofacies
Facies 4	**Facies 4A:** Heterolithic interbedded fine- and coarse-grained siltstone	Horizontal planar-parallel laminae, current ripples, starved ripples; less common: wavy laminae, hummocky cross laminae. Convolute bedding. Phosphatic sand/gravel	Rare shell debris	Alternating storm deposition and fair-weather deposition	Proximal offshore transition setting (storm weather)
	Facies 4B: Bioturbated heterolithic interbedded fine- and coarse-grained siltstone	Horizontal planar-parallel laminae, current ripples, starved ripples; less common: wavy laminae, hummocky cross laminae. Convolute bedding. Phosphatic sand/gravel	*Bergaueria, Conichnus, Planolites, Palaeophycus, Scolicia*, fugichnia (BI = 2-5).	Alternating storm deposition and fair-weather deposition	Proximal offshore transition setting (fair weather) Stressed *Cruziana* ichnofacies
	Facies 5: Calcisphere-rich siltstone	Horizontal planar-parallel laminae	Abundant calcispheres	Sedimentation from suspension in a quiescent environment	Proximal offshore setting
	Facies 6: Bioclastic siltstone with horizontal planar-parallel laminae	Horizontal planar-parallel laminae	Abundant Claraia sp. shells parallel to bedding planes; can be fragmented	Biostrome growth associated with sedimentation from suspension	Distal offshore transition to proximal offshore
	Facies 7: Interbedded bioclastic packstone and fine-grained siltstone	Horizontal planar- and wavy-parallel laminae. Less common: current ripples and starved ripples. Concretionary carbonate intervals	Whole and fragmented bivalves, brachiopods and ammonoids; rare fish and reptile bones	Alternating storm-deposition and fair-weather deposition	Distal offshore transition to proximal offshore
	Facies 8: Isolated sharp-based coarse-grained siltstone to very fine-grained sandstone	Low-angle cross laminae, hummocky cross laminae; less commonly: horizontal planar-parallel laminae, ripples. Commonly 8-15 cm thick beds	Rare fugichnia	Storm deposition, tempestites	Tempestites in offshore transition setting
	Facies 9: Intensely bioturbated fine- to coarse-grained siltstone	Rare preservation of horizontal planar-parallel laminae. Phosphate-rich lenses	Primarily *Helminthopsis* and *Phycosiphon*; less common: *Planolites*, *Teichichnus, Bergaueria, Zoophycos* (BI = 4-6)	Sedimentation from suspension. Low sedimentation rates	Distal offshore transition to proximal offshore. Distal *Cruziana* ichnofacies
	Facies 10: Cross-stratified sandstone	Sharp-based, horizontal planar- and wavy-parallel laminae, planar cross laminae, hummocky cross laminae, current/wave ripples. Individual beds 20 cm-1m thick	Cryptobioturbation (BI = 6), *Planolites*, *Palaeophycus*, escape trace fossils (fugichnia) (BI = 1).	Storm deposition	Tempestites in lower shoreface setting.
	Facies 11: Burrowed firm ground	Burrowed firm ground associated with phosphatic lag deposits.	*Glossifungites* ichnofacies with: *Thalassinoides, Planolites, Rhizocorallium, Cylindrichnus, Skolithos*	Erosion of underlying strata followed by colonization of firm ground substrates	*Glossifungites*-demarcated surface in marginal-marine setting
	Facies 12: Intraclast breccia	Poorly sorted conglomerate; pebble- to cobble-sized angular intraclasts; ~5-20 cm thick	When found: fragmented shell material and ammonoids	Erosion of underlying strata during sea-level rise	Transgressive surface of erosion in marginal-marine setting

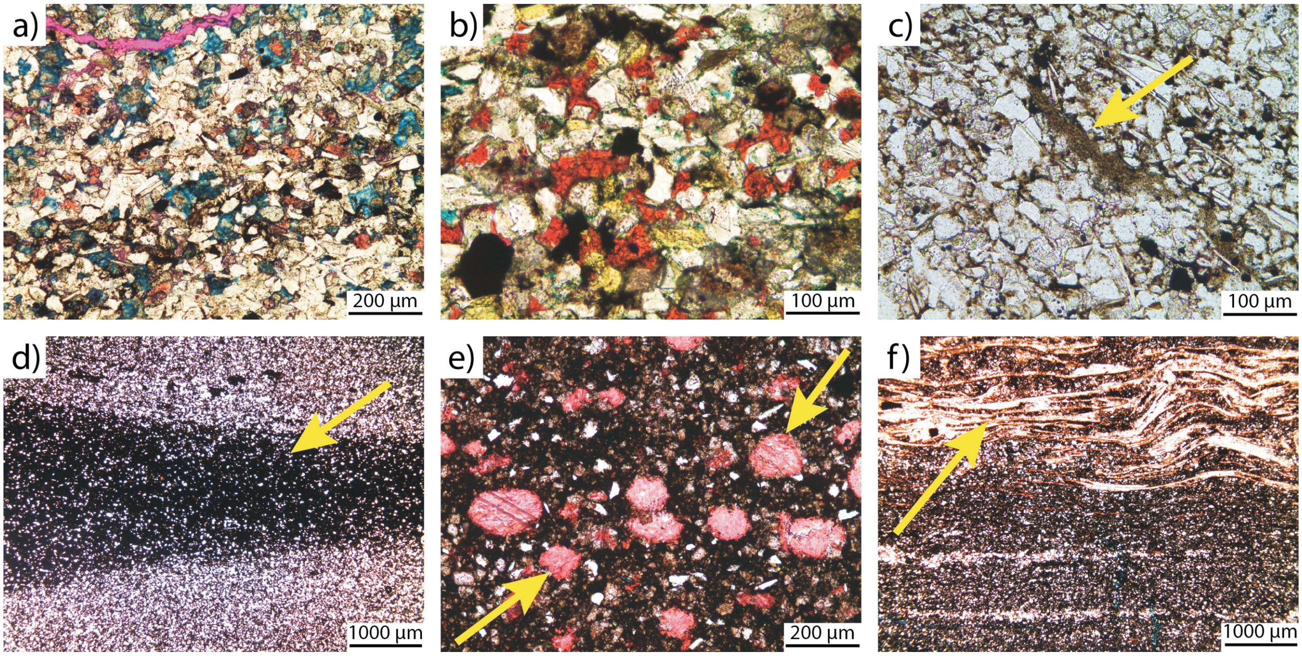

Figure 3. Photomicrographs showing the mineralogical composition and bioclastic components of the Lower Triassic Montney Formation in northeastern British Columbia, as observed in thin section (photos taken in transmitted plane-polarized light): **a)** mineralogy of coarse-grained siltstone laminae from facies 4 (well c-74-G/94-B-09 at 1882.40 m), where red-stained calcite cement and blue-stained ferroan-dolomite cement can be differentiated; **b)** mineralogy along coarse-grained siltstone laminae from facies 4 (well d-67-J/94-B-09 at 1908.87 m), showing yellow-stained common feldspar grains, and red-stained calcite cement and dolomite cement; **c)** clay aggregate (arrow) within coarse-grained siltstone laminae of facies 4 (well c-74-G/94-B-09 at 1870.60 m); **d)** fine-grained siltstone with phosphate-rich lenses (arrow) of facies 1 (well c-74-G/94-B-09 at 1932.30 m); **e)** red-stained calcite-cemented calcispheres (arrows) within the calcisphere-rich siltstone of facies 5 (well c-006-L/94-B-08 at 2646.10 m); **f)** contact between fine-grained siltstone of facies 2 at the bottom and bioclastic-rich beds of facies 7 at the top (well c-006-L/94-B-08 at 2664.90 m), showing abundant bivalves (arrow).

phatic facies are most commonly found within the lowermost Upper Montney Member.

Facies Association B

Facies association B (Figure 4) represents a coarsening-upward, progradational succession of mixed siliciclastic-carbonate sediments, dominated by the carbonate-rich beds of facies 6 and 7. Facies 6 is characterized by abundant *Claraia* sp. shells, which are parallel to bedding planes and encased within a dark, fine-grained siltstone. Facies 6 is stratigraphically restricted to the Dienerian-aged (Moslow et al., 2018) Pocketknife Member (Figure 1). Facies 7 consists of bioclastic packstone beds thinly interbedded with fine- and coarse-grained siltstone beds; bioclastic intervals of facies 7 consist of abundant cemented shell fragments, including bivalves, brachiopods and ammonoids. Facies 7 is present within the latest Smithian-aged (Golding et al., 2014) Altares Member only (Figure 1). Other facies present within this facies association include facies 2, 3 and 8:

- facies 2 is dominated by fine-grained siltstone and horizontal planar-parallel laminae
- facies 3 consists predominantly of fine-grained siltstone beds interbedded with coarse-grained siltstone, showing sedimentary structures such as wavy laminae, symmetric ripples and horizontal planar-parallel laminae, with sporadic bioturbation
- facies 8 is characterized by sharp-based coarse-grained siltstone to very fine grained sandstone beds with hummocky cross-stratification, symmetric ripples and flame structures, interpreted as tempestite sediments deposited within the offshore transition setting (facies 8 is geographically restricted to the northern portion of the study area).

In facies association B, the bioclastic-rich intervals of facies 6 and 7 are interbedded with the siliciclastic beds of facies 2, 3 and, less commonly, facies 8, showing an overall coarsening-upward pattern with facies 2 and 3 at the bottom, grading upward to facies 6, 7 and/or 8, depending on the location. Based on its characteristics, facies association B has been interpreted to represent deposition near storm wave base, within a mixed siliciclastic-carbonate offshore to offshore-transition setting, intermittently influenced by storms.

Facies Association C

Facies association C (Figure 5) consists of a siliciclastic, coarsening-upward succession of facies 2, 3, 4 and 10, and is characterized by storm-dominated sediments; facies 10 is rarely observed and is geographically restricted to the eastern portion of the study area. Overall, ‘lam-scram’ bedding (Pemberton et al., 1992) is characteristic of these deposits, representing interbedded storm-weather (non bioturbated

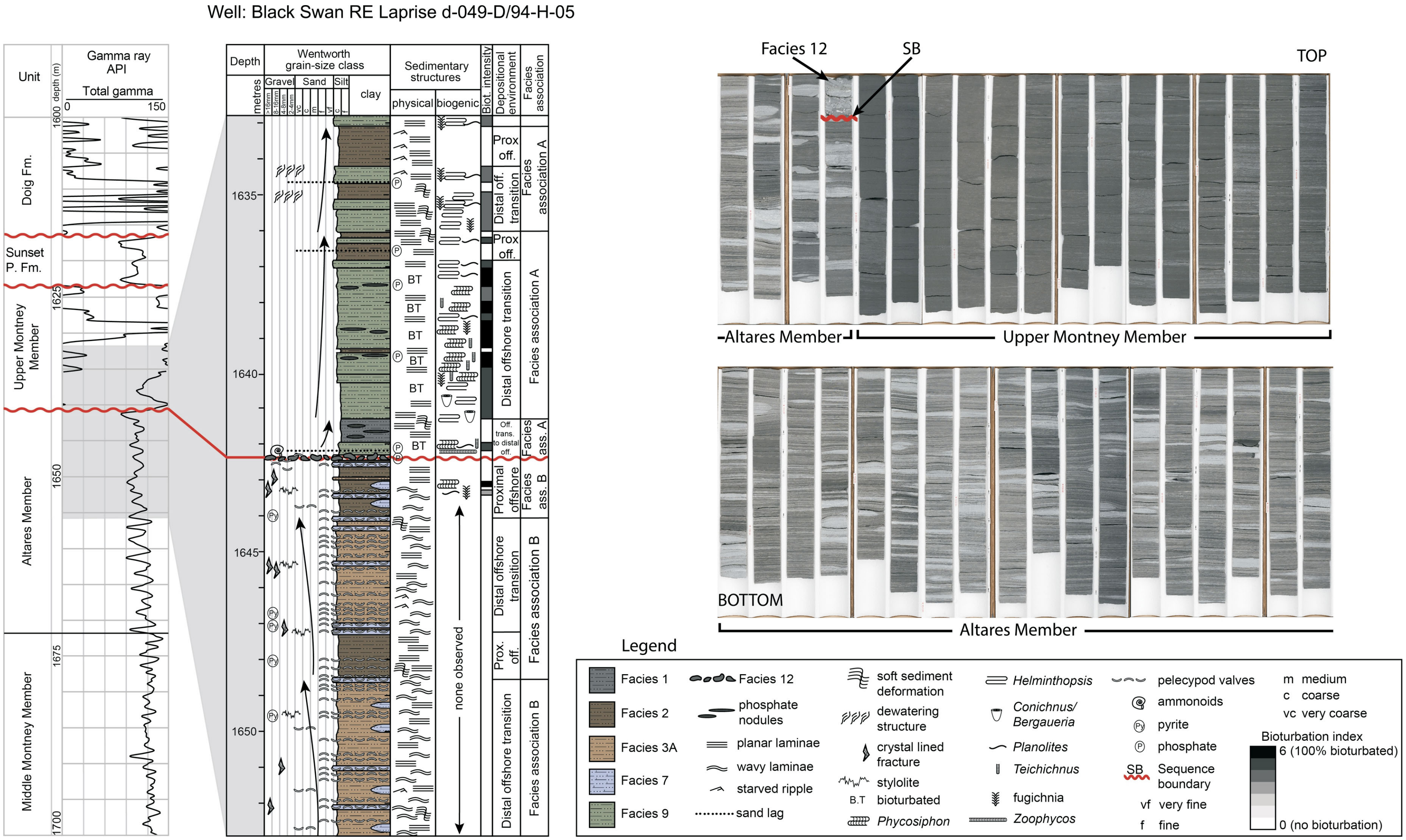

Figure 4. Detailed lithological log and corresponding core photographs, showing the common vertical-facies successions in facies associations A and B, from the Black Swan Laprise d-049-D/94-H-05 well (depth 1632.80–1653 m) in northeastern British Columbia. Abbreviations: ass., association; Biot., bioturbation; Dist., distal; Fm., formation; off., offshore; P., Prairie; Prox. and px., proximal.

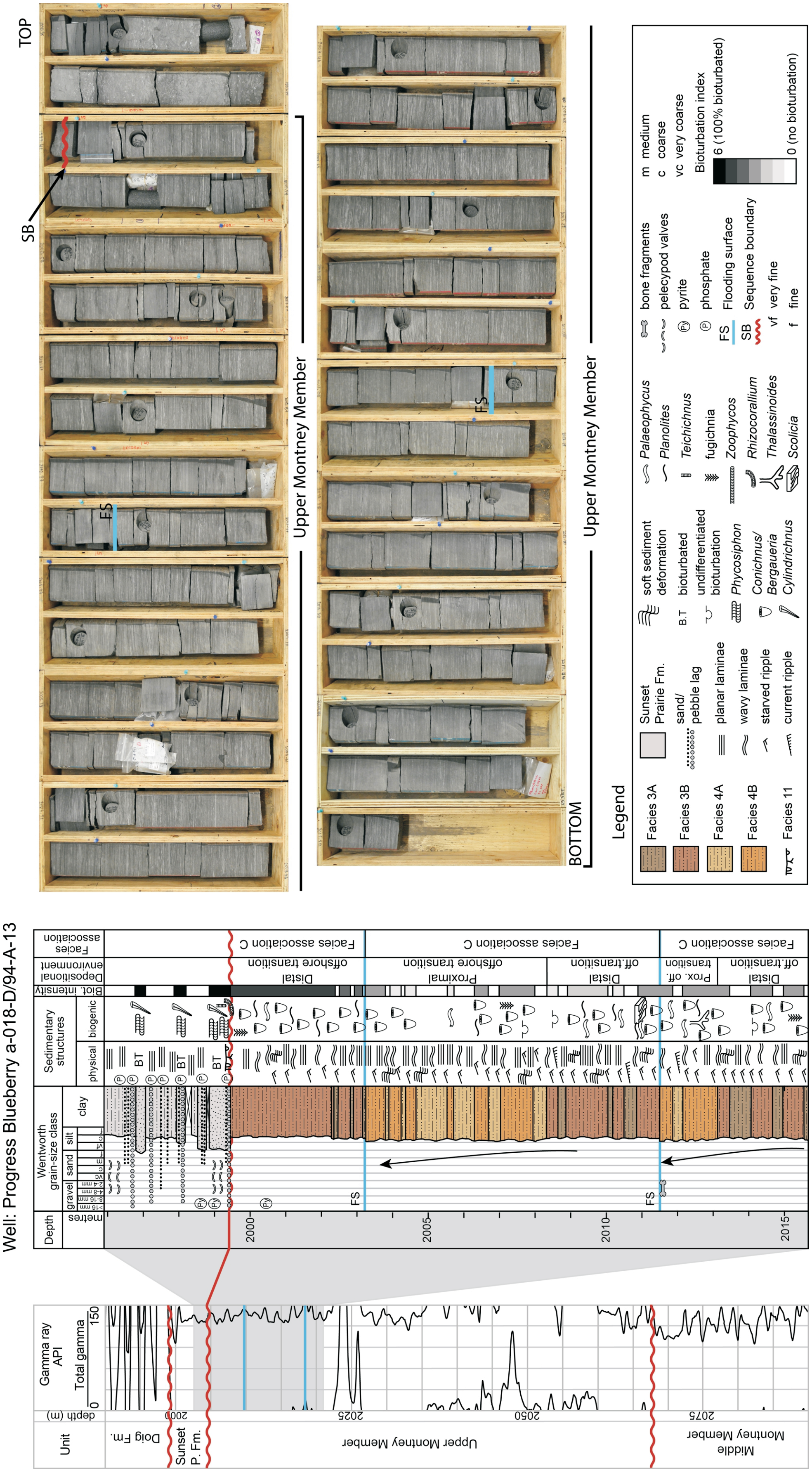

Figure 5. Detailed lithological log and corresponding core photographs, showing the vertical-facies successions in facies association C, from the Progress Blueberry a-018-D/94-A-13 well (depth 1995.91–2015.67 m), in northeastern British Columbia. Abbreviations: Biot., bioturbation; Fm., formation; offs., offshore; P., Prairie; Prox., proximal.

intervals of subfacies 3A and 4A) and fair-weather (bioturbated intervals of subfacies 3B and 4B) sediments. Storm-weather sediments contain sedimentary structures, including low-angle and hummocky cross-stratification, symmetric and asymmetric ripples, horizontal planar-parallel laminae and scour surfaces. Fair-weather sediments are represented by bioturbated intervals with moderate to low preservation of sedimentary structures (BI = 2–5) and containing trace-fossil assemblages dominated by *Bergaueria*, *Conichnus*, *Planolites*, *Palaeophycus* and *Scolicia*, overall indicative of a stressed *Cruziana* Ichnofacies. A typical facies succession in facies association C consists of fine-grained siltstone beds of facies 2, grading upward into the relatively coarser sediments of facies 3 and 4, and less commonly, of facies 10. Based on these characteristics, facies association C has been interpreted as a progradational succession deposited within a storm-dominated siliciclastic offshore transition to lower shoreface setting.

Discussion

The facies associations identified within the Montney Formation in the study area are interpreted as deposition across a storm-dominated ramp, between the offshore and lower shoreface environments, intermittently influenced by upwelling processes (Figure 6). More proximal depositional settings are not identified within the study area and are likely located more proximally within the basin or have been erosionally removed. Storm processes are interpreted from sharp- to scoured-based coarse-grained siltstone and very fine grained sandstone beds with storm-generated structures, including hummocky cross-stratification, wavy laminae and symmetric ripples, with very rare bioturbation (facies 3A, 4A, 8, 10; Figure 6); fragmented shell material found in facies 6 and 7 may also indicate storm influence. Interstorm intervals are represented by intensely bioturbated siltstone beds (BI = 4–6), with trace-fossil assemblages indicative of a stressed *Cruziana* Ichnofacies (facies 3B, 4B, 9; Figure 6).

Upwelling influence was interpreted from the presence of calcisphere structures (facies 5) and phosphate nodules (facies 1 and 9). Calcispheres found within the Montney Formation have been interpreted as planktonic structures derived from algal blooms that became concentrated in the photic zone as a result of upwelling processes. These structures were subsequently deposited out of suspension and preserved within sediments below storm wave base (Chau and Henderson, 2010; Moslow et al., 2018; Zonneveld and Moslow, 2018). Phosphate deposition has been largely associated with upwelling, during which low sedimentation rates and large influx of organic material, both essential elements for formation of phosphate, are favoured (Glenn et al., 1994; Dornbos, 2010; Filipelli, 2011; Li and Schieber, 2015). However, it must be noted that other mechanisms for phosphate enrichment have been proposed, including hydrothermal processes, microbial concentration, redox pumping of phosphorus via iron oxyhydroxides, fish-bone dissolution and weathering of terrestrial settings (Glenn et al., 1994; Brookfield et al., 2009; Dornbos, 2010; Nelson et al., 2010; Filipelli, 2011; Li and Schieber, 2015).

Additionally, two facies associated with stratigraphic surfaces were recognized in the study area; these include the burrowed firm ground of facies 11 and the intraclast breccia of facies 12 (Table 1; Figure 6). Facies 11 comprises a substrate-controlled, burrowed firm ground characterized by a trace-fossil assemblage that includes *Thalassinoides*, *Planolites*, *Rhizocorallium*, *Cylindrichnus* and *Skolithos*. Facies 11 has been interpreted as a *Glossifungites* Ichnofacies-demarcated surface and represents an erosional unconformity associated with a flooding event, at the contact between the Montney Formation and the overlying Sunset Prairie Formation. The intraclast breccia of facies 12 is found as 5–20 cm thick beds at the contact between proximal offshore/offshore-transition deposits below and distal offshore-transition deposits above, representing a conglomeratic lag resulting from erosion of underlying strata during a marine transgression (Cattaneo and Steel, 2003; Clifton, 2003). Facies 12 is found at the contact between the Middle Montney/Altares Member below and the Upper Montney Member above, and has been interpreted as a coplanar transgressive surface of erosion and sequence boundary coincident with the Smithian–Spathian boundary (Golding et al., 2014).

Summary and Future Work

A preliminary interpretation of the facies variability and the depositional setting of the Montney Formation in northeastern BC was presented using data from 38 drillcores, wireline data and 56 thin-section samples. Cores covered the Lower Montney, Pocketknife, Middle Montney, Altares and Upper Montney members, as well as the lower and upper contacts with Permian and Middle Triassic units, respectively. Detailed analysis of sedimentological, ichnological and paleontological data suggests the Montney Formation in northeastern BC was deposited along a storm-dominated, mixed carbonate-siliciclastic ramp setting, between the offshore and shoreface depositional environments, intermittently influenced by upwelling processes. Significant stratigraphic surfaces were identified in core, including discontinuity surfaces at the top of the Middle Montney/Altares Member and at the top of the Montney Formation; both are regional surfaces correlatable throughout the study area.

This study is part of a project that investigates the facies variability and stratigraphic architecture of the Montney Formation in the Western Canada Sedimentary Basin. Future work includes integrating the sedimentological core data with petrophysical logs; producing detailed strike- and

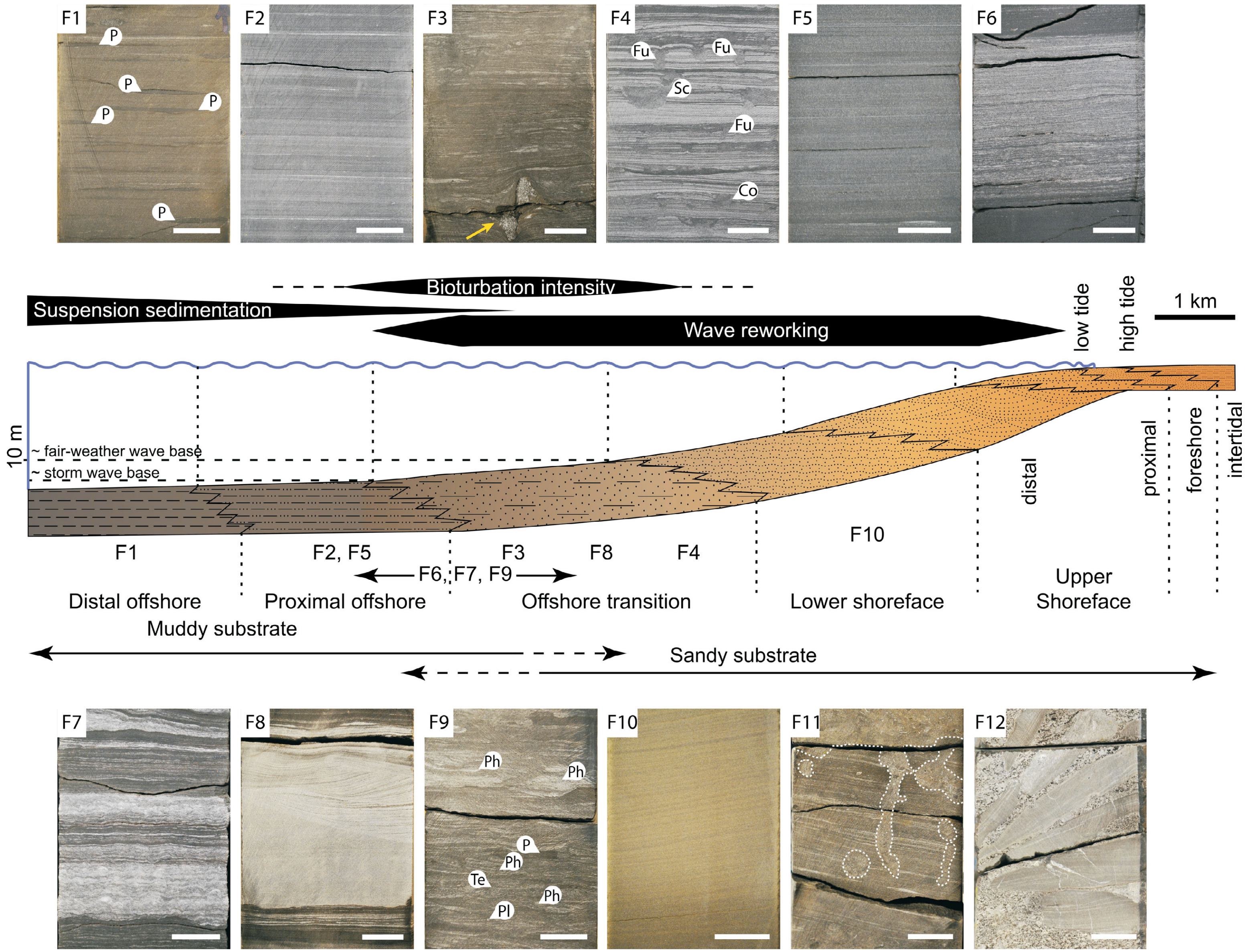

Figure 6. Summary of facies present within the Lower Triassic Montney Formation and their distribution along a schematic facies model; modified from Walker and Plint (1992), Reading and Collinson (1996), Plint (2010) and Zonneveld et al. (2010b). The twelve sedimentary facies are shown as F1–F12; the yellow arrow in F3 indicates the presence of an ichthyosaur vertebra. Scale bar in the facies photographs is 2 cm. Abbreviations: Co, *Conichnus*; Fu, fugichnia; P, phosphate; Ph: *Phycosiphon*; Pl, *Planolites*; Sc, *Scolicia*; Te, *Teichichnus*.

dip-oriented cross-sections to establish regional correlations; and incorporating inorganic geochemistry analysis to interpret more detailed paleoenvironmental conditions and relative sea-level changes. This will provide detail on the lateral-facies variability of the Montney Formation across the study area, and on its overall stratigraphic architecture, both of which are essential for defining and correlating potential reservoir units.

Acknowledgments

The authors acknowledge the financial support of Geoscience BC, Canbriam Energy Inc., Shell Canada, Birchcliff Energy Ltd., Sasol Canada, Progress Energy Canada Ltd. and TAQA North Ltd. Additional financial support was provided by a Natural Sciences and Engineering Research Council of Canada Collaborative Research and Development grant awarded to J.-P. Zonnneveld and M.K. Gingras. The authors would like to thank T. Playter for reviewing this paper and providing comments and suggestions that improved the final manuscript.

References

Abdolmaleki, J. and Tavakoli, V. (2016): Anachronistic facies in the early Triassic successions of the Persian Gulf and its palaeoenvironmental reconstruction; Palaeogeography, Palaeoclimatology, Palaeoecology, v. 446, p. 213–224.

BC Oil and Gas Commission. (2012): Montney Formation Play Atlas NEBC; BC Oil and Gas Commission Report, 35 p., URL <https://www.bcogc.ca/montney-formation-play-atlas-nebc> [August 2016].

BC Oil and Gas Commission. (2017): British Columbia's Oil and Gas Reserves and Production Report; BC Oil and Gas Commission Report, 40 p., URL <https://www.bcogc.ca/node/15405/download> [June 2019].

Beatty, T.W., Zonneveld, J.-P. and Henderson, C.M. (2008): Anomalously diverse Early Triassic ichnofossil assemblages in northwest Pangea: a case for a shallow-marine habitable zone; Geology, v. 36, no. 10, p. 771–774.

Brookfield, M.E., Hemmings, D.P. and Van Straaten, P. (2009): Palaeoenvironments and origin of the sedimentary phosphorites of the Napo Formation (Late Cretaceous, Oriente Basin, Ecuador); Journal of South American Earth Sciences, v. 28, no. 2, p. 180–192.

Cattaneo, A. and Steel, R.J. (2003): Transgressive deposits: a review of their variability; Earth-Science Reviews, v. 62, p. 187–228.

Clifton, H.E. (2003): Supply, segregation, successions, and significance of shallow marine conglomeratic deposits; Bulletin of Canadian Petroleum Geology, v. 51, no. 4, p. 370–388.

Chau, Y.P. and Henderson, C.M. (2010): The Lower Triassic Sulphur Mountain Formation, Mount Crum section, east-central British Columbia: age, tectonic implications and Montney lithofacies comparisons; Canadian Society of Petroleum Geologists-Canadian Society of Exploration Geophysicists-Canadian Well Logging Society, Joint Annual Convention (GeoCanada 2010), 10–14 May 2010, Calgary, Alberta, extended abstract, 4 p., URL <https://www.geoconvention.com/archives/2010/0902_GC2010_The_Lower_Triassic_Sulphur_Mountain_Fm.pdf> [May 2019].

Davies, G.R., Moslow, T.F. and Sherwin, M. (1997): The Lower Triassic Montney Formation, west-central Alberta; Bulletin of Canadian Petroleum Geology, v. 45, no. 4, p. 474–505.

Dornbos, S.Q. (2010): Chapter 14: Phosphatization through the Phanerozoic; *in* Taphonomy: Process and Bias Through Time, P.A. Allison and D. Bottjer (ed.), Topics in Geobiology 32, p. 435–456.

Edwards, D.E., Barclay, J. E., Gibson, D.W., Kvill, G. E. and Halton, E. (1994): Triassic strata of the Western Canadian Sedimentary Basin; *in* Geological Atlas of the Western Canada Sedimentary Basin, G.D. Mossop and I. Shetsen (comp.), Canadian Society of Petroleum Geologists, Calgary, Alberta and Alberta Research Council, Edmonton, Alberta, Special Report 4, p. 159–275.

Fillipelli, G.M. (2011): Phosphate rock formation and marine phosphorous geochemistry: the deep time perspective; Chemosphere, v. 84, p. 759–766.

Furlong, C.M., Gegolick, A., Gingras, M.K., González, P., Moslow, T.F., Prenoslo, D., Playter, T. and Zonneveld, J.-P. (2018a): Sedimentology and ichnology of the Middle Triassic (Anisian) Sunset Prairie Formation of the Western Canada Sedimentary Basin; *in* The Montney Play of Western Canada: Deposition to Development, T. Euzen, T.F. Moslow and M. Caplan (ed.), Bulletin of Canadian Petroleum Geology, v. 66, no. 1, p. 215–236.

Furlong, C.M., Gingras, M.K., Moslow, T.F. and Zonneveld, J.-P. (2018b): The Sunset Prairie Formation: designation of a new Middle Triassic formation between the Lower Triassic Montney Formation and Middle Triassic Doig Formation in the Western Canada Sedimentary Basin, northeast British Columbia; *in* The Montney Play of Western Canada: Deposition to Development, T. Euzen, T.F. Moslow and M. Caplan (ed.), Bulletin of Canadian Petroleum Geology, v. 66, no. 1, p. 193–214.

Gibson, D.W. and Edwards, D.E. (1990): An overview of Triassic stratigraphy and depositional environments in the Rocky Mountain Foothills and Western Interior Plains, Peace River Arch area, northeastern British Columbia; Bulletin of Canadian Petroleum Geology, v. 38A, p. 146–158.

Glenn, C.R., Föllmi, K.B., Riggs, S.R., Baturin, G.N., Grimm, K.A., Trappe, J., Abed, A.M., Galli-Olivier, C., Garrison, R.E., Ilyin, A.V., Jehl, C., Rohrlich, V., Sadaqah, R.M., Schidlowski, M., Sheldon, R.E. and Siegmund, H. (1994): Phosphorous and phosphorites: sedimentology and environments of formation; Eclogae Geologicae Helvetiae, v. 87, no. 3, p. 747–788.

Golding, M.L., Orchard, M.J., Zonneveld, J.-P., Henderson, C.M. and Dunn, L. (2014): An exceptional record of the sedimentology and biostratigraphy of the Montney and Doig formations in British Columbia; Bulletin of Canadian Petroleum Geology, v. 62, p. 157–176.

Hallam, A. (1994): The earliest Triassic as an anoxic event, and its relationship to the end-Palaeozoic mass extinction; Canadian Society of Petroleum Geologists, Memoir 17, p. 797–804.

Isozaki, Y. (1994): Superanoxia across the Permo-Triassic boundary: record in accreted deep-sea pelagic chert in Japan; Canadian Society of Petroleum Geologists, Memoir 17, p. 805–812.

Kendall, D. (1999): Sedimentology and stratigraphy of the Lower Triassic Montney Formation, Peace River Basin, subsurface of northwestern Alberta; M.Sc. thesis, University of Calgary, Calgary, Alberta, 368 p.

Kendall, D., Panek, R. and Henderson, C. (1998): Coquina facies of the Lower Triassic Montney Formation, Peace River Embayment, northwestern Alberta; Canadian Society of Petroleum Geologists, Geo-Triad ’98, Joint Convention, 16–19 June 1998, Calgary, Alberta, Special Publication, extended abstract, p. 464–465, URL <http://archives.datapages.com/data/cspg_sp/data/CSPG-SP-022/022001/464_cspgsp220464.htm> [May 2016].

Li, Y. and Schieber, J. (2015): On the origin of a phosphate enriched interval in the Chattanooga Shale (Upper Devonian) of Tennessee – A combined sedimentologic, petrographic, and geochemical study; Sedimentary Geology, v. 329, p. 40–61.

Moslow, T.F. (2000): Reservoir architecture of a fine-grained turbidite system: Lower Triassic Montney Formation, Western Canada Sedimentary Basin; *in* Deep-water Reservoirs of the World, P. Weimer, R.M. Slatt, J. Coleman, N.C. Rosen, H. Nelson, A.H. Bouma, M.J. Styzen and D.T. Lawrence (ed.), Society of Economic Paleontologists and Mineralogists, Gulf Coast Section, Conference Proceedings, December 3–6, 2000, Houston, Texas, v. 20, p. 686–713.

Moslow, T.F. (2001): Reservoir compartmentalization and architecture of a fine-grained turbidite system: lower Triassic Montney Formation, Alberta; Rock the Foundation Convention, Canadian Society of Petroleum Geologists, 18–22 June 2001, Calgary, Alberta, p. 409–410, URL <http://archives.datapages.com/data/cspg_sp/data/CSPG-SP-024/024001/409_cspgsp240409.htm> [May 2016].

Moslow, T.F. and Davies, G.R. (1996): Reservoir heterogeneity and performance of turbidite facies, Montney Formation, Sexsmith-Valhalla-LaGlace fields; *in* Oil and Gas Pools of the Western Canada Sedimentary Basin, Canadian Society of Petroleum Geologists, Special Publication, Abstract, p. 161-161, URL <http://archives.datapages.com/data/cspg_sp/data/019/019001/161_cspgsp190161.htm> [May 2016].

Moslow, T.F. and Davies, G.R. (1997): Turbidite reservoir facies in the Lower Triassic Montney Formation, west-central Alberta; *in* Triassic of the Western Canada Sedimentary Basin, T.F. Moslow and J. Wittemberg (ed.), Bulletin of Canadian Petroleum Geology, v. 45, no. 4, p. 507–536.

Moslow, T.F., Haverslew, B. and Henderson, C.M. (2018): Sedimentary facies, petrology, reservoir characteristics, conodont biostratigraphy and sequence stratigraphic framework of a continuous (395 m) full diameter core of the Lower Triassic Montney Fm, northeastern British Columbia; *in* The Montney Play of Western Canada: Deposition to Development, T. Euzen, T.F. Moslow and M. Caplan (ed.), Bulletin of Canadian Petroleum Geology, v. 66, no. 1, p. 259–287.

National Energy Board, BC Oil and Gas Commission, Alberta Energy Regulator and BC Ministry of Natural Gas Development (2013): The ultimate potential for unconventional petroleum from the Montney Formation of British Columbia and Alberta – Energy briefing note; National Energy Board, BC Oil and Gas Commission, Alberta Energy Regulator and BC Ministry of Natural Gas Development, 17 p., URL <https://www.cer-rec.gc.ca/nrg/sttstc/ntrlgs/rprt/ltmtptntlmntnyfrmtn2013/ltmtptntlmntnyfrmtn2013-eng.pdf> [August 2016].

Nelson, G.J., Pufahl, P.K. and Hiatt, E.E. (2010): Paleoceanographic constraints on Precambrian phosphorite accumulation, Baraga Group, Michigan, USA; Sedimentary Geology, v. 226, p. 9–21.

Pemberton, S.G., Van Wagoner, J.C. and Wach, G.D. (1992): Ichnofacies of a wave-dominated shoreline; *in* Applications of Ichnology to Petroleum Exploration: A Core Workshop, S.G. Pemberton (ed.), Society of Economic Paleontologists and Mineralogists, Core Workshop, v. 17, p. 339–382.

Plint. A.G. (2010): Wave- and storm-dominated shoreline and shallow-marine systems; *in* Facies Models 4, N.P. James and R.W. Dalrymple (ed.), Geological Association of Canada, St. John’s, Newfoundland, Geotext 6, v. 4, p. 167–200.

Reading, H.G. and Collinson, J.D. (1996): Clastic coasts; *in* Sedimentary Environments: Processes, Facies and Stratigraphy, third edition, H.G. Reading (ed.), Wiley-Blackwell Publishing, Oxford, United Kingdom, p. 154–231.

Walker, R.G. and Plint, A.G. (1992): Wave- and storm-dominated shallow marine systems; *in* Facies Models: Response to Sea-Level Change, R.G. Walker and N.P. James (ed.), Geological Association of Canada, St. John’s, Newfoundland, Geotext 1, p. 219–238.

Wignall, P.B. and Twitchett, R. (2002): Extent, duration and nature of the Permian-Triassic superanoxic event; *in* Catastrophic Events and Mass Extinctions: Impacts and Beyond, C. Koeberl and K.C. MacLeod (ed.), Geological Society of America Special Paper, v. 356, p. 395–413.

Winguth, A.M.E., Shields, C.A. and Winguth, C. (2015): Transition into a hothouse world at the Permian–Triassic boundary – a model study; Palaeogeography, Palaeoclimatology, Palaeoecology, v. 440, p. 316–327.

Zonneveld, J.-P., Gingras, M.K. and Beatty, T.W. (2010a): Diverse ichnofossil assemblages following the P–T mass extinction, Lower Triassic, Alberta and British Columbia, Canada: evidence for shallow marine refugia on the northwestern coast of Pangaea; Palaios, v. 25, p. 368–392.

Zonneveld, J.-P., MacNaughton, R.B., Utting, J., Beatty, T.W., Pemberton., S.G. and Henderson, C.M. (2010b): Sedimentology and ichnology of the Lower Triassic Montney Formation in the Pedigree-Ring/Border-Kahntah River area, northwestern Alberta and northeastern British Columbia; Bulletin of Canadian Petroleum Geology, v. 58, p. 115–140.

Zonneveld, J.-P. and Moslow, T.F. (2014): Perennial river deltas of the Montney Formation: Alberta and British Columbia subcrop edge; Canadian Society of Petroleum Geologists-Canadian Society of Exploration Geophysicists-Canadian Well Logging Society, Joint Annual Convention (GeoConvention 2014), 12–16 May 2014, Calgary, Alberta, extended abstract, URL <https://cseg.ca/assets/files/resources/abstracts/2014/core/490_GC2014_Perennial_River_Deltas_of_the_Montney_Fm.pdf> [August 2017].

Zonneveld, J.-P. and Moslow, T.F. (2017): Palaeogeographic evolution of the Montney in the Western Canada Sedimentary Basin; Canadian Society of Petroleum Geologists-Canadian Society of Exploration Geophysicists-Canadian Well Logging Society, Joint Annual Convention (GeoConvention 2017), 15–19 May 2017, Calgary, Alberta, extended abstract, URL <https://www.geoconvention.com/archives/2017/312_GC2017_Depositional_history_and_Palaeogeographic_evolution_Montney_WCSB.pdf> [July 2017].

Zonneveld, J.-P., and Moslow, T.F. (2018): Palaeogeographic setting, lithostratigraphy, and sedimentary framework of the Lower Triassic Montney Formation of western Alberta and northeastern British Columbia; *in* The Montney Play of Western Canada: Deposition to Development, T. Euzen, T.F. Moslow and M. Caplan (ed.), Bulletin of Canadian Petroleum Geology, v. 66, no. 1, p. 93–127.

Hydrocarbon-Generation Kinetics of the Doig Formation, Northeastern British Columbia and West-Central Alberta

P.L. Silva[1], The University of British Columbia, Vancouver, British Columbia, pablols@alumni.ubc.ca

R.M. Bustin, The University of British Columbia, Vancouver, British Columbia

Silva, P.L. and Bustin, R.M. (2020): Hydrocarbon-generation kinetics of the Doig Formation, northeastern British Columbia and west-central Alberta; *in* Geoscience BC Summary of Activities 2019: Energy and Water, Geoscience BC, Report 2020-02, p. 65–76.

Introduction

Reliable petroleum-system models require kinetic parameters of the reaction induced by thermal decomposition of kerogen into hydrocarbons to be calibrated to the source rock (Peters et al., 2018). Formation-specific kinetic parameters for the Doig Formation are not in the public domain; therefore, any previous attempt to model the hydrocarbon generation history would have required kinetic analyses to be undertaken or reliance on analogue data, both of which may produce erroneous results.

The Lower to Middle Triassic Doig Formation of the Western Canada Sedimentary Basin (WCSB) extends continuously across northeastern British Columbia (BC) and west-central Alberta. Historically, the Doig and the underlying Montney formations were viewed as source rocks for other conventional reservoirs in the basin, mainly in other Triassic and Cretaceous strata (Du Rouchet, 1985; Creaney and Allan, 1990; Riediger et al., 1990; Edwards et al., 1994). With the industry shifting the focus of development to unconventional reservoirs, the Doig Formation has been recognized as an important resource of gas and natural-gas liquids. The Gas Technology Institute (Faraj et al., 2002) estimated the total gas-in-place in the Doig Formation at 4 trillion m^3 (140 tcf), whereas Walsh et al. (2006) estimated the total gas-in-place as ranging from 1.1 to 5.7 trillion m^3 (40–200 tcf). A more recent study by the United States Energy Information Administration (2013) estimated 2.8 trillion m^3 (100 tcf) of gas-in-place for the Doig Phosphate Zone alone.

This paper presents the results of the reaction kinetics parameter modelling for immature rocks of the Doig Formation source rock. The Doig kinetic parameters are compared with those published for other North American shale plays and the variability of activation energies is explained. This study is part of a broader research project on the Doig Formation petroleum system and the results of the reaction kinetics presented here provide the inputs required to proceed with the subsequent steps in modelling thermogenic hydrocarbon generation across the basin.

Geological Framework

The Doig was deposited in the Middle Triassic, between the Anisian and Ladinian, and is part of the Diaber Group along with the underlying Montney Formation (Figure 1). The sedimentation in the Triassic of the WCSB is marked by a transition from carbonate-dominated intracratonic and passive-margin conditions, predominant during the Paleozoic, to a siliciclastic-dominated, active embryonic foreland basin. The Triassic succession was deposited in a series of three major third- or fourth-order transgressive-regressive cycles (Gibson and Barclay, 1989; Edwards et al., 1994). The interval from the Doig through the Halfway and Charlie Lake formations corresponds to the second cycle and the phosphatic interval at the base of the Doig represents a condensed section formed during the initial transgression of the second cycle (Gibson and Barclay, 1989).

The main elements that influenced the distribution of the Triassic interval were the underlying Devonian Leduc and Swan Hills reefs, and the Mesozoic reactivation of the Mississippian Dawson Creek graben complex (DCGC), which includes the Fort St. John graben and the Hines Creek graben. The DCGC formed in response to localized differential subsidence in the Peace River Embayment. The DCGC faults continued to be active during the Triassic, imposing significant controls on the distribution of sediments (Marshall et al., 1987; Barclay et al., 1990; Davies, 1997; Eaton et al., 1999). The Devonian reefs exerted a topographic influence on Triassic sedimentation by controlling facies changes (Davies, 1997), and may also have influenced subsidence rates and, hence, thickness variation.

The Doig Formation consists of mudstone, siltstone and subordinate sandstone, bioclastic packstone and grainstone, deposited under marine conditions in environments ranging from shoreface through offshore (Evoy and Moslow, 1995). The Doig can be informally subdivided into three units, as proposed by Chalmers and Bustin

---

[1] *The lead author is a 2019 Geoscience BC Scholarship recipient.*

This publication is also available, free of charge, as colour digital files in Adobe Acrobat® PDF format from the Geoscience BC website: http://www.geosciencebc.com/updates/summary-of-activities/.

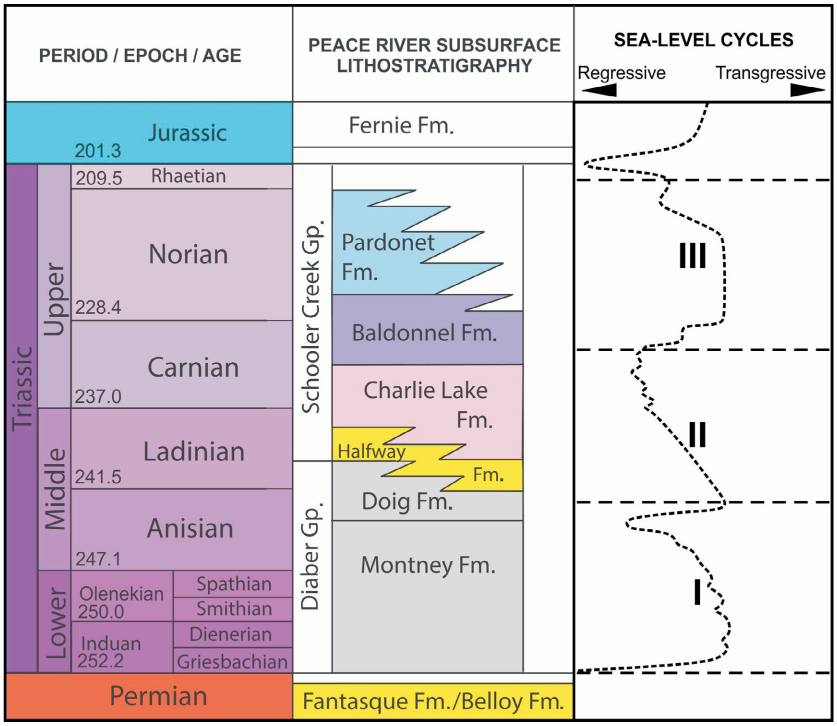

Figure 1. Stratigraphic chart of the Triassic, in the subsurface of the Peace River area, northeastern British Columbia and adjacent areas (after Gibson and Barclay, 1989; Golding et al., 2015). Eustatic level based on Hardenbol et al. (1998). Abbreviations: Fm., Formation; Gp., Group.

(2012): the basal unit, Doig A, corresponding to the also informal but widely referred to 'Doig Phosphate Zone' (DPZ), composed of organic-rich radioactive dark mudstone with common phosphate granules and nodules (the DPZ is generally readily distinguishable in well logs by its high gamma-ray signature); the intermediate Doig B, primarily composed of medium to dark grey argillaceous siltstone and mudstone intercalated with localized sandstone; and the upper Doig C, composed of relatively organic-lean siltstone and argillaceous fine-grained sandstone. The DPZ is considered a good to excellent hydrocarbon source rock and an important source for many conventionally hosted hydrocarbons in the basin, including Triassic strata, such as Halfway, Charlie Lake and Doig sands. Previous studies found type II oil and gas-prone kerogen with total organic carbon content ranging from 1.8 to 11 wt. % (Riediger et al., 1990; Faraj et al., 2002; Ibrahimbas and Riediger, 2004).

Material and Methods

Twenty-three samples were selected for reaction-kinetics analysis through multiple heating-ramp open-system pyrolysis. These samples cover a significant portion of the Doig Formation subcrop area and a wide range of maturities (Figure 2), as well as all its stratigraphic subdivisions (Figure 3). The samples were chosen from among more than 440 analyses carried out on cuttings and whole-rock core using the Rock-Eval pyrolysis method (Espitalié et al., 1977), based on sharpness and intensity of the kerogen conversion peak, and a wide range of hydrogen index (HI) and oxygen index (OI) values to capture all of the pseudo–van Krevelen kerogen types identified (Figure 4). Samples were classified in discrete kerogen-type categories based on the pseudo–van Krevelen crossplot. Approximately 70 mg of powdered bulk rock (i.e., not concentrated kerogen) of each sample was pyrolyzed, using a HAWK® instrument from Wildcat Technologies, at 5°C, 25°C and 45°C per minute to 600–700°C, following an isothermal plateau of up to 260–310°C to purge free hydrocarbons. The pyrolysis curves were trimmed in the time domain and the flame-ionization detector signal was baseline corrected, smoothed, integrated and processed using the commercially sourced Kinetics2015 software (GeoIsoChem Corporation, 2019). Reaction-activation energies and pre-exponential factors were modelled through a distributed-reactivity method (Braun and Burnham, 1987; Ungerer and Pelet, 1987) with a fixed activation energy (E) spacing of 1 kcal/mol, and an isoconversional method (Friedman, 1964; Vyazovkin and Lesnikovich, 1988), assuming a series of parallel first-order reactions in 0.01 conversion-fraction increments, to determine the variation of activation energy as a function of conversion.

Results and Discussion

Approximately half of the samples analyzed are of kerogen type II, as determined by hydrogen- and oxygen-index evo-

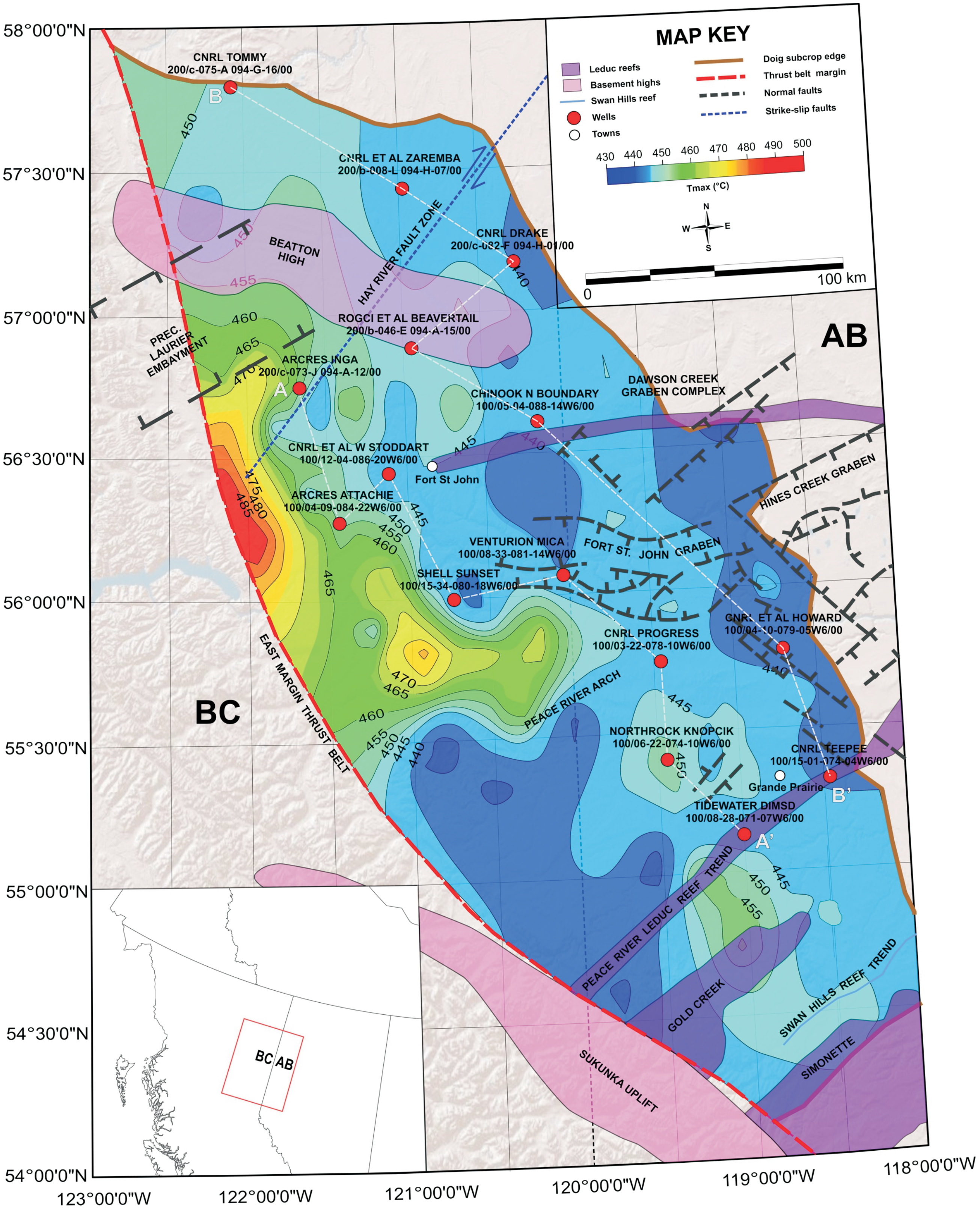

Figure 2. Location of wells from which samples were selected for reaction kinetics analysis in northeastern British Columbia and adjacent area, against a backdrop of the Doig Formation thermal-maturity map (after Silva and Bustin, 2018) and main structural elements that influenced the Triassic deposition (after Davies, 1997). Cross-sections shown in Figure 3 indicated by A–A' and B–B'. Abbreviation: Prec., Precambrian.

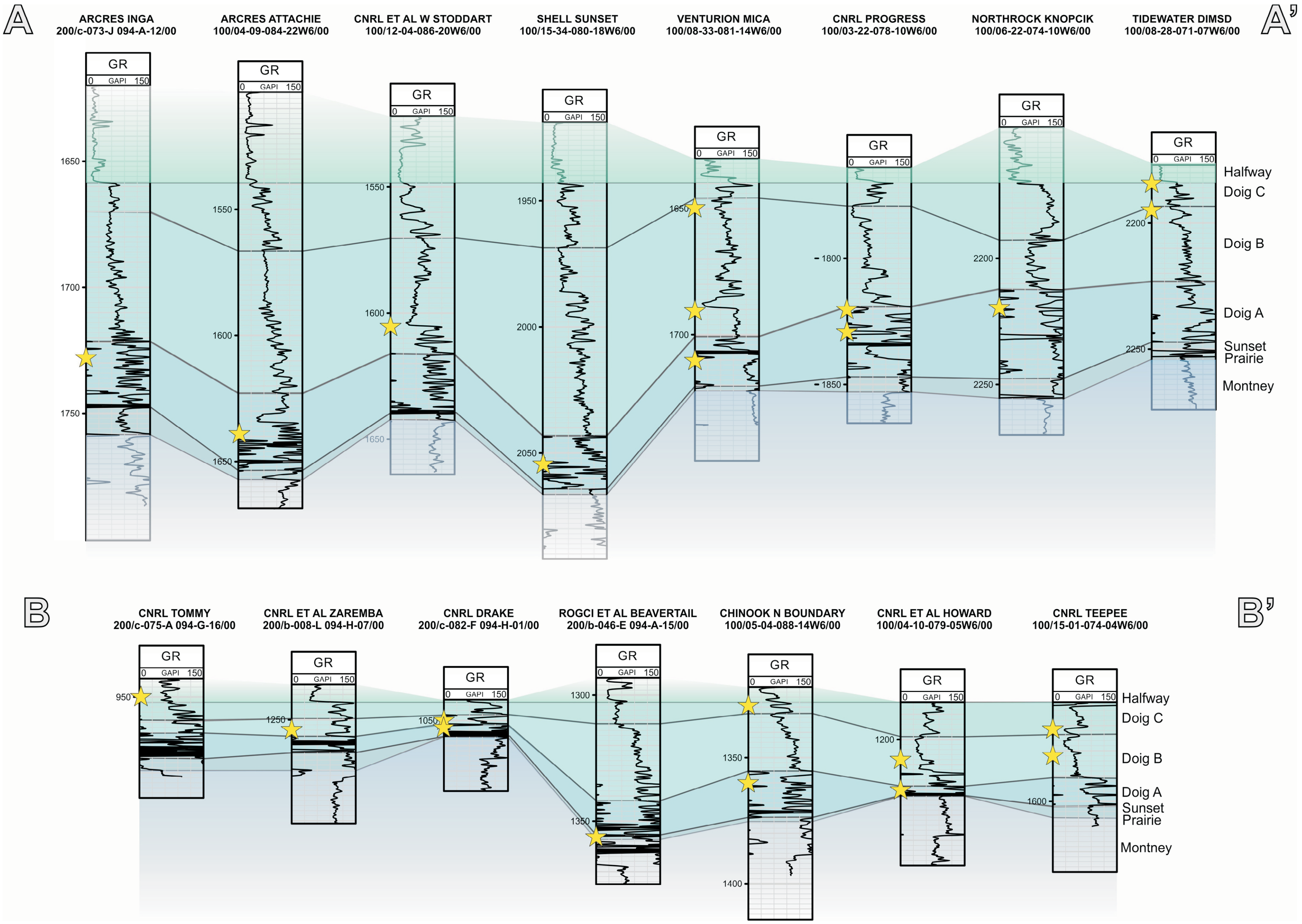

Figure 3. Stratigraphic cross-sections (along strike) of wells in northeastern BC and adjacent area, with the top of the Doig Formation as datum, showing the stratigraphic subdivisions of the Doig and the location of the samples (yellow stars) analyzed for reaction kinetics (location of A–A’ and B–B’ shown in Figure 2). Abbreviation: GR, gamma ray.

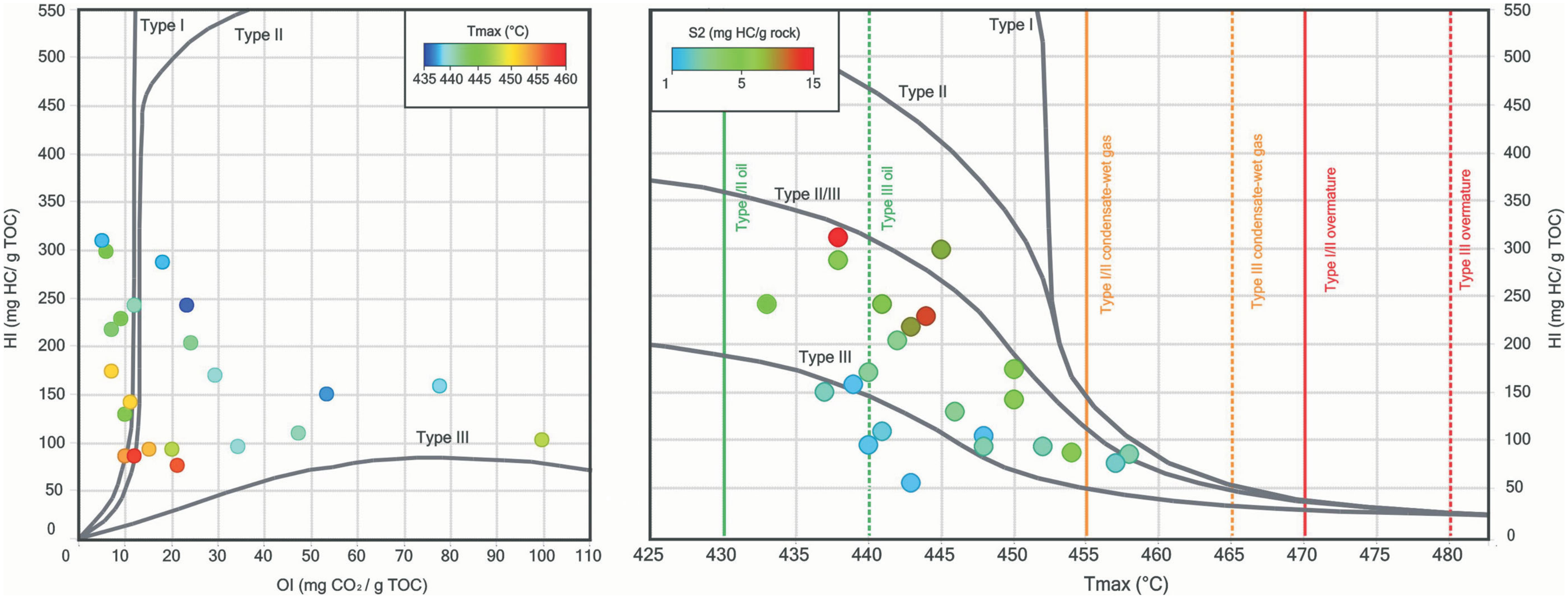

Figure 4. Identification of kerogen types II to III: **Left**, pseudo–van Krevelen crossplot; **Right**, hydrogen index (HI) versus T_{max} crossplot of the samples selected for reaction kinetics analysis. The samples cover a wide range of degrees of maturity, ranging from immature to late oil and condensate. Boundaries between generation windows for different kerogen types are after Dow (1977) and Petersen (2003). Abbreviations: HC, hydrocarbon; OI, oxygen index; TOC, total organic carbon.

lution paths, whereas one third is of type III. The remaining are classified as type II/III, due to either kerogen mixing, contamination or high maturity causing points to plot too close to the origin. The median value of the activation energy of all Doig samples analyzed ranges from 51 to 67 kcal/mol with a pre-exponential factor that varies from 5.3×10^{13} to 2.7×10^{18} (Figure 5). The correlation between the median activation-energy and frequency factor is log linear, with an r^2 of 0.98. The activation-energy distribution of kerogen type II samples is noticeably narrower than that of type III, with median values ranging from 53 to 63 kcal/mol. The precision of the global kinetic parameters was determined by repeated analyses of a standard sample. The 95% confidence interval (i.e., two standard deviations divided by the median) is ±1.2 kcal/mol around the median activation-energy value of 55 kcal/mol, and within a factor of 2 for the average frequency factor of 2×10^{15}.

There is a clear thermal-maturity influence on the activation-energy distributions, despite a scatter of up to 5 kcal/mol for a given temperature of maximum rate of hydrocarbon-generation (T_{max}) value (Figure 6). The correlation is obscured due to variations in activation energies introduced by mixture of kerogen types during deposition, and possibly to cross-contamination between cuttings samples of different depths containing different kerogen types. Nonetheless, it is possible to distinguish two different trends and generate linear regressions for kerogen types II (blue dashed line in Figure 6) and III (black dashed line in Figure 6), with r^2 values of 0.49 and 0.22, respectively. The lowest maturity samples analyzed in this study, for which kerogen type can be determined with reasonable confidence, fall between 438 and 439°C. By comparing the extrapolated trends for kerogens type II and type III to thermally immature samples (i.e., lower than 430°C) from the literature, there appears to be an inflection point in the decreasing activation energy, with decreasing maturity levelling off at approximately 435°C.

Due to a shift toward higher activation energies as thermal maturation progresses, the standard deviation of the activation-energy distributions for each sample also has a positive correlation with T_{max} values. Similarly to the regression of median activation energies, a distinct trend can be generated for kerogen type II (Figure 7) and a less well-defined trend for type III (Figure 7), with r^2 values of 0.54 and 0.25, respectively.

Based on the regression of median and standard deviation values for different maturities, the median activation energies ($\bar{E}$) and standard deviation (σ_E) of lower maturity type II (equations 1 and 2) and III (equations 3 and 4) kerogens of the Doig Formation can be determined as a function of T_{max} according to the following equations:

$$\bar{E}_{\text{type II}} = -108.98 + (0.37 \times T_{max}) \tag{1}$$

$$\sigma_{E\,\text{type II}} = -38.53 + (0.0930 \times T_{max}) \tag{2}$$

$$\bar{E}_{\text{type III}} = -137.34 + (0.44 \times T_{max}) \tag{3}$$

$$\sigma_{E\,\text{type III}} = -27.14 + (0.0687 \times T_{max}) \tag{4}$$

Based on the 435°C inflection point in the decreasing trend of the median activation energy with decreasing maturity, median values of activation-energy distributions are deter-

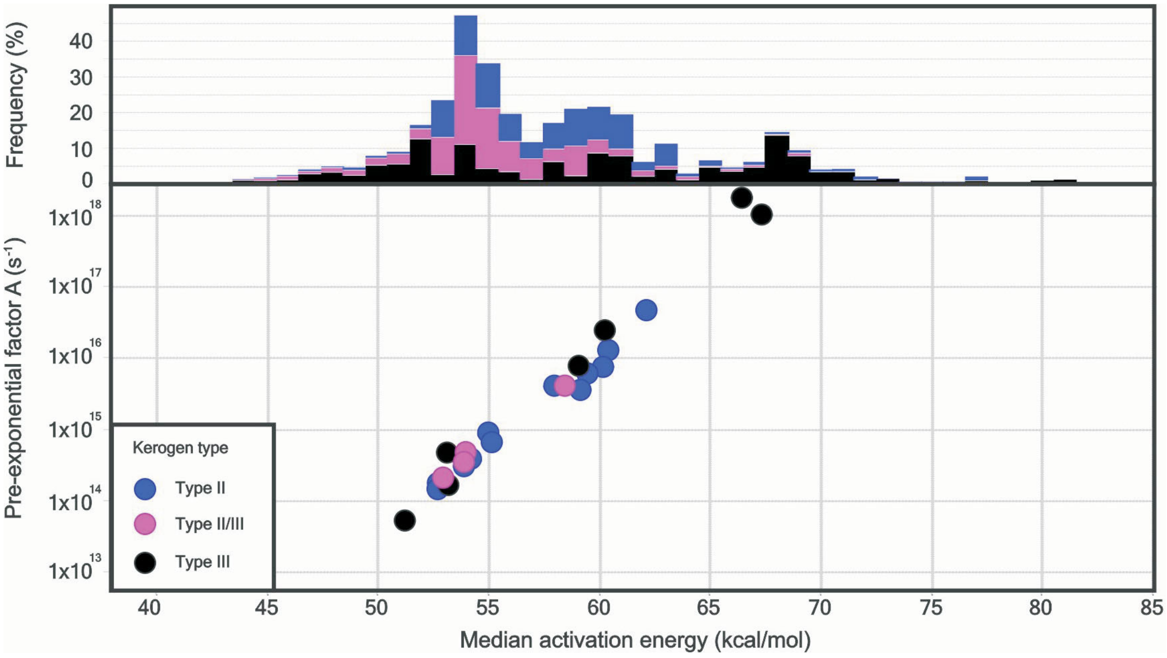

Figure 5. Pre-exponential factor versus median activation-energy crossplot of all samples, and frequency distribution of all activation energies classified by kerogen type.

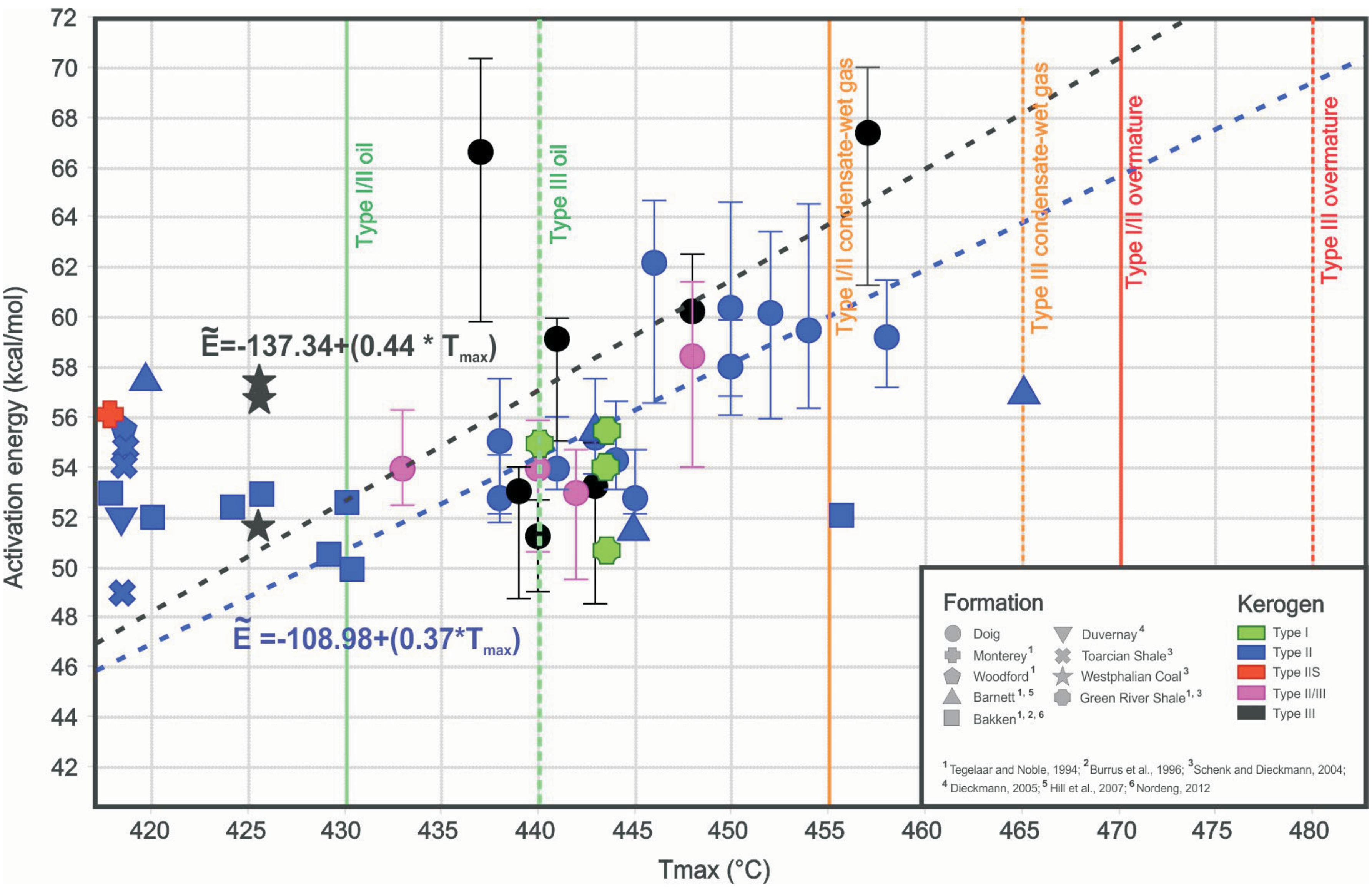

Figure 6. Crossplot of median activation energy versus Rock-Eval pyrolysis T_{max} of the Doig Formation samples from the study area in northeastern BC and west-central Alberta, and select samples from other kerogen-rich rocks from literature for comparison (Tegelaar and Noble, 1994; Burrus et al., 1996; Schenk and Dieckmann, 2004; Dieckmann, 2005; Hill et al., 2007; Nordeng, 2012), showing the trend of decreasing activation energies toward lower maturity samples. Data points from the study-area samples are plotted as the median value of the distribution, with the 80% range as vertical bars. Blue and black dashed lines represent the linear regression for type II and type III kerogens, respectively. Literature data are plotted as a single activation energy or the median value of the distribution. Boundaries between generation windows for different kerogen types are after Dow (1977) and Petersen (2003).

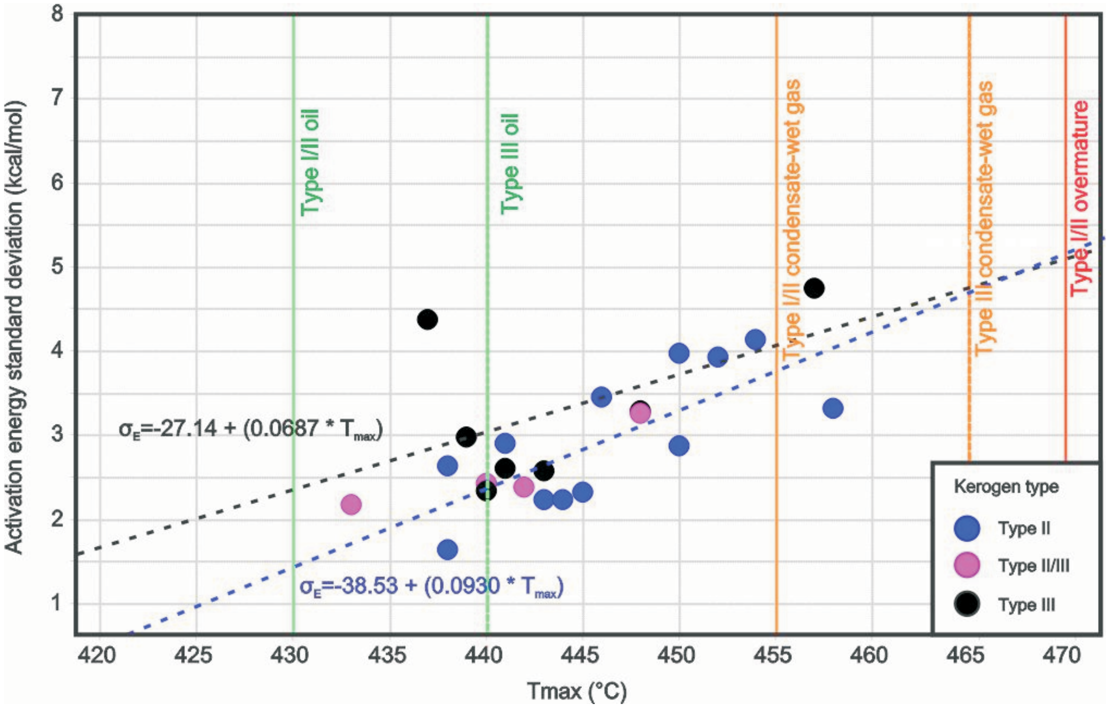

Figure 7. Crossplot of the standard deviation of the activation-energy distributions versus Rock-Eval pyrolysis T_{max} of the Doig Formation samples from the study area in northeastern BC and west-central Alberta, showing the trend of decreasing standard deviations toward lower maturity samples. Blue and black dashed lines represent the linear regression for type II and type III kerogens, respectively. Boundaries between generation windows for different kerogen types are after Dow (1977) and Petersen (2003).

mined to be 52 and 54.1 kcal/mol for immature kerogen of types II and III, respectively. Conversely, the standard deviations for immature type II and type III are determined to be 1.93 and 2.75 kcal/mol, respectively. Based on these statistical parameters, synthetic activation-energy Gaussian distributions were created for kerogen types II and III of the Doig Formation (Figure 8).

The wider activation-energy distributions of kerogen type III are not only evident on the discrete activation-energy distribution histograms but can also be observed in the reaction profile generated by the isoconversional kinetic modelling. The isoconversional results are plotted as a single activation energy for conversion rates from 10 to 90% (Figure 9), since the first and last 10% values are often unreliable due to analytical noise in the data (Burnham, 2017). This profile shows that for lower present-day maturity samples, predominant activation energies range from 40 to 58 kcal/mol at 10% conversion. These lower activation energies are associated with samples predominantly of kerogen type III and are likely the product of the breaking of C–O bonds, and possibly C–S bonds. Activation energies at 10% conversion for most lower present-day maturity kerogen type II samples are higher than 50 kcal/mol. At 50% conversion, lower maturity samples have activation energies in the 48 to 60 kcal/mol range. Within this conversion range, bitumen decomposition is probably the cause of the narrower spread and large overlap between activation energies of kerogen types II and III. At 90% conversion, the high end of activation-energy distributions of type III kerogen causes the spread of dominant activation energies to increase again, ranging from 52 to 90 kcal/mol for low present-day maturities. The results of this study suggest that mixing between kerogen types II and III in the Doig Formation translates into an early hydrocarbon-generation window due to the low activation energies of type III. Furthermore, the kerogen mixing extends the generation process over a broader temperature range due to the combined effect of the lower end of type II activation energies and upper end of those of type III.

Ongoing Work

The work presented here will serve as foundation for a reconstruction of the Doig Formation thermal history through basin modelling. The modelled kerogen activation-energy distributions for different types of kerogen will be used as reaction-kinetics input for the model thermal-maturation simulation, providing reliable source-rock–calibrated parameters, thus decreasing the uncertainty related to timing and type of hydrocarbons generated across the basin.

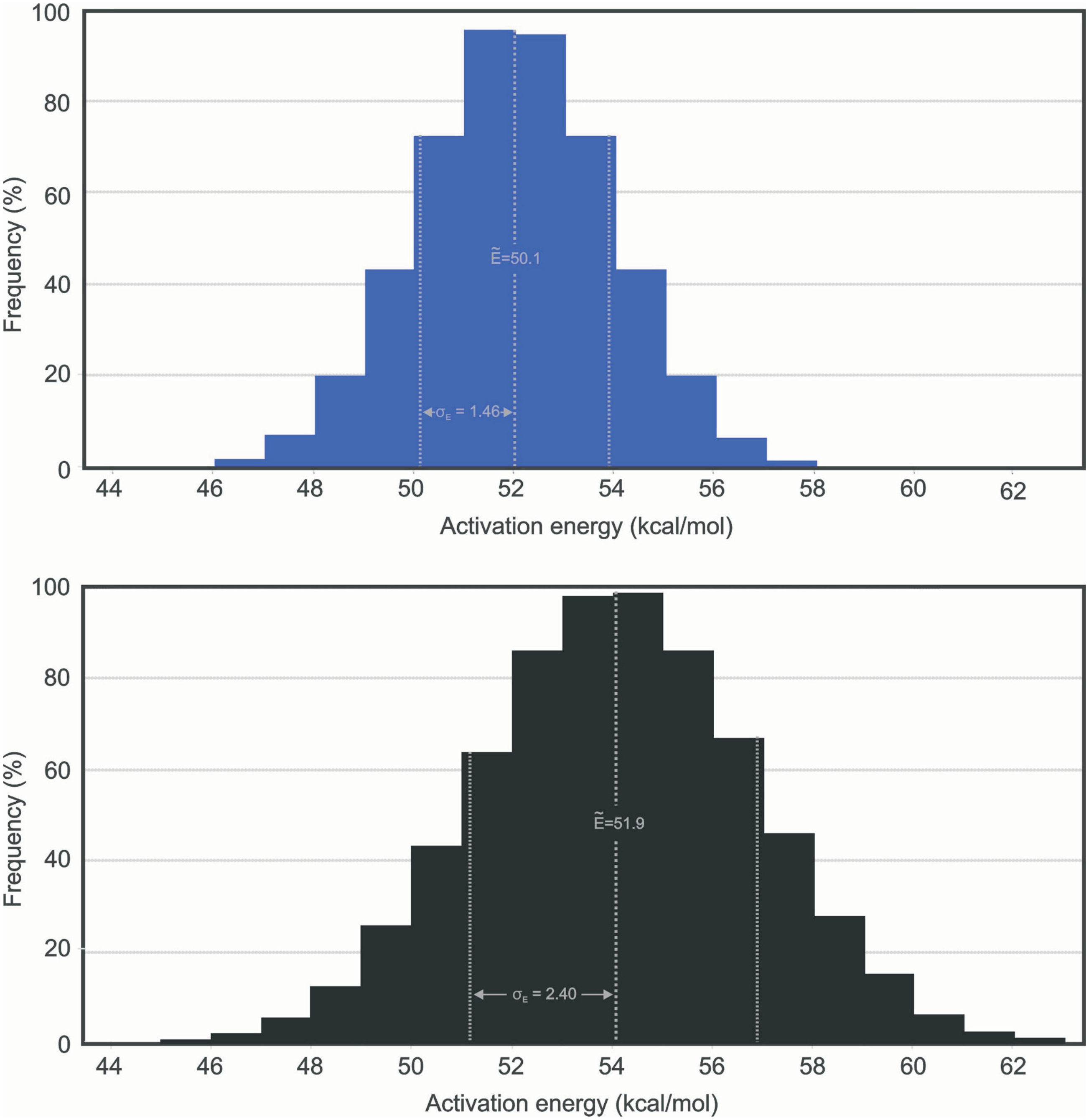

Figure 8. Histograms of modelled activation-energy distributions of the Doig Formation, northeastern British Columbia and west-central Alberta, based on samples of varying degrees of maturity: **Top**, immature kerogen type II; **Bottom**, immature kerogen type III.

Acknowledgments

The authors acknowledge financial support from Geoscience BC, Canadian Natural Resources Limited, Chevron Canada Limited, Devon Energy Corporation, EnCana Corporation, geoLOGIC systems ltd., Husky Energy Inc. and AGAT Laboratories. The donation of software by geoLOGIC systems ltd. and Paradigm Geophysical Canada Limited was also instrumental in handling the well and core data, and greatly appreciated. The authors would also like to acknowledge the time and effort dedicated to the thorough review of the manuscript by G. Chalmers, research associate at The University of British Columbia.

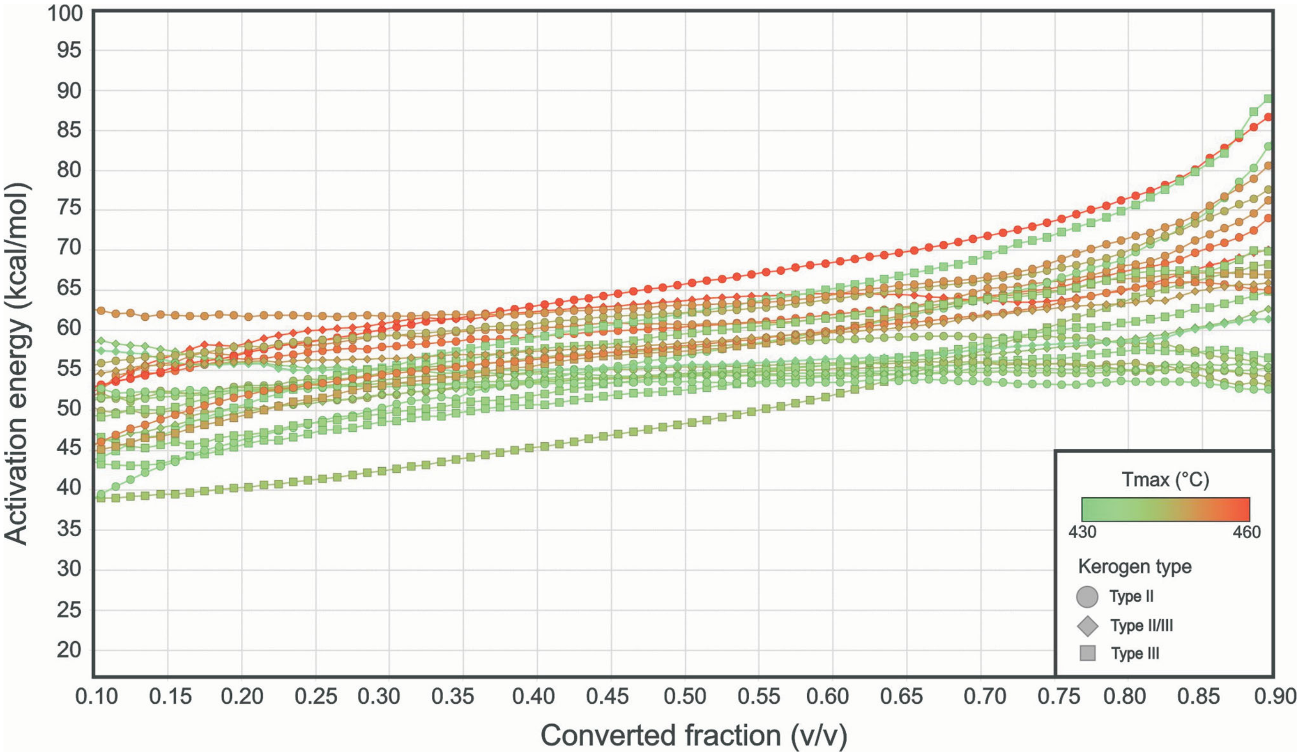

Figure 9. Kerogen conversion profile, showing reaction progress generated by the isoconversional method.

References

Barclay, J.E., Krause, F.F., Campbell, R.I. and Utting, J. (1990): Dynamic casting of the Dawson Creek Graben Complex: Carboniferous–Permian Peace River Embayment, western Canada; Bulletin of Canadian Petroleum Geology, v. 38(A), p. 115–145.

Braun, R.L. and Burnham, A.K. (1987): Analysis of chemical reaction kinetics using a distribution of activation energies and simpler models; Energy and Fuels, v. 1, no. 2, p. 153–161.

Burnham, A.K. (2017): Global Chemical Kinetics of Fossil Fuels: How to Model Maturation and Pyrolysis (1st edition); Springer-Verlag, 315 p.

Burrus, J., Wolf, S., Osadetz, K. and Visser, K. (1996): Physical and numerical modelling constraints on oil expulsion and accumulation in the Bakken and Lodgepole petroleum systems of the Williston Basin (Canada-USA); Bulletin of Canadian Petroleum Geology, v. 44, no. 3, p. 429–445.

Chalmers, G.R.L. and Bustin, R.M. (2012): Geological evaluation of Halfway–Doig–Montney hybrid gas shale-tight gas reservoir, northeastern British Columbia; Marine and Petroleum Geology, v. 38, no. 1, p. 53–72.

Creaney, S. and Allan, J. (1990): Hydrocarbon generation and migration in the Western Canada sedimentary basin; *in* Classic Petroleum Provinces, J. Brooks (ed.), Geological Society of London, Geological Society Special Publications, v. 50, p. 189–202.

Davies, G.R. (1997): The Triassic of the Western Canada Sedimentary Basin: tectonic and stratigraphic framework, paleogeography, paleoclimate and biota; Bulletin of Canadian Petroleum Geology, v. 45, no. 4, p. 434–460.

Dieckmann, V. (2005): Modelling petroleum formation from heterogeneous source rocks: the influence of frequency factors on activation energy distribution and geological prediction; Marine and Petroleum Geology, v. 22, no. 3, p. 375–390.

Dow, W. (1977): Kerogen studies and geological interpretations; Journal of Geochemical Exploration, v. 7, p. 79–99.

Du Rouchet, J. (1985): The origin and migration paths of hydrocarbons accumulated in the Lower Cretaceous sandstone 'giant' tar accumulations of Alberta – Part II; Journal of Petroleum Geology, v. 8, no. 1, p. 101–114.

Eaton, D.W., Ross, G.M. and Hope, J. (1999): The rise and fall of a cratonic arch: a regional seismic perspective on the Peace River Arch, Alberta; Bulletin of Canadian Petroleum Geology, v. 47, no. 4, p. 346–361.

Edwards, D.E., Barclay, J.E., Gibson, D.W., Kvill, G.E. and Halton, E. (1994): Triassic strata of the Western Canada Sedimentary Basin; Chapter 16 *in* Geological Atlas of the Western Canada Sedimentary Basin, G.D. Mossop and I. Shetsen (comp.), Canadian Society of Petroleum Geologists and Alberta Research Council, Edmonton, Alberta, p. 257–275, URL <https://ags.aer.ca/publications/chapter-16-triassic-strata>[October 2018].

Espitalié, J., Laporte, J.L., Madec, M., Marquis, F., Leplat, P., Paulet, J. and Boutefeu, A. (1977): Méthode rapide de caractérisation des roches mères, de leur potentiel pétrolier et de leur degré d'évolution; Revue de l'Institut Français du Pétrole, v. 32, no. 1, p. 23–42.

Evoy, R.W. and Moslow, T.F. (1995): Lithofacies associations and depositional environments in the Middle Triassic Doig Formation, Buick Creek Field, northeastern British Columbia; Bulletin of Canadian Petroleum Geology, v. 43, no. 4, p. 461–475.

Faraj, B., Harold, W., Addison, G., McKinstry, B., Donaleshen, R., Sloan, G., Lee, J., Anderson, T., Leal, R., Anderson, C., Lafleur, C. and Ahlstrom, A. (2002): Shale gas potential of selected Upper Cretaceous, Jurassic, Triassic and Devonian shale formations in the WCSB of Western Canada: implications for shale gas production; Gas Technology Institute, Report GRI-02/0233, 258 p.

Friedman, H.L. (1964): Kinetics of thermal degradation of char-forming plastics from thermogravimetry: Application to a phenolic plastic; Journal of Polymer Science, v. 6, no. 1, p. 183–195.

GeoIsoChem Corporation (2019): Kinetics2015: chemical reaction kinetics analysis and applications; GUI-based computer program for Windows, URL <http://www.geoisochem.com/software/kinetics2015/index.html> [November 2019].

Gibson, D.W. and Barclay, J.E. (1989): Middle Absaroka sequence – the Triassic stable craton; *in* Western Canada Sedimentary Basin – A Case History, B.D. Ricketts, (ed.), Canadian Society of Petroleum Geologists, Calgary, Special Publication, p. 219–232.

Golding, M.L., Orchard, M.J., Zonneveld, J.P. and Wilson, N.S.F. (2015): Determining the age and depositional model of the Doig phosphate zone in northeastern British Columbia using conodont biostratigraphy; Bulletin of Canadian Petroleum Geology, v. 63, no. 2, p. 143–170.

Hardenbol, J., Thierry, J., Farley, M.B., Jacquin, T., De Graciansky, P.-C. and Vail, P.R. (1998): Cenozoic sequence chronostratigraphy; *in* Mesozoic and Cenozoic Sequence Chronostratigraphic Framework of European Basins, P.C. De Graciansky, J. Hardenbol, T. Jacqui and P.R. Vail (ed.), Society for Sedimentary Geology, SEPM Special Publication 60, p. 3–13.

Hill, R.J., Zhang, E., Katz, B.J. and Tang, Y. (2007): Modeling of gas generation from the Barnett Shale, Fort Worth Basin, Texas; American Association of Petroleum Geologists Bulletin, v. 91, no. 4, p. 501–521.

Ibrahimbas, A. and Riediger, C. (2004): Hydrocarbon source rock potential as determined by Rock-Eval 6/TOC pyrolysis, northeast British Columbia and northwest Alberta; *in* Summary of Activities 2004, British Columbia Ministry of Energy, Mines and Petroleum Resources, Resource Development and Geoscience Branch, p. 7–18.

Marshall, G.M., Noble, I.A.R. and Tang, C.W. (1987): Triassic/Jurassic fields; Chapter 7 *in* Geophysical Atlas of Western Canadian Hydrocarbon Pools, N.L. Anderson, L.V. Hills and D.A. Cederwall (ed.), Canadian Society of Exploration Geophysicists and Canadian Society of Petroleum Geologists, Calgary, Alberta, p. 187–215, URL <https://cseg.ca/assets/files/atlas/L_Chapter_7.pdf> [October 2018].

Nordeng, S.H. (2012): Determination of activation energy and frequency factor for samples of the Bakken Formation (Miss.-Dev.): Williston Basin, ND; North Dakota Geological Survey, Geological Investigations No. 163, 15 p.

Peters, K.E., Burnham, A.K., Walters, C.C. and Schenk, O. (2018): Guidelines for kinetic input to petroleum system models from open-system pyrolysis; Marine and Petroleum Geology, v. 92, p. 979–986.

Petersen, H.I. (2003): A reconsideration of the ‘oil window’ for humic coal and kerogen type III source rocks; Journal of Petroleum Geology, v. 25, no. 4, p. 407–432.

Riediger, C.L., Fowler, M.G., Brooks, P.W. and Snowdon, L.R. (1990): Triassic oils and potential Mesozoic source rocks, Peace River Arch area, Western Canada Basin; Organic Geochemistry, v. 16, no. 1–3, p. 295–305.

Schenk, H.J. and Dieckmann, V. (2004): Prediction of petroleum formation: The influence of laboratory heating rates on kinetic parameters and geological extrapolations; Marine and Petroleum Geology, v. 21, no. 1, p. 79–95.

Silva, P.L. and Bustin, R.M. (2018): Preliminary liquid hydrocarbon potential assessment of the Doig Formation, northeastern British Columbia and west-central Alberta, based on thickness, organic richness and maturity; *in* Geoscience BC Summary of Activities 2017: Energy, Geoscience BC, Report 2018-04, p. 39–50, URL <http://www.geosciencebc.com/i/pdf/SummaryofActivities2017/Energy/SoA2017_E_Silva.pdf> [October 2019].

Tegelaar, E.W. and Noble, R.A. (1994): Kinetics of hydrocarbon generation as a function of the molecular structure of kerogen as revealed by pyrolysis-gas chromatography; Organic Geochemistry, v. 22, no. 3–5, p. 543–574.

Ungerer, P. and Pelet, R. (1987): Extrapolation of kinetics of oil and gas formation from laboratory experiments to sedimentary basins; Nature, v. 327, p. 52–54.

United States Energy Information Administration (2013): Technically recoverable shale oil and shale gas resources: an assessment of 131 shale formations in 41 countries outside the United States; United States Department of Energy, 76 p., URL <https://www.eia.gov/analysis/studies/worldshalegas/pdf/overview.pdf> [October 2018].

Vyazovkin, S.V. and Lesnikovich, A.I. (1988): Estimation of the pre-exponential factor in the isoconversional calculation of effective kinetic parameters; Thermochimica Acta, v. 128, p. 297–300.

Walsh, W., Adams, C., Kerr, B. and Korol, J. (2006): Regional “shale gas” potential of the Triassic Doig and Montney formations, northeastern British Columbia; BC Ministry of Energy Mines and Petroleum Resources, Oil and Gas Division, Resource Development and Geoscience Branch, Open File 2006-0, 19 p., URL <https://www2.gov.bc.ca/assets/gov/farming-natural-resources-and-industry/natural-gas-oil/petroleum-geoscience/petroleum-open-files/pgof20062.pdf> [October 2018].

BC Natural Gas Atlas: Creation of the Geochemical Database for Northeastern British Columbia (Parts of NTS 093, 094)

M.J. Whiticar, University of Victoria, Victoria, BC, whiticar@uvic.ca

C. Evans, University of Victoria, Victoria, BC

Whiticar, M.J. and Evans, C. (2020): BC Natural Gas Atlas: creation of the geochemical database for northeastern British Columbia (parts of NTS 093, 094); *in* Geoscience BC Summary of Activities 2019: Energy and Water, Geoscience BC, Report 2020-02, p. 77–86.

Introduction

Natural gas is an important resource in British Columbia (BC) both as an economic driver and environmental concern. Natural gas is a mixture of hydrocarbon gases, predominantly methane, and typically includes higher hydrocarbons (e.g., ethane through pentane) and frequently nonhydrocarbons, such as carbon dioxide, nitrogen, hydrogen, noble gases and hydrogen sulphide.

BC's history of petroleum activity dates back over 90 years, since the 1920s. About 26 600 oil and gas wells have been drilled in BC (BC Oil and Gas Commission, 2019a). The first commercial production of natural gas in 1948 (Pouce Coupe) delivered gas to Dawson Creek (Figure 1). This was followed by the natural gas discovery in 1956 at Clarke Lake in the Fort Nelson area (Figure 1). Today, the development continues to centre upon BC's reserves of conventional and unconventional natural gas located in the strata forming the edge of the Western Canada Sedimentary Basin (WCSB) in the province's northeast (Figure 1). BC currently produces about 30% of Canada's natural gas (Canadian Association of Petroleum Producers, 2019). In 2017, the unconventional gas types present in BC accounted for 87% of natural gas production, according to the BC Oil and Gas Commission (BC Oil and Gas Commission, 2019b), and includes tight and shale gas. Coalbed gas (coalbed methane) remains a substantial unconventional gas resource in BC, but there has been no production in recent years.

In northeastern BC, the major unconventional gas deposits are in the Montney, Jean Marie and Cadomin plays, the Liard, Horn River and Deep basins, and the Cordova Embayment (Figure 2). They are among the largest shale-gas deposits in North America, equivalent to the original-gas-in-place (OGIP) of the Eagle Ford, Marcellus, Barnett and Haynesville plays of the United States combined (Canadian Association of Petroleum Producers, 2016). These BC deposits are part of the rich, interprovincial oil and gas reserves of the WCSB connecting northeastern BC and Alberta. Of the estimated 94 500 bcm (3337 tcf) OGIP (basin total resource[1]), approximately 82 000 bcm (2900 tcf[2]) are in BC (BC Oil and Gas Commission, 2019c). The estimated ultimate potential marketable resource is 15 000 bcm (532 tcf). The estimated proven reserves (initial raw gas reserves[1]) are considerably less at 1300 bcm (45.9 tcf), i.e., the reserve is only 1.4% of the total resource, of which 250 bcm (8.85 tcf) has already been produced as of 2017 (BC Oil and Gas Commission, 2019b).

The Montney play accounts for the vast majority of drilling activity in BC (92.4%; BC Oil and Gas Commission, 2019b). In 2017, the estimated Montney gas-in-place resource was approximately 55 600 bcm (1965 tcf) compared with the estimated initial raw gas reserve of 1184 bcm (41.8 tcf), i.e., the Montney reserve was 2.1% of the total resource (BC Oil and Gas Commission, 2019b).

In comparison to the Montney play, the other BC unconventional natural gas plays have lower resource and reserve estimates. The most notable is the Liard Basin (Exshaw-Patry shales, Figure 2) with an estimated gas-in-place resource of 24 000 bcm (848 tcf) and initial raw gas reserve of 2.8 bcm (0.1 tcf; BC Oil and Gas Commission, 2019b). The Horn River Basin (Figure 2), which has seen low drilling activity in the past years, has an estimated gas-in-place resource of 12 700 bcm (448 tcf) and initial raw gas reserve of 79 bcm (2.8 tcf; BC Oil and Gas Commission, 2019b).

BC has several other sedimentary basins and regions that have had more limited exploration, including Bowser, Whitehorse Trough, Nechako, Fernie, Georgia, Queen Charlotte, Winona and Tofino (Figure 1). These contain oil and/or both conventional and unconventional gas. The lat-

---

This publication is also available, free of charge, as colour digital files in Adobe Acrobat® PDF format from the Geoscience BC website: http://www.geosciencebc.com/updates/summary-of-activities/.

[1] *The BC Oil and Gas Commission (2019b) defines 'resources' as an estimate of the amount of natural gas in the region/play that includes proven reserves, produced quantities and unproven resources that may not be recoverable with current technology and economics. 'Reserves' are defined as proven quantities of natural gas that are commercially recoverable, economic and marketable.*

[2] *1 trillion cubic feet (tcf) = 28.32 billion cubic metres (bcm)*

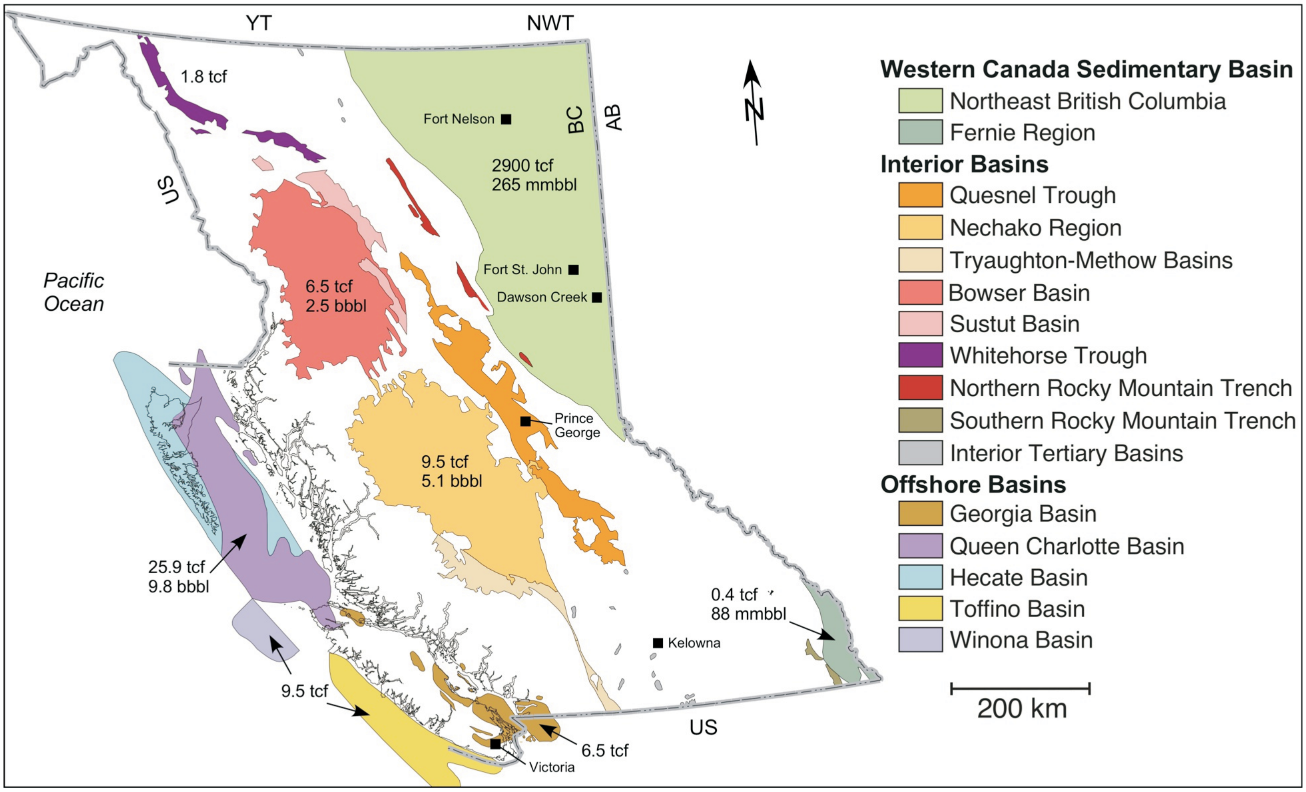

Figure 1. Major natural gas and oil basins of British Columbia (modified after Ferri, 2019, with permission). Gas and oil resource estimates are in trillion cubic feet (tcf) gas-in-place and billion barrels (bbbl) oil-in-place or million barrels (mmbbl) oil-in-place, respectively (BC Ministry of Energy, Mines and Petroleum Resources, 2007). Coalbed gas estimates are not shown. Note: 1 trillion cubic feet (tcf) = 28.32 billion cubic metres (bcm), 1 million barrels (mmbbl) oil = 1.5 x 10^5 cubic metres (m^3) oil, 1 billion barrels (bbbl) oil = 1.5 x 10^8 cubic metres (m^3) oil.

ter includes coalbed methane (CBM; also referred to as coalbed gas, CBG) found in essentially every coalfield throughout the province. The major estimated reserves of CBM include those in the Peace River (northeastern BC), Klappan and Groundhog (northern Nechako Basin), Elk Valley and Crowsnest (southeastern corner of BC), Hat Creek (central interior BC), and Comox and Nanaimo (Vancouver Island portion of Georgia Basin) coalfields. Exploratory wells in the Peace River and Elk Valley coalfields assessed the CBM but currently there is only minor production.

Global atmospheric methane has long been recognized as a major greenhouse gas (GHG), which has doubled in abundance in the troposphere to 1862 ppm since the pre-industrial Holocene (Hopcroft et al., 2017). Methane currently contributes a radiative forcing of approximately 0.5 watts per square metre (W/m^2; approx. 17% of total GHGs; Myhre et al., 2001). Globally, the oil and gas industry contributes an estimated 24% of global anthropogenic methane emissions (Saunois et al., 2016). In the United States, these fugitive emissions are approximately 2.3% of total natural gas production (Alvarez et al., 2018), so they represent a financial loss, as well as an environmental concern.

In Canada, methane emissions in 2017 were 93 Mt CO_2eq (1 Mt CH_4 equals 25 Mt CO_{2eq} [carbon dioxide equivalent on a 100-year time scale]) or 13% of the Canadian total (Environment and Climate Change Canada, 2019a). The oil and gas sector is the largest industrial emitter of methane (44%; Environment and Climate Change Canada, 2018) and in 2017 this sector contributed 195 Mt CO_2eq (27%) to Canada's total GHG emissions (716 Mt CO_2eq; Environment and Climate Change Canada, 2019c). Studies report that 53% of active wells in Alberta are leaking methane (GreenPath Energy Ltd., 2016) and 47% in BC (Atherton et al., 2017). Oil and gas operations in Canada, such as flaring and fugitive emission from equipment and well leaks, contribute approximately 8.5% to total greenhouse gas emissions (Bachu, 2017). After the energy combustion (44.5%) and transportation (28.2%) sectors, fugitive releases (8.5%) are the third largest contributor to Canadian GHG emissions (The Conference Board of Canada, 2013).

New legislation is being introduced to reduce Canadian emissions by 40–45% (Canada Department of Justice, 2019; Environment and Climate Change Canada, 2019b). In BC, the Climate Action Plan (Province of British Columbia, 2008) was created in 2008 to provide stewardship to climate change issues. The BC Climate Leadership Plan (Province of British Columbia, 2016) and then CleanBC

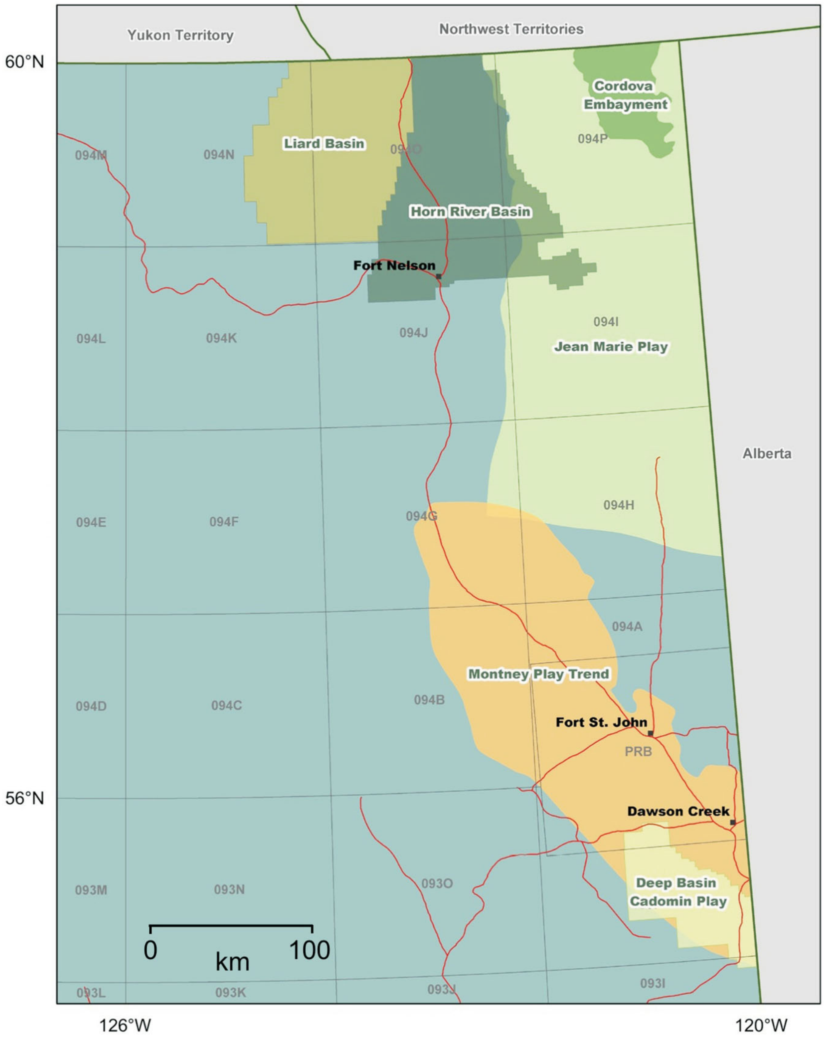

Figure 2. Unconventional hydrocarbon plays and basins in northeastern British Columbia (BC Oil and Gas Commission, 2014, with permission).

(Province of British Columbia, 2018) specifically target methane emissions from upstream natural gas, with the goal of reducing emissions (production and fugitive) by 45% by 2025. The activity focuses on production from the Montney Formation, which accounts for approximately 90% of the gas currently produced in BC (predominantly unconventional gas; BC Oil and Gas Commission, 2019c). There are approximately 5000 active and 4700 inactive/abandoned/restored/orphan wells in the Montney Formation. Initial studies (Atherton et al., 2017) indicate that approximately 47% of the active wells emit approximately 110 kt of methane per year to the atmosphere. Approximately 35% of inactive wells are reported to have fugitive methane emissions (Werring, 2018).

British Columbia Natural Gas Atlas (BC-NGA)

In recognition of the increasing natural gas activity in northeastern BC, Geoscience BC launched the multiyear British Columbia Natural Gas Atlas (BC-NGA) project in 2016. The primary objective is to systematically catalogue the molecular and stable isotope composition of natural gases produced in northeastern BC to establish geochemical fingerprints within a regional geological framework (Evans and Whiticar, 2017). The BC-NGA project provides an open source of comprehensive natural gas data, including searchable datasets (e.g., geochemical), maps and other interpretative tools (www.bcnga.ca).

By providing an integrated compilation of all available natural gas data in northeastern BC, the BC-NGA seeks to improve overall understanding of the distribution and types of natural gas that occur in northeastern BC. The data compilation allows various stakeholders, such as governments, First Nations, industries and other parties to increase their knowledge of existing and potential natural gas activities in the region, for example, by identifying specific geochemical characteristics that delineate more or less productive regions.

By identifying unique natural gas signatures in northeastern BC, the BC-NGA could have the ability to detect and identify the source of fugitive gas emissions (airborne and waterborne) coming from subsurface accumulations in northeastern BC, i.e., from specific geological formations and plays, and from other parts of the natural gas supply chain in the region. This information is critical for distinguishing and apportioning the different methane types being emitted, both natural and anthropogenic, i.e., microbial, thermogenic, pyrogenic, etc. (e.g., Whiticar, 1994). This will potentially aid the responsible development and monitoring of energy resources, while aiding remediation efforts and helping reduce greenhouse gas emissions in BC and contributing to the health of the environment and communities.

The BC-NGA is a compilation of available gas geochemical data from northeastern BC, some of which underwent a quality assurance–quality control (QA-QC) process, leading to the creation of open BC-NGA datasets. The data relies extensively on input from the BCOGC datasets, but also from analyses performed at the University of Victoria on new samples acquired for the BC-NGA project. Currently, if stable isotope analyses of mud gas, headspace gas, produced gas, surface casing vent flow gas, or any other gas

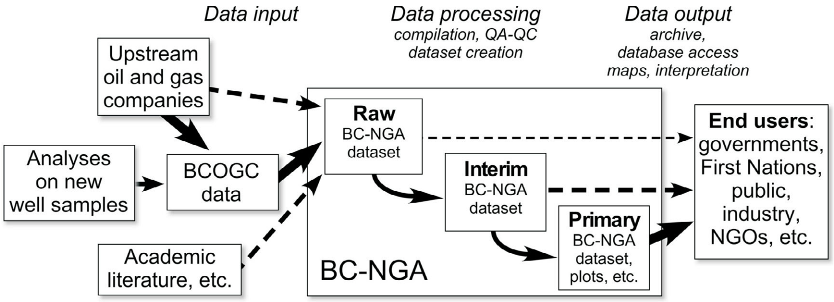

Figure 3. Schematic structure of British Columbia Natural Gas Atlas (BC-NGA) workflow. The thicker arrows indicate the most common pathway. Abbreviations: BCOGC, BC Oil and Gas Commission; NGO, nongovernmental organization; QA-QC, quality assurance–quality control.

associated with production are completed, the BCOGC requires that the information be included in the well data submission, under the requirements outlined in Section 34(5)(b) of the Drilling and Production Regulation (BC Oil and Gas Commission, 2016; Province of British Columbia, 2019). Once any confidentiality is waived, the data can be obtained from the BCOGC and incorporated into the BC-NGA.

BC-NGA Data Sources

The BC-NGA workflow and products comprise several steps. Figure 3 illustrates the various stages from data input, processing to output.

The data input stage includes acquiring the existing molecular and stable isotope data on natural gases in northeastern BC. The predominant source of data is the existing BCOGC dataset. Some of the data entries from the BCOGC dataset are confidential and may not be used until released, whereas other input data have issues that first need to be addressed before a reliable dataset is offered for general use. In many cases, a full suite of gas geochemical parameters was not measured or not available. In some instances, additional data were obtained from other sources, i.e., directly from oil and gas companies, service companies or academic investigators. For example, the BC-NGA received data from Shell Canada Limited and Dr. K. Muehlenbachs (pers. comm., 2018) that was subsequently shared with the BCOGC.

Another source of data was from new natural gas stable isotope analyses performed as part of the BC-NGA scope of work by the Biogeochemistry Facility in the School of Earth and Ocean Sciences at the University of Victoria. The samples were from vertical wells, horizontal wells and surface-equipment in northeastern BC. A brief description of the hydrocarbon gas isotope methodology used is as follows. The $^{13}C/^{12}C$ ratios ($\delta^{13}C$) and, where possible, $^{2}H/^{1}H$ ratios ($\delta^{2}H$) were determined on methane, ethane, propane, *i*-butane, *n*-butane and carbon dioxide. All isotope analyses were made using continuous flow–isotope ratio mass spectrometry (CF-IRMS; Meier-Augenstein, 1999; Whiticar and Eek, 2001; Niemann, 2006). Briefly, the gases are partitioned on a GSQ PLOT column with a Varian, Inc. 3400 GC gas chromatograph, then combusted and transferred online in a Cu/Pt wire micro-combustion oven at 870°C to a Thermo Scientific™ Finnigan MAT Delta XL IRMS. Carbon and hydrogen isotope ratios are reported in the usual delta notation ($\delta^{13}C$, $\delta^{2}H$ in ‰) relative to Vienna Pee Dee Belemnite (VPDB) and Vienna Standard Mean Ocean Water (VSMOW), respectively, according to equation (1), e.g., Coplen (2011):

$$\delta^{13}C_x = \left[\frac{(^{13}C/^{12}C)_{sample}}{(^{13}C/^{12}C)_{VPDB}} - 1\right] \times 10^3 \text{, and}$$

$$\delta^{2}H = \left[\frac{(^{2}H/^{1}H)_{sample}}{(^{2}H/^{1}H)_{VSMOW}} - 1\right] \times 10^3 \tag{1}$$

BC-NGA Data Structure

The BC-NGA includes three stages of data preparation from raw to final (Primary) for transparency and traceability (Figure 3). The Primary BC-NGA dataset is the level that most users of the data will require, but for those wishing to rework the data in a different manner, or verify the original input data, the Raw and Interim BC-NGA datasets are also available. The datasets offer the user the flexibility to tailor and configure the data from the various stages according to their own needs. Another advantage of the Raw and Interim BC-NGA datasets is that the BC-NGA has developed a script to import future data from the BCOGC, which will assist in keeping the BC-NGA datasets up-to-date.

There are three levels of data in the BC-NGA, with an increasing level of QA-QC, editing and commenting:

1) Raw BC-NGA dataset – original unmodified data, derived from existing data, e.g., BCOGC data or new analytical data. The format of the data here is often inconsistent (i.e., entry errors, replicate entries, dates stored as text, numbers stored as text) and the some of the data requires correction. The purpose of publishing the Raw BC-NGA dataset is not for direct use, rather it provides a verifiable paper trail from the reliable Primary BC-NGA dataset back to the initial raw input data.
2) Interim BC-NGA dataset – this dataset uses the Raw BC-NGA dataset as the data source, but with corrections made for format issues and for replicated entries. In addition, a series of criteria were established to flag the data at this stage for anomalous data entries, e.g., total

gas >100%. Again, this dataset is not intended for use, but continues the paper trail of corrections.

3) Primary BC-NGA dataset – this dataset uses the Interim BC-NGA dataset as the data source. This dataset includes data corrections and edits that were made as part of a QA-QC process. This includes the flagging of replicate sample entries. To clearly identify the QA-QC issues that have been addressed, the status of the same data flags used in the Interim BC-NGA dataset have been updated. In addition, the Primary BC-NGA dataset has a comment field that provides an explanation for any changes made to the Interim BC-NGA dataset.

All three datasets are published on the BC-NGA website as Microsoft® Excel® (.xls) and universal text (.csv) files for unrestricted downloading and use. Users are requested to acknowledge the source of the BC-NGA data used in any presentation or publication. In the future, the datasets will be converted to a Microsoft Access® database management file (.accdb) and hosted on the Geoscience BC website (www.geosciencebc.com). All datasets are presented with a ReadMe file for clarity and explanation of the dataset contents and use.

Raw BC-NGA Dataset

As of October 1, 2019, the Raw BC-NGA dataset had 37 258 sample entries. As described, this is the initial, unmodified raw data, prior to any QA-QC treatment. This dataset still contains replicate sample entries that have not been flagged or removed. In addition, there are numerous errors in some of the entries that have **not** been corrected in this raw level. The dataset has 128 parameter fields (Table 1), which have the basic molecular and stable isotope gas geochemical data, as well as sample identifiers, locations, dates, formations and other metadata on the sample. To aid the user, there is a ReadMe file accompanying the Raw BC-NGA dataset. The data are input as retrieved, without regard for significant digits, etc. Numerous samples do not have entries in some parameter fields. This is evident by gaps in the datasets, which are inherent in a dataset with samples that extend back well over a decade. Figure 4 maps the locations of the samples and colour-codes samples according to their interpreted geological formation (Evans and Hayes, 2018).

Interim BC-NGA Dataset

The Interim BC-NGA dataset had, as of October 1, 2019, 37 258 sample entries. The Interim BC-NGA dataset is generated by running the Raw BC-NGA dataset through a script that simply identifies potential erroneous or anomalous entry values. The objective with the Interim BC-NGA dataset is to create formatted data, identify those with potential QA-QC concerns, and make minor edits (formatting, dates, etc.). The script allows for rapid inspection of the data and can then be automatically applied to future iterations of the Raw BC-NGA dataset. The Interim BC-NGA dataset includes the fields of the Raw BC-NGA dataset and augments them with

- the anomalous value flags,
- calculation from the mol % total gas of the relative abundances of hydrocarbons (hc% for C_1 to C_6) for each of the light hydrocarbon gases (C_1 to C_6), according to the following equation:

$$\text{relative abundance } C_x \text{ (hc\%)} = C_x \text{ (mol \%)} / \Sigma(C_1 \text{ (mol \%) to } C_6 \text{ (mol \%)}) \quad (2)$$

- automatic calculation of some simple ratios using methane (C_1), ethane (C_2) propane (C_3) and butane (C_4) data, (e.g., Whiticar, 1994):

$$\text{Bernard ratio (mol \% / mol \%)} = C_1 / (C_2{+}C_3) \quad (3)$$

$$\text{wetness ratio (mol \% / mol \%)} = (\Sigma C_2{-}C_4) / (\Sigma C_1{-}C_4) \quad (4)$$

$$\text{dryness ratio (mol \% / mol \%)} = C_1 / (\Sigma C_1{-}C_4) \quad (5)$$

Generally, an entry in the Interim BC-NGA dataset is flagged as anomalous for a specific parameter if the value falls outside ±2 standard deviations (σ) from the mean for all samples of that parameter in the dataset (±2σ is defined as ±2 standard deviations from the average value), as shown in Figures 5 and 6. In a normal distribution, roughly 95% of random variation will be within ±2σ. The ±2σ is a typical cutoff value in hypothesis testing, and is used to set confidence intervals here for setting the flags. The selection of ±2σ to flag parameter values is a conservative approach and only used to easily identify values that may be anomalous or incorrect. It has been assumed that the data population is normally distributed for this classification, which may be incorrect and could lead to some misclassifications and therefore incorrect flags. However, no samples are eliminated from the Interim BC-NGA dataset and all entries and flags are reviewed in the Primary BC-NGA dataset.

Primary BC-NGA Dataset

In contrast to the Raw and Interim BC-NGA datasets, the Primary BC-NGA dataset has undergone line-by-line, close inspection and rigorous QC. The Primary BC-NGA dataset had, as of October 1, 2019, 37 258 sample entries. Each QA-QC change or evaluation has been noted in the file so that replicates, duplicates and samples with suspect data are clearly identified, thus they are transparent and accountable. No samples are added or deleted at this level, however, each data change is detailed in the comments. To aid in quick data assessment, an additional flag is added for each sample showing the overall data quality with three categories: pass (p), fail (f) and conditional (c). Pass indicates that there are no obvious issues with the sample or data entry. Fail means that some data for this sample is a replicate, corrupted and/or cannot be reliably corrected. The conditional flag means that some of the data for the sample ap-

Table 1. List of parameters in the Raw BC-NGA (British Columbia Natural Gas Atlas) dataset.

Parameter name
1 BCNGA_test_index
2 WA_num
3 Gas_anlyss_base_depth_m
4 Gas_anlyss_top_depth_m
5 Sample_date
6 Formtn_code
7 Data_filter_flag
8 C1_Methane_mole_fraction
9 C2_Ethane_mole_fraction
10 C2H4_Ethene_mole_fraction
11 C3_Propane_mole_fraction
12 C3H6_Propene_mole_fraction
13 C3H4_Propyne_mole_fraction
14 iC4_iButane_mole_fraction
15 nC4_nButane_mole_fraction
16 iC5_iPentane_mole_fraction
17 nC5_nPentane_mole_fraction
18 C6+_Hexanes_Plus_mole_fraction
19 C7_mole_fraction
20 C8_mole_fraction
21 C9_mole_fraction
22 C10_mole_fraction
23 N2_Nitrogen_mole_fraction
24 Ar_Argon_mole_fraction
25 O2_Oxygen_mole_fraction
26 O2+Ar_combined_mole_fraction
27 CO2_Carbon_Dioxide_mole_fraction
28 H2S_Sour_Gas_mole_fraction
29 He_Helium_mole_fraction
30 H2_Hydrogen_mole_fraction
31 CO_Carbon_Monoxide_mole_fraction
32 C1_Methane_mole%
33 C2_Ethane_mole%
34 C2H4_Ethene_mole%
35 C3_Propane_mole%
36 C3H6_Propene_mole%
37 C3H4_Propyne_mole%
38 iC4_iButane_mole%
39 nC4_nButane_mole%
40 iC5_iPentane_mole%
41 nC5_nPentane_mole%
42 C6+_Hexanes_Plus_mole%
43 N2_Nitrogen_mole%
44 Ar_Argon_mole%
45 O2_Oxygen_mole%
46 O2+Ar_combined_mole%
47 CO2_Carbon_Dioxide_mole%
48 H2S_Sour_Gas_mole%
49 He_Helium_mole%
50 H2_Hydrogen_mole%
51 CO_Carbon_Monoxide_mole%
52 C1_Methane_ppm
53 C2_Ethane_ppm
54 C2H4_Ethene_ppm
55 C3_Propane_ppm
56 C3H6_Propene_ppm
57 C3H4_Propyne_ppm
58 iC4_iButane_ppm
59 nC4_nButane_ppm
60 iC5_iPentane_ppm
61 nC5_nPentane_ppm
62 C6+_Hexanes_Plus_ppm
63 N2_Nitrogen_ppm
64 Ar_Argon_ppm
65 O2_Oxygen_ppm
66 O2+Ar_combined_ppm
67 CO2_Carbon_Dioxide_ppm
68 H2S_Sour_Gas_ppm
69 He_Helium_ppm
70 H2_Hydrogen_ppm
71 CO_Carbon_Monoxide_ppm
72 d13C-C1_permil
73 d13C-C2_permil
74 d13C-C3_permil
75 d13C-iC4_permil
76 d13C-nC4_permil
77 d13C-iC5_permil
78 d13C-nC5_permil
79 d2H-C1_permil
80 d2H-C2_permil
81 d2H-C3_permil
82 d2H-iC4_permil
83 d2H-nC4_permil
84 d2H-iC5_permil
85 d2H-nC5_permil
86 d13C-CO2_permil
87 Uwi_or_Name
88 Area_Code
89 formation
90 Pool_seq
91 Drillng_event_seq
92 Sample_point_code
93 Reltv_densty_calc
94 Test_num
95 Test_perf_flag
96 Temp_recvd_C
97 Press_recvd_kPa
98 Ghv_meas
99 Ghv_calc
100 Vapour_press
101 Reltv_densty_meas
102 Pcp_ppc_kPa
103 Pcp_ptc_K
104 Field_lab_flag
105 Molclr_wt_of_c7
106 C5_ml_mol
107 Molclr_wt_of_gas
108 Recmbnd_flag
109 Project_code
110 match_injection_disposal
111 data_source
112 replicate_report
113 report_error
114 report_MC_units
115 flag_comment
116 Gas_lab_num_OGC
117 Isotech_Lab_No
118 Job
119 CoreTrac
120 Company_Lab_No
121 W_Sample_ID
122 Sample_Time
123 gas_units
124 GC_Date
125 MS_Date
126 Specific_Gravity
127 BTU
128 Comments

pears to be unusable, but the remaining data for the sample may still be usable, so the entry is not a complete fail. For example, a sample may have an incorrect isotope ratio entry (e.g., $\delta^{13}\text{C-CH}_4 = -200$ ‰) that cannot be reconciled, yet the molecular data appear correct. Part of the QC process for the Primary BC-NGA dataset involves going to the original data sources, e.g., individual well reports, when available (paper or digital versions) to assess suspect data against the original lab report. Based on the QC work up to October 1, 2019, 16 940 samples passed (p) without obvious issues. There are 18 412 samples with a conditional (c) classification and 1906 that have failed (f). Samples fail or

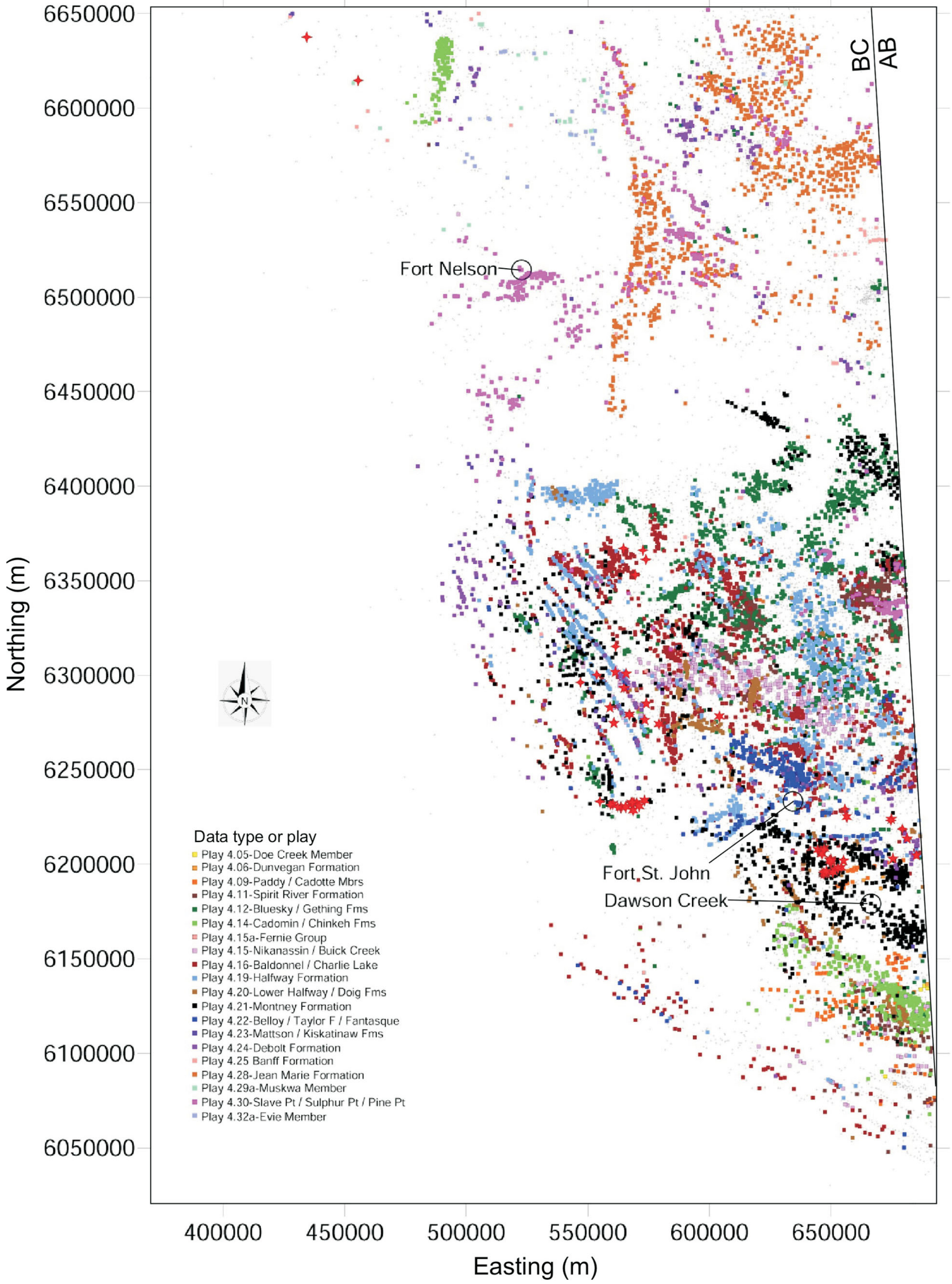

Figure 4. Map showing distribution of sample locations in the BC-NGA (British Columbia Natural Gas Atlas) dataset, colour coded according to geological formation/member. Co-ordinates are in UTM Zone 10, NAD83.

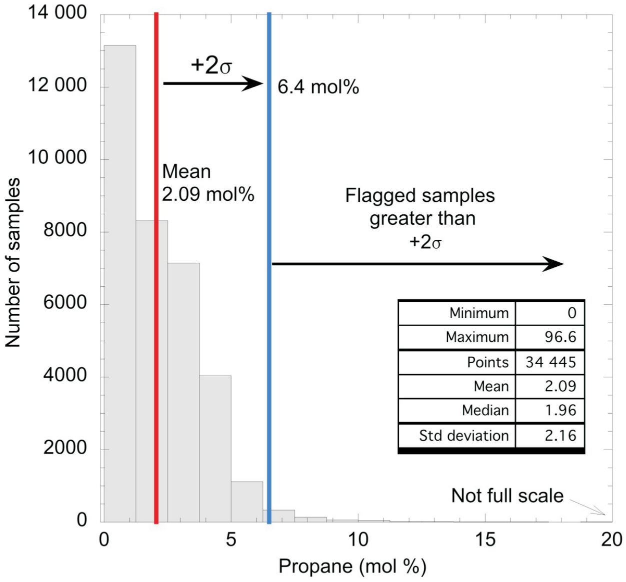

Figure 5. Histogram of propane mol % for entire Primary BC-NGA (British Columbia Natural Gas Atlas) dataset. Note that the horizontal axis is not full scale. The mean and 2 standard deviations (σ) are shown. Values >±2σ are flagged as anomalous and prompted for further inspection. Abbreviation: Std, standard.

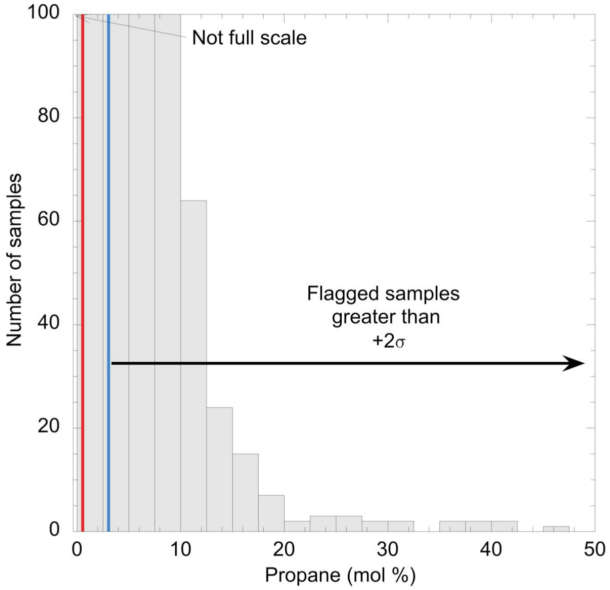

Figure 6. Expanded vertical scale of Figure 5 showing the anomalous samples with propane values flagged for further inspection. Abbreviation: σ, standard deviation.

are conditional for various reasons, including but not limited to the following:

- invalid sample type, e.g., injection well sample;
- corrupted record that cannot be resolved;
- surface casing vent flow (SCVF) or other shallow samples contaminated with air;
- replicate sample entries;
- mud-gas samples with inherently low hydrocarbon content and zero isotope data;
- samples with anomalously high CO_2 or N_2;
- samples of extremely low (e.g., <100 ppm) gas composition and high precision of isotope data;
- isotope data with abnormally high values of noble gases and blank isotope fields;
- isotope data from oil or water samples;
- obvious microbial gas formed during sample storage;
- locations outside northeastern BC;
- a non-injection well with high H_2S that might be an observation well.

Although the failed samples are not eliminated from the Primary BC-NGA dataset, their reliability and utility are questionable. The conditional samples need further user inspection before use, e.g., review of the flags to ensure the user understands the data limitations.

A further feature of the Primary BC-NGA dataset is the calculation and inclusion of additional analytical parameters that are commonly used to assess geochemical signatures. These include ratios such as C_1 to C_4 mol % and differences with stable carbon isotope ($\delta^{13}C_1$ to $\delta^{13}C_3$) data (e.g., Whiticar, 1994; Berner and Faber, 1996; Prinzhofer and Battani, 2003; Tilley and Muehlenbachs, 2013; Niemann and Whiticar, 2017). Parameters included in the BC-NGA for advanced assessment are shown below:

$$C_1\,(\text{mol\%})\,/\,C_2\,(\text{mol\,\%}) \tag{6}$$

$$C_2\,(\text{mol\,\%})\,/\,C_3\,(\text{mol\,\%}) \tag{7}$$

$$i\text{-}C_4\,(\text{mol\,\%})\,/\,n\text{-}C_4\,(\text{mol\,\%}) \tag{8}$$

$$C_2\,(\text{mol\,\%})\,/\,i\text{-}C_4\,(\text{mol\,\%}) \tag{9}$$

$$N_2\,(\text{mol\,\%})\,/\,O_2\,(\text{mol\,\%}) \tag{10}$$

$$\delta^{13}C_2 - \delta^{13}C_1\,(‰) \tag{11}$$

$$\delta^{13}C_2 - \delta^{13}C_3\,(‰) \tag{12}$$

$$\delta^{13}C_1 - \delta^{13}C_3\,(‰) \tag{13}$$

BC-NGA Database Next Steps

With the completion of the Primary BC-NGA dataset the next steps include

- release the datasets as .xls and .csv files for public access at www.bcnga.com;
- port the datasets into Microsoft Access and release the entire BC-NGA database on the Geoscience BC website (www.geosciencebc.com);
- create publicly accessible mapping and interpretative modules in GIS to use with the Primary BC-NGA dataset; and
- publish initial results in scientific journals.

Acknowledgments

The British Columbia Natural Gas Atlas (BC-NGA) team would like to thank:

- C. Salas and L. Wytrykush of Geoscience BC, for all their enduring proactive support and assistance;
- the assistance of the BC Oil and Gas Commission, in particular J. Johnson and S. Venables; and
- S. Verenitch, Biogeochemistry Facility in the School of Earth and Ocean Sciences at the University of Victoria, for conducting the stable isotope ratio analyses on the new samples.

Funding for BC-NGA is generously provided by grants from Geoscience BC and the BC Oil and Gas Research and Innovation Society, which are gratefully acknowledged.

References

Alvarez, R.A., Zavala-Araiza, D., Lyon, D.R., Allen, D.T., Barkley, Z.R., Brandt, A.R., Davis, K.J., Herndon, S.C., Jacob, D.J., Karion, A. and Kort, E.A. (2018): Assessment of methane emissions from the US oil and gas supply chain; Science, v. 361, issue 6398, p. 186–188.

Atherton, E., Risk, D., Fougere, C., Lavoie, M., Marshall, A., Werring, J., Williams, J.P. and Minions, C. (2017): Mobile measurement of methane emissions from natural gas developments in northeastern British Columbia, Canada; Atmospheric Chemistry and Physics, v. 17, p. 12405–12420.

Bachu, S. (2017): Analysis of gas leakage occurrence along wells in Alberta, Canada, from a GHG perspective – gas migration outside well casing; International Journal of Greenhouse Gas Control, v. 61, p. 146–154, URL <https://doi.org/10.1016/j.ijggc.2017.04.003> [November 2019].

BC Ministry of Energy, Mines and Petroleum Resources (2007): Oil and gas production and activity in British Columbia - statistics and resource potential 1996–2006; BC Ministry of Energy, Mines and Petroleum Resources, QP #4500163961, URL <http://www.sfu.ca/~heaps/362/2006OilnGas_Bro.pdf> [December 2019].

BC Oil and Gas Commission (2014): Horn River Basin unconventional shale gas play atlas; BC Oil and Gas Commission, 27 p., URL <https://bcogc.ca/node/11238/download> [November 2019].

BC Oil and Gas Commission (2016): Submission of isotopic gas analyses; BC Oil and Gas Commission, Industry Bulletin 2016-07, 1 p., URL <https://www.bcogc.ca/indb-2016-07-submission-isotopic-gas-analyses> [November 2019].

BC Oil and Gas Commission (2019a): 2019/20 – 2021/22 service plan; BC Oil and Gas Commission, 17 p., URL <https://www.bcogc.ca/node/15357/download> [November 2019].

BC Oil and Gas Commission (2019b): British Columbia's oil and gas reserves and production report 2017; BC Oil and Gas Commission, 29 p., URL <https://www.bcogc.ca/node/15405/download>, [November 2019].

BC Oil and Gas Commission (2019c): Number of wells drilled in B.C. - annually; BC Oil and Gas Commission, URL <https://iris.bcogc.ca/reports/rwservlet?prd_ogcr9960a> [September 2019].

Berner, U. and Faber, E. (1996): Empirical carbon isotope/maturity relationships for gases from algal kerogens and terrigenous organic matter, based on dry, open-system pyrolysis; Organic Geochemistry, v. 24, p. 947–955.

Canada Department of Justice (2019): Regulations respecting reduction in the release of methane and certain volatile organic compounds (upstream oil and gas sector); Canada Department of Justice, Statutory Orders and Regulations SOR/2018-66, 45 p., URL <https://laws-lois.justice.gc.ca/eng/regulations/SOR-2018-66/index.html> [November 2019].

Canadian Association of Petroleum Producers (2016): State of the industry overview; Mayor's Roundtable, November 17, 2016, Dawson Creek, British Columbia, slide presentation, 16 p., URL <https://www.dawsoncreek.ca/wordpress/wp-content/uploads/2016-mayors-roundtable/CAPP.pdf> [November 2019].

Canadian Association of Petroleum Producers (2019): Regional perspectives on oil and natural gas: British Columbia; Canadian Association of Petroleum Producers, Publication 2019-0050, 2 p.

Coplen, T.B. (2011): Guidelines and recommended terms for expression of stable-isotope-ratio and gas-ratio measurement results; Rapid Communications in Mass Spectrometry, v. 25, p. 2538–2560, URL <https://www.doi.org/10.1002/rcm.5129> [November 2019].

Environment and Climate Change Canada (2018): Canada's methane regulations for the upstream oil and gas sector; Government of Canada, URL <https://www.canada.ca/en/environment-climate-change/services/canadian-environmental-protection-act-registry/proposed-methane-regulations-additional-information.html> [November 2019].

Environment and Climate Change Canada (2019a): 2019 national inventory report 1990–2017: greenhouse gas sources and sinks in Canada, Canada's submission to the United Nations framework convention on climate change, executive summary; Environment and Climate Change Canada, 14 p., URL <https://www.canada.ca/en/environment-climate-change/services/climate-change/greenhouse-gas-emissions/sources-sinks-executive-summary-2019.html> [November 2019].

Environment and Climate Change Canada (2019b): About methane emissions; Government of Canada, URL <https://www.canada.ca/en/environment-climate-change/services/climate-change/global-methane-initiative/about-methane-emissions.html> [November 2019].

Environment and Climate Change Canada (2019c): Canadian environmental sustainability indicators: greenhouse gas emissions; Environment and Climate Change Canada, 16 p., URL <www.canada.ca/en/environment-climate-change/services/environmental-indicators/greenhouse-gas-emissions.html> [November 2019].

Evans, C. and Hayes, B.J. (2018): British Columbia Natural Gas Atlas update 2017: recorrelation changes the picture; *in* Geoscience BC Summary of Activities 2017, Geoscience BC, Report 2018-1, p. 11–14, URL <http://cdn.geosciencebc.com/pdf/SummaryofActivities2017/Energy/SoA2017_E_Evans.pdf> [November 2019].

Evans, C. and Whiticar, M.J. (2017): British Columbia Natural Gas Atlas project: 2016 project update; *in* Geoscience BC Summary of Activities 2016, Geoscience BC, Report 2017-1, p. 75–78, URL <http://www.geosciencebc.com/i/pdf/SummaryofActivities2016/SoA2016_Evans.pdf> [November 2019].

Ferri, F. (2019): Principal sedimentary basins of British Columbia; BC Ministry of Energy, Mines and Petroleum Resources, 1 p., URL <http://www2.gov.bc.ca/assets/gov/farming-natural-resources-and-industry/natural-gas-oil/petroleum-geoscience/princ_sedimentary_basins_map.pdf/> [November 2019].

GreenPath Energy Ltd. (2016): GreenPath 2016 Alberta fugitive and vented emissions inventory study; prepared for Alberta Energy Regulator, 40 p., URL <https://www.aer.ca/documents/GreenPathAER%20Survey-Methane.pdf> [November 2019].

Hopcroft, P.O., Valdes, P.J., O'Connor, F.M., Kaplan, J.O. and Beerling, D.J. (2017): Understanding the glacial methane cycle; Nature Communications, v. 8, article no. 14383, 10 p.

Meier-Augenstein, W. (1999): Applied gas chromatography coupled to isotope ratio mass spectrometry; Journal of Chromatography, v. 842, p. 351–371.

Myhre, G., Myhre, A. and Stordal, F. (2001): Historical evolution of radiative forcing of climate; Atmospheric Environment; v. 35, issue 13, p. 2361–2373.

Niemann, M. (2006): Stable isotope systematics of coalbed methane; Ph.D. thesis, University of Victoria, 285 p.

Niemann, M., and Whiticar, M. (2017): Stable isotope systematics of coalbed gas during desorption and production; Geosciences, v. 7, issue 2, p. 43.

Prinzhofer, A. and Battani, A. (2003): Gas isotopes tracing: an important tool for hydrocarbon exploration; Oil & Gas Science and Technology – Revue IFP, v. 58, no. 2, p. 299–311.

Province of British Columbia (2008): Climate Action Plan; Province of British Columbia, 73 p., URL <https://www2.gov.bc.ca/assets/gov/environment/climate-change/action/cap/climateaction_plan_web.pdf> [November 2019].

Province of British Columbia (2016): Climate Leadership Plan; Province of British Columbia, 45 p., URL <https://www2.gov.bc.ca/assets/gov/environment/climate-change/action/clp/clp_booklet_web.pdf> [November 2019].

Province of British Columbia (2018): CleanBC our nature. our power. our future; Province of British Columbia, 62 p., URL <https://www2.gov.bc.ca/assets/gov/environment/climate-change/action/cleanbc/cleanbc_2018-bc-climate-strategy.pdf> [November 2019].

Province of British Columbia (2019): Oil and Gas Activities Act, Drilling and Production Regulation; British Columbia Regulation 282/2010 (Oil and Gas Commission), URL <http://www.bclaws.ca/civix/document/id/complete/statreg/282_2010> [November 2019].

Saunois, M., Bousquet, P., Poulter, B., Peregon, A., Ciais, P., Canadell, J.G., Dlugokencky, E.J., Etiope, G., Bastviken, D., Houweling, S., Janssens-Maenhout, G., Tubiello, F.N., Castaldi, S., Jackson, R.B., Alexe, M., Arora, V.K., Beerling, D.J., Bergamaschi, P., Blake, D.R. and Brailsford, G. (2016): The global methane budget 2000–2012; Earth System Science Data, v. 8, p. 697–751.

The Conference Board of Canada (2013): Greenhouse gas (GHG) emissions; The Conference Board of Canada, URL <http://www.conferenceboard.ca/hcp/details/environment/greenhouse-gas-emissions.aspx> [November 2019].

Tilley, B. and Muehlenbachs, K. (2013): Isotope reversals and universal stages and trends of gas maturation in sealed, self-contained petroleum systems; Chemical Geology, v. 339, p. 194–204,

Werring, J.H. (2018): Fugitives in our midst - investigating fugitive emissions from abandoned, suspended and active oil and gas wells in the Montney Basin in northeastern British Columbia; David Suzuki Foundation, Vancouver, British Columbia, 32 p., URL <https://davidsuzuki.org/science-learning-centre-article/fugitives-midst-investigating-fugitive-emissions-abandoned-suspended-active-oil-gas-wells-montney-basin-northeastern-british-columbia/> [November 2019].

Whiticar, M.J. (1994): Correlation of natural gases with their sources; *in* The Petroleum System – From Source to Trap, L.B. Magoon and W.G. Dow (ed.), AAPG Memoir 60, p. 261–283.

Whiticar, M.J. and Eek, M. (2001): Challenges of $^{13}C/^{12}C$ measurements by CF-IRMS of biogeochemical samples at sub-nanomolar levels; *in* New Approaches for Stable Isotope Ratio Measurements, International Atomic Energy Agency, Proceedings of an Advisory Group Meeting, September 20–23, 1999, Vienna, Austria, IAEA-TECDOC-1247, p. 75–95.

Geothermal Resource Potential of the Garibaldi Volcanic Belt, Southwestern British Columbia (Part of NTS 092J)

S.E. Grasby, Natural Resources Canada, Geological Survey of Canada–Calgary, Calgary, Alberta, steve.grasby@canada.ca

S.M. Ansari, Natural Resources Canada, Geological Survey of Canada–Central, Ottawa, Ontario

A. Calahorrano-Di Patre, Simon Fraser University, Burnaby, British Columbia

Z. Chen, Natural Resources Canada, Geological Survey of Canada–Calgary, Calgary, Alberta

J.A. Craven, Natural Resources Canada, Geological Survey of Canada–Central, Ottawa, Ontario

J. Dettmer, University of Calgary, Calgary, Alberta

H. Gilbert, University of Calgary, Calgary, Alberta

C. Hanneson, University of Alberta, Edmonton, Alberta

M. Harris, University of British Columbia, Vancouver, British Columbia

J. Liu, Natural Resources Canada, Geological Survey of Canada–Calgary, Calgary, Alberta

M. Muhammad, Simon Fraser University, Burnaby, British Columbia

K. Russell, University of British Columbia, Vancouver, British Columbia

R.O. Salvage, University of Calgary, Calgary, Alberta

G. Savard, University of Calgary, Calgary, Alberta

V. Tschirhart, Natural Resources Canada, Geological Survey of Canada–Central, Ottawa, Ontario

M.J. Unsworth, University of Alberta, Edmonton, Alberta

N. Vigouroux-Caillibot, Douglas College, New Westminster, British Columbia

G. Williams-Jones, Simon Fraser University, Burnaby, British Columbia

Grasby, S.E., Ansari, S.M., Calahorrano-Di Patre, A., Chen, Z., Craven, J.A., Dettmer, J., Gilbert, H., Hanneson, C., Harris, M., Liu, J., Muhammad, M., Russell, K., Salvage, R.O. Savard, G. Tschirhart, V., Unsworth, M.J., Vigouroux-Caillibot, N. and Williams-Jones, G. (2020): Geothermal resource potential of the Garibaldi volcanic belt, southwestern British Columbia (part of NTS 092J); *in* Geoscience BC Summary of Activities 2019: Energy and Water, Geoscience BC, Report 2020-02, p. 103–108.

Introduction

Growing policy demand to shift the Canadian economy to one supported by renewable energy resources has raised interest in geothermal energy potential. Compared to other renewables, geothermal energy has numerous advantages, namely in its low environmental footprint and ability to provide a stable baseload-power supply without the need for energy-storage solutions. Much greater exploration risk related to finding hot aquifers in the deep subsurface counters these advantages. The federal government's Geothermal Energy Program (1975–1985) provided essential insight into the thermal regime of Canada (Jessop, 2008; Grasby et al., 2011). This included highlighting some of the highest temperature systems related to hot sedimentary basins (found in the Northwest Territories, Yukon, British Columbia [BC], Alberta and Saskatchewan), as well as volcanic belts (Yukon and BC). One particular success of this program was geothermal-exploration wells drilled in the Garibaldi volcanic belt of southwestern BC, specifically on the southern flank of Mount Meager. This work defined high-temperature geothermal resources, exceeding 250°C (Jessop, 2008; Witter, 2019). Despite this success, the project was never economically viable because flow rates were too low to justify the power-transition cost over the distance required. Essentially, the technical success of the exploration program was limited by the ability to predict the occurrence of permeability at depth. To address this issue, a new research project was initiated to help reduce explora-

---

This publication is also available, free of charge, as colour digital files in Adobe Acrobat® PDF format from the Geoscience BC website: http://www.geosciencebc.com/updates/summary-of-activities/.

tion risk for geothermal energy associated with volcanic systems, with a focus on the Garibaldi volcanic belt. As part of the overall project goal, a multidisciplinary field program was conducted at Mount Meager in the summer of 2019, with a focus on developing novel tools to image zones of high permeability. This paper reports on the nature of the field program and data collected.

Garibaldi Project

The Garibaldi volcanic belt represents a chain of young (less than 11 000 years old) volcanoes in southwestern BC, in a region also known to have abundant thermal springs. In the 1980s, Natural Resources Canada (NRCan), along with BC Hydro, conducted initial exploration drilling at one of the volcanoes, Mount Meager. These results defined the highest temperature geothermal resources in Canada. While this will produce electricity, the fluid-production rate was not sufficient to justify the cost of the 60 km of new transmission lines required to reach the site (power generation is a function of both temperature of the fluid and the rate at which the fluid can be produced to surface). A key outcome of this research project was that, although a world-class thermal resource was found, the geological conditions required to exploit it were not economical. Despite the defined thermal resource, lack of geoscience information regarding the regional controls on permeability posed a significant drilling risk for subsequent industry exploration in the region (Witter, 2019).

A project was initiated in 2019 by the Geological Survey of Canada (GSC) of NRCan, in partnership with The University of British Columbia (UBC), Simon Fraser University (SFU), Douglas College (DC), University of Calgary (UofC) and University of Alberta (UofA), to develop a multidisciplinary approach to reduce exploration risk through an integrated geological and geophysical field campaign. Project funding was provided through NRCan (Renewable and Electrical Energy Division and GSC), together with Geoscience BC. The project incorporates a range of geoscience tools, including remote sensing, bedrock mapping, fracture measurements, geochemistry, and magnetotelluric (MT), gravity and passive-seismic surveys. The ultimate project goal is to extrapolate new knowledge gained from the Mount Meager field campaign to the overall Garibaldi volcanic belt, thereby developing new predictive tools for finding permeable aquifers at depth. Results will also aid development of new geothermal-resource models, creating greater certainty in national geothermal-resource assessments and supporting development of effective regulatory environments.

Mount Meager Field Program

Given the difficulties of access, a helicopter-supported field program operated from July 2 to 24, supporting field teams from UBC, SFU, UofA, UofC, DC and GSC. Field plans began with consultation with First Nations and co-development of a modified field plan that limited impacts in areas of special concern. This included movement of planned survey points to new locations that still meet science goals but did not disturb the areas of special concern and, in other areas, focusing survey work on previously disturbed lands, which had the additional benefit of easier field access. The local knowledge provided through the consultation process was of significant benefit to field operations. Thirty-four project participants, including the pilot and a wildlife monitor from the Lil'wat First Nation, spent a total of 375 person days in the field. One field camp was established and the remainder of the field crew conducted daily set-outs by helicopter and worked from logging roads. The field program focused on establishing an array of seismometers (UofC), an array of MT stations focused on the shallow geothermal system (GSC) and the deeper volcanic plumbing (UofA), a gravity survey (SFU), bedrock mapping (UBC), fracture and rock-property studies (GSC), and thermal-spring geochemistry (DC and GSC; Figure 1).

Passive Seismic

Fifty-nine passive-seismic sites, each consisting of a Hawk field-station unit (INOVA Geophysical) connected to 10 Hz three-component geophones, were established (Figure 1). Each Hawk station is powered by a 288 watt-hour battery pack. Sampling Mount Meager in its entirety allows for characterizing crustal structures associated with the area of high geothermal heat and how those vary within the geothermal system. The observations from this array will be used to identify the distribution of low seismic-wave speeds, which can mark the distribution of fractures that serve as pathways for geothermal fluids, as well as magma chambers. Detecting and locating the local seismicity during this brief seismic deployment will provide constraints on the pattern of faults and fractures within Mount Meager that allow for fluid circulation through this geothermal system. The Hawk systems are also being tested for their ability to record more distant earthquakes and whether those signals can be used to measure structures within the Garibaldi volcanic belt.

In addition, a fibre-optic distributed-sensing network with 380 channels was installed on the East Ridge of Mount Meager. While this type of instrument installation is unprecedented, the data are expected to contribute improved resolution to the geophone array. Data will be analyzed in terms of seismicity in the area, tomographic studies for reservoir imaging and assessment of natural hazards.

Magnetotelluric

Collection of magnetotelluric (MT) data was aimed at greatly expanding coverage beyond that collected in the

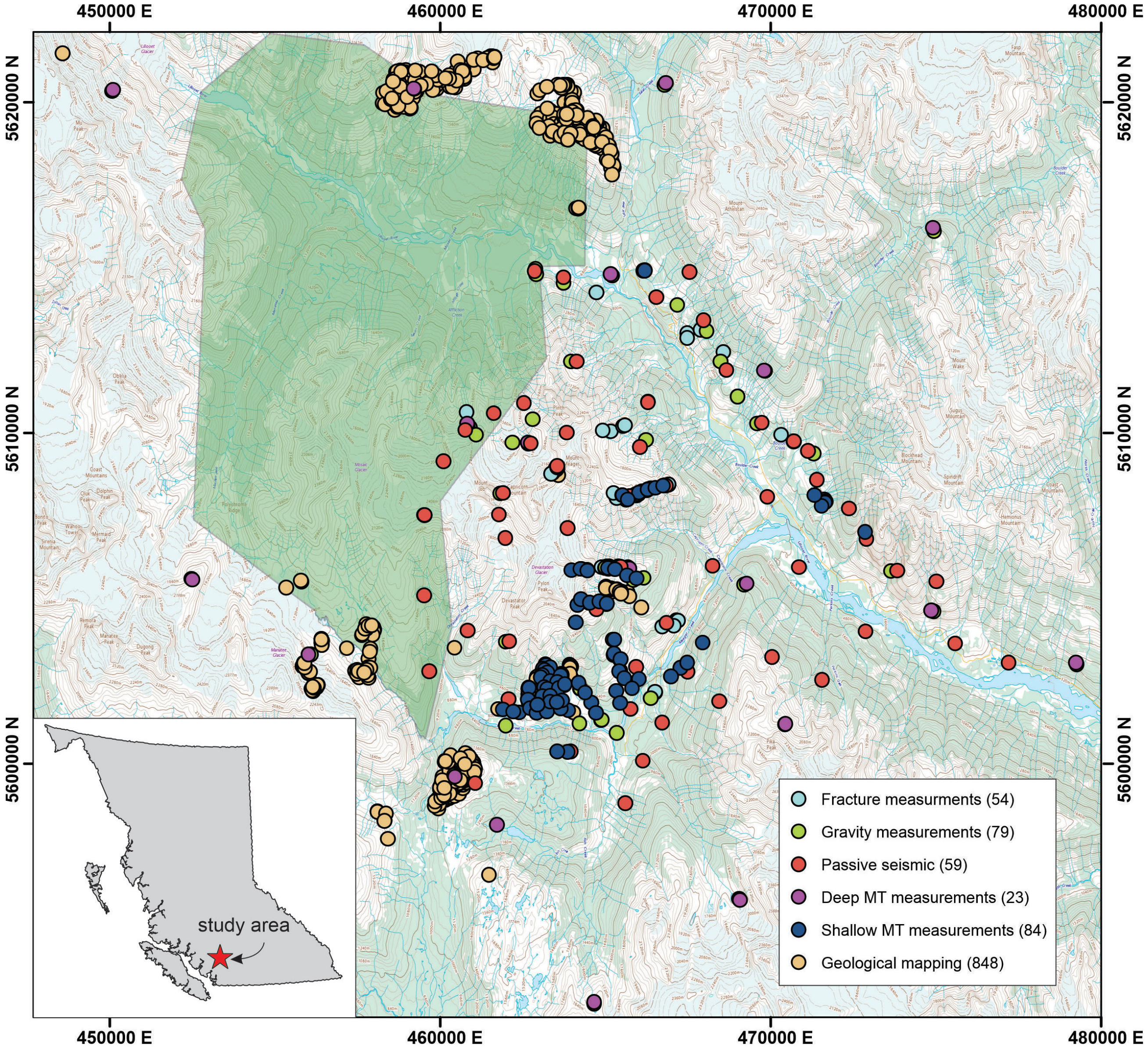

Figure 1. Mount Meager study area, showing field stations visited during the 2019 research program.

1980s (Jones and Dumas, 1993), using modern and more field-portable instruments. When combined with recently developed 3-D inversion techniques, a fully 3-D subsurface resistivity model will be developed. The MT data collection in 2019 at the Mount Meager Volcanic Complex was performed on two spatial scales. In the region of the geothermal reservoir on the south side of Pylon Peak, MT measurements were made in a dense grid of 84 stations by the GSC MT group to study the details of the geothermal reservoir (Figures 1, 2). The goal of the survey was to use the new MT data to determine permeability variations in the subsurface and link these to flow rates observed at the surface. Since the target was in the upper 1–2 km, this only requires high-frequency MT measurements in the band 1–10000 Hz, referred to as 'audio-magnetotelluric' (AMT) data. A related set of 23 MT measurements was taken by the UofA MT group to understand the deeper structure of the system, which requires longer recording time and consequently reduced the total number of measurement locations. The deeper focus MT survey was designed to image pathways that carry fluids to the geothermal reservoir and the fumaroles on Job Glacier. These deep MT measurements will also define the size and content of any magma bodies beneath the volcano. With the deeper exploration targets, lower frequencies were used in a broadband-magnetotelluric (BBMT) survey.

A key aspect of MT data analysis will be to elucidate the cause of zones of high and low resistivity found beneath Mount Meager. Resistivity contrasts in this type of environment can be caused by saline fluids, molten rock or minerals formed by hydrothermal alteration. External constraints are

Figure 2. Survey crew being set out by helicopter.

often needed to distinguish between these alternatives. It was once assumed that both geothermal reservoirs and magma bodies always had a low resistivity. However, careful laboratory experiments in recent years have shown that these assumptions are not always valid. The resistivity of magma depends on the composition, and a high silica content can often produce molten rock with a relatively high resistivity, thus making detection with electromagnetic methods challenging. Similarly, in high-temperature geothermal fields, the clay alteration minerals formed do not necessarily have a low resistivity, resulting in a reservoir that can be relatively resistive compared to the surrounding rock. Analysis of the new resistivity 3-D models from Mount Meager will be supported by other geological and geophysical datasets collected in the 2019 field campaign and from previous exploration activity.

Gravity

Spatial gravity measurements, in conjunction with other geophysical methods, are particularly useful in mapping the magmatic and hydrothermal subsurface features of volcanoes. During the summer of 2019, gravity measurements were taken at 79 stations around the Mount Meager Volcanic Complex (Figure 1), with the aim of mapping its internal structure. Gravity was measured with a Lacoste & Romberg spring gravity meter in order to develop a Bouguer anomaly map of the area. The network comprises both a dense distribution of sites near the volcanic edifice and more broadly spaced stations with increasing distance from the mountain. This distribution seeks to investigate the deep magmatic structures (depth >10 km) by comparing data from distal stations with data from the proximal dense network of stations. Smaller scale structures, such as the hydrothermal system of Mount Meager, will be mapped by analyzing gravity change between stations closer to the edifice. The measured Bouguer anomalies will be analyzed via an informed inverse-modelling approach, which combines information from geological and structural mapping, AMT, MT and seismic measurements. This will restrict the number of possible solutions for the inversion and ensure that the results best reflect plausible subsurface geological features.

Bedrock Mapping

Detailed bedrock mapping was conducted to enhance understanding of the nature of the spatial distribution of volcanic rocks that form the Mount Meager Volcanic Complex, with a particular focus on rock types with enhanced reservoir properties. Field mapping included recording rock-property observations at 848 field stations (Figure 1). These results will support the development of hydrogeological models for bulk-rock permeability to better characterize potential fluid flow at depth. High-density fracture zones appear to be associated with major fault and deformation belts. Identification and mapping of these zones using all available means (Landsat imagery and regional geophysical data, field observations, earthquake records) at a regional level will provide the basis for construction of geothermal-resource models. As well, regional mapping of faults and fracture systems will provide new predictive models of preferential orientation of fracture systems. Refined radiometric dating will also aid definition of the youngest (and hottest) flow units with the greatest heat-generation potential; this is critical information for outlining potential ‘sweet spots’ of geothermal resources.

Fracture Analyses

In order to develop an understanding of the nature of fracture systems and their potential influence on bulk-rock permeability, fieldwork was conducted to measure spatial distribution and variability in fracture orientation and fracture density (Figure 1). This was combined with remote-sensing image analyses and artificial intelligence to define trends, orientations and densities of lineaments through the study area. Identified lineaments were ground-truthed as part of the geological and geophysical mapping program to assess if they represent higher permeability fracture systems. Determination of the regional stress fields is more complex in areas of high topographic relief, as the free surface cannot be assumed to be flat. Methods being used for stress-field determination include well-borehole breakout analyses and bedding slip. Regional data will assist in refinement of the tensile portion of the regional-stress field, which would provide insight into preferred fluid-flow directions. The current stress system will be incorporated using geoscience information (magnitude, location and sense of motion) from historical records of earthquakes in the study area and surrounding vicinities, and constrained by deformation patterns and additional geoscience information from previously drilled boreholes.

Thermal-Spring Geochemistry

The occurrence of natural thermal anomalies in the form of thermal springs, and the chemistry of their water, are important geothermal-exploration tools. Temperature records from hot springs, coupled with water geochemistry, provide physical data that can be used to better understand heat energy in the deeper, hard-to-sample intervals and for critical physical properties of the hostrock. Thermodynamic modelling can also help in understanding fluid-flow paths and depths of steam separation, to better constrain the geothermal system. Calculations of aqueous geothermometers also require detailed fluid geochemistry to allow estimation of maximum temperatures of fluids at depth. Gas geochemistry, including that of noble gases, can also provide insight into the geothermal system. Therefore, new data will be collected through site visits to known thermal and mineral springs in the Mount Meager area, along with geochemical sampling and analyses, and thermodynamic modelling of heat flow in those thermal-spring systems.

Conclusions

The summer 2019 field program was a great success, with abundant new geophysical and geological data collected. These data are still being processed and will be incorporated into projects of three post-doctoral fellows, six Ph.D. projects, one M.Sc. thesis and one B.Sc. study. Final results will be integrated into a new 3-D model of the geothermal and volcanic plumbing of the Mount Meager complex. Results will provide novel new methods to help predict the occurrence of permeability at depth and greatly reduce the risk associated with drilling for geothermal reservoirs in volcanic systems of British Columbia.

Acknowledgments

The authors gratefully acknowledge the support of T. Jenkins and M. Bruce of Lil'wat First Nation in providing guidance in the field and logistical planning. Pilots M. Accurrso, D. Vincent and R. Slinger of No Limits Helicopters provided expert service. Innergex Renewable Energy Inc. provided significant support to the field program through access to their field bunkhouse. Field assistance was provided by K. Biegel, R. Bryant, J. Smale, H. Su, A. Williamson and A. Wilson. Funding for this project was provided by Geoscience BC and Natural Resources Canada. The University of Alberta group was supported by funding from the Natural Sciences and Engineering Council of Canada (NSERC) through a Canada First Research Excellence Fund (CFREF) award (Future Energy Systems) and a Discovery Grant to M. Unsworth. The University of Calgary group was supported by funding from the Canada Research Co-ordinating Committee through a New Frontiers in Research Fund award and a Discovery Grant to J. Dettmer. Financial assistance was provided to R. Salvage by the Microseismic Industry Consortium. E. Little provided a helpful review of this manuscript.

References

Grasby, S.E., Allen, D.M., Bell, S., Chen, Z., Ferguson, G., Jessop, A., Kelman, M., Ko, M., Majorowicz, J., Moore, M., Raymond, J. and Therrien, R. (2011): Geothermal energy resource potential of Canada; Geological Survey of Canada, Open File 6914, 322 p., <https://doi.org/10.4095/288745> [October 2019].

Jessop, A. (2008): Review of National Geothermal Energy Program, Phase 2 – geothermal potential of the Cordillera; Geological Survey of Canada, Open File 5906, 86 p., <https://doi.org/10.4095/225917> [October 2019].

Jones, A.G. and Dumas, I. (1993): Electromagnetic images of a volcanic zone; Physics of the Earth and Planetary Interiors, v. 81, no. 1–4, p. 289–314, <https://doi.org/10.1016/0031-9201(93)90137-X> [October 2019].

Witter, J. (2019): South Meager geothermal project – new perspectives from recently unearthed data; Geoscience BC, Report 2019-07, 5 p., URL <http://www.geosciencebc.com/i/pdf/Report-2019-07-Innovate-Geothermal.pdf> [November 2019].

Preliminary Field Investigations of Sloquet Hot Springs, Southwestern British Columbia (NTS 092G)

A. Van Acken[1], **University of Victoria, Department of Earth and Ocean Sciences, Victoria, British Columbia, ashleyvanacken@uvic.ca**

T. Gleeson, University of Victoria, Department of Civil Engineering, Victoria, British Columbia

Van Acken, A. and Gleeson, T. (2020): Preliminary field investigations of Sloquet Hot Springs, southwestern British Columbia (NTS 092G); *in* Geoscience BC Summary of Activities 2019: Energy and Water, Geoscience BC, Report 2020-02, p. 109–114.

Introduction

Geothermal resources across the southern Canadian Cordillera are of increasing interest for provincial, national and Indigenous governments, researchers, and local communities. To date, research in the southern Canadian Cordillera has been focused on investigating the distribution of thermal spring systems and their relation to major geological features, as these structures are understood to control thermal fluid flow (Grasby and Hutcheon, 2001). Sloquet Hot Springs is one of the many thermal systems in southwestern British Columbia (BC) and is located within the western Coast Belt (Journeay and Cstontos, 1989). The area is characterized by steep terrain, with undulating slopes that are covered by dense vegetation and unconsolidated material. Bedrock exposures are localized along forest service roads and along Sloquet Creek, where numerous cold, warm and hot springs discharge near the creek. Due to the lack of access to the exposures, the hydrogeologic controls of the geothermal system at Sloquet remain poorly understood.

The purpose of the research presented in this paper was to work collaboratively with Xa'xtsa First Nations' TTQ Economic Development Corporation, and Recreation Sites and Trails BC to conceptualize the hydrogeologic and geothermal setting of Sloquet Hot Springs, which is located on the traditional territory of the St'at'imc peoples. Sloquet Hot Springs is a remote recreational area that has naturally occurring soaking pools. This summary highlights methods, results and future work after the first summer of fieldwork around Sloquet. The focus of this initial work was on investigating the localized system, to capture the relationship between topography, climate, geological setting, fluid flow and temperature gradients. This research will enhance understanding of geothermal resources in the southwestern Canadian Cordillera, while also contributing to future decision-making and capacity-building for the Xa'xtsa First Nation.

Community Collaboration

Research approaches were developed using protocols that honoured diverse perspectives and ways of life, to cultivate relationships on multiple levels, not only a business level. Community consultation initially began in May 2018 and included management from TTQ Economic Development Corporation as well as members from the community. Interactive community gatherings were held that included a feast, question period, and general discussion about potential project development. Community gatherings provided partners with an opportunity to build relationships amongst one another while also gaining perspective on the cultural significance of Sloquet Hot Springs. During this process, two documents were developed and signed in conjunction with the University of Victoria and TTQ Economic Development Corporation. First, a letter of intent approved site investigations, to conduct visual surveys, mapping, drilling and reporting into the location and availability of the resource. Second, an agreement between TTQ and the University of Victoria was signed regarding wells to be drilled near Sloquet, to establish purpose, consent for scientific monitoring, and protocols for well development if cultural artifacts are encountered.

Regional Setting

Sloquet Hot Springs are located in the Coast Mountain physiographic region on the edge of two biogeoclimatic zones: coastal western hemlock, with 2893 mm of mean annual precipitation and mean annual temperatures of 6.7°C; and mountain hemlock, with 3119 mm of mean annual precipitation and mean annual temperatures of 2.8°C (Moore et al., 2010). Biogeoclimatic zones and their associated climatic regime will be used as reference in this paper because of the limited local meteorological data.

The thermal system is situated adjacent to Sloquet Creek, at a topographic low of approximately 200 m above sea level (asl) and in steep terrain that rises to over 1500 m asl. Sloquet Hot Springs are located within the Coast Belt of south-

---

[1] *The lead author is a 2019 Geoscience BC Scholarship recipient.*

This publication is also available, free of charge, as colour digital files in Adobe Acrobat® PDF format from the Geoscience BC website: http://www.geosciencebc.com/updates/summary-of-activities/.

western BC, which formed along the western edge of the Insular terrane during the Late Cretaceous (Journeay and Friedman, 1993). The contractional belt is composed of a frontal thrust system that imbricates supracrustal arc sequences and related plutonic suites from the Jurassic and Early Cretaceous, and is dominated by an array of fault-bounded island-arc and oceanic terranes that accreted along the continental margin in the Middle Jurassic to Early Cretaceous (Journeay and Friedman, 1993). Due to the size and extent of the Coast Belt, Journeay and Friedman (1993) further subdivided the system into three distinct tectonic domains that included the western, central and eastern Coast belts.

Sloquet Hot Springs are located within the western Coast Belt, which is composed of Middle Jurassic to Miocene age magmatic suites of the Coast Plutonic Complex (Journeay and Friedman, 1993). The plutonic suites have intruded arc sequences such as the Gambier–Fire Lake Group and Harrison Lake Formation (Journeay and Friedman, 1993). Gambier Group rocks have been considered part of the Fire Lake Group because of their lithological similarities (Lynch, 1990; Journeay and Friedman, 1993), however, the Gambier Group contains a larger proportion of volcanic rocks (Roddick, 1965). Studies conducted by Lynch (1990) suggest that the Fire Lake Group may be broken into the older Peninsula Formation (primarily conglomerate and arkosic sandstone) and the younger Brokenback Hill Formation (four primarily volcanic members) as shown in Figure 1.

Field Methods

Exposures of surficial deposits, bedrock and geological structures are limited in the area, therefore field reconnaissance and geological mapping was focused along the north and south sides of Sloquet Creek. Field methodologies included local-scale (hundreds of metres) site investigations that comprised the following steps:

1) mapping of bedrock, geological structures, and hot springs along portions of the northern and southern sides of Sloquet Creek at the main recreation site. Each side of the creek was evaluated along a set transect line. Data collected included length of bedrock exposure, temperature of the spring, conductivity of the bedrock, flow rate of the springs, and structural measurements that included orientation of joints and fractures. Where possible, water temperature and conductivity data were collected with a Hach HQ40D Portable Multi Meter. Measurements could not be taken at some springs, as flow was too low, or the probe could not be submerged deep enough to collect an accurate reading. Flow rates were assessed both semiquantitatively and through bucket tests, where the time it takes water to fill a container with known volume is recorded. Ninety-eight structural measurements were plotted using Stereonet software to visualize data density patterns.
2) equipment installation to monitor water levels and temperature at various locations over time. DS1922L-F5 Thermochron iButtons and Solinst leveloggers were installed in discreet areas to record water fluctuations and temperature over time. Solinst leveloggers record pressure and temperature, to interpret water level changes over time, and are being used to calculate discharge rates at the source spring. A small V-notch weir was also installed within a tributary that discharges thermal water from the main source spring, labelled HS138 on Figure 2, into Sloquet Creek. A Solinst Levelogger® and Thermochron iButton® were installed at the base of the weir.
3) well development planning, to site future well installation locations. The well will be used for evaluating the local lithology and hydraulic properties of the subsurface, while also monitoring groundwater levels at depth and the geothermal gradient of the subsurface. Possible locations for well installation were evaluated during fieldwork to allow for the most accessible and practical location.

Results

Five lithological units were identified along Sloquet Creek: unconsolidated material, clast-supported conglomerate,

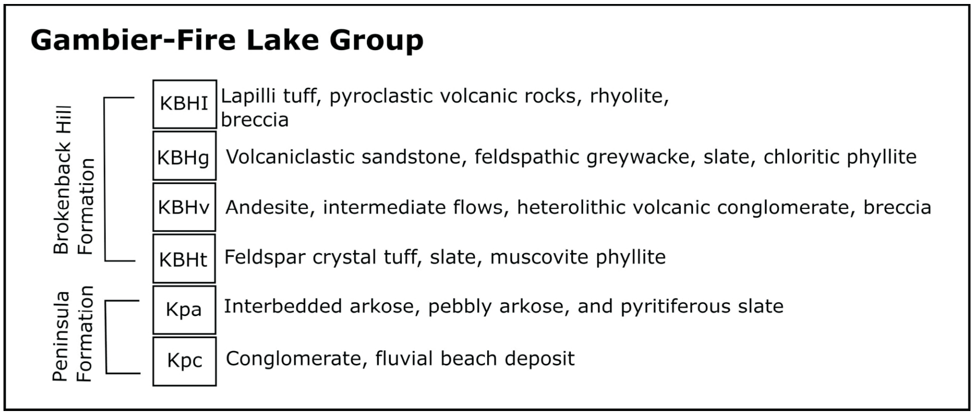

Figure 1. Geological units within the Gambier–Fire Lake Group (based on Lynch, 1990).

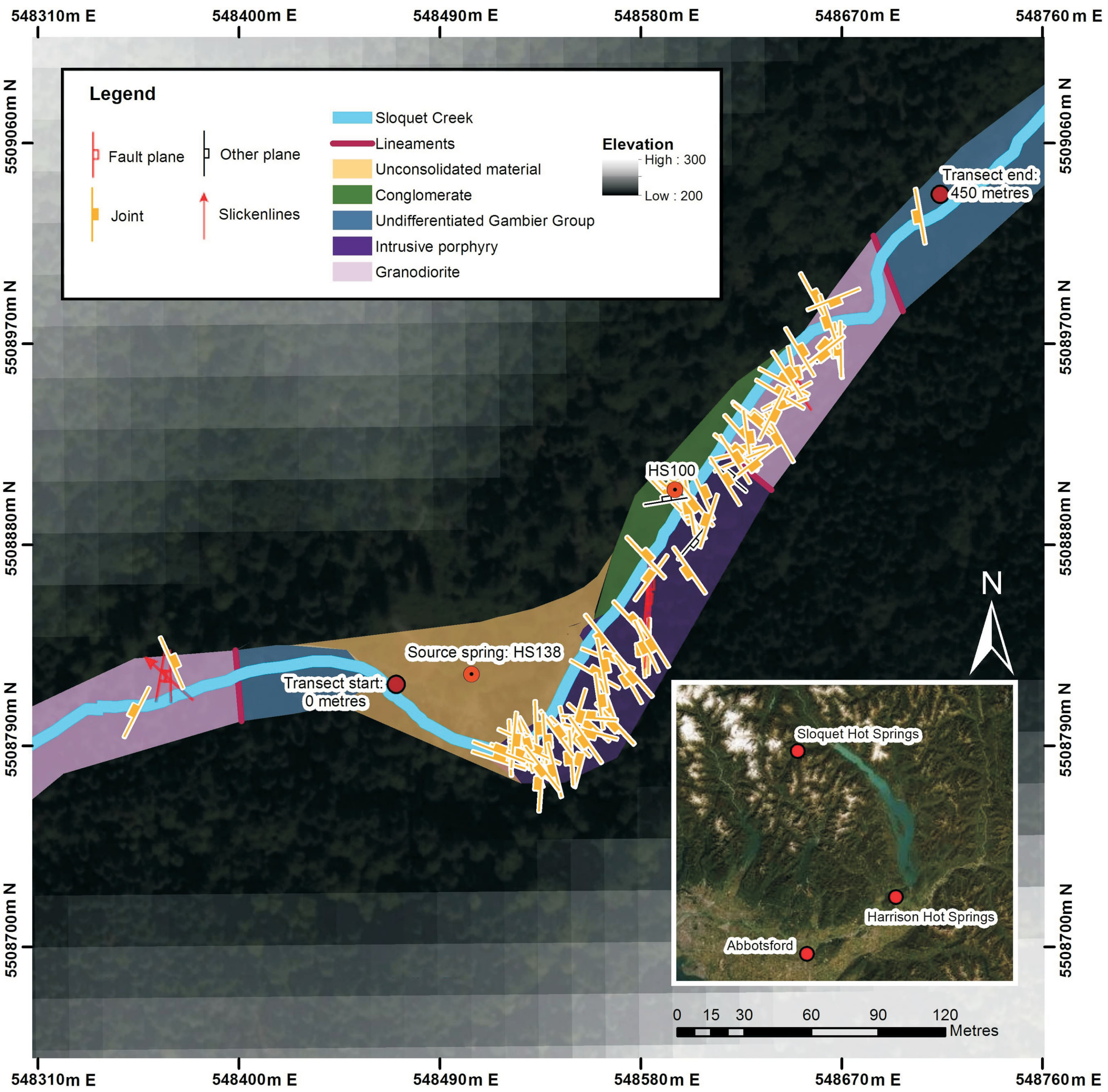

Figure 2. Details from bedrock and structural mapping in the area surrounding the Sloquet recreation site. Features were mapped along set transect lines, to gather a more detailed understanding of the area. Base for inset in lower right is from GeoBase (2019). UTM co-ordinates are in NAD83, Zone 10N.

granodiorite, undifferentiated Gambier Group rocks, and an intrusive porphyry (Figure 2). The type of bedrock along the transect lines appeared significantly more diverse than previously mapped by Journeay and Monger (1998), who suggested the area was underlain solely by mid-Cretaceous granodiorite and undifferentiated Gambier Group rocks. Updated mapping in Figure 2 shows that Sloquet Hot Springs is bound by granodiorite, likely from the mid to Late Cretaceous (Journeay and Monger, 1998), as well as undifferentiated Gambier Group volcanic rocks. However, the main bedrock unit mapped along the northern side of Sloquet Creek included a clast-supported conglomerate that is draped unconformably over an intrusive porphyry (Figure 3). In contrast, the southern side of Sloquet Creek is predominantly intrusive porphyry. Structural measurements collected from the porphyry, granodiorite and undifferentiated Gambier Group rocks show a strong clustering of joints with a northeast to southwest orientation (Figure 4).

Thermal spring discharge is visible along a 420 m stretch of the north and south sides of Sloquet Creek, with discharge from unconsolidated material, conglomerate, intrusive porphyry and undifferentiated Gambier Group rocks. Water

Figure 3. Exposure of the contact between the clast-supported conglomerate (green overlay) and intrusive porphyry (purple overlay). Distinct joint sets are visible within the porphyry and thermal seeps are seen discharging from joints with a northwest orientation.

temperature varied significantly, from 22 to 68.8°C, depending on location and lithology. Figure 5 shows the distribution of water temperature of the springs along the mapped transect lines in relation to flow rate and lithology. Most springs that exceeded 60°C discharged from the intrusive porphyry and had flow rates of less than 5 litres per minute (L/minute). Two high-temperature and high-flow springs were also observed, discharging at 15 m (main spring, herein called HS138, possibly discharging from unconsolidated material) and at 185 m (spring herein called HS100, discharging from conglomerate) along the north side of the creek (Figure 2). All the high-temperature and high-flow springs were observed along the north side of Sloquet Creek. Springs discharging from the conglomerate had the greatest range of temperature and average flow. Overall, most thermal springs appeared to be discharging from the conglomerate and porphyry, with fewer springs discharging from the unconsolidated sediments and undifferentiated Gambier Group volcanic rocks.

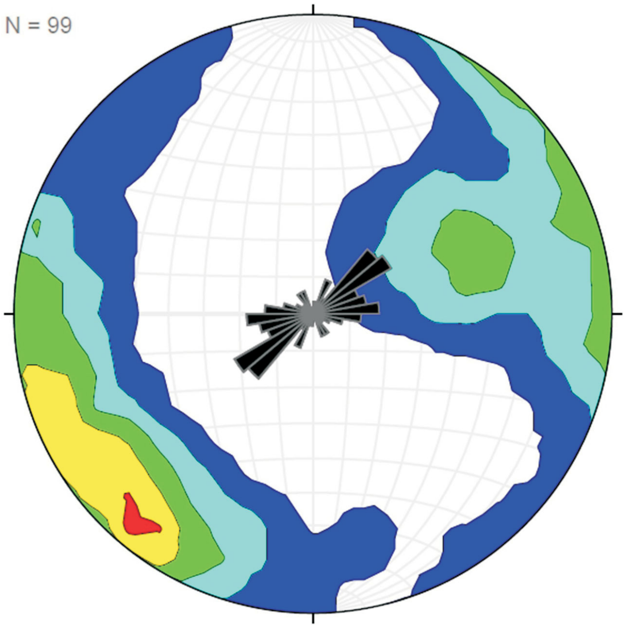

Figure 4. Structural data collected during fieldwork (orientation of joints and fractures measured in bedrock) plotted on an equal-area stereonet. The distribution of the data shows a strong preferred orientation of northeast, and a secondary clustering of west to east orientations. N = number of measurements.

Discussion

Data collected during the 2019 field season show a significant variation in bedrock geology, spring temperature and flow rate at the local scale (hundreds of metres). It is apparent that the hydraulic properties of each lithological unit control the distribution and location of hot and warm springs at Sloquet. These properties have likely been altered by tectonic processes that formed secondary structures within the rocks, and by mineralization from geothermal waters. Typically, unfractured bedrock has low permeability and low hydraulic conductivity, making it an unlikely source for springs or water resources (Freeze and Cherry, 1979), whereas fractured rock is more likely to have higher hydraulic conductivity and permeability along faults, fractures and joints.

The intrusive porphyry appeared to have the most well-developed joints, with a northwest orientation, likely developed during the complex tectonic deformation in the region, which discharge thermal fluids at numerous scattered locations. However, the average flow rate for springs discharging from these joints was relatively low and did not exceed 5 L/minute (Figure 5). The spring with the highest temperature (68.8°C) discharged from the intrusive porphyry along a northwest-trending joint, suggesting these structures may control thermal fluid flow through the rock mass and potentially also at Sloquet. The unit appears to be lithologically distinct from the mid to Late Cretaceous granodiorite, as the mineralogy varies significantly, appearing of intermediate composition, with large, well-developed quartz phenocrysts. The intrusive unit was only observed over a 100 m portion of the creek, suggesting it

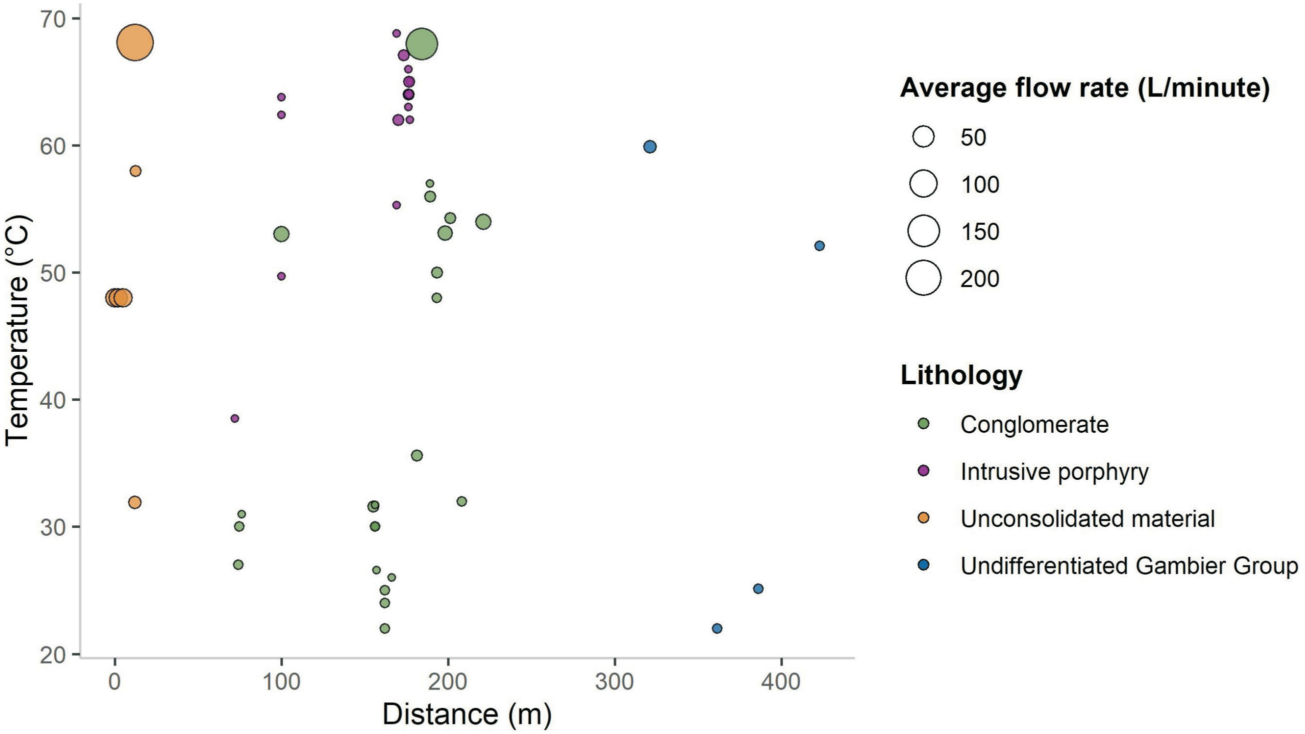

Figure 5. Graph showing the variation in temperature and average flow rate (in litres per minute, L/minute) of springs mapped along the transect lines ('Distance (m)' is distance relative to the start of the transect (see Figure 2), in metres). The size of the circles indicates magnitude of the average flow rate, and the colour represents the lithological unit from which the springs were discharging.

could be a localized, younger intrusion cutting through an existing plutonic body.

The porphyry is overlain by a clast-supported, highly lithified conglomerate that does not appear to be a part of the Peninsula Formation due to the rock types comprising the clasts and the draping nature of the contact with the porphyry (Figure 3), suggesting the sedimentary strata were deposited after emplacement of the intrusion. Clasts within the conglomerate range from pebble to boulder size and are predominantly granodiorite with minor amounts of volcanic clasts, suggesting the unit may be Pleistocene or Holocene in age. If the conglomerate was Cretaceous in age, it would be likely that volcanic clasts would dominate. Springs discharged as pore flow from anastomosing fractures that formed along planes of weakness surrounding clasts within the conglomerate. There was visible hydrothermal alteration of the conglomerate, in contrast to the porphyry, which showed no such alteration.

Overall, the springs with the highest flow rate were observed to be discharging from unconsolidated material at HS138 and the clast-supported conglomerate. The two high-temperature and high-flow springs may originate from the intrusive porphyry, which is at or near the surface where these springs are discharging.

Hydrological data collected from the weir installed at HS138, the main spring source, will not be reviewed within this paper, as it is currently being analyzed to understand trends through the summer season. Further, flow rates and temperature likely fluctuate throughout the year, therefore the data presented herein only represent a snapshot of time.

Next Steps

Research conducted to date represents analysis of the findings from only the first few months of data collection. The findings to date will be further refined to incorporate stereonet interpretations, petrographic analysis of rock samples, as well as analysis of hydrological data from equipment that has been installed at the study site. Mapping to update the geology of the Sloquet area will continue, as there is significantly more lithological variation than was expected along the 500 m stretch of Sloquet Creek and along the forest service road that leads to the site. Further analysis of rock samples will be conducted through examination of thin sections, to understand the mineral composition of the cement within the conglomerate and the hydraulic properties of these constituents. Next steps for analyzing subsurface conditions in the area surrounding Sloquet will include the development of a research well. The location and layout of the well site was established during the 2019 field season, in consultation with TTQ Economic Development Corporation and the University of Victoria. Further, hydrological data collected by equipment installed for this study will be analyzed and interpreted to review changes over time. Water samples will also be collected for geothermometry, to understand the source location of the thermal waters, and to determine if the porphyry is the host unit for the hot springs. Lastly, thermal infrared imaging of the land surface will be conducted during the winter months, to analyze thermal anomalies across the land surface surrounding Sloquet Hot Springs. All data gathered will contribute to development of a conceptual model that integrates the findings from well development, hydrogeology, temperature gradients and system behaviour at local scales (hundreds of metres) to regional scales (tens of kilometres).

Conclusions

During the 2019 summer field season research was focused on identifying an ideal location for well development, while also conducting localized research along the north and south sides of Sloquet Creek, as well as the main recreation area. In total, 49 springs were mapped, and 98 structural features were measured (joints, faults and bedding planes) to provide baseline data on the setting at Sloquet Hot Springs. The main lithological units observed in the area around Sloquet included mid to Late Cretaceous granodiorite, undifferentiated Gambier Group volcanic rocks, intrusive porphyry, conglomerate, and unconsolidated sediments. Overall, spring temperature and flow rate varied significantly depending on location and rock type, suggesting hydraulic properties of the different rocks play a role in the diffuse pattern of the springs in the area. The highest temperature springs discharged from steeply dipping, northwest-trending joints within the porphyry.

All data collected will contribute to the development of conceptual models showing the hydrogeological regime and geothermal conditions at Sloquet. The completed report for this work will be presented to TTQ Economic Development Corporation and disseminated at their discretion.

Acknowledgments

A special thank you is extended to D. Peters, Business Manager of TTQ Economic Development Corporation at Xa’xtsa First Nation, for his continual support and guidance throughout this project. The authors would also like to thank A. McCrone from Recreation Sites and Trails BC for his support to pursue field investigations at the co-managed recreation site, Sloquet Hot Springs. Another thank you to Q. Li, T. Boerman and X. Huggins from the team at University of Victoria’s Groundwater Sustainability and Research Lab for their peer review of this paper. The authors continue to be grateful to the members of the public from Xa’xtsa First Nation who support collaborative research on the traditional territory of the St’at’imc peoples.

References

Freeze, A. and Cherry, J. (1979): Groundwater; Prentice-Hall Inc., Englewood Cliffs, New Jersey, 624 p.

GeoBase (2019): Canadian digital elevation model; Natural Resources Canada, URL <https://maps.canada.ca/czs/index-en.html> [November 2019].

Grasby, S. and Hutcheon, I. (2001): Controls on the distribution of thermal springs of the southern Canadian Cordillera; Canadian Journal of Earth Sciences, v. 38(3), p. 427–440, URL <https://www.nrcresearchpress.com/doi/10.1139/e00-091#.XaZ6I0ZKg2w> [August 2019].

Journeay, J. and Cstontos, L. (1989): Preliminary report on the structural setting of the southern Coast Belt, British Columbia; *in* Current Research, Part E, Geological Survey of Canada, Paper 89-1E, p. 177–187, URL <https://geoscan.nrcan.gc.ca/starweb/geoscan/servlet.starweb?path=geoscan/fulle.web&search1=R=127480> [August 2019].

Journeay, J. and Friedman, R. (1993): The Coast Belt thrust system: Evidence of Late Cretaceous shortening in southwest British Columbia; Tectonics, v. 12, p. 756–775, URL <https://geoscan.nrcan.gc.ca/starweb/geoscan/servlet.starweb> [August 2019].

Journeay, J. and Monger, J. (1998): Geology and crustal structure of the southern Coast and Intermontane belts, southern Canadian Cordillera, British Columbia (92G, 92H, 92I, 92J); Geological Survey of Canada, Open File 3276, CD-ROM, URL <https://geoscan.nrcan.gc.ca/starweb/geoscan/servlet.starweb> [March 2019].

Lynch, J.V.G. (1990): Geology of the Fire Lake Group, southeast Coast Mountains, British Columbia; *in* Current Research, Part E, Geological Survey of Canada, Paper 90-1E, p. 197–204, URL <https://geoscan.nrcan.gc.ca/starweb/geoscan/servlet.starweb> [March 2019].

Moore, R.D., Spittlehouse, D.L., Whitfield, P.H. and Stahl, K. (2010): Weather and climate; Chapter 3 *in* Compendium of Forest Hydrology and Geomorphology in British Columbia, R.G. Pike, T.E. Redding, R.D. Moore, R.D. Winkler and K.D. Bladon (ed.), Forests and Range, Research Branch, Land Management Handbook 66, p. 47–81, URL <https://www.for.gov.bc.ca/hfd/pubs/Docs/Lmh/Lmh66/Lmh66_ch03.pdf> [September 2019].

Roddick, J.A. (1965): Vancouver North, Coquitlam and Pitt Lake map-areas, British Columbia with special emphasis on the evolution of the plutonic rocks; Geological Survey of Canada, Memoir 335, 291 p. (6 sheets), URL <https://geoscan.nrcan.gc.ca/starweb/geoscan/servlet.starweb> [August 2019].

Structural Settings of Convective Hydrothermal Systems in Southeastern British Columbia (Parts of NTS 082E–G, J–O, 083C, D)

T.D. Finley[1], Department of Earth and Atmospheric Sciences, University of Alberta, Edmonton, Alberta, tfinley@ualberta.ca

S.T. Johnston, Department of Earth and Atmospheric Sciences, University of Alberta, Edmonton, Alberta

M.J. Unsworth, Department of Physics, University of Alberta, Edmonton, Alberta

J. Banks, Department of Earth and Atmospheric Sciences, University of Alberta, Edmonton, Alberta

D. Pana, Alberta Energy Regulator / Alberta Geological Survey, Edmonton, Alberta

C. Hanneson, Department of Physics, University of Alberta, Edmonton, Alberta

Finley, T.D., Johnston, S.T., Unsworth, M.J., Banks, J., Pana, D. and Hanneson, C. (2020): Structural settings of convective hydrothermal systems in southeastern British Columbia (parts of NTS 082E–G, J–O, 083C, D); *in* Geoscience BC Summary of Activities 2019: Energy and Water, Geoscience BC, Report 2020-02, p. 115–130.

Introduction

There has long been interest in developing geothermal energy in western Canada (Jessop et al., 1991; Grasby et al., 2012), but as yet, there are no operating geothermal power plants or direct heating systems (excluding shallow geo-exchange). Part of the problem is limited geological understanding of the regions where geothermal potential is highest, particularly the complexly deformed Canadian Cordillera of British Columbia (BC) and Yukon. Crustal heat flow in the Cordillera is relatively high (~80–100 milliwatts per square metre [mW/m^2]; Davis and Lewis, 1984), and the occurrence of more than 130 thermal springs has attracted the interest of geothermal developers. However, data constraining the subsurface are limited, which discourages investment.

Most geothermal systems occur in magmatically and tectonically active areas (e.g., western United States, Japan, New Zealand, Iceland). This is due in part to the elevated enthalpy in the crust, but also to the enhanced permeability of brittle faults, which act as conduits for circulating hydrothermal fluids (Moeck, 2014). Several characteristics of fault zones influence their structure, including age and amount of seismic activity (e.g., Curewitz and Karson, 1997), kinematics (e.g., Meixner et al., 2016) and subsurface geometry (e.g., Moreno et al., 2018). Understanding these parameters is key to understanding the geothermal systems fault zones may host.

Hydrothermal systems (i.e., thermal springs) in the Canadian Cordillera are broadly associated with major fault zones (Grasby and Hutcheon, 2001). However, detailed investigations of the significant hydrogeological properties of many of these faults have not previously been conducted. The research presented in this paper focuses on hydrothermal systems in three specific regions in the southern Canadian Cordillera (Figure 1b): Valemount and Canoe Reach, Nakusp and the West Kootenays, and the southern Rocky Mountain Trench. These regions were chosen because of their concentrations of high-temperature thermal springs, elevated crustal heat flow, proximity to population centres, and commercial interest in geothermal development in these areas. Herein are presented new structural data collected within fault zones that appear to control hydrothermal systems in these areas. The current stress field of the crust, and its relationship to fault kinematics and geometry is also considered. These data provide new insight into the age, kinematics and geometry of these fault zones.

Background

Regional Geology

The Canadian Cordillera is an ~800 km wide mountain belt that stretches from the Arctic Ocean to the United States border, mostly within the Northwest and Yukon territories and the provinces of British Columbia and Alberta. Its elevated topography, rugged relief and complex geology reflect a protracted and ongoing interaction between various oceanic plates, accreted terranes, and continental North America (Gabrielse and Yorath, 1991). For simplicity, the Cordillera is divided into five major morphogeological belts (Figure 1a; Gabrielse et al., 1991). The easternmost Foreland Belt is composed of folded and thrusted—but largely unmetamorphosed—carbonate and siliciclastic

---

[1] *The lead author is a 2019 Geoscience BC Scholarship recipient.*

This publication is also available, free of charge, as colour digital files in Adobe Acrobat® PDF format from the Geoscience BC website: http://www.geosciencebc.com/updates/summary-of-activities/.

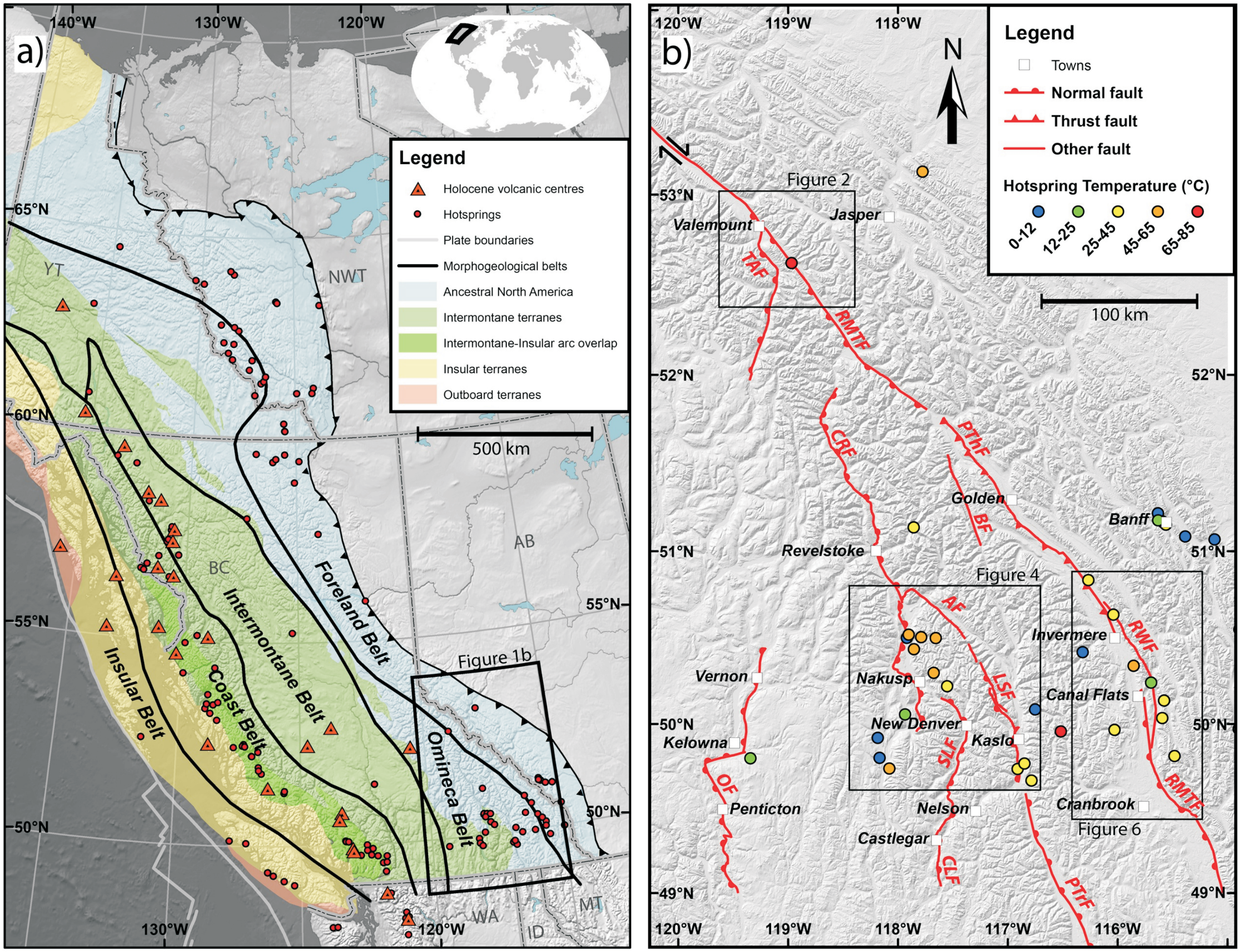

Figure 1. a) Regional geological setting of the Canadian Cordillera. Morphogeological belts are after Gabrielse et al. (1991), and the boundaries of allochthonous and autochthonous superterranes are after Colpron and Nelson (2011). Volcanoes active in the Holocene (American Geological Institute, 2003) occur predominantly within the Coast Belt. Concentrations of thermal springs occur along the axis of the Coast Belt, in the northern Omineca and Foreland belts, and in the southern Omineca and Foreland belts (Woodsworth and Woodsworth, 2014). Note that the latter two clusters do not correspond to regions of active volcanism, but do correspond to significant (>100 milliwatts per square metre [mW/m^2]) heat-flow anomalies (see Majorowicz and Grasby, 2010). The current study areas are located in the southern Omineca and Foreland belts. **b)** Major faults in southeastern British Columbia. Abbreviations: AF, Adit fault; BF, Beaver fault; CLF, Champion Lakes fault; CRF, Columbia River fault; LSF, Lakeshore fault; OF, Okanagan fault; PThF, Purcell Thrust fault; PTrF, Purcell Trench fault; RMTF, Rocky Mountain Trench fault; RWF, Redwall fault; SLF, Slocan Lake fault; TAF, Tintina fault.

rocks of an ancestral passive margin and a subsequent foreland basin. Adjacent and to the west is the Omineca Belt, which is dominantly composed of metamorphosed sedimentary rocks coeval with those in the Foreland Belt and deformed during the same mountain-building events. The Omineca Belt is intruded by numerous Jurassic and Cretaceous continental arc–type plutonic suites (Armstrong, 1988), and tectonic windows expose metamorphosed crystalline rocks, interpreted as cratonic basement exhumed during Eocene extension (Parrish et al., 1988). Contractional deformation of the Omineca and Foreland belts is associated with Jurassic and younger accretionary and collisional events, including accretion of oceanic arc terranes that make up the more westerly Intermontane Belt (Evenchick et al., 2007). West of the Intermontane Belt lies the Coast Belt, which is largely composed of intrusive and metamorphic rocks associated with the Cretaceous to Eocene subduction and accretion of the westernmost Insular Belt, which underlies Vancouver Island, Haida Gwaii and the Alaska Panhandle (Evenchick et al., 2007). Young and active continental arc volcanoes are being constructed atop the Coast Belt as a result of ongoing subduction of the Juan de Fuca Plate and other micro-plates off the western margin of the continent (Green et al., 1988). This study is focused on hydrothermal systems in the southern Omineca Belt, from the United States border to ~53°N (Figure 1b).

Sources and Expressions of Heat Flow in the Canadian Cordillera

The Cordillera is one of the most promising regions in Canada for geothermal energy development due to its high heat flow and steep geothermal gradients (Grasby et al., 2012). Whereas much of eastern and central Canada is underlain by old and cold cratonic lithosphere and ancient orogenic belts, the Cordillera is geologically young and is subject to ongoing tectonic and magmatic processes that enhance geothermal conditions. The presence of more than 130 thermal springs throughout the Cordillera (Figure 1a) provides a first-order indication that heat flow might be sufficient for geothermal energy extraction. Outlet temperatures of these springs range from ~20° to 80°C (Woodsworth and Woodsworth, 2014). Aqueous geothermometry indicates that the maximum temperatures reached by some of these systems exceeds 180°C, with maximum circulation depths estimated to be ~2–5 km (Grasby and Hutcheon, 2001; Allen et al., 2006; Caron et al., 2007). Although thermal springs are not necessarily the best indicator of geothermal prospectivity (Ferguson and Grasby, 2011), they do provide a basic indication of geothermal resource potential, in a subsurface environment that is otherwise poorly constrained by data.

The geothermal gradient of the Cordillera ranges from ~20° to 50°C/km (Hitchon, 1984; Lewis et al., 1992; Grasby and Hutcheon, 2001). These values, though lower than most conventional (high enthalpy) geothermal energy resources, are similar to gradients measured in low enthalpy systems being explored and developed for electricity generation in Europe and New Zealand (e.g., Agemar et al., 2014; Reyes, 2015; Farquharson et al., 2016). Crustal heat flow in the Cordillera ranges from ~40 to 130 mW/m^2 (Hyndman and Lewis, 1995; Blackwell and Richards, 2004; Majorowicz and Grasby, 2010). Heat flow is locally very high (>200 mW/m^2) near active volcanoes in the Garibaldi volcanic belt in southwestern BC (e.g., Mount Meager), but these values do not reflect the bulk of thermal conditions in the Cordillera. In several broad regions heat flow exceeds 100 mW/m^2 (see Majorowicz and Grasby, 2010), which is comparable to geothermal energy–producing regions like Nevada and Utah (Blackwell and Richards, 2004). Interestingly, one of these regions, the southern Omineca Belt (Columbia Mountains) of southeastern BC, does not contain any active or recently active volcanoes, which suggests that the heat might come from shallow intrusions in the crust. Indeed, radioactive heat generation measured in Cretaceous and Paleogene intrusive suites is high in the Omineca Belt (Lewis et al., 1992).

Major Fault Zones and their Relation to Hydrothermal Systems

Grasby and Hutcheon (2001) compared several parameters, including heat flow, permeability, topography/relief, infiltration rate, and the presence of fault zones, with regards to their influence on the location of thermal springs in the southern Canadian Cordillera. Ultimately they determined that—with the exception of springs within the Garibaldi volcanic belt—fault zones act as a primary control on the position of thermal springs in the Canadian Cordillera, whereas the other factors have a negligible influence. From east to west, the significant fault zones in the southeastern Cordillera identified by Grasby and Hutcheon (2001) as hydrogeologically significant are (see Figure 1b): the southern Rocky Mountain Trench fault (RMTF), Purcell Trench fault (PTrF), Columbia River fault (CRF), and Okanagan fault (OF). All of these structures have been interpreted as hosting significant normal displacement during Eocene extension of the Cordillera (Parrish et al., 1988; van der Velden and Cook, 1996).

Fault zones typically have an anisotropic permeability structure, dependent on the relative percentages of clay fault gouge and fractured wall rock (Caine et al., 1996). Typically, cross-fault flow is impeded by the impermeable (clay rich) core material, while along-fault flow is facilitated by the permeable damaged (fractured) zone. Grasby and Hutcheon (2001) presented a conceptual model for hydrothermal convection cells in the Canadian Cordillera in which meteoric water percolates vertically down through the crust until it encounters a shallowly dipping fault plane, and is then forced back up to the surface via the damaged zone conduit. Because faults tend to crop out in valleys due to accelerated erosion of comminuted fault rock, there is a natural topographic drive to such systems, with recharge occurring in mountainous highlands.

What remains unanswered is why certain faults host thermal springs while others do not, and why thermal springs are distributed unevenly along fault zones. Variations in crustal heat flow, precipitation/infiltration rate, and topographic relief occur on wavelengths too broad to explain the pattern of hotspring occurrence (Grasby and Hutcheon, 2001; Ferguson and Grasby, 2011). It is therefore likely that inter- and intra-fault variations in geometry and permeability structure are critical parameters. It has been shown in other structurally controlled geothermal systems that the current stress state of the crust and resulting fault kinematics can predict which fault segments are most permeable; faults oriented parallel or oblique to S_{Hmax} (maximum horizontal compression) are more likely to be permeable than those oriented perpendicular to S_{Hmax} (e.g., Meixner et al., 2016). Furthermore, there is a positive relationship between strain rate and fault permeability—seismic activity has been shown to maintain fault permeability via episodic refracturing of minerals precipitating within the fault zone (Curewitz and Karson, 1997). Below, these parameters are discussed for major faults in three areas of southeastern BC (Figure 1b).

Structural Settings of Hydrothermal Systems in the Canadian Cordillera

Valemount and Canoe Reach

Background

The town of Valemount has attracted commercial interest in geothermal energy production due to the presence of the Canoe River thermal spring ~30 km south of the townsite, on the west shore of Kinbasket Lake hydroelectric reservoir (Figure 2) in the southern Rocky Mountain Trench (SRMT). The Canoe River spring is one of the hottest thermal springs in BC, with outlet temperatures measured at 80°C and maximum temperatures derived from aqueous geothermometers exceeding 200°C (Ghomshei, 2007). The Town of Valemount is interested in the possibility of low-carbon baseload power and heat, along with the tourism draw that a geothermal spa would bring. Recently, Borealis GeoPower has undertaken a geothermal exploration program in the area, conducting soil sampling, geophysical surveying and slim-hole drilling (see http://www.borealisgeopower.com/).

The crustal structure of the Valemount area is complex (Figure 2), and there are limited constraints on the structures that might control hydrothermal circulation. Much of the area is underlain by Paleoproterozoic basement gneiss, referred to as the Malton Gneiss on the southwest side of the SRMT valley, and the Bulldog and Yellowjacket gneisses on the northeast side. Some authors have asserted that the eastern and western gneiss packages are geochemically and geophysically distinct, arguing for a major transcurrent fault between them (Chamberlain and Lambert, 1985; Chamberlain et al., 1985). However, all three packages are similar, and may represent exhumed cratonic basement (McDonough and Simony, 1988). The gneiss complex is overlain by a metasedimentary cover sequence assigned to the Neoproterozoic Miette Group. The gneiss complex and a thin slice of lower Miette Group are carried northeastward over middle and upper Miette rocks on the Bear Foot thrust, a synmetamorphic dextral-oblique reverse fault assumed to have accommodated 50 km of dip-slip displacement (McDonough and Simony, 1988, 1989). Orogen-parallel ductile stretching lineations in the footwall of the Bear Foot thrust indicate that the thrust predates Cenozoic brittle structures (McDonough and Simony, 1989). The Malton and Bulldog gneiss packages are carried in the hangingwall of the northeast-verging Purcell Thrust, a large, out-of-sequence thrust fault that is mapped for several hundred kilometres to the south (Price, 1981). The western extent of the Malton Gneiss is defined by the steeply west-dipping Thompson–Albreda fault, a fault associated with Eocene extension of the orogenic belt. Separating the Malton and Bulldog/Yellowjacket gneiss packages, on the floor of the SRMT, is the Rocky Mountain Trench fault, a steeply dipping west-side-down normal fault. Its exact trace is obscured by Quaternary cover and the hydroelectric reservoir, and its presence is inferred from offset metamorphic isograds and stratigraphic horizons. The RMT fault is mapped as far south as 52°N, where it disappears, and the trench floor is instead occupied by the Purcell Thrust fault. The RMT fault reappears south of Canal Flats and can be traced as far south as Flathead Lake in Montana. Notably, north of Valemount, the RMT fault and its northern continuation, the Tintina fault, are known to host significant dextral slip (Roddick, 1967; Gabrielse, 1985; McMechan, 2000). Murphy (1990) identified dextral mylonitic fabrics at the north end of Kinbasket Lake (12 km southeast of Valemount), but dextral strike-slip is not believed to continue any farther southeast along the SRMT, and transpression is instead accommodated on structures like the Fraser River fault ~250 km to the west (Price and Carmichael, 1986; Struik, 1993).

New Observations

Detailed structural fieldwork was conducted in the spring of 2018 in the Valemount area and south along Kinbasket Lake (Figures 2, 3). Work was focused on the shorelines of the reservoir in an attempt to capture kinematic indicators proximal to the RMT fault zone, which parallels the lakeshore. Nearly 150 measurements of fault plane and slickenline orientations were collected, especially in the continuous exposures of the basal Windermere Supergroup and

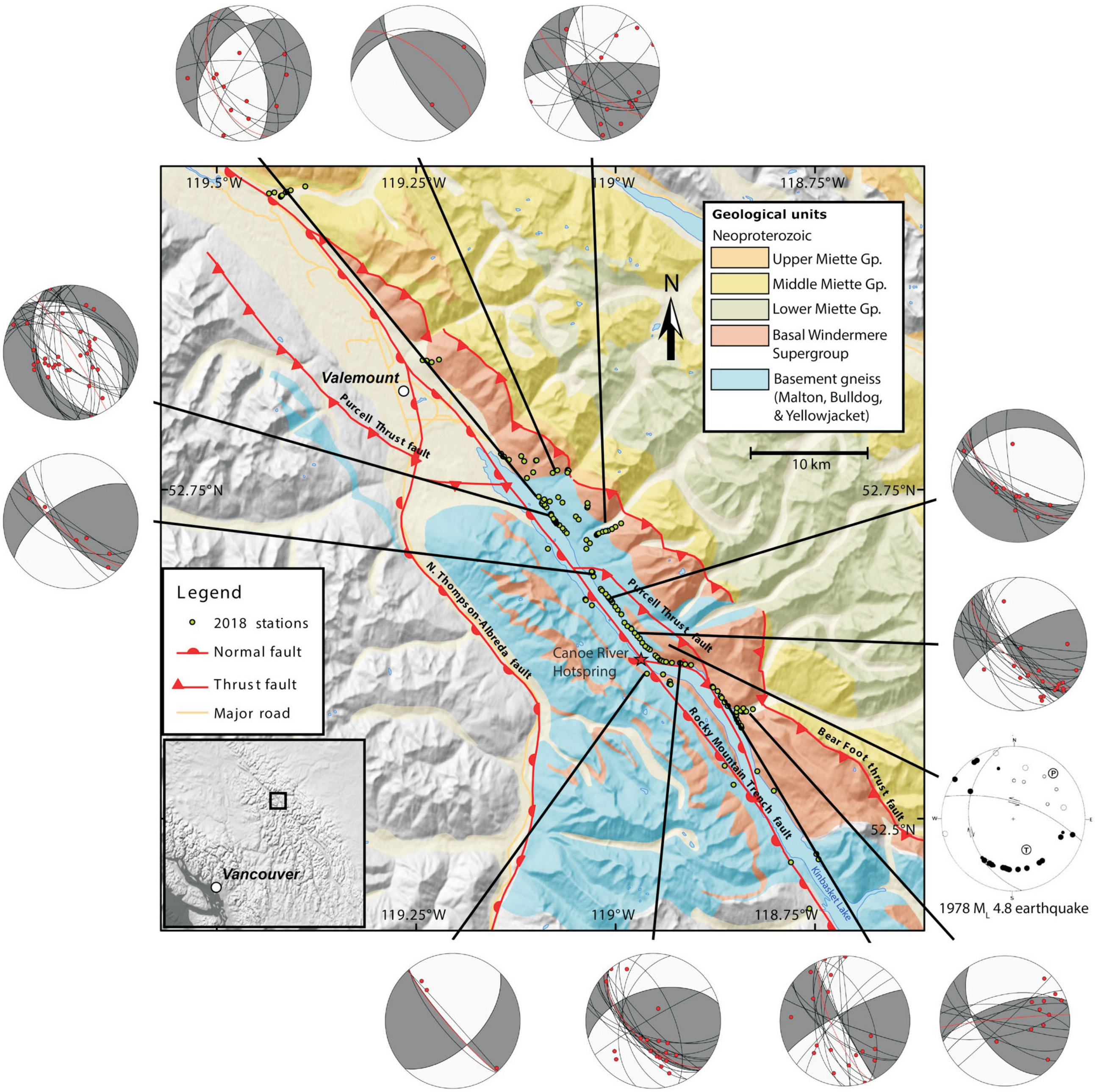

Figure 2. Geology of the Valemount and Canoe Reach area, on northern Kinbasket hydroelectric reservoir, south of Valemount, after Murphy (2007). Green dots are sites examined in the field. Lower-hemisphere stereonets ('beachball' plots) show fault plane and slickenline orientations for subsets of stations along Kinbasket Lake. Compressional (P) and dilational (T) quadrants represent the average kinematics for each subset. The focal mechanism for the 1978 Richter (local) magnitude (M_L) 4.8 McNaughton Lake earthquake (Rogers et al., 1980) is provided for comparison (lower right). Abbreviation: Gp., Group.

Bulldog Gneiss on the northeast side of the reservoir (Figure 3). Slickenlines were ranked according to confidence, and care was taken to avoid mistaking riedel shears for the more diagnostic mineral growths on the lee side of fault plane asperities. Abundant subhorizontal slickenlines were found, generally on subvertical fault planes on numerous outcrops, distributed for 40 km south along the lake. The majority of slickenlines indicated dextral slip. Few west-side-down dip-slip slickenlines were observed. Subsets of slickenlines were identified manually, and kinematic analysis was performed on each subset using the Orient software package (Vollmer, 2019). 'Beachball' plots (Figure 2) showing compressional (P) and dilational (T) quadrants were calculated based on the average kinematics of all faults within each subset.

A Richter (local) magnitude (M_L) 4.8 earthquake occurred in the area on May 14, 1978 (Rogers et al., 1980), and was initially investigated due to concerns that it may have been

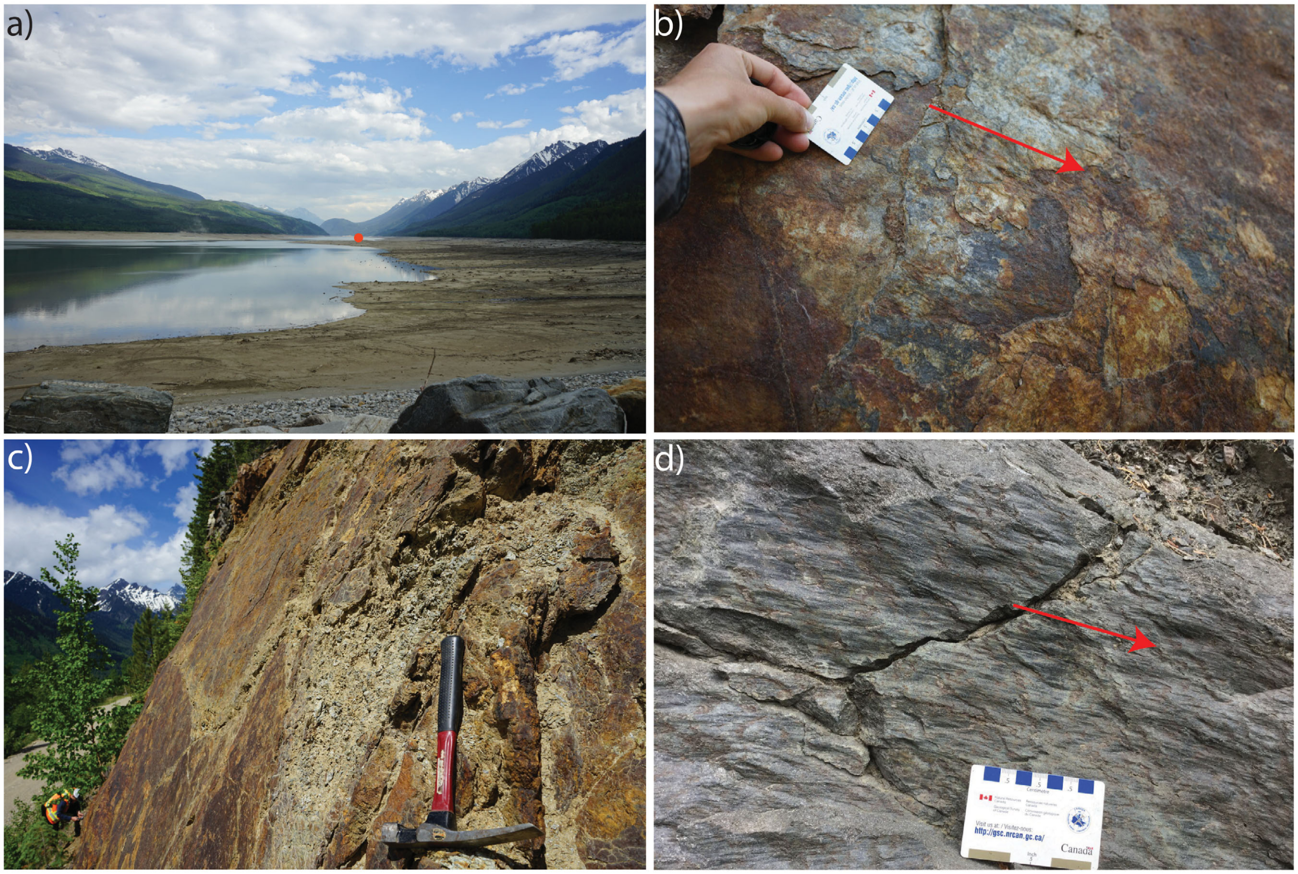

Figure 3. a) View south from the north end of the Kinbasket hydroelectric reservoir, captured at low water level in May 2018. Red dot shows the location of the Canoe River thermal spring. **b)** Vestiges of dextral slickenlines in basal Neoproterozoic Windermere Supergroup on the northeast side of the lake (lat. 52.5691°N, long. 118.8420°W). Fault is oriented 168°/63°, slickenlines (red arrow) are oriented 19°→192°. **c)** Large, oxidized, fault plane in basal Windermere Supergroup on northeast side of lake (lat. 52.6202°N, long. 118.9424°W). Fault is oriented 170°/54°, dextral slickenlines (not pictured) are oriented 15°→333°. **d)** Dextral slickenlines in Paleoproterozoic Bulldog Gneiss on northeast side of lake (lat. 52.6412°N, long. 118.9759°W). Fault is oriented 139°/84°, slickenlines (red arrow) are oriented 15°→143°.

caused by the filling of the Kinbasket Lake reservoir (historically referred to as McNaughton Lake). The preferred focal mechanism for this earthquake was dominantly right lateral, with a reverse component, on a south-southeast–striking fault plane. Ultimately it was concluded that the earthquake was not induced by the reservoir, but rather was attributed to "stresses associated with residual strain energy stored during the mountain building process" (Rogers et al., 1980). The orientation of the focal mechanism of the McNaughton Lake earthquake is similar to the orientation of fault planes and slickenlines observed in the area (Figure 2).

Nakusp and the West Kootenay Region

Background

The West Kootenay region of southeastern BC has some of the highest heat flow values in Canada (Blackwell and Richards, 2004; Majorowicz and Grasby, 2010), and the town of Nakusp bills itself as the Hot Spring capital of Canada. Some of Canada's hottest thermal springs, with the highest estimates of maximum temperatures (Grasby and Hutcheon, 2001), exist in the area. Many thermal springs in this area issue from the Kuskanax batholith (Figure 4), a mid-Jurassic (173 ±5 Ma) batholith that underlies most of the mountain range to the northeast of Nakusp (Parrish and Wheeler, 1983).

There are two fault zones in this area that are likely significant controls on the local hydrogeology: the Columbia River fault and the Slocan Lake fault. Both have previously been interpreted as low-angle, east-dipping, brittle normal faults, with a range of possible displacement. In the footwall (west side) of the Columbia River and Slocan Lake faults there are amphibolite- to granulite-grade metamorphic complexes, the Monashee and Valhalla, respectively. These, like the Malton gneiss complex near Valemount, are interpreted to be fragments of exhumed cratonic basement (Ross, 1991). Rocks in the hangingwalls are generally greenschist-grade metasedimentary rocks, and unmetamorphosed Jurassic and Cretaceous plutonic suites.

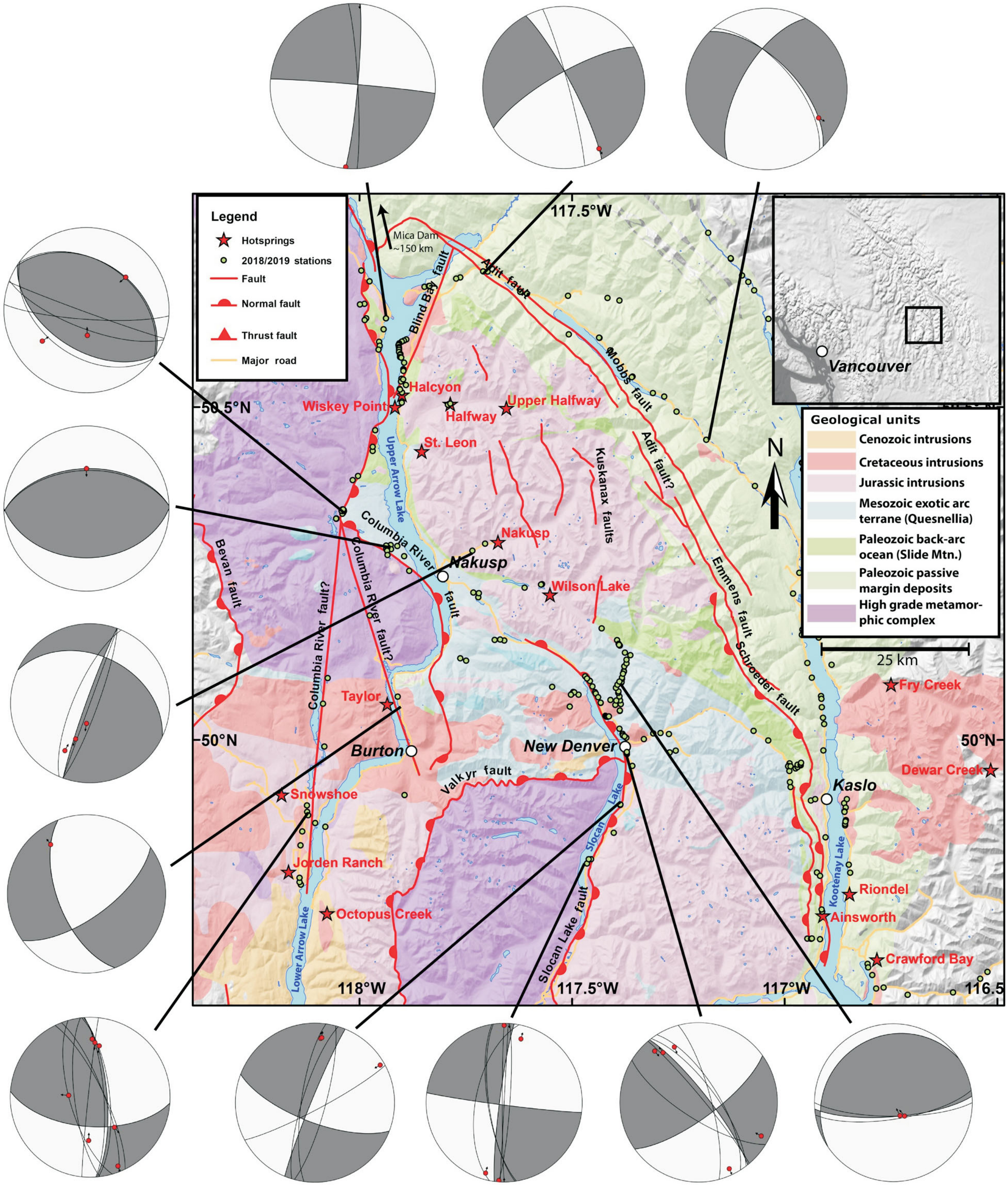

Figure 4. Geology of the West Kootenay region around Nakusp, British Columbia, after Cui et al. (2017). Lower-hemisphere stereonets show fault plane and slickenline orientations for subsets of stations. Compressional (P) and dilational (T) quadrants represent the average kinematics for each subset. Dextral kinematics were observed on the Columbia River fault and Slocan Lake fault, whereas reverse kinematics were observed in the transfer zone between Nakusp and New Denver.

The Columbia River fault (CRF) extends ~225 km southward from the Mica hydroelectric dam (52°N) to the hamlet of Burton on Lower Arrow Lake (50°N). At its northern end, it merges with the RMT fault in Kinbasket Lake (Figure 1b). At its southern end, mapped displacement across the fault gradually wanes to zero. Dip-slip displacements estimated on the basis of offset metamorphic isograds range from <1 km (Lemieux et al., 2003), 1–10 km (Lane, 1984), 15–80 km (Read and Brown, 1981) and 30 km (Parrish et al., 1988). Excavations during construction of the Revelstoke hydroelectric dam in the late 1970s provided the opportunity for detailed structural analysis of the brittle Columbia River fault. Lane (1984) measured the orientation of kinematic indicators at the damsite and at several sites along Highway 23 to the north of the dam. He concluded that primary displacement was extensional dip-slip, with a later phase of dextral strike-slip motion that was deemed insignificant. He also concluded that the right-hand step in the trace of the fault at the damsite might be associated with vertical axis rotation during dextral transpression. South of Revelstoke, the fault is parallel to Upper Arrow Lake, and a segment is exposed onshore on the east side of the lake immediately south of the Galena Bay ferry terminal. Near Halcyon Hot Spring, the fault swings southwest across the lake, and then trends parallel to the west side of Saddle Mountain before terminating at the hamlet of Burton (Figure 4).

The Slocan Lake–Champion Lakes fault system extends ~140 km from Summit Lake along Highway 6 between Nakusp and New Denver, south along Slocan Lake, through Castlegar, ending near Montrose. Interpreted deep seismic reflection profiles from the Lithoprobe project indicate that the fault zone dips shallowly east, penetrating the Moho (Cook et al., 1992). The Slocan Lake fault (SLF) is coincident with and overprints the surface trace of a broad zone of ductile deformation, the Valkyr shear zone, that arches over the Valhalla metamorphic complex to the east (Carr et al., 1987). South of Castlegar, the SLF becomes known as the Champion Lakes fault, and is mapped as a moderate to steeply (40–80°) east-dipping normal fault with a minimum of 1–2 km of offset (Corbett and Simony, 1984).

New Observations

Exposures of the brittle CRF and SLF described by previous authors were revisited in 2018 and 2019. At the Revelstoke damsite, both normal dip-slip and dextral strike-slip kinematic indicators were observed in a splay of the CRF, an observation consistent with that of Lane (1984). Farther south along the CRF, west of Nakusp, across Upper Arrow Lake, an outcrop of fault gouge originally interpreted as an exposure of the locally northwestward-striking CRF by Lemieux et al. (2003) was visited. The main schistose fabric of the footwall rock was observed to strike west, and is folded, forming small-amplitude south-vergent folds. Such deformation is consistent with reverse faulting during north-south shortening, rather than east-west extension. A similar reinterpretation was made at a nearby outcrop originally mapped by Thompson et al. (2004).

In the region between southern Upper Arrow Lake and northern Slocan Lake, a belt of east-west-trending faults and folds occurs at a high angle to the regional strike. Cretaceous and Cenozoic intrusions appear to be affected by this deformation: brittle faults are observed on the margins of plutons, and felsic sills that intruded along the primary cleavage planes are folded, forming south-verging folds (Figure 5b). Age constraints on these intrusions are sparse, so it is difficult to confirm the timing of this deformation, but it is at least post-Cretaceous, if not post-Eocene. This suggests that this region between the northern tip of the Slocan Lake fault and the southern tip of the Columbia River fault could be a restraining bend in a dextral system.

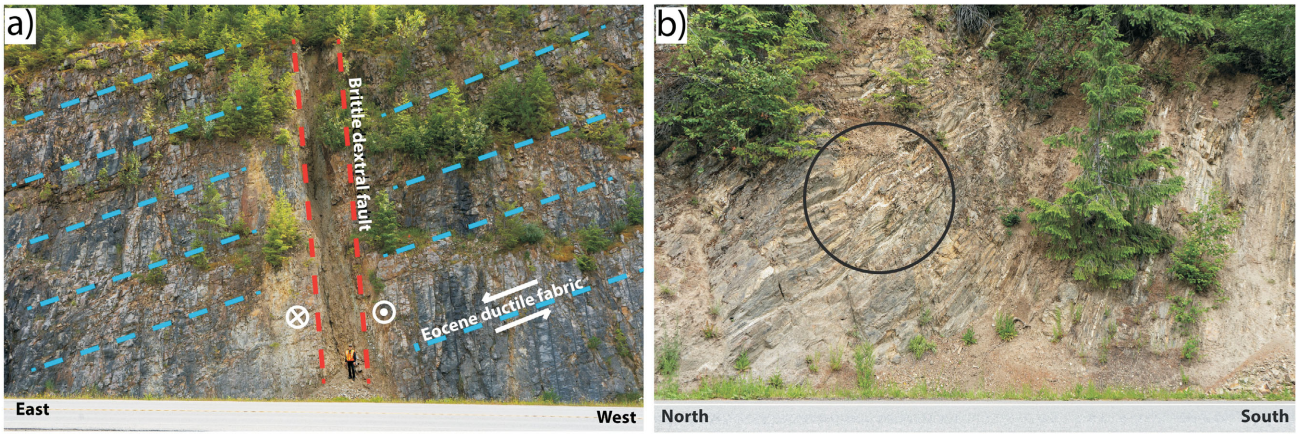

Figure 5. a) View south at outcrop on Highway 6 south of New Denver (lat. 49.8189°N, long. 117.4549°W). A 2 m wide subvertical brittle dextral fault oriented 172°/74° cuts across shallowly east-dipping (008°/31°) ductile fabric of the Slocan Lake fault/Valkyr shear zone. White encircled dot and "x" indicate motion towards and away from the viewer, respectively. **b)** View east at outcrop on Highway 6 north of New Denver (lat. 50.0555°N, long. 117.4323°W). Small, 20 cm wavelength, south-vergent folds are observed in felsic sills intruded parallel to the S_1 cleavage (oriented 278°/51°) of the Slocan phyllite. Circle is approximately 1.5 m wide.

At two locations along the east side of Slocan Lake, where the SLF crosses Highway 6, subhorizontal dextral slickenlines were observed on subvertical fault planes, in one case on a brittle fault that cuts through the Eocene-aged Ladybird granite (Carr, 1992), and on another that cuts at a high angle (Figure 5a) across the Eocene-aged ductile fabric of the Valkyr shear zone (Carr et al., 1987).

The Jurassic Kuskanax batholith, from which several thermal springs issue, has several north-south-striking faults mapped through its core, which appear to be subvertical based on their linear intersection with topography (Figure 4). Thompson et al. (2009) mapped these faults as dextrally offsetting roof pendants of Paleozoic metavolcanic rocks. It seems likely that these faults arose from the same transpression that caused dextral motion on the CRF.

The Southern Rocky Mountain Trench and the Redwall Fault

Background

There are seven thermal springs that occur along the eastern edge the southern Rocky Mountain Trench between the towns of Golden and Cranbrook (Figure 1b). Although the springs along the SRMT are not extremely hot, neither at depth nor at the surface (Grasby and Hutcheon, 2001), their close association with the Redwall fault (Figure 6) make them an interesting case study in structural controls of thermal springs in the Cordillera.

The Redwall fault is an enigmatic structure that has not been investigated in great detail since it was first mapped by Henderson (1954). Its surface trace extends from the hamlet of Edgeworth in the southern Rocky Mountain Trench, passing just east of Radium Hot Springs. It continues south along the Stanford Range, intersecting the Kootenay River at the Red Rock warm springs, before disappearing near Premier Lake. It has been suggested that it merges with the Lussier River fault to the south, which also hosts several thermal springs (Foo, 1979). The fault is subvertical for its entire length, leading several authors to conclude that it hosted either sinistral (Henderson, 1954) or dextral (Charlesworth, 1959) motion. More recently, Foo (1979) considered the Redwall fault to be a back-rotated thrust fault.

The Redwall Fault is so-named due to the striking red colour of the fault zone, caused by hematite oxidation (Figure 7b). The fault zone occurs in conjunction with a zone of subangular to subrounded, matrix-supported pebble to boulder conglomerate. This texture was originally interpreted to represent a zone of Cretaceous fault breccia (Henderson, 1954), but subsequent investigations have suggested that most of the breccia may be due to pre-Cretaceous evaporite-solution collapse (Stanton, 1966; Price, 2000), a theory supported by the proximity of extensive gypsum deposits (Henderson, 1954). Stratigraphic offsets, and evidence of shearing within the conglomerate, indicate that it has subsequently been reworked by faulting (of uncertain kinematics), following a décollement in the evaporites.

New Observations

Exposures of the Redwall fault near Radium, Invermere and Canal Flats were visited in 2019. Dextral kinematic indicators were observed at exposures of the fault immediately east of Radium Hot Springs, along the Westroc mine road east of Invermere, and at the Red Rock warm springs on the Kootenay River forest service road (Figures 6, 7). An outcrop on a forest service road southwest of Lussier Hot Springs displays red- and orange-stained microbreccia and abundant slickenlines. It appears to share similar characteristics with the Redwall fault, suggesting the Redwall fault does not continue into the Lussier River fault as previously suggested, but instead re-merges with the Rocky Mountain Trench fault to the south-southwest (Figure 6). Dextral kinematics were also observed near the south end of the Lussier River fault, on a small splay fault, indicating that dextral shear is distributed throughout the area.

It seems likely that the combination of primary permeability of the conglomerate, and secondary permeability of fractures, is what makes this single structure such a great host of thermal springs. It is clear from the oxidation of conglomerate clasts and surrounding matrix material, that the Redwall fault has a protracted history of hydrothermal flow. For example, at Red Rock warm springs, a large, layered tufa dome is present at the top of the cliff on the north side of the Kootenay River. The dome is bisected by the cliff such that the interior is visible, and no thermal water presently flows. Another tufa deposit occurs a few kilometres to the east along the forestry road. It is evident that hydrothermal flow on the Redwall fault is ephemeral, and that thermal springs have migrated along it through time.

Discussion

Fault Kinematics, Regional Stress and Fault Permeability

New field observations and structural measurements from this study have revealed three significant insights into the structural characteristics governing fluid flow on fault zones in the southeastern Canadian Cordillera: 1) the most recent brittle fabric developed in these fault zones includes subvertical, rather than shallowly dipping, shear surfaces; 2) dominant fault kinematics are dextral, and perhaps reflect a reactivation of older extensional structures; and 3) crosscutting relationships show that at least some of these faults were active after the Eocene. These insights are important for understanding where local zones of active

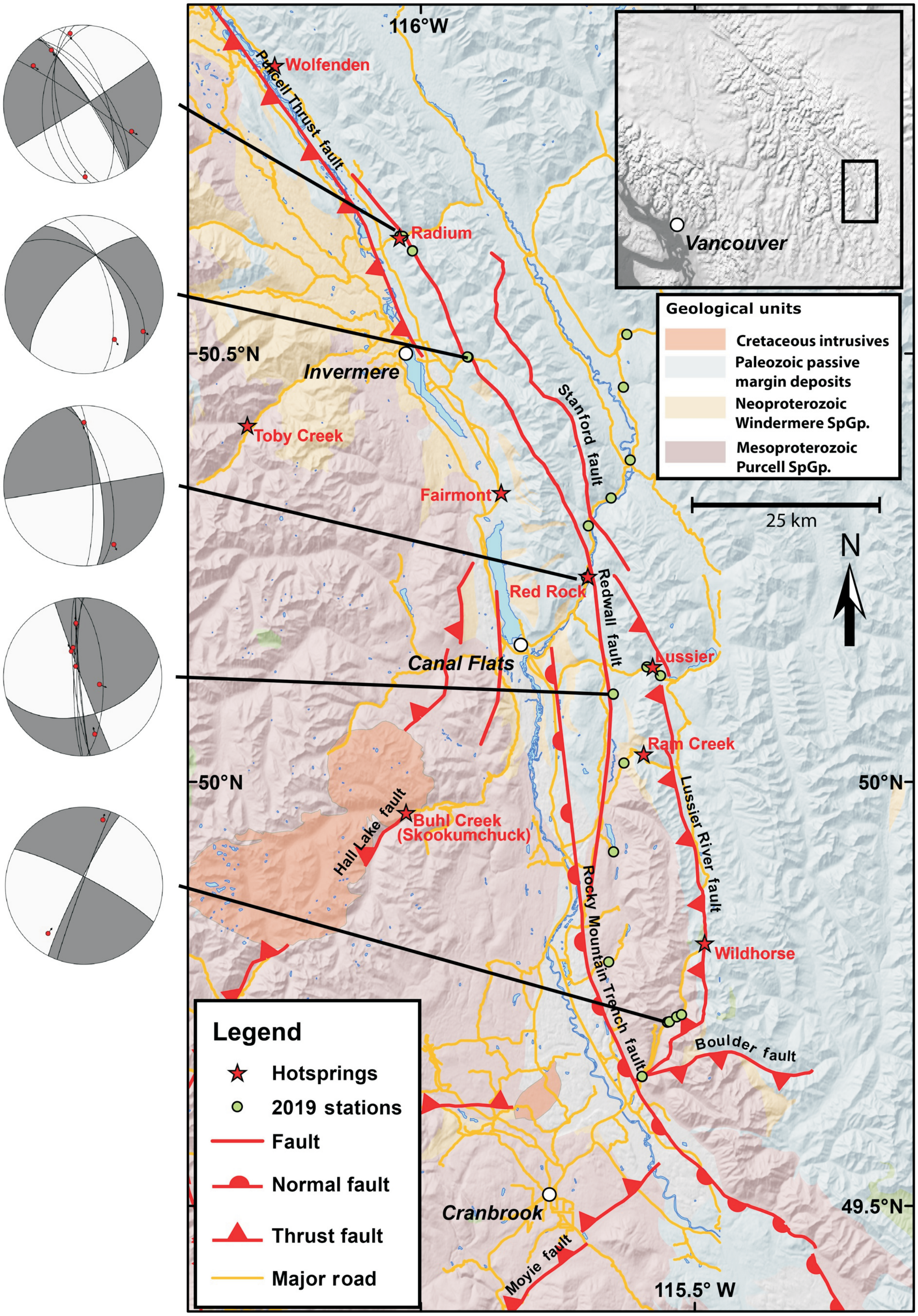

Figure 6. Geology of the southern Rocky Mountain Trench from Radium to Cranbrook, after Cui et al. (2017). Lower-hemisphere stereonets show fault plane and slickenline orientations for subsets of stations. Compressional (P) and dilational (T) quadrants represent the average kinematics for each subset. Dextral fault kinematics were observed on the Redwall fault at several locations. Abbreviation: SpGp., Supergroup.

Figure 7. a) Looking southwest at a tufa dome atop a cliff at the Red Rock warm springs on the Kootenay River (lat. 50.2389°N, long. 115.6963°W). No thermal water currently issues from the tufa dome. **b)** View south of the Redwall fault zone from Redstreak Mountain (lat. 50.6149°N, long. 116.0242°W). **c)** Looking east at a dextral fault plane oriented 304°/86° within the Redwall fault zone near Radium Hot Springs. Red arrow shows slickenline orientation (30°→119°).

slip, dilation and extension might facilitate the upward flow of thermal water.

In amagmatic, structurally controlled geothermal systems, the orientation of the current regional stress field relative to crustal faults is a critical factor in characterizing fault permeability. Faults and fractures that are oriented parallel to, or between 30° and 45° to the stress field, will either dilate or slip, respectively, thus permitting the flow of fluid (Sibson, 1994; Barton et al., 1995). Furthermore, it has been shown that local regions of extension (e.g., releasing bends), especially in active transpressional systems, are particularly favourable for fluid flow (Curewitz and Karson, 1997; Faulds and Hinz, 2015).

The current stress state of the crust within the Cordillera is not well constrained. The measurements that do exist are derived from the inversion of moment tensors for earthquakes of moment magnitude (M_w) 4 and greater (Ristau et al., 2007). Southeastern BC has a low level of seismic activity compared to the active margin on the west coast, and only four earthquakes of M_w 4 or greater have occurred since record-keeping began in 1976. However, it is noteworthy that all these earthquakes have focal mechanisms that are consistent with dextral strike-slip motion on roughly north-south-striking fault planes due to a north-northeast–south-southwest oriented S_{Hmax} (Ristau et al., 2007).

The alignment of the current S_{Hmax} vectors with the T-axes of 'beachball' plots derived from field measurements further suggests that the crustal earthquakes and observed fault kinematics are both manifestations of neotectonic strain in the Cordillera. In other words, it is possible that these faults are still active at a low level due to the current stress field. Thus, a rudimentary analysis of slip and dilation tendency (e.g., Meixner et al., 2018) can be performed, in order to determine which faults may be most permeable under the present stress field. Maximum dilation will occur on faults and fractures oriented parallel to S_{Hmax}, whereas maximum slip will occur on segments oriented 30–45° oblique to S_{Hmax} (Figure 8). Faults oriented perpendicular to S_{Hmax} will likely be less permeable. In Figure 8, the average orientation of the SLF, CRF, PTrF and RMTF are plot-

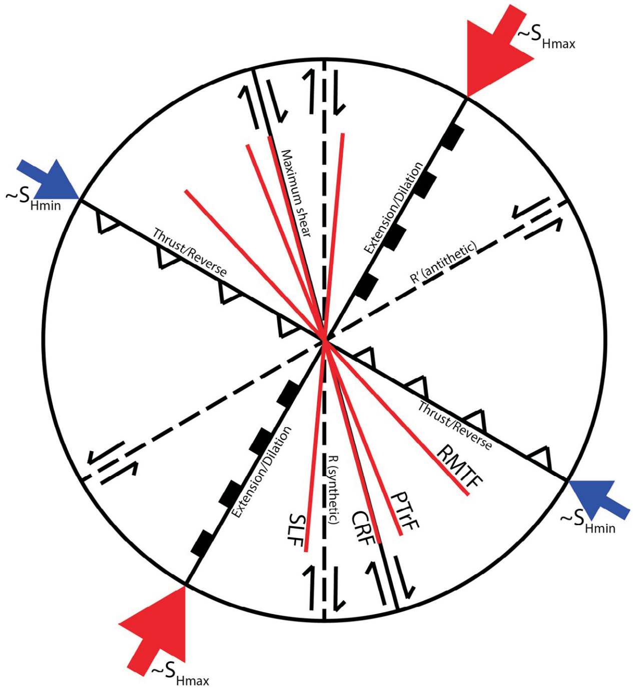

Figure 8. Strain ellipse for approximate S_{Hmax} (maximum horizontal compression) orientation in southeastern British Columbia (Ristau et al., 2007), and corresponding predicted modes of brittle deformation on faults and fractures. Average orientations of the Rocky Mountain Trench fault (RMTF), Purcell Trench fault (PTrF), Columbia River fault (CRF) and Slocan Lake fault (SLF) are shown for reference.

ted relative to the approximate S_{Hmax} orientation in the southeastern Cordillera (Ristau et al., 2007). In this configuration, the CRF, SLF and PTrF are oriented favourably for dextral slip, whereas the RMTF might experience more transpression. However, this simplistic representation of the regional strain does not capture local variability in fault geometry and stress orientations.

The Possibility of Blind Geothermal Systems

Convective geothermal systems with no modern surface manifestation (called blind systems) are known to occur in active geothermal fields throughout the world. For example, blind systems constitute nearly 40% of known systems in Nevada, and it is likely that far more are yet to be discovered (Faulds and Hinz, 2015). Conceptual models for these inconspicuous geothermal resources vary, but typically an impermeable layer blocks the ascent of fluids, or cold influx of shallow groundwater may dilute or divert a rising plume (Dobson, 2016). It is conceivable that similar blind systems exist in the Canadian Cordillera, masked by high infiltration rates of cold meteoric water. Precipitation rates are much higher in the Canadian Cordillera than in the arid Great Basin of the southwestern United States, and thick glaciogenic overburden may facilitate near-surface dispersion and dilution of any ascending plumes of geothermal brine. At least one blind geothermal system has been identified in the Canadian Cordillera, in the Bluebell mine at Riondel (Figure 4). During mine operation in 1956, workers encountered water approximately 20–30°C flowing from cracks at 90–1000 L/s at a depth of ~300 m below ground (Desrochers, 1992). This thermal water did not flow to the surface, or, if it did, it had already cooled below detectable levels. It is a statistical likelihood that other blind systems remain undiscovered elsewhere in the Canadian Cordillera, particularly due to the low "degree-of-exploration" (Coolbaugh et al., 2006) in the area. A first-order prediction of their location may come from identifying where local zones of slip and dilation occur, given the orientation of faults in the current crustal stress field.

Conclusions

Potential geothermal resources in southeastern British Columbia (BC) are likely amagmatic and rely on the deep circulation of thermal fluid along permeable fracture pathways. This regional-scale investigation of the structural settings of hydrothermal systems in southeastern BC has revealed a consistent pattern of dextral kinematics on brittle subvertical fault planes coincident with the surface traces of faults previously mapped as Eocene and Jura-Cretaceous in age; dextral kinematic indicators characterize the Rocky Mountain Trench fault near Valemount, the Redwall fault near Invermere, the Columbia River fault near Nakusp, and the Slocan Lake fault near New Denver. The timing of this transpressional deformation is constrained to post-Eocene, based on crosscutting relationships observed in Eocene-aged rocks. The north-northeast–south-southwest stress field required for these kinematics is consistent with the focal mechanisms of several crustal earthquakes that have occurred in the region, suggesting that transpressional strain has persisted from the Eocene to recent. Faults oriented at 30–45° to S_{Hmax} (maximum horizontal compression) are most likely to slip, thereby maintaining fault permeability. Likewise, fractures oriented parallel to S_{Hmax} are most likely to dilate and allow for fluid flow. Future geothermal exploration efforts in southeastern BC should focus on fault segments oriented favourably in the stress field, especially in light of the possibility of blind geothermal systems.

Acknowledgments

This research was conducted as part of the University of Alberta's Future Energy Systems project: Imaging, Characterizing and Modelling Canada's Geothermal Resources, a research initiative funded by the Canada First Research Excellence Fund. Additional support came from a Canada Graduate Scholarships-Masters Program award from the Natural Sciences and Engineering Research Council and a Hugh C. Morris Fellowship.

N. Van Camp, S. Johnson, J. Beales, N. Lee and K. Purdon are thanked for their efforts as field assistants. M. Hesketh is thanked for his help configuring the digital mapping software for tablet computers used in the field.

References

Agemar, T., Weber, J. and Schulz, R. (2014): Deep geothermal energy production in Germany; Energies, v. 7, p. 4397–4416, URL <https://doi.org/10.3390/en7074397> [November 2019].

Allen, D.M., Grasby, S.E. and Voormeij, D.A. (2006): Determining the circulation depth of thermal springs in the southern Rocky Mountain Trench, south-eastern British Columbia, Canada using geothermometry and borehole temperature logs; Hydrogeology Journal, v. 14, p. 159–172, URL <https://doi.org/10.1007/s10040-004-0428-z> [November 2019].

American Geological Institute (2003): Global GIS: volcanoes of the world; American Geological Institute, URL <https://earthworks.stanford.edu/catalog/harvard-glb-volc> [July 2019].

Armstrong, R.L. (1988): Mesozoic and early Cenozoic magmatic evolution of the Canadian Cordillera; *in* Processes in Continental Lithospheric Deformation, S.P. Clark, Jr., B.C. Birchfiel and J. Suppe (ed.), Geological Society of America Special Papers, v. 218, p. 55–92, URL <https://pubs.geoscienceworld.org/books/book/356/chapter/3796583/Mesozoic-and-early-Cenozoic-magmatic-evolution-of> [November 2019].

Barton, C.A., Zoback, M.D. and Moos, D. (1995): Fluid flow along potentially active faults in crystalline rock; Geology, v. 23, p. 683–686, URL <https://doi.org/10.1130/0091-7613(1995)023<0683:FFAPAF>2.3.CO;2>[November 2019].

Blackwell, D. and Richards, M. (2004): Geothermal map of North America; American Association of Petroleum Geologists, Product Code 423, scale 1:6 500 000.

Caine, J.S., Evans, J.P. and Forster, C.B. (1996): Fault zone architecture and permeability structure; Geology, v. 24, p. 1025–1028, URL <https://pubs.geoscienceworld.org/gsa/geology/article-abstract/24/11/1025/187969/Fault-zone-architecture-and-permeability-structure?redirectedFrom=fulltext> [November 2019].

Caron, M., Grasby, S.E. and Ryan, M.C. (2007): Spring geochemistry: a tool for mineral exploration in the south Nahanni River basin of the Mackenzie Mountains, Northwest Territories; *in* Mineral and Energy Resource Assessment of the Greater Nahanni Ecosystem Under Consideration for the Expansion of the Nahanni National Park Reserve, Northwest Territories, D.F. Wright, D. Lemkow and J.R. Harris (ed.), Geological Survey of Canada, Open File 5344, p. 31–74.

Carr, S.D. (1992): Tectonic setting and U-Pb geochronology of the Early Tertiary Ladybird Leucogranite Suite, Thor–Odin–Pinnacles area, southern Omineca Belt, British Columbia; Tectonics, v. 11, p. 258–278, URL <https://doi.org/10.1029/91TC01644> [November 2019].

Carr, S.D., Parrish, R.R. and Brown, R.L. (1987): Eocene structural development of the Valhalla Complex, southeastern British Columbia; Tectonics, v. 6, p. 175–196, URL <https://doi.org/10.1029/TC006i002p00175> [November 2019].

Chamberlain, V.E. and Lambert, R.St.J. (1985): Cordilleria, a newly defined Canadian microcontinent; Nature, v. 314, p. 707–713, URL <https://www.nature.com/articles/314707a0> [November 2019].

Chamberlain, V.E., Lambert, R.St.J. and Holland, J.G. (1985): Geochemistry and geochronology of the gneisses east of the southern Rocky Mountain Trench, near Valemount, British Columbia; Canadian Journal of Earth Sciences, v. 22, p. 980–991, URL <https://doi.org/10.1139/e85-103> [November 2019].

Charlesworth, H.A.K. (1959): Some suggestions on the structural development of the Rocky Mountains of Canada; Journal of the Alberta Society of Petroleum Geologists, v. 7, no. 11, p. 249–256.

Colpron, M. and Nelson, J. (2011): A digital atlas of terranes for the northern Cordillera; Yukon Geological Survey, URL <http://www.geology.gov.yk.ca/> [July 2019].

Cook, F.A., Varsek, J.L., Clowes, R.M., Kanasewich, E.R., Spencer, C.S., Parrish, R.R., Brown, R.L., Carr, S.D. and Johnson, B.J. (1992): LITHOPROBE crustal reflection cross section of the southern Canadian Cordillera, 1, Foreland thrust and fold belt to Fraser River Fault; Tectonics, v. 11, p. 12–35.

Coolbaugh, M.F., Raines, G.L., Zehner, R.S.E., Shevenell, L. and Williams, C.F. (2006): Prediction and discovery of new geothermal resources in the Great Basin: multiple evidence of a large undiscovered resource base; GRC Transactions, v. 30, p. 867–873.

Corbett, C.R. and Simony, P.S. (1984): The Champion Lake Fault in the Trail-Castlegar area of southeastern British Columbia; *in* Current Research, Part A, Geological Survey of Canada, Paper 84-1A, p. 103–104.

Cui, Y., Miller, D., Schiarizza, P. and Diakow, L.J. (2017): British Columbia digital geology; BC Ministry of Energy, Mines and Petroleum Resources, BC Geological Survey, Open File 2017-8, 9 p., URL <https://www2.gov.bc.ca/gov/content/industry/mineral-exploration-mining/british-columbia-geological-survey/geology/bcdigitalgeology> [July 2019].

Curewitz, D. and Karson, J.A. (1997): Structural settings of hydrothermal outflow: fracture permeability maintained by fault propagation and interaction; Journal of Volcanology and Geothermal Research, v. 79, p. 149–168, URL <https://doi.org/10.1016/S0377-0273(97)00027-9> [November 2019].

Davis, E.E. and Lewis, T.J. (1984): Heat flow in a back-arc environment: Intermontane and Omineca crystalline belts, southern Canadian Cordillera; Canadian Journal of Earth Sciences, v. 21, p. 715–726.

Desrochers, D.T. (1992): Geothermal feasibility study for the use of hot water near Riondel, British Columbia; Geological Survey of Canada, Open File 2502, 108 p.

Dobson, P.F. (2016): A review of exploration methods for discovering hidden geothermal systems; GRC Transactions, v. 40, p. 695–706.

Evenchick, C., McMechan, M.E., McNicoll, V.J. and Carr, S.D. (2007): A synthesis of the Jurassic–Cretaceous tectonic evolution of the central and southeastern Canadian Cordillera: Exploring links across the orogen; *in* Geological Society of America, Special Paper 433, p. 117–145.

Farquharson, N., Schubert, A. and Steiner, U. (2016): Geothermal energy in Munich (and beyond): a geothermal city case study; GRC Transactions, v. 40, p. 189–196.

Faulds, J.E. and Hinz, N.H. (2015): Favorable tectonic and structural settings of geothermal systems in the Great Basin Region, western USA: proxies for discovering blind geothermal systems; *in* Proceedings World Geothermal Congress 2015, April 19–25, 2015, Melbourne, Australia, p. 1–6.

Ferguson, G. and Grasby, S.E. (2011): Thermal springs and heat flow in North America; Geofluids, v. 11, p. 294–301, URL <https://doi.org/10.1111/j.1468-8123.2011.00339.x> [November 2019].

Foo, W.K. (1979): Evolution of transverse structures linking the Purcell Anticlinorium to the western Rocky Mountains near Canal Flats, British Columbia; M.Sc. thesis, Queen's University.

Gabrielse, H. (1985): Major dextral transcurrent displacements along the Northern Rocky Mountain Trench and related lineaments in north-central British Columbia; Geological Society of America Bulletin, v. 96, p. 1–14, URL <https://doi.org/10.1130/0016-7606(1985)96<1:MDTDAT>2.0.CO;2>[November 2019].

Gabrielse, H. and Yorath, C.J. (1991): Tectonic synthesis; Chapter 18 *in* Geology of the Cordilleran Orogen in Canada, H. Gabrielse and C.J. Yorath (ed.), Geological Survey of Canada, Geology of Canada, no. 4, p. 677–705 (also Geological Society of America, Geology of North America, v. G-2).

Gabrielse, H., Monger, J.W.H., Wheeler, J.O. and Yorath, C.J. (1991): Part A: morphogeological belts, tectonic assemblages and terranes; Chapter 2 *in* Geology of the Cordilleran Orogen in Canada, H. Gabrielse and C.J. Yorath (ed.), Geological Survey of Canada, Geology of Canada, no. 4, p. 15–28.

Ghomshei, M.M. (2007): Qualifying report on: a high-grade geothermal resource in the Canadian Rockies, Canoe Hot Springs, Valemount, British Columbia; internal company report prepared for Comstock Energy Inc.

Grasby, S.E. and Hutcheon, I. (2001): Controls on the distribution of thermal springs in the southern Canadian Cordillera; Canadian Journal of Earth Sciences, v. 38, p. 427–440, URL <https://www.researchgate.net/publication/249543830_Controls_on_the_distribution_of_thermal_springs_in_the_southern_Canadian_Cordillera> [November 2019].

Grasby, S., Allen, D.M., Bell, S., Chen, Z., Ferguson, G., Jessop, A., Kelman, M., Ko, M., Majorowicz, J., Moore, M., Raymond, J. and Therrien, R. (2012): Geothermal energy resource potential of Canada; Geological Survey of Canada, Open File 6914 (revised), 322 p., URL <http://publications.gc.ca/collections/collection_2013/rncan-nrcan/M183-2-6914-eng.pdf> [November 2019].

Green, N.L., Armstrong, R.L., Harakal, J.E., Souther, J.G. and Read, P.B. (1988): Eruptive history and K-Ar geochronology of the late Cenozoic Garibaldi volcanic belt, southwestern British Columbia; Geological Society of America Bulletin, v. 100, p. 563–579, URL <https://doi.org/10.1130/0016-7606(1988)100<0563:EHAKAG>2.3.CO;2> [November 2019].

Henderson, G.G.L. (1954): Geology of the Stanford Range of the Rocky Mountains; BC Ministry of Energy, Mines and Petroleum Resources, BC Geological Survey, Bulletin 35.

Hitchon, B. (1984): Geothermal gradients, hydrodynamics, and hydrocarbon occurrences, Alberta, Canada; American Association of Petroleum Geologists Bulletin, v. 68, p. 713–743.

Hyndman, R.D. and Lewis, T.J. (1995): Review: the thermal regime along the southern Canadian Cordillera Lithoprobe corridor; Canadian Journal of Earth Sciences, v. 32, p. 1611–1617, URL <https://doi.org/10.1139/e95-129> [November 2019].

Jessop, A.M., Ghomshei, M.M. and Drury, M.J. (1991): Geothermal energy in Canada; Geothermics, v. 20, p. 369–385.

Lane, L.S. (1984): Brittle deformation in the Columbia River fault zone near Revelstoke, southeastern British Columbia; Canadian Journal of Earth Sciences, v. 21, p. 584–598, URL <https://doi.org/10.1139/e84-063> [November 2019].

Lemieux, Y., Thompson, R.I. and Erdmer, P. (2003): Stratigraphy and structure of the Upper Arrow Lake area, southeastern British Columbia: new perspectives for the Columbia River Fault Zone; Geological Survey of Canada, Current Research 2003-A7, 11 p.

Lewis, T.J., Bentkowski, W.H. and Hyndman, R.D. (1992): Crustal temperatures near the Lithoprobe Southern Canadian Cordillera Transect; Canadian Journal of Earth Sciences, v. 29, p. 1197–1214, URL <https://doi.org/10.1139/e92-096> [November 2019].

Majorowicz, J. and Grasby, S.E. (2010): Heat flow, depth–temperature variations and stored thermal energy for enhanced geothermal systems in Canada; Journal of Geophysics and Engineering, v. 7, p. 232–241, URL <https://www.researchgate.net/publication/228077909_Heat_flow_depth-temperature_variations_and_stored_thermal_energy_for_enhanced_geothermal_systems_in_Canada> [November 2019].

McDonough, M.R. and Simony, P.S. (1988): Structural evolution of basement gneisses and Hadrynian cover, Bulldog Creek area, Rocky Mountains, British Columbia; Canadian Journal of Earth Sciences, v. 25, p. 1687–1702, URL <https://doi.org/10.1139/e88-159> [November 2019].

McDonough, M.R. and Simony, P.S. (1989): Valemount strain zone: a dextral oblique-slip thrust system linking the Rocky Mountain and Omineca belts of the southeastern Canadian Cordillera; Geology, v. 17, p. 237–240, URL <https://doi.org/10.1130/0091-7613(1989)017<0237:VSZADO>2.3.CO;2> [November 2019].

McMechan, M.E. (2000): Walker Creek fault zone, central Rocky Mountains, British Columbia-southern continuation of the Northern Rocky Mountain Trench fault zone; Canadian Journal of Earth Sciences, v. 37, p. 1259–1273, URL <https://doi.org/10.1139/e00-038> [November 2019].

Meixner, J., Grimmer, J.C., Becker, A., Schill, E. and Kohl, T. (2018): Comparison of different digital elevation models and satellite imagery for lineament analysis: implications for identification and spatial arrangement of fault zones in crystalline basement rocks of the southern Black Forest (Germany); Journal of Structural Geology, v. 108, p. 256–268, URL <https://doi.org/10.1016/j.jsg.2017.11.006> [November 2019].

Meixner, J., Schill, E., Grimmer, J.C., Gaucher, E., Kohl, T. and Klingler, P. (2016): Structural control of geothermal reservoirs in extensional tectonic settings: an example from the Upper Rhine Graben; Journal of Structural Geology, v. 82, p. 1–15, URL <https://doi.org/10.1016/j.jsg.2015.11.003> [November 2019].

Moeck, I.S. (2014): Catalog of geothermal play types based on geologic controls; Renewable and Sustainable Energy Reviews, v. 37, p. 867–882, URL <https://doi.org/10.1016/j.rser.2014.05.032> [November 2019].

Moreno, D., Lopez-Sanchez, J., Blessent, D. and Raymond, J. (2018): Fault characterization and heat-transfer modeling to the Northwest of Nevado del Ruiz Volcano; Journal of South American Earth Sciences, v. 88, p. 50–63, URL <https://doi.org/10.1016/j.jsames.2018.08.008> [November 2019].

Murphy, D.C. (1990): Direct evidence for dextral strike-slip displacement from mylonites in the southern Rocky Mountain Trench near Valemount, British Columbia; *in* Current Research, Part E, Geological Survey of Canada, Paper 90-1E, p. 91–96.

Murphy, D.C. (2007): Geology: Canoe River; Geological Survey of Canada, "A" Series Map 2110A, scale 1:250 000.

Parrish, R.R. and Wheeler, J.O. (1983): A U-Pb zircon age from the Kuskanax batholith, southeastern British Columbia; Canadian Journal of Earth Sciences, v. 20, p. 1751–1756, URL <https://doi.org/10.1139/e83-165> [November 2019].

Parrish, R.R., Carr, S.D. and Parkinson, D.L. (1988): Eocene extensional tectonics and geochronology of the Southern Omineca Belt, British Columbia and Washington; Tectonics, v. 7, p. 181–212, URL <https://doi.org/10.1029/TC007i002p00181> [November 2019].

Price, R.A. (1981): The Cordilleran foreland thrust and fold belt in the southern Canadian Rocky Mountains; Geological Society London, Special Publications, v. 9, p. 427–448, URL <https://www.researchgate.net/publication/249548179_The_Cordilleran_foreland_thrust_and_fold_belt_in_the_southern_Canadian_Rocky_Mountains> [November 2019].

Price, R.A. (2000): The southern Canadian Rockies: evolution of a foreland thrust and fold belt; GeoCanada Conference, May 29–June 2, 2000, Calgary, Alberta, Field Trip Guidebook, 244 p.

Price, R.A. and Carmichael, D.M. (1986): Geometric test for Late Cretaceous-Paleogene intracontinental transform faulting in the Canadian Cordillera; Geology, v. 14, p. 468–471, URL <https://doi.org/10.1130/0091-7613(1986)14<468:GTFLCI>2.0.CO;2> [November 2019].

Read, B. and Brown, R.L. (1981): Columbia River fault zone: southeastern margin of the Shuswap and Monashee complexes, southern British Columbia; Canadian Journal of Earth Sciences, v. 18, p. 1127–1145.

Reyes, A.G. (2015): Low-temperature geothermal reserves in New Zealand; Geothermics, v. 56, p. 138–161, URL <https://doi.org/10.1016/j.geothermics.2015.04.004> [November 2019].

Ristau, J., Rogers, G.C. and Cassidy, J.F. (2007): Stress in western Canada from regional moment tensor analysis; Canadian Journal of Earth Sciences, v. 44, p. 127–148, URL <https://doi.org/10.1139/e06-057> [November 2019].

Roddick, J.A. (1967): Tintina Trench; Journal of Geology, v. 75, p. 23–33.

Rogers, G.C., Ellis, R.M. and Hasegawa, H.S. (1980): The McNaughton Lake earthquake of May 14, 1978; Bulletin of the Seismological Society of America, v. 70, p. 1771–1786.

Ross, G.M. (1991): Precambrian basement in the Canadian Cordillera: an introduction; Canadian Journal of Earth Sciences, v. 28, p. 1133–1139, URL <https://doi.org/10.1139/e91-103> [November 2019].

Sibson, H. (1994): Crustal stress, faulting and fluid flow; *in* Geofluids: Origin, Migration, and Evolution of Fluids in Sedimentary Basins, Geological Society Special Publication 78, p. 69–84.

Stanton, R.J., Jr. (1966): The solution brecciation process; Geological Society of America Bulletin, v. 77, p. 843–848, URL <https://doi.org/10.1130/0016-7606(1966)77[843:TSBP]2.0.CO;2> [November 2019].

Struik, L.C. (1993): Intersecting intracontinental Tertiary transform fault systems in the North American Cordillera; Canadian Journal of Earth Sciences, v. 30, p. 1262–1274, URL <https://doi.org/10.1139/e93-108> [November 2019].

Thompson, R.I., Glombick, P. and Lemieux, Y. (2004): Geology: Mount Fosthall; Geological Survey of Canada, Open File 4377, scale 1:50 000.

Thompson, R.I., Lemieux, Y., Glombick, P. and Dhesi, P. (2009): Geology: St. Leon Creek; Geological Survey of Canada, Open File 6185, scale 1:50 000.

van der Velden, A.J. and Cook, F.A. (1996): Structure and tectonic development of the southern Rocky Mountain trench; Tectonics, v. 15, p. 517–544, URL <https://doi.org/10.1029/95TC03288> [November 2019].

Vollmer, F.W. (2019): Orient: spherical projection and orientation data analysis software user manual; Frederick W. Vollmer, URL <https://www.frederickvollmer.com/orient/download/Orient_User_Manual.pdf> [July 2019].

Woodsworth, G. and Woodsworth, D. (2014): Hot Springs of Western Canada: A Complete Guide, 3rd Edition; Gordon Soules Book Publishers, West Vancouver, British Columbia, 303 p.

Installation of a Purpose-Built Groundwater Monitoring Well Network to Characterize Groundwater Methane in the Peace Region, Northeastern British Columbia (NTS 093P/09–16, 094A/01–08)

B. Ladd, The University of British Columbia, Vancouver, British Columbia, bladd@eoas.ubc.ca

A.G. Cahill, The Lyell Centre, Heriot-Watt University, Edinburgh, Scotland

M. Goetz, The University of British Columbia, Vancouver, British Columbia

A. Allen, Simon Fraser University, Burnaby, British Columbia

L. Welch, British Columbia Oil and Gas Commission, Kelowna, British Columbia

B. Mayer, University of Calgary, Calgary, Alberta

C. van Geloven, British Columbia Ministry of Forests, Lands, Natural Resource Operations and Rural Development, Prince George, British Columbia

D. Kirste, Simon Fraser University, Burnaby, British Columbia

R.D. Beckie, The University of British Columbia, Vancouver, British Columbia

Ladd, B., Cahill, A.G., Goetz, M., Allen, A., Welch, L., Mayer, B., van Geloven, C., Kirste, D. and Beckie, R.D. (2020): Installation of a purpose-built groundwater monitoring well network to characterize groundwater methane in the Peace Region, northeastern British Columbia (NTS 093P/09–16, 094A/01–08); *in* Geoscience BC Summary of Activities 2019: Energy and Water, Geoscience BC, Report 2020-02, p. 131–144.

Introduction

Western Canada has experienced rapid oil and gas development over recent decades, particularly involving the exploitation of unconventional resources such as shale oil and gas. In British Columbia (BC) alone, approximately 15 000 wells have been drilled since 2000, 64% of which are hydraulically fractured natural gas wells (BC Oil and Gas Commission, 2018; E. Sandl, pers. comm., 2018). Concerns about environmental impacts from such activities have grown alongside this development, with a particular focus on fugitive gas migration (Council of Canadian Academies, 2014). Environmental impacts associated with fugitive gas, composed primarily of methane (Darrah et al., 2014), include degradation of groundwater quality (Kelly et al., 1985; Van Stempvoort et al., 2005; Cahill et al., 2017), explosive risk and greenhouse gas emissions (Vidic et al., 2013; Bachu, 2017; Forde et al., 2019a).

In particular, groundwater methane is a topic of great interest and concern in areas of intensive oil and gas development. Due to methane's ubiquitous natural presence in groundwater, it can be difficult to delineate and distinguish dissolved methane sources and distribution, and assess if elevated levels bear any relation to oil and gas activity (e.g., Osborn et al., 2011a, b; Saba and Orzechowski, 2011). This is particularly true in regions where little or no baseline information is available, which is typically the case. Current limitations in resolving the origins and nature of elevated dissolved methane in regions of petroleum resource development include 1) a lack of baseline data and 2) general reliance on domestic well data, which may introduce data biases and uncertainties (e.g., missing or unreliable well construction information, unregulated sample collection points, maintenance issues, etc.). Overall, great uncertainty persists regarding the true extent of impacts from fugitive gas due to a lack of conclusive data and systematic monitoring.

In this project, the aim is to address such uncertainties in the Peace Region of northeastern BC, an area of intensive historical conventional and ongoing unconventional development. Key aims of the project are to determine current groundwater quality in the Peace Region with a specific focus on the distribution, concentration and origin of dissolved methane. Ultimately, the project aims to characterize groundwater systems across the Peace Region and provide insights to assess potential anthropogenic impacts to groundwater from oil and gas development and related activities. The key aims will be achieved by 1) installing a dedicated, targeted, purpose-built and scientifically designed groundwater monitoring well network proximal to energy wells for collecting samples to be analyzed for all major aqueous chemistry parameters (including dissolved

---

This publication is also available, free of charge, as colour digital files in Adobe Acrobat® PDF format from the Geoscience BC website: http://www.geosciencebc.com/updates/summary-of-activities/.

methane), and 2) installing a portion of these wells in areas distant from oil and gas development to assess baseline groundwater conditions in the region. Through the drilling (including high-resolution geological logging and sampling of sediment core) and installation of a groundwater well network followed by regular, systematic geochemical sampling, data will be collected to determine methane distribution and origin and its potential relationship to oil and gas activity in the Peace Region. Additionally, as a legacy the installed groundwater monitoring infrastructure will be available for ongoing assessment of cumulative effects in the context of continued natural gas development in the region over the coming decades and provide a platform for future research activities.

This paper describes the installation of the network and initial sampling program. Installation began in the summer of 2018 and was completed in the fall of 2019, with a total of 29 monitoring wells in the network. The first round of groundwater samples from the completed network was collected after the final wells were drilled and developed; laboratory analytical results are currently pending. This paper explains the design, planning and logistics for the monitoring network installation, with details on project stages including a) desktop studies, field reconnaissance and permission process; b) drilling logistics and methods, core logging and sampling, and well completions; and c) water sampling conducted to date and plans for the future. The data collected from these wells will complement existing domestic and monitoring well data, and will be used to create a comprehensive, robust and scientifically defensible groundwater dataset from which policy and regulation can be informed.

Background

Fugitive Gas Migration

Fugitive gas migration occurs when natural gas from target or intermediate formations is unintentionally mobilized in the subsurface during oil and gas development activities; usually as a result of wellbore integrity failure or other casing issues (Cahill et al., 2019). Fugitive gas primarily consists of methane (Darrah et al., 2014) and can travel to ground surface where it may manifest as bubbling around the wellhead or stressed vegetation, or often, go undetected (Briskin, 2015; Province of British Columbia, 2018; Forde et al., 2019b). The number of oil and gas wells with gas migration in Canada is not well known, but the current documented percentage of gas migration occurrences is 0.58% (out of more than 25 000 wells) and 0.73% (out of more than 300 000 wells) in BC and Alberta, respectively (Bachu, 2017; E. Sandl, pers. comm., 2018). Current documentation may not reflect the true extent of the problem, as identifying gas migration is often dependent on the effort and resources spent to do so (e.g., Forde et al., 2019b). Fugitive gas migration is an existing and potentially growing problem, which requires somewhat urgent consideration as the population of active and inactive energy wells across Canada and the world continues to grow, and age, with more cases of leakage almost certain to manifest in the future.

Geological Setting

The project area is a subset of the Peace Region, which is located in the northeastern portion of BC, with an average elevation of 610 m. The Peace Region is situated primarily within the Alberta Plateau of the Interior Plains physiographic subdivision of BC (Holland, 1964). In this area, the plateau has been dissected by the Peace River forming the Peace River Lowland (Holland, 1964). It is of low relief with flat to gently undulating terrain. It includes the communities of Fort St. John to the north, Dawson Creek to the east and Chetwynd to the west and Tumbler Ridge to the south of the project area. There are six main rivers flowing within the area. They are the Peace, Pine, Murray, Halfway, Beatton and Kiskatinaw rivers, serving to divide both the overall Peace Region and the project area into five watersheds. The climate is characterized by long cold winters and short warm summers with mean annual temperatures below 0ºC in the northern valleys. The average annual precipitation is estimated between 350 and 500 mm with approximately 200 mm falling as snow (Schaefer, 1978; Environment and Climate Change Canada, 2019). The region soils are dominated by luvisols, and land cover consists of forest, grasslands and cultivated areas. Topography includes mountainous terrain in the south and west, capturing a small portion of the Rocky Mountain Foothills, and a relatively flat area in the northeastern portion (Holland, 1964; Catto, 1991).

Installation of the Energy and Environment Research Initiative Groundwater Monitoring Well Network

Overview

Commencing in August 2018 and ending in September of 2019, a regional groundwater monitoring well network was installed in the Peace Region consisting of 29 monitoring well stations (Figure 1). The project area was chosen as a subset of the Peace Region that encompassed major population centres and areas of both historical and ongoing resource development. Drilling and associated activities were contracted to third parties, and all other work was carried out primarily by The University of British Columbia’s Energy and Environment Research Initiative (EERI) Monitoring Well Installation Project (MWIP) team, in particular M.Sc. students M. Goetz and A. Allen. Significant support was provided by BC Oil and Gas Commission, BC Ministry of Forests, Lands, Natural Resource Operations and Rural Development, and Geoscience BC personnel. Local

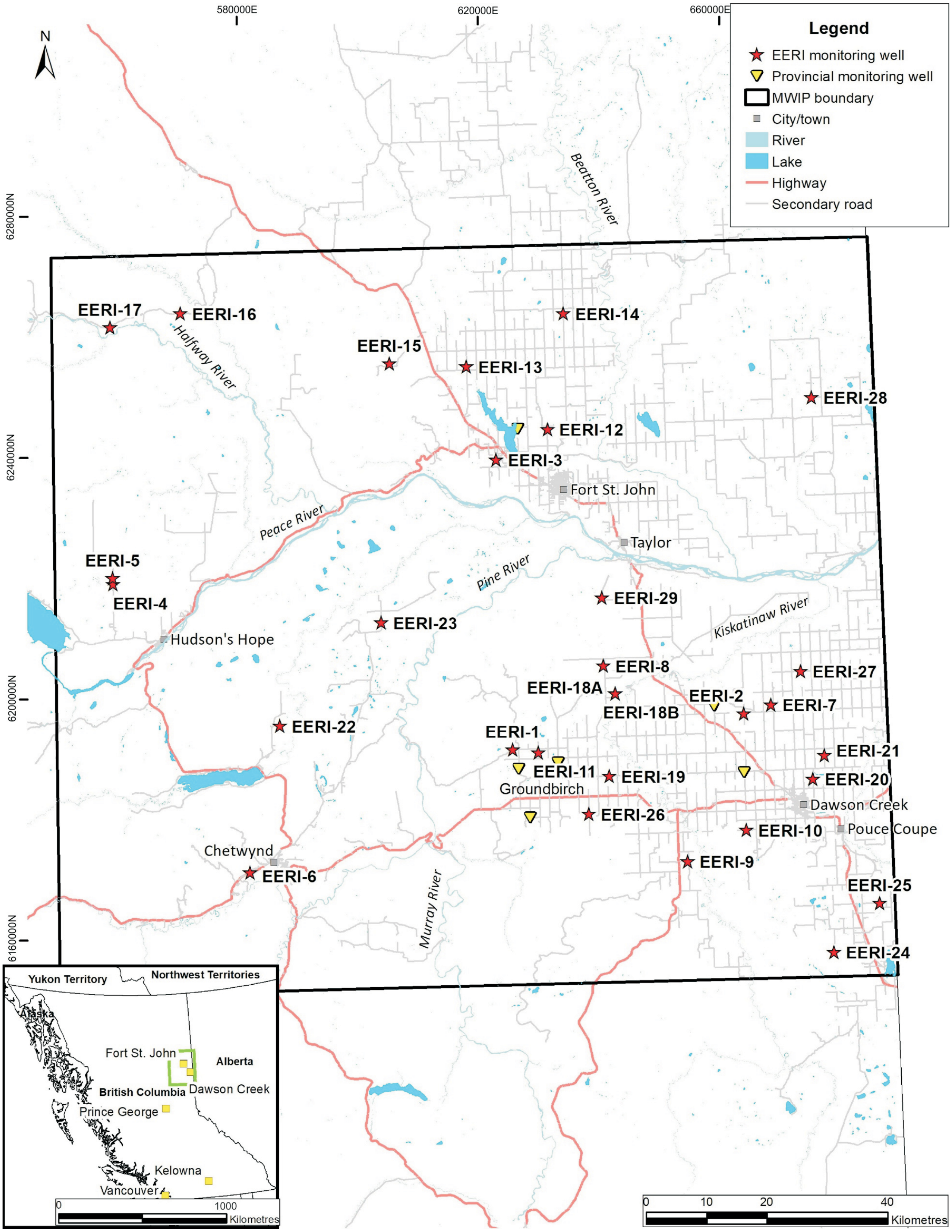

Figure 1. The project area (black outline) and the locations of the 29 Energy and Environment Research Initiative (EERI) monitoring well stations (stars). Abbreviation: MWIP, Monitoring Well Installation Project.

community and government consultation was sought throughout.

Table 1 provides an overview of well details, including location, completion details, and relation to nearby energy and domestic water wells. Nine out of the 29 monitoring well stations are baseline stations, whose purpose are to provide data for understanding the baseline groundwater geochemistry in the region, including determining baseline levels of dissolved methane. The other 20 stations are proximal stations, which were positioned in areas of high energy well density based on a set of criteria. One station, EERI-18, contains two wells, EERI-18A and EERI-18B, which have different well installations, the second to accommodate a Westbay Instruments (Westbay) installation (see 'Westbay Multilevel Installations' section for more detail). Further information on site selection and installation of the well network will be reported in subsequent sections.

Pre-Drilling Planning and Preparation

Well Selection Criteria

At the outset of the project, the MWIP team set a goal of approximately 30 wells for the network in consideration of budgetary and other logistical factors. A general framework was developed as a starting point to locate well sites, with the foremost stipulation being that about one third of the wells would be baseline wells and the rest proximal wells. General criteria that applied to all wells included factors such as

- regional coverage within the project area—spatially and geologically representative;
- hydrogeological considerations such as targeting topographic lows in order to capture representative samples of more evolved groundwater in nonrecharge areas, locating paleovalleys and targeting areas of low drift thickness, and using available domestic and provincial groundwater well resources to increase chances of penetrating groundwater zones;
- reasonable road access and preference for sites on Crown land for ease of permissions and continued long-term access; and
- consideration of provincial observation well locations to avoid duplication.

The main criteria used to classify wells as baseline and proximal were the distance from the nearest energy well and the density of energy wells within a 3 km radius. For baseline wells, the following initial criteria were used as guidelines for siting the wells:

- primarily, preferably no closer than 1.5 km from an energy well, with 1 km as a stricter bound (one groundwater monitoring well became an exception to this criterion);
- secondarily, energy well density should be kept to a minimum in the surrounding 3 km radius; and
- an effort was made to select a portion of baseline sites within 0.5–1 km distance from an existing water well (domestic or provincial), which was assigned a paired status as opposed to an unpaired status.

For proximal wells, the following initial criteria were used as guidelines for siting the wells:

- less than 400 m from the surveyed location of an energy wellhead (as close as logistically possible);
- maximize energy well density in the surrounding 3 km radius; and
- as much as possible, given the small quantity of EERI proximal groundwater monitoring wells compared to the number of energy wells in the project area (approximately 7580 energy wells; BC Oil and Gas Commission, 2019), the closest energy wells to EERI proximal wells should provide a general representation of the overall energy well population in the project area, which includes consideration of well status (active/abandoned/orphaned), orientation (vertical/horizontal/deviated), and fluid type (gas/oil/mix), as well as future development.

Even though great effort was given to adhere to the above guidelines, some exceptions were made due to the need to balance other criteria and field logistics. Site selection quickly became limited due to a preference for installation on Crown land. Installing wells on accessible public land severely restricted the area available to locate wells in the project area. If Ministry of Transportation and Infrastructure (MOTI) Crown land was selected, it was generally just the width of a roadway corridor. The presence of buried and overhead utilities and pipelines also restricted the use of other available locations. An additional key constraint for determining monitoring well location involved ensuring appropriate space and terrain for a drill rig to operate, which further limited options.

Wells were drilled over the course of the project in five campaigns, each following the general work plan of desktop spatial analysis, ground-truthing, acquiring permissions, drilling and installation. Each campaign informed subsequent activities, in an iterative manner such that the project progress became more streamlined. The first two campaigns focused on drilling baseline wells, and the latter three focused on proximal wells.

Spatial Analysis GIS Process

Prior to each of the five MWIP drilling campaigns, preliminary locations that conformed to the criteria above were assessed using a GIS-based spatial analysis. Esri's ArcMap was used to visualize data from various sources. Domestic well data, and surficial attributes (such as hydrology, roads, elevation contours) were retrieved from the BC Data Catalogue (DataBC, 2019a). Groundwater geochemical data, used primarily for baseline well site selection, was taken

Table 1. Overview of well details for the 29 groundwater monitoring well stations in the Energy and Environment Research Initiative (EERI) network. Type refers to whether the well adheres to baseline or proximal criteria.

Well name	Latitude	Longitude	Type	Total depth (mbgl)	Static water level (mbtoc)	Completion type	Screened lithology	Energy wells within 3 km radius	Proximity to nearest energy well (m)	Proximity to nearest domestic water well (m)	Nearest energy well orientation	Nearest energy well fluid type	Nearest energy well status	Nearest energy well: hydraulic fracturing?
EERI-1	55.8543	-120.9896	Baseline	53	Artesian	ML	Sandy gravel/sand	3	1557	60	N/a	N/a	N/a	N/a
EERI-2	55.8962	-120.3754	Baseline	46	28.86	ML w/ SG	Shale	37	1331	609	N/a	N/a	N/a	N/a
EERI-3	56.2864	-121.0119	Baseline	54	46.55	SS	Sandstone/ shale/siltstone	4	883	197	N/a	N/a	N/a	N/a
EERI-4	56.1129	-122.0418	Baseline	49	36.31	ML w/ SG	Siltstone/ sandy gravel and diamict/ silt-sand	1	2378	680	N/a	N/a	N/a	N/a
EERI-5	56.122	-122.0425	Baseline	78	23.8	SS w/ pump[1]	Shale	0	3263	120	N/a	N/a	N/a	N/a
EERI-6	55.6804	-121.6906	Baseline	103	23.64	OH	Shale/ sandstone	1	1666	405	N/a	N/a	N/a	N/a
EERI-7	55.9083	-120.3026	Proximal	39	29.24	SS	Sandstone	48	70	1481	Vertical	Gas	Aban.	No
EERI-8	55.9749	-120.7433	Proximal	30	28.84	SS	Sandstone/ shale	55	438	2631	Vertical and horizontal	Gas	Active	Yes
EERI-9	55.6795	-120.5379	Proximal	70	21.52	SS	Sandy gravel	39	214	2008	Horizontal	Gas	Active	Yes
EERI-10	55.7231	-120.3799	Baseline	32	8.34	SS	Shale	6	1729	723	N/a	N/a	N/a	N/a
EERI-11	55.8486	-120.9226	Proximal	77	Artesian	WB	Sandstone/ siltstone	21	321	960	Vertical	Gas	Active	Yes
EERI-12	56.3294	-120.8716	Proximal	38.5	29.65	SS	Sandstone	42	265	696	Vertical	Mixed oil and gas	Aban.	No
EERI-13	56.4262	-121.0851	Proximal	69	26.17	SS	Sandstone	52	175	719	Vertical	Oil	Susp.	Yes
EERI-14	56.5008	-120.8204	Proximal	65	52.38	SS	Shale	46	541	737	Vertical	Gas	Active	Yes
EERI-15	56.4335	-121.2908	Proximal	87	56.97	SS	Sandstone	20	183	5085	Horizontal	Gas	Cased	No

Table 1 (continued)

Well name	Latitude	Longitude	Type	Total depth (mbgl)	Static water level (mbtoc)	Completion type	Screened lithology	Energy wells within 3 km radius	Proximity to nearest energy well (m)	Proximity to nearest domestic water well (m)	Nearest energy well orientation	Nearest energy well fluid type	Nearest energy well status	Nearest energy well: hydraulic fracturing?
EERI-16	56.5148	-121.8509	Proximal	42	10.95	SS	Mudstone	21	106	647	Horizontal	Gas	Aban.	Yes
EERI-17	56.4956	-122.0409	Proximal	23	9.92	ML w/ SG	Sandy gravel	13	152	853	Deviated	Gas	Active	Yes
EERI18A	55.9329	-120.7145	Proximal	21	3.73	SS	Sandstone/ siltstone	108	140	2396	Horizontal	Gas	Active	Yes
EERI-18B	55.9329	-120.7145	Proximal	47	4.02	WB	Sandstone/ siltstone	108	140	2396	Horizontal	Gas	Active	Yes
EERI-19	55.8105	-120.7375	Proximal	69	38.41	SS	Mudstone	42	345	543	Horizontal	Gas	Active	Yes
EERI-20	55.7952	-120.1988	Proximal	99	9.67	SS	Mudstone	23	97	2250	Horizontal	Gas	Active	Yes
EERI-21	55.8296	-120.1665	Proximal	106	65.91	SS	Conglomerate	49	173	1246	Horizontal	Gas	Active	Yes
EERI-22	55.8979	-121.6046	Baseline	44.5	17.38	SS	Sandy gravel	0	7498	424	N/a	N/a	N/a	N/a
EERI-23	56.0484	-121.3304	Proximal	40	22.65	SS	Shale	15	259	879	Deviated	Gas	Susp.	Yes
EERI-24	55.5362	-120.162	Proximal	87.2	55.96	SS	Siltstone/ mudstone	40	180	1493	Horizontal	Gas	Active	Yes
EERI-25	55.6062	-120.037	Baseline	38.4	9.71	SS	Diamict	50	1132	881	N/a	N/a	N/a	N/a
EERI-26	55.755	-120.794	Proximal	18.3	4.77	SS	Mudstone/fine sandstone	13	180	1260	Horizontal	Gas	Susp.	Yes
EERI-27	55.9562	-120.22	Proximal	123	>93	SS	Sandy silt/ clay	23	306	2812	Horizontal	Gas	Active	Yes
EERI-28	56.3627	-120.162	Proximal	57.9	44.15	SS	Shale	29	301	3588	Vertical	Undefined	Aban.	No
EERI-29	56.0765	-120.741	Proximal	59.4	36.79	SS	Silt/sand, lesser diamict	32	198	2891	Horizontal	Gas	Active	Yes

[1] Permanent pump installed due to agreement with landowner

Abbreviations: Aban., abandoned; mbgl, metres below ground level; mbtoc, metres below top of casing; ML, multilevel well; N/a, not available; OH, open hole in bedrock; SG, soil-gas port; SS, single screen well; Susp., suspended; WB, Westbay Instruments multilevel well from a database of groundwater in northeastern BC, which has been compiled as part of the Northeast BC Aquifer Characterization Project (D. Kirste, work in progress). Energy well data was retrieved from the BC Oil and Gas Commission Open Data Portal (BC Oil and Gas Commission, 2019). Drift thickness and bedrock topography were obtained from Hickin and Fournier's (2011) preliminary maps. Unfortunately, the drift thickness data did not cover the entire MWIP area and the drilling results from this program did not match the small scale preliminary interpretation. Data from drilling programs such as this will be useful for refining the understanding of local bedrock topography and drift thickness.

Buffers for the domestic water wells and energy wells were subsequently created in ArcMap using their corresponding criteria's radii. The energy well density was determined and visualized using the BC Data Catalogue's British Columbia Geographic System (BCGS) 1:5000 scale grid (DataBC, 2019b) to create grid cells of 9 km^2, in combination with the 'Spatial Join' tool to attribute the number of energy wells per grid cell. The grid cell size of 9 km^2 was chosen in order to be large enough to capture multiple energy well pads in a single cell, and to be reproducible using a publicly accessible grid.

Buried Utilities and Ground-Truthing

Two methods were used in concert to determine viability of a site based on the location of underground utilities:

1) AccuMap™ oil and gas mapping software (IHS Markit, 2019) was used to visualize locations of high-pressure oil and gas pipelines. For monitoring well site selection, a minimum distance of 30 m from pipeline right-of-ways would have to be maintained to avoid requiring a Proximity Agreement from the corresponding energy company. This agreement requires some lead time, and was avoided in all site selection cases in order to reduce logistical delay.
2) The online BC 1 Call website (https://www.bc1c.ca/) was used to locate all underground utility types. Tickets were submitted online for each location of interest, BC 1 Call identified any buried lines and the appropriate utility companies were subsequently contacted for permission. Types of utilities included telecommunication lines, underground ducts, low-pressure gas pipelines and high-pressure energy pipelines.

Prospective locations that passed the buried utility investigation graduated to ground-truthing. Team members travelled to these locations for field reconnaissance/verification. Field reconnaissance involved checking to see if 1) the location was viable for drill rig access, 2) overhead utilities would interfere with the drill rig and 3) the surface area was large enough for drill rig set up. During these trips, any landowners located in proximity of potential drill locations were contacted in person to be informed of drilling activities. This process typically took place a couple weeks before the drilling campaign commenced and was combined with prior drilling campaigns when possible.

Permissions Process

The MWIP permission requirements can broadly be divided into four categories according to land ownership type:

- the majority of monitoring wells are located on MOTI land, which are narrow strips (<20 m) of Crown land between public roads and the property lines of private landowners, these monitoring well locations required a permit from MOTI prior to drilling;
- two monitoring wells are located on Crown community pasture land (EERI-8 and EERI-24), these locations did not require any official permission;
- several monitoring wells are located adjacent to energy well pad access roads, which are on private land; these locations required verbal, email and/or contractual permission from both the private landowner and the energy well pad owner; these locations were selected to ensure some monitoring well locations attained the greatest proximity to energy wells;
- two monitoring wells are located on private land (EERI-4 and EERI-5), owned by a ranch owner with long-term involvement in other EERI-related research.

Challenges and Limitations

Key limitations which inhibited installing monitoring wells in ideal locations included

- buried utilities: areas of interest with high density energy wells typically had a high density of buried high-pressure pipelines, many of which run parallel to public roads, under MOTI land;
- incompatible land use/cover: power lines, steep/narrow ditches and marshes prevent drill rig access and set up, which requires a relatively flat, dry working space with a minimum footprint of 25 by 4 m; these hazards were not always evident when siting the wells using Google Earth;
- private land ownership: most private landowners were in support of monitoring well installation on or adjacent to their property; in some instances, landowners did not support monitoring well installation on their property for various personal reasons (e.g., noise while drilling, stigma of potentially contaminating or exhausting their water source);
- energy well pads: energy well pads are typically 100–200 m in length and width, and drilling directly on the well pads was not viable due to additional permissions needed from the well pad owner; finding sites off well pads but within the 400 m criterion was challenging, as the selection area was limited and factors such as roadside ditches, fences, tree cover and other terrain obstacles further restricted options.

Drilling Campaigns

The timeline of the five campaigns conducted for the EERI groundwater monitoring well network is shown in Table 2. Drilling contractors, drilling method and installation types evolved throughout the project as the MWIP team learned from challenges and new information during each campaign. Overall, installations were designed to conform to provincial groundwater monitoring well standards, with two boreholes reserved for Westbay multilevel installations. The latter were chosen during drilling, based on geological, hydrogeological and geographic suitability. In some cases, other multilevel installations and soil gas ports were constructed (Table 1). A summary of each drilling campaign is given below.

Campaign 1: The first four baseline monitoring wells were installed using a truck-mounted Terra Sonic International TSi 150T SONIC rig. A primary reason for choosing a sonic drilling method was that sonic coring results in highly preserved intact samples from unconsolidated sediments, which show the highest level of lithological detail. However, a major limitation was the TSi drill's inability to advance through the top portion of weathered bedrock (e.g., incompetent shale), which is a common lithology in the

Table 2. Timeline of the five drilling campaigns conducted over the course of the project.

Drilling campaign	Dates	EERI wells completed	Drilling methods
1	Aug. 22–Sep. 1, 2018	1 to 4	Sonic
2	Feb. 3–12, 2019	5 to 6	Air rotary
3	Jun. 19–Jul. 7, 2019	7 to 14	Sonic, air rotary, diamond (HQ core)
4	Aug. 1–20, 2019	15 to 23	Sonic, air rotary, diamond (HQ core)
5	Sep. 15–27, 2019	24 to 29	Sonic, air rotary

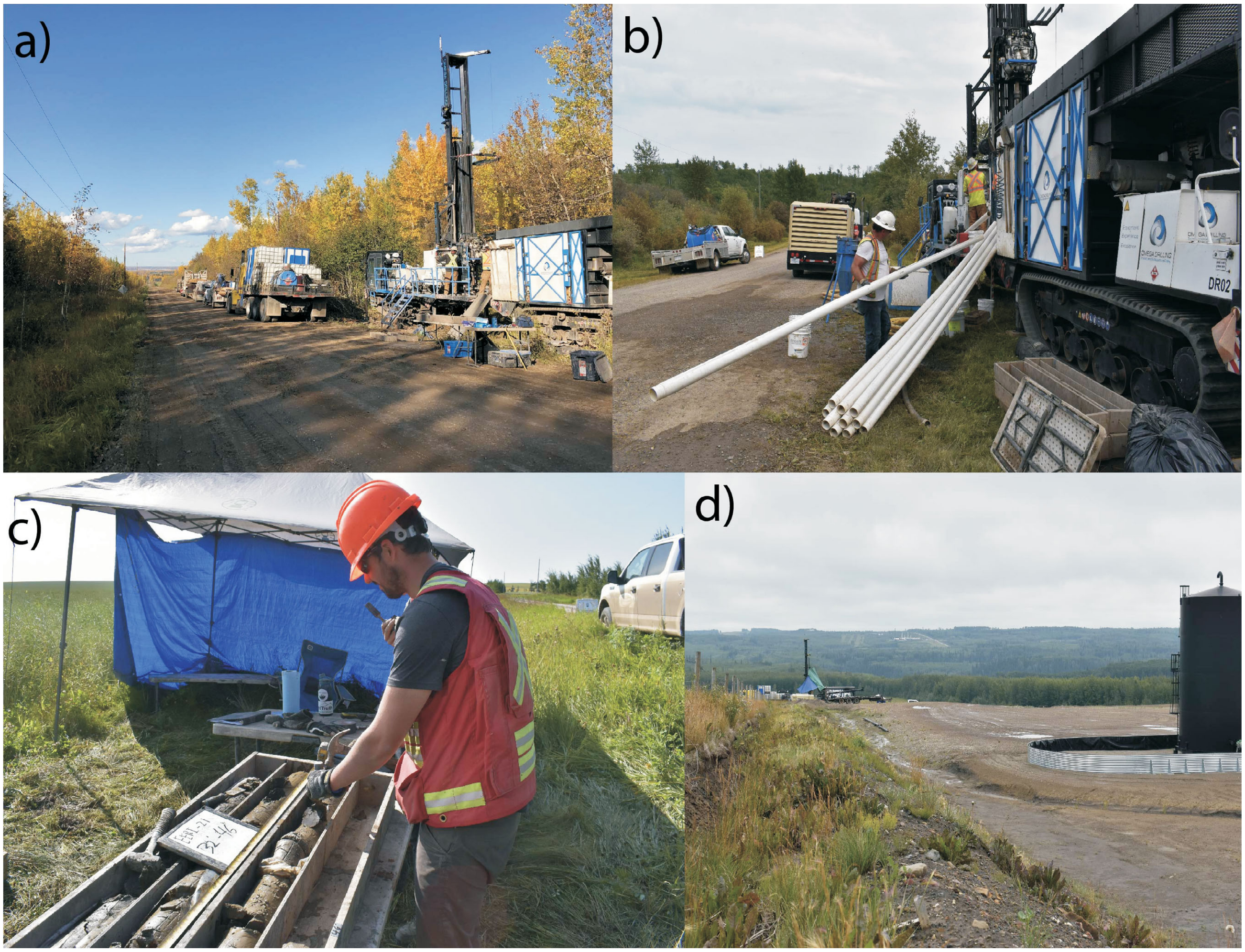

Figure 2. Drilling activity during the summer of 2019 campaigns: **a)** drilling at well EERI-26; **b)** installing polyvinyl chloride (PVC) pipe at well EERI-15; **c)** logging core at well EERI-21; **d)** view of well EERI-18 drill site (left-middle) with well pad in the foreground (right) and a natural gas processing plant in the distant background (on the ridge).

Peace Region. As a result, target depths were not reached in most cases on this campaign.

Campaign 2: This campaign used a truck-mounted Ingersoll Rand TH60 air rotary rig with bedrock coring abilities. Air rotary drilling was chosen in response to the difficulties encountered during the previous campaign with sonic methods in bedrock. This campaign was plagued by unexpected extreme cold conditions (a severe cold weather warning issued the day prior to commencement leading to temperatures lower than –40°C), which resulted in several delays and only two monitoring wells being completed out of a planned four. Monitoring well installations for this campaign were 17.8 cm (7 in.) steel surface casing through overburden, with the bedrock section left open-hole due to cold weather–related complications. Leaving the boreholes open-hole allowed flexibility in constructing other well installations at a later date in better conditions.

Campaign 3: Eight monitoring wells were installed using a Boart Longyear LS™600 track-mounted sonic rig. This drill rig was capable of switching between sonic, air rotary and diamond core drilling methods, which was found to be very advantageous for this project. The track mount was an additional advantage, providing more flexibility to drill in variable terrain. The typical drilling sequence was drilling sonic through the overburden and then through the incompetent bedrock (which the LS 600 was able to do). If no productive formation had been encountered at that point, the driller would switch to air rotary to continue through competent bedrock in search of productive fracture networks. Monitoring well installations for this campaign were single screen 7.6 cm (3 in.) PVC pipe, with 3–6 m of screen. The only exception was EERI-11, which was drilled with HQ diamond coring through bedrock and left open-hole for subsequent Westbay installation.

Campaigns 4 and 5: Due to the success of the third campaign, the same drill rig, method and equipment were used for these remaining campaigns. The majority of completed monitoring wells were single screen 7.6 cm (3 in.) PVC pipe, with 3–9 m of screen. The exceptions were EERI-17, which had an additional shallow gas tubing port; EERI-18B, which was drilled with the same method as EERI-11, HQ diamond coring and left open-hole for subsequent Westbay installation; and EERI-22, which used 10.2 cm (4 in.) PVC pipe instead of 7.6 cm (3 in.) PVC pipe due to material limitations.

Well Development

All wells, except for the two artesian wells and the two wells slated for Westbay installations, were developed during campaigns 3–5 using the airlift method with a trailer-mounted air compressor. Wells were screened with 20-slot PVC screen of varying length depending on the well and geology, generally 3 m, and sand packed with 10/20 filter sand to a minimum of 3 m above the top of the screen. Well development typically took place between two and ten days following the well completion, and wells were airlifted for a minimum of two hours or until the water was clear or clarity was no longer seen to be improving noticeably.

Geology and Core Sampling

The well-documented heterogeneity and unpredictability of the Peace Region Quaternary geology presents a great challenge for shallow monitoring well installation. The main confining units, diamict (Figure 3a) and glaciolacustrine clay (Figure 3b), were the most common sediment types encountered. Drill core was logged throughout drill-

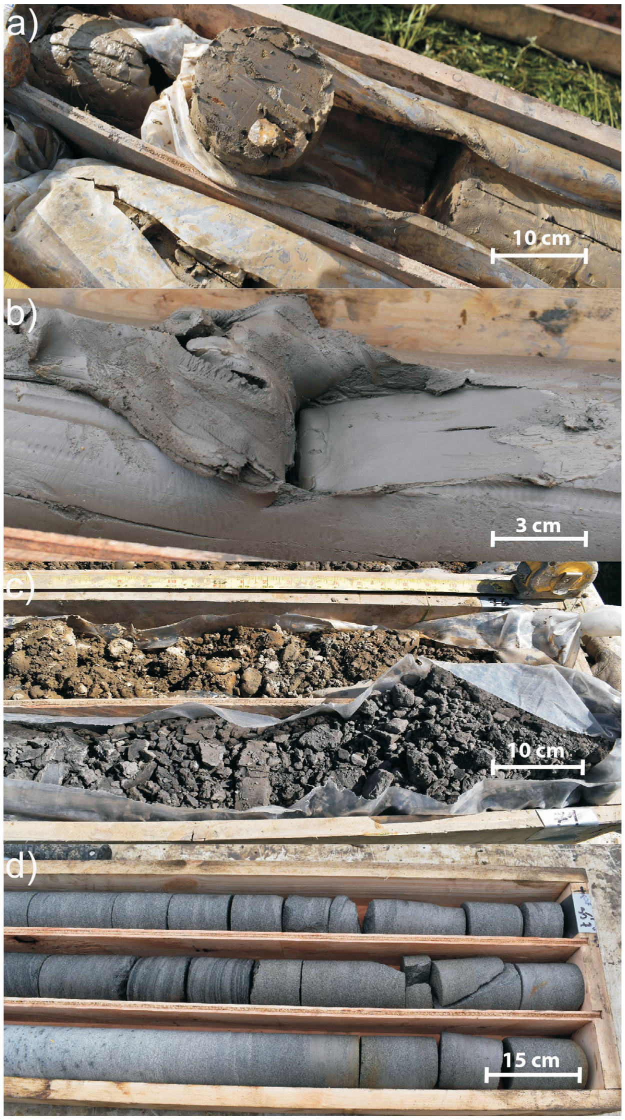

Figure 3. Examples of common lithologies found during drilling in the Peace Region: **a)** core from well EERI-12 showing silty, fine sand diamict (10 metres below ground level [mbgl]); **b)** core from well EERI-9 showing glaciolacustrine clay (15 mbgl); **c)** core from well EERI-17 showing sandy gravel overlying bedrock shale (contact at 23 mbgl); and **d)** HQ core from well EERI-18B showing Dunvegan Formation medium sandstone (11 mbgl).

ing and the EERI monitoring wells were generally screened in four different lithologies:

1) sand/silt: this was the least common screened lithology, as these sediments were encountered at very shallow depths and were not very productive in most cases;
2) gravel: gravel units were typically encountered near the centre of paleovalleys, and sometimes overlaid the top of the bedrock as a basal gravel (Figure 3c);
3) sandstone/conglomerate: the most productive monitoring wells were screened in Dunvegan Formation sandstone (Figure 3d), which is a common aquifer source for domestic wells in the Peace Region; conglomerate was only encountered in EERI-21;
4) shale/siltstone/mudstone: monitoring wells in these bedrock units have moderate to low yield, and they were typically screened because a more permeable unit had not been encountered.

Sediment core samples were taken of every EERI monitoring well during logging and are in the process of being analyzed in the Aqueous Geochemistry Lab in Earth Sciences at Simon Fraser University (Burnaby, BC) and the ALS-Geochemistry laboratory (North Vancouver, BC) in order to determine a depth profile of various physical and chemical properties. During air rotary drilling, grab samples of drill cuttings were collected directly from the cyclone. Samples for targeted sequential extractions and cation exchange capacity analysis were taken every 1.5 m (5 ft.), and samples for permeability and grain size distribution analysis were taken once per hydrostratigraphic unit. Select samples will be used for X-ray diffraction and energy-dispersive X-ray spectrometry analysis.

Figure 4. Installation of Westbay Instruments system in well EERI-11. The foreground shows the layout of the packers (green) and casing with measurement and pumping ports (white casing) during installation.

Westbay Multilevel Installations

Westbay systems provide the advantage of allowing data collection at multiple discrete depths within a single well. These systems consist of a series of alternating packers and casing that contain hydraulic head measurement and pumping ports (Figure 4). The packers hydraulically seal different zones from one another, whereas the measurement and pumping ports allow direct connection with the formation in the designated monitoring zone. Westbay systems therefore allow the attainment of high-resolution vertical profiles of chemistry and hydraulics, which is advantageous in tracking variations and sources of methane concentrations in groundwater and delineating flow systems and vertical hydraulic connectivity. Two proximal wells were completed with Westbay systems in the Groundbirch area west of Dawson Creek, EERI-11 and EERI-18B (Figure 1). Based on lithological logs and wireline geophysics data from EERI-11, the Westbay systems were designed by the MWIP team and Westbay personnel and customized to each borehole (Table 3). The MWIP team assisted with installation and were trained on the Westbay sampling system. The first set of samples from these wells was collected in late September.

Groundwater Sampling

Groundwater samples will be collected from the newly installed EERI monitoring well network three times per year: early spring, summer and late autumn. To date, one full

Table 3. Depth of zones, measurement ports and pumping ports for Westbay Instruments systems in wells EERI-11 and EERI-18B. All depth measurements are metres below ground level.

Zone	Measurement port depth	Pumping port depth	Top of zone	Bottom of zone
		EERI-11		
1	70.9	72.4	70.7	76.6
2	64.8	66.3	64.6	66.7
3	58.7	60.2	58.5	60.6
4	55.7	57.2	55.4	57.6
5	52.6	54.1	52.4	54.5
6	49.6	51.1	49.4	51.5
7	45.0	46.5	44.8	48.5
		EERI-18B		
1	39.7	41.2	39.5	41.6
2	33.6	35.1	33.4	35.5
3	25.4	26.9	25.1	27.3
4	19.6	21.1	19.3	21.5
5	16.5	18.0	16.3	18.4

sampling round has been carried out for the entire network (with the exception of EERI-27), which occurred late September–early October 2019, and wells that were installed at the beginning of the drilling process have had additional samples taken at earlier dates (Table 4). Water samples are obtained using either a Grundfos MP1 groundwater sampling pump or a Waterra Pumps Limited D-25 inertial foot valve when necessary.

Sample types, collection methods and analytical methodology are summarized in Table 5. Groundwater field parameters including temperature, pH, electrical conductivity

Table 4. Record of number and date of sampling rounds taken at each well in the Energy and Environment Research Initiative groundwater monitoring well network. Sampling rounds generally consist of measuring field parameters (temperature, pH, electrical conductivity, dissolved oxygen and oxidation-reduction potential) and collecting water samples for analyses described in Table 5. Where sampling deviated from this collection regime, a note is made.

Well name	Number of sampling rounds	Sample dates	Notes
EERI-1	3	Dec. 4, 2018; Jun. 28, 2019; Sep. 28, 2019	Laboratory analysis of major and minor cations, trace metals, and anions completed for first two sample suites collected. Other analyses and third round sample analyses are in progress.
EERI-2	3	Dec. 4, 2018; Jun. 26, 2019; Oct. 1, 2019	Same as above.
EERI-3	2	Jun. 28, 2019; Oct. 7, 2019	Laboratory analysis of major and minor cations, trace metals, and anions completed for first sample suite collected. Other analyses and second round sample analyses are in progress.
EERI-4	2	Dec. 5, 2018; Oct. 5, 2019	Same as above.
EERI-5	2	Jul. 2, 2019; Oct. 5, 2019	Same as above.
EERI-6	2	Jun. 27, 2019; Oct. 4, 2019	Same as above.
EERI-7	2	Jun. 26, 2019; Oct. 1, 2019	Same as above.
EERI-8	2	Jul. 8, 2019; Sep. 30, 2019	Same as above.
EERI-9	2	Jul. 10, 2019; Oct. 3, 2019	Same as above.
EERI-10	2	Jul. 8, 2019; Oct. 3, 2019	Same as above.
EERI-11	1	Sep. 27, 2019	Westbay multilevel well. Water sample suite taken, but system precludes use of flow-through cell for field parameters to be measured. Laboratory analysis is in progress.
EERI-12	2	Jul. 8, 2019; Sep. 29, 2019	Laboratory analysis of major and minor cations, trace metals, and anions completed for first sample suite collected. Other analyses and second round sample analyses are in progress.
EERI-13	2	Jul. 8, 2019; Oct. 6, 2019	Same as above.
EERI-14	2	Jul. 12, 2019; Oct. 6, 2019	Same as above.
EERI-15	1	Oct. 6, 2019	Laboratory analysis is in progress.
EERI-16	1	Oct. 7, 2019	Laboratory analysis is in progress.
EERI-17	1	Oct. 7, 2019	Laboratory analysis is in progress.
EERI-18A	1	Sep. 30, 2019	Laboratory analysis is in progress.
EERI-18B	1	Sep. 25, 2019	Westbay multilevel well. Water sample suite taken, but system precludes use of flow-through cell for field parameters to be measured. Laboratory analysis is in progress.
EERI-19	1	Oct. 3, 2019	Laboratory analysis is in progress.
EERI-20	1	Oct. 2, 2019	Laboratory analysis is in progress.
EERI-21	1	Oct. 1, 2019	Laboratory analysis is in progress.
EERI-22	1	Oct. 5, 2019	Laboratory analysis is in progress.
EERI-23	1	Oct. 5, 2019	Laboratory analysis is in progress.
EERI-24	1	Oct. 2, 2019	Laboratory analysis is in progress.
EERI-25	1	Oct. 2, 2019	Laboratory analysis is in progress.
EERI-26	1	Oct. 3, 2019	Laboratory analysis is in progress.
EERI-27	0	N/a	Water level was deeper than the length of the pump; field parameters and samples unable to be collected.
EERI-28	1	Sep. 29, 2019	Laboratory analysis is in progress.
EERI-29	1	Sep. 30, 2019	Laboratory analysis is in progress.

Abbreviations: N/a, not available; Westbay, Westbay Instruments.

Table 5. Summary of sample types, collection method and analysis methodology to be performed three times per year for all wells in the Energy and Environment Research Initiative groundwater monitoring well network.

Sample type	Collection/preservation	Analysis method	Analytical results
ICP	125 mL volume, filtered and preserved with ultra-pure nitric acid to 2% by volume	Inductively coupled plasma–emission spectrometry (ICP-ES) and inductively coupled plasma–mass spectrometry (ICP-MS)	Major and minor cations, trace metals, rare-earth elements
Anions	250 mL volume, filtered	Ion chromatography, alkalinity titration, isotope ratio mass spectrometry	Alkalinty (as HCO_3^-), major anions, oxygen-deuterium isotopes
Carbon-14	500 mL volume, filtered, preserved with 2 mL of 5M NaOH and $SrCl_2$	Accelerator mass spectrometry (^{14}C), isotope ratio mass spectrometry ($\delta^{13}C$)	$\delta^{13}C$ and $\delta^{14}C$
^3H	1000 mL volume, filtered, no headspace	Liquid scintillation counting (LSC)	Tritium enrichment
Dissolved gas and soil gas	~250 mL volume, collected in evacuated sample vials containing bactericide	Numerous	He, H_2, O_2, N_2, CH_4, CO_2, H_2S, and higher chain hydrocarbons, as well as $\delta^{13}C$ for CH_4 and CO_2

Abbreviation: M, molar

(EC), dissolved oxygen (DO), and oxidation-reduction potential were measured onsite using Thermo Scientific™ Orion™ 3-Star digital multiparameter meters during sample collection. Alkalinity (as HCO_3^-) was measured by titration using a Mettler Toledo EasyPlus Titrator Easy pH system.

Filtered samples were collected from each well for anion and elemental analysis, as well as determining stable isotopes of water, dissolved gases, tritium and carbon-14 contents. Groundwater samples for major and minor cations, trace metals and rare-earth elements were preserved with ultra-pure nitric acid (HNO_3) to 2% by volume, for analysis by inductively coupled plasma–emission spectrometry (ICP-ES) and inductively coupled plasma–mass spectrometry (ICP-MS) at the Applied Geochemistry group (AGg) Chemistry Lab at the University of Calgary (Calgary, AB). Separate samples remained unacidified for analysis of major and minor anions by ion chromatography (IC), dating analysis of tritium isotope (^3H) by liquid scintillation counting (LSC), and analysis for deuterium and oxygen isotope composition by isotope ratio mass spectrometry (IRMS). Additional samples were preserved by precipitation of dissolved inorganic carbon as $SrCO_3$ through the addition of NaOH and $SrCl_2$ for analysis of $\delta^{13}C$ using IRMS. Groundwater samples will be analyzed for tritium content by enrichment and low level proportional counting at the University of Miami's Tritium Laboratory (Miami, Florida). Samples for carbon-14 will be determined by accelerator mass spectrometry (AMS) and $\delta^{13}C$ by IRMS at the André E. Lalonde Accelerator Mass Spectrometry Laboratory at the University of Ottawa (Ottawa, ON). Dissolved gas and soil-gas samples were analyzed at the AGg Chemistry Lab using gas chromatography (Varian, Inc. CP4800 portable gas chromatograph). Isotopes of carbon and hydrogen of methane were analyzed by isotope ratio mass spectrometer (Thermo Electron Corporation Finnigan™ MAT 253 with Thermo Scientific TRACE™ GC Ultra gas chromatograph and GC IsoLink™ IRMS system), at the University of Calgary's Isotope Science Laboratory.

Conclusions

The EERI groundwater monitoring well network was successfully completed with 29 monitoring stations installed across the Peace Region. These stations were strategically located to monitor both baseline groundwater geochemistry and groundwater geochemistry in proximity to oil and gas activity. Initial groundwater samples of the entire network were collected in September to October 2019, with continued sampling planned to occur three times each year. Furthermore, the EERI groundwater monitoring well network will provide opportunities for collaboration and use by other parties who may benefit from the network. The EERI wells have already been used for downhole seismic studies (Monahan et al., 2020), and there is current interest in future work with other partners. Thus, the EERI groundwater monitoring well network will not only allow ongoing data collection to better understand groundwater methane in the context of oil and gas development, but also offer a resource for additional scientific studies in the Peace Region.

Acknowledgments

The authors gratefully acknowledge:

- L. Smith for peer-reviewing this manuscript;
- C. and E. Weder for granting permission to drill EERI-4 and EERI-5 on their property;
- the combined efforts of BC Ministry of Forests, Lands, Natural Resource Operations and Rural Development and Ministry of Transportation and Infrastructure for granting permissions to drill on roadside Crown land; and

- the many private landowners and energy companies who gave their approvals to drill next to their lands.

This work was funded by Geoscience BC and the BC Oil and Gas Commission.

References

Bachu, S. (2017): Analysis of gas leakage occurrence along wells in Alberta, Canada, from a GHG perspective – gas migration outside well casing; International Journal of Greenhouse Gas Control, v. 61, p. 146–154, URL <https://doi.org/10.1016/j.ijggc.2017.04.003> [November 2019].

BC Oil and Gas Commission (2018): Number of wells drilled in B.C. - annually; BC Oil and Gas Commission, URL <https://iris.bcogc.ca/reports/rwservlet?prd_ogcr9960a> [September 2018].

BC Oil and Gas Commission (2019): Open data portal; BC Oil and Gas Commission, web application, <https://data-bcogc.opendata.arcgis.com/> [April 2019].

Briskin, J. (2015): Potential impacts of hydraulic fracturing for oil and gas on drinking water resources; Groundwater, v. 53, no. 1, p. 19–21.

Cahill, A.G., Beckie, R.D., Goetz, M., Allen, A., Ladd, B., Welch, L., Kirste, D., Mayer, B. and van Geloven, C. (2019): Characterizing dissolved methane in groundwater in the Peace Region, northeastern British Columbia, using a regional, dedicated, groundwater monitoring well network; *in* Geoscience BC Summary of Activities 2018: Energy and Water, Geoscience BC, Report 2019-02, p. 105–122, URL <http://cdn.geosciencebc.com/pdf/SummaryofActivities2018/EW/2017-002_SoA 2018_EW_Cahill_DissolvedMethane.pdf> [October 2019].

Cahill, A.G., Steelman, C.M., Forde, O., Kuloyo, O., Emil Ruff, S., Mayer, B., Mayer, K.U., Strous, M., Ryan, M.C., Cherry, J.A. and Parker, B.L. (2017): Mobility and persistence of methane in groundwater in a controlled-release field experiment; Nature Geoscience, v. 10, no. 4, p. 289–294, URL <https://doi.org/10.1038/ngeo2919> [April 2017].

Catto, N.R. (1991): Quaternary geology and landforms of the eastern Peace River region, British Columbia, NTS 94A/1, 2, 7, 8; BC Ministry of Energy, Mines and Petroleum Resources, BC Geological Survey, Open File 1991-11, 19 p.

Council of Canadian Academies (2014): Environmental impacts of shale gas extraction in Canada: the expert panel on harnessing science and technology to understand the environmental impacts of shale gas extraction; Council of Canadian Academies, Ottawa, Ontario, 262 p.

Darrah, T.H., Vengosh, A., Jackson, R.B., Warner, N.R. and Poreda, R.J. (2014): Noble gases identify the mechanisms of fugitive gas contamination in drinking-water wells overlying the Marcellus and Barnett shales; Proceedings of the National Academy of Sciences of the United States of America, v. 111, no. 39, p. 14076–14081, URL <https://doi.org/10.1073/pnas.1322107111> [November 2019].

DataBC (2019a): B.C. Data Catalogue; Government of British Columbia, datasets, URL <https://catalogue.data.gov.bc.ca/dataset?download_audience=Public> [October 2019].

DataBC (2019b): BCGS 1:5,000 grid; BC Ministry of Lands, Forests, Natural Resource Operations and Rural Development and GeoBC, dataset, URL <https://catalogue.data.gov.bc.ca/dataset/bcgs-1-5-000-grid> [November 2019].

Environment and Climate Change Canada (2019): Canadian climate normals 1981-2010 station data: Fort St John A; Government of Canada, URL <https://climate.weather.gc.ca/climate_normals/results_1981_2010_e.html?searchType=stnName&txtStationName=fort+st+john&searchMethod=contains&txtCentralLatMin=0&txtCentralLatSec=0&txtCentralLongMin=0&txtCentralLongSec=0&stnID=1413&dispBack=1> [October 2019].

Forde, O.N., Cahill, A.G., Beckie, R.D. and Mayer, K.U. (2019a): Barometric-pumping controls fugitive gas emissions from a vadose zone natural gas release; Scientific Reports, v. 9, article no. 14080, 9 p., URL <https://doi.org/10.1038/s41598-019-50426-3> [October 2019].

Forde, O.N., Mayer, K.U. and Hunkeler, D. (2019b): Identification, spatial extent and distribution of fugitive gas migration on the well pad scale; Science of the Total Environment, v. 652, p. 356–366, URL <https://doi.org/10.1016/j.scitotenv.2018.10.217> [November 2019].

Hickin, A.S. and Fournier, C.M.A. (2011): Preliminary bedrock topography and drift thickness of the Montney Play area; BC Ministry of Energy, Mines and Petroleum Resources, Energy Open File 2011-1 and Geoscience BC, Report 2011-07, 2 maps, scale 1:500 000, URL <http://cdn.geosciencebc.com/project_data/GBC_Report2011-7/GBC_Report2011-07_BCMEM%20OF2011-1.pdf> [November 2019].

Holland, S.S. (1964): Landforms of British Columbia, a physiographic outline; BC Ministry of Energy, Mines and Petroleum Resources, Bulletin No. 48, 138 p.

IHS Markit (2019): AccuMap™; IHS Markit, mapping, data management and analysis software, URL <https://ihsmarkit.com/products/oil-gas-tools-accumap.html> [October 2019].

Kelly, W.R., Matisoff, G. and Fisher, J.B. (1985): The effects of a gas well blow out on groundwater chemistry; Environmental Geology and Water Sciences, v. 7, issue 4, p. 205–213, URL <http://link.springer.com/article/10.1007/BF02509921> [November 2019].

Monahan, P.A., Hayes, B.J., Perra, M., Mykula, Y., Clarke, J., Galambos, B., Griffiths, D., Bayarsaikhan, O. and Oki, U. (2020): Amplification of seismic ground motion in the Fort St. John–Dawson Creek area, northeastern British Columbia (NTS 093P, 094A); *in* Geoscience BC Summary of Activities 2019, Geoscience BC, Report 2020-02, p. 1–12.

Osborn, S.G., Vengosh, A., Warner, N.R. and Jackson, R.B. (2011a): Methane contamination of drinking water accompanying gas-well drilling and hydraulic fracturing; Proceedings of the National Academy of Sciences of the United States, v. 108, issue 20, p. 8172–8176, URL <https://doi.org/10.1073/pnas.1100682108> [November 2019].

Osborn, S.G., Vengosh, A., Warner, N.R. and Jackson, R.B. (2011b): Reply to Saba and Orzechowski and Schon: methane contamination of drinking water accompanying gas-well drilling and hydraulic fracturing; Proceedings of the National Academy of Sciences of the United States of America, v. 108, issue 37, p. E665–E666.

Province of British Columbia (2018): Oil and Gas Activities Act, Drilling and Production Regulation; British Columbia Regulation 282/2010 (Oil and Gas Commission), URL <http://www.bclaws.ca/civix/document/id/complete/statreg/282_2010> [November 2018].

Saba, T. and Orzechowski, M. (2011): Lack of data to support a relationship between methane contamination of drinking water wells and hydraulic fracturing; Proceedings of the National Academy of Sciences, v. 108, issue 37, p. E663–E663, URL <https://doi.org/10.1073/pnas.1108435108> [November 2019].

Schaefer, D.G. (1978): Climate; *in* The Soil Landscapes of British Columbia, K.W.G. Valentine, P.N. Sprout, T.E. Baker and L.M. Lawkulich (ed.), BC Ministry of Environment, p. 3–10, URL <http://www.env.gov.bc.ca/esd/distdata/ecosystems/Soils_Reports/Soil_Landscapes_of_BC_1986.pdf> [November 2019].

Van Stempvoort, D., Maathuis, H., Jaworski, E., Mayer, B. and Rich, K. (2005): Oxidation of fugitive methane in ground water linked to bacterial sulfate reduction; Groundwater, v. 43, issue 2, p. 187–199, URL <https://doi.org/10.1111/j.1745-6584.2005.0005.x> [November 2019].

Vidic, R.D., Brantley, S.L., Vandenbossche, J.M., Yoxtheimer, D. and Abad, J.D. (2013): Impact of shale gas development on regional water quality; Science, v. 340, no. 6134, URL <https://doi.org/10.1126/science.1235009> [November 2019].

Controlled Natural Gas Release Experiment in a Confined Aquifer, Northeastern British Columbia (NTS 094A/04): Activity Report 2018–2019

A.G. Cahill, The Lyell Centre, Heriot-Watt University, Edinburgh, Scotland

B. Ladd, The University of British Columbia, Vancouver, British Columbia

J. Chao, The University of British Columbia, Vancouver, British Columbia

J. Soares, The University of British Columbia, Vancouver, British Columbia

T. Cary, University of Calgary, Calgary, Alberta

N. Finke, The University of British Columbia, Vancouver, British Columbia

C. Manning, The University of British Columbia, Vancouver, British Columbia

A.L. Popp, Swiss Federal Institute of Technology and Swiss Federal Institute of Aquatic Science and Technology, Switzerland

C. Chopra, The University of British Columbia, Vancouver, British Columbia

K.U. Mayer, The University of British Columbia, Vancouver, British Columbia

A. Black, The University of British Columbia, Vancouver, British Columbia

R. Lauer, University of Calgary, Calgary, Alberta

C. van Geloven, British Columbia Ministry of Forests, Lands, Natural Resource Operations and Rural Development, Prince George, British Columbia

L. Welch, British Columbia Oil and Gas Commission, Kelowna, British Columbia

S. Crowe, The University of British Columbia, Vancouver, British Columbia

B. Mayer, University of Calgary, Calgary, Alberta

R.D. Beckie, The University of British Columbia, Vancouver, British Columbia, rbeckie@eoas.ubc.ca

Cahill, A.G., Ladd, B., Chao, J., Soares, J., Cary, T., Finke, N., Manning, C., Popp, A.L., Chopra, C., Mayer, K.U., Black, A., Lauer, R., van Geloven, C., Welch, L., Crowe, S., Mayer, B. and Beckie, R.D. (2020): Controlled natural gas release experiment in a confined aquifer, northeastern British Columbia (NTS 094A/04): activity report 2018–2019; *in* Geoscience BC Summary of Activities 2019, Geoscience BC, Report 2020-02, p. 145–160.

Introduction

This paper summarizes the past twelve months of a research program aimed at advancing knowledge on fugitive natural gas migration in groundwater. Research activities were carried out at the Hudson's Hope Field Research Station (HHFRS) located in northeastern British Columbia (BC; Figure 1). In the summer of 2018, natural gas was intentionally injected into the subsurface; the physical and biogeochemical conditions associated with this injection have been monitored ever since. The installation of HHFRS and previous activities at the site are described in Cahill et al. (2019a, b).

Fugitive gas (FG) describes natural gas that has been unintentionally released in the subsurface in the context of energy resource development. Gas migration (GM) occurs when fugitive gas is released in the subsurface outside of an energy well casing and into the adjacent formation(s), as opposed to fugitive gas that leaks inside the well casing and manifests as surface casing vent flow (SCVF). Although both FG and GM were identified long ago (Chafin, 1994; Dusseault et al., 2000), significant knowledge gaps regarding gas migration, environmental impacts and environmental fate still exist, largely because of the complexity of the physical and biogeochemical processes involved, but also due to the distinct geological environments of the various resource plays. Consequently, there is a pressing need to address knowledge gaps related to FG and GM in northeastern BC, particularly in light of the technological improvements in unconventional production methods in the

---

This publication is also available, free of charge, as colour digital files in Adobe Acrobat® PDF format from the Geoscience BC website: http://www.geosciencebc.com/updates/summary-of-activities/.

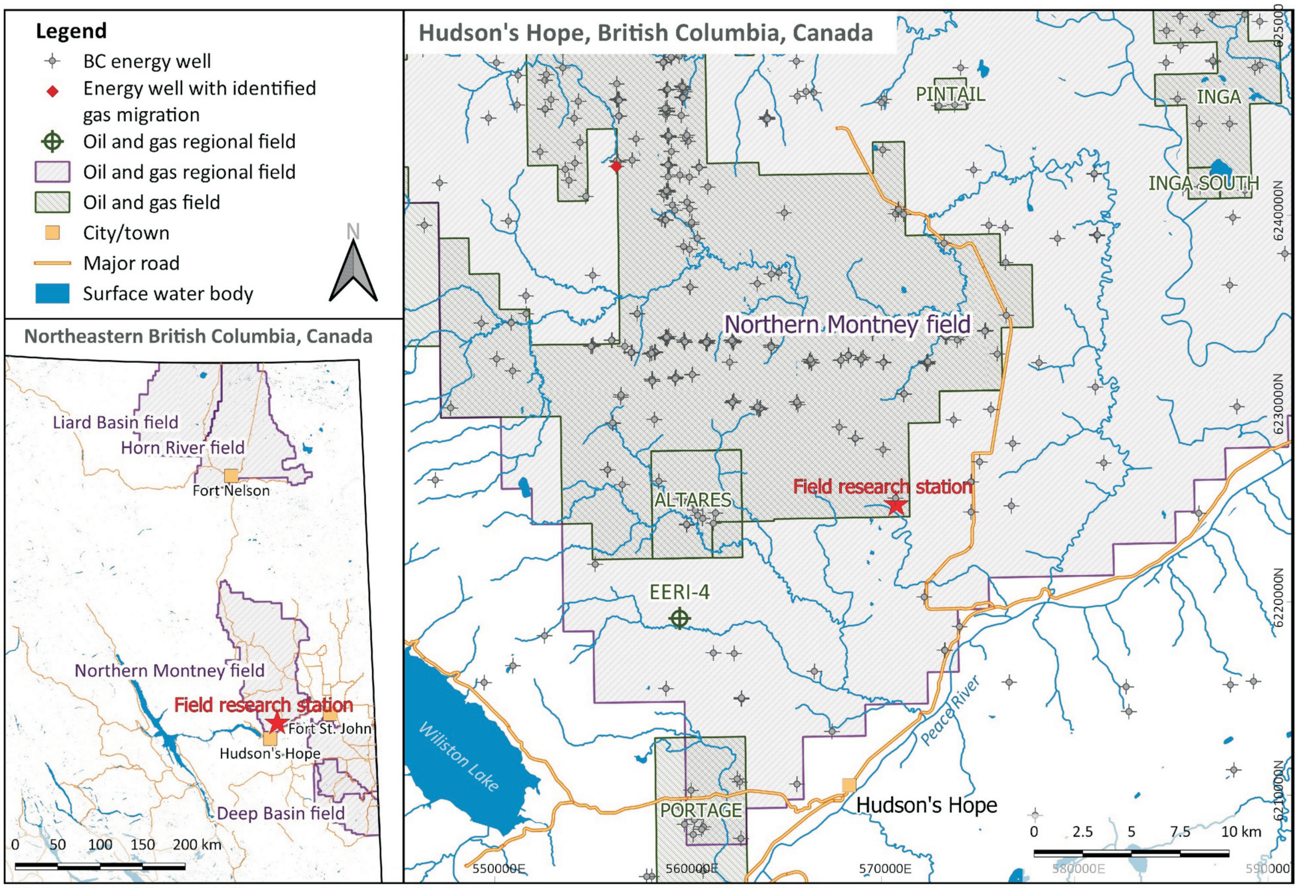

Figure 1. Location of the Hudson's Hope Field Research Station in the context of oil and gas activity in northeastern British Columbia (Cahill et al., 2019a). Co-ordinates are in NAD83 BC Albers. Well locations retrieved from AccuMap™ (IHS Markit, 2019). Oil and gas regional fields and base map features retrieved from DataBC (2019a–d).

last decade and the accompanying increase in exploration and development of petroleum resources (Council of Canadian Academies, 2014). A principal objective of this research program, and the Energy and Environment Research Initiative (EERI) at The University of British Columbia (UBC), is to provide the science knowledge base that can be used to inform the management of oil and gas development in BC. By conducting a controlled natural gas release experiment in an area of active oil and gas development, the aim is to 1) characterize the physical and biogeochemical processes that control subsurface gas migration and impact, and quantify the amount of natural gas that remains, degrades or leaves the subsurface; 2) test FG monitoring and detection methodologies; and 3) inform regulations to facilitate safe and sustainable development of natural gas resources.

Background

Subsurface Gas Movement Fundamentals

In the subsurface, natural gas can move in a gas phase, sometimes called a free-phase gas, or as a dissolved component in groundwater. The GM in the subsurface is therefore governed by multiphase (gas phase and liquid phase) flow and transport, which are controlled by the complex physics and chemistry of the two fluids and the porous media (Parker, 1989; Mercer and Cohen, 1990). Below the water table, free-phase gas will move principally in response to buoyancy and viscosity forces, whereas dissolved gas will move as a solute with groundwater flow, which is controlled by the hydrogeological conditions at a given site (i.e., recharge area locations, topography, etc.). Free-phase gas is subjected to vertical buoyancy forces that will induce vertical movement toward the surface unless intercepted by low-permeability strata such that entry into pore space is inhibited. If not intercepted, free-phase gas will advance from the saturated zone and enter the vadose zone, where, following any degradation processes, it will emit to atmosphere.

The process by which free-phase gas moves, that is, enters into a pore space originally occupied by a liquid, is controlled by the pressure difference between the gas phase and the adjacent liquid phase. This difference in pressure between the phases is called the capillary pressure, which is controlled by the properties of the gas, liquid, geological materials and the pore sizes of the material. For the gas to enter pores that are occupied by liquid, the gas must displace or 'push' the liquid out. It can do this if the capillary pressure is greater than the pressure required to displace the liquid, called the gas-entry pressure.

These free-phase gas dynamics allow a general statement to be made about where to find free-phase gas in the subsurface: because gas-entry pressures are lower for larger pores (Berg, 1975), the free-phase gas will tend to occupy and move through the larger pores and/or fractures in the subsurface. Conversely, free-phase gas movement will be inhibited by materials with smaller pore sizes, which typically have low permeability and require higher entry pressures to advance. The materials or strata that inhibit gas entry into their pore space are called capillary breaks or capillary barriers. With this background, a simple conceptual description of the physical transport of gas in the subsurface can be introduced that will apply at this field research station. This will be followed by a conceptual description of the associated biogeochemical processes in the subsurface.

Conceptual Model of Free-Phase Gas and Dissolved Gas Flow and Transport

The upward flow of free-phase gas below the water table in the subsurface is similar to the downward flow of a dense liquid through a less dense liquid. If a dense liquid is poured into water in a tank, it will move vertically downward until it encounters the bottom of the tank, where the denser liquid will pool and then spread horizontally along the tank bottom. If the tank bottom is not horizontal, the denser liquid will move downslope by gravity along the tank bottom. If there is a local depression, the denser liquid will pool and become trapped in the depression. These same ideas apply for a free-phase gas except that buoyancy forces act vertically upward as opposed to downward. A free-phase gas issuing from a source below the water table will move vertically upward until it encounters a capillary break, where it will pool and spread, and move upslope if the surface of the capillary break material (e.g., a silt or clay) is not horizontal, or pool and become trapped if there is a local convex impression in the bottom of the strata. Examples of this can be found in air-sparging literature, which describes when air is injected into the subsurface to enhance the removal of volatile contaminants (Ji et al., 1993).

If while moving along the bottom of the capillary-break surface, the gas encounters pores or fractures that are sufficiently large for the prevailing capillary pressures, the gas will enter the large pore or fracture and move upward. The gas pool under the capillary break will then be able to 'drain' upward until it either encounters another capillary break, or it crosses the water table. Larger pores, coarser materials and wider fractures are therefore important preferential flow paths for free-gas movement in the subsurface.

A key question for a given site where gas is leaking at some depth into the subsurface is whether that gas can cross the water table and enter into the near-surface pore space that is connected to the atmosphere in the vadose zone. If so, it can then be emitted through the unsaturated subsurface and reach the atmosphere, where methane acts as a greenhouse gas (Forde et al., 2019a).

Natural gas can also move with groundwater as a dissolved gas. The hydrogeology of the subsurface controls groundwater flow directions, magnitudes and velocities, whereas the total flux of dissolved gas that can be transported in groundwater depends upon the amount of gas that can dissolve and the groundwater flow rate. The amount of gas that can dissolve per unit volume of water at equilibrium increases with water pressure (the dissolution of carbon dioxide is also affected by pH) and to a lesser degree temperature. Generally speaking, deeper groundwater has higher water pressure (and in general temperatures) and accordingly can dissolve more gas. The rate at which gas dissolves will depend strongly on the surface-to-volume ratio of the free-phase gas and the rate at which water flows by the free-phase gas zones in the subsurface. Gas will dissolve into water more readily if the free-phase gas has a relatively large surface area, and the water flow past the free-phase gas is relatively fast.

The principal biogeochemical process that affects GM in the subsurface is oxidation of methane. With the exception of explosive conditions, methane oxidation is kinetic; that is, it does not occur instantaneously, but at rates that depend upon biogeochemical conditions and temperature. Fundamentally, oxidation is a transfer of electrons from the carbon in methane to an electron acceptor such as oxygen. Generally speaking, bacteria in the subsurface mediate many, if not most, of the oxidation reactions for their respiration (Lovley and Chapelle, 1995). Bacteria can 'burn' methane by 'breathing' oxygen, creating carbon dioxide and water. Other dissolved and mineral phases can also serve as electron acceptors, most notably dissolved nitrate and sulphate and solid oxide mineral phases, principally of iron and manganese (Christensen et al., 2001). Methane can be oxidized in absence of oxygen in the subsurface in a process called anaerobic oxidation, affecting the concentrations of nitrate, sulphate and iron dissolved in water and generating several byproducts including hydrogen sulphide and trace metals such as arsenic (Forde et al., 2019b).

An important question is if, and how quickly, will methane in natural gas oxidize in the subsurface. Most often, oxidation in the presence of oxygen is faster than anaerobic oxidation, and oxidation at higher temperatures is faster than at lower temperatures (Appelo and Postma, 2005). This suggests that oxidation of methane in groundwater or in the soil gas will be more rapid near the surface where oxygen is more likely to be present, and in the summer when tempera-

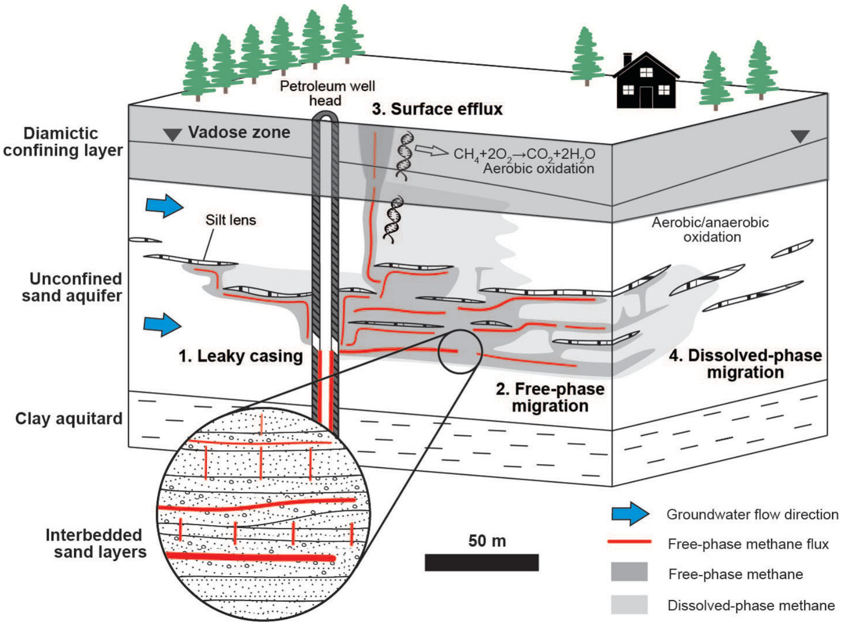

Figure 2. Conceptual model of gas migration and fugitive gas associated with energy wells (modified from Cahill et al., 2017). Fugitive gas may affect the saturated zone (below the water table), the unsaturated zone (with a gas phase connected to the atmosphere) and the atmosphere. Gas moves vertically but can be directed laterally along capillary breaks such as silt or clay layers.

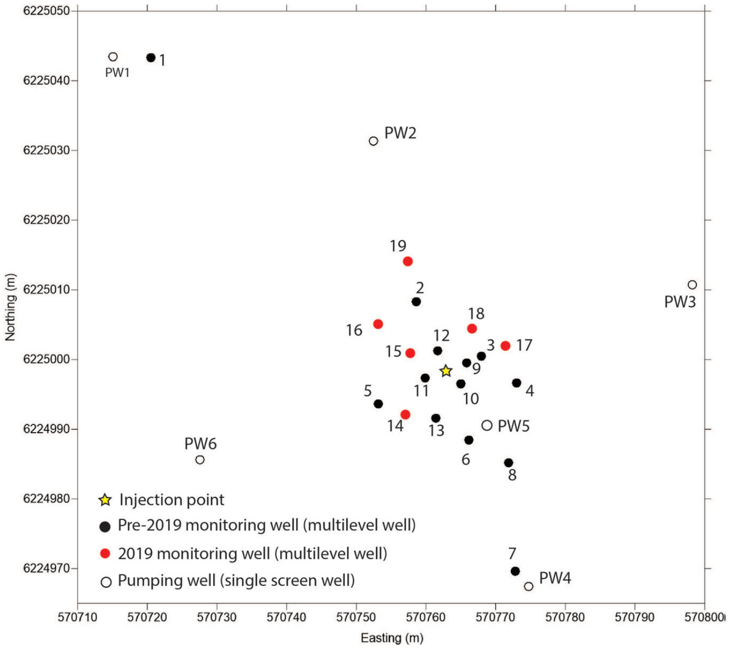

Figure 3. Surface location of monitoring wells in the study area as of October 2019.

tures are higher. These processes are summarized in Cahill et al. (2017) and shown in Figure 2.

These physical and biogeochemical processes depend upon the prevailing subsurface properties such as grain size, distribution of capillary breaks and large pores/channels, subsurface mineralogy and geochemistry, and are best investigated through an experimental program. At the HHFRS, a leak of gas from a point source in the subsurface was emulated and its physical movement and geochemical effects on groundwater and rates of emission to the atmosphere are being monitored. Research activities over the last twelve months at HHFRS are described below. These build on previous efforts, described in Cahill et al. (2019b).

Summary of Activities and Progress

Saturated Zone Injection Experiment

At HHFRS, an active controlled natural-gas injection period lasted 66 days, during June to August 2018. From fall 2018 to present, efforts have focused on characterization and monitoring of groundwater quality, flow conditions, surface effluxes, gas compositions and changes in geophysical conditions.

To better constrain the sedimentary architecture at HHFRS following observations of gas migration, a total of 15 new sampling ports in six nested wells were added to the groundwater monitoring well network in September 2019 (Figure 3). Boreholes were drilled by sonic method allowing core to be logged, intact sediment samples to be collected for characterization of permeability, analysis of gas in sediments via ISOPAK™ containers from Isotech Laboratories, Inc., and collection of samples for incubation studies to characterize microbial activity. The new sampling wells were installed with 5 cm (2 in.) diameter screens to facilitate groundwater collection with displacement pumps, particularly beneficial for points completed in lower permeability materials.

Discipline-Specific Activities

Hydrogeology and Groundwater Monitoring

Physical and geochemical properties of groundwater and dissolved gas have been monitored from May 2018 to present (October 2019). Groundwater samples were collected approximately monthly, with the exception of winter months, from the pre-September 2019 sampling points, which include sample ports in 13 multilevel monitoring wells and from six single-depth screened piezometers (see Table 1). In the field, temperature, specific conductance and pH were measured using probes installed in flow-through cells. Alkalinity was determined onsite by Gran titration of filtered samples. Trace

Table 1. Completion details for installed nested sampling wells, as of September 2019. Abbreviations: MW, monitoring well; PW, pumping well.

Pre-2019 wells			
Well ID	Sampling port	Completion intervals	
		from (m)	to (m)
PW1	N/a	23.2	26.2
PW2	N/a	22.3	25.3
PW3	N/a	22.3	25.3
PW4	N/a	19.8	22.9
PW5	N/a	18.5	20.0
PW6	N/a	15.8	25.0
MW1	2	16.0	16.6
MW2	1	11.6	12.5
	2	14.6	15.8
	3	18.9	19.6
MW3	2	14.6	15.5
MW4	1	11.6	12.2
	2	14.6	15.2
	3	16.8	17.7
	4	19.5	20.1
MW5	2	16.9	17.5
	3	19.2	19.8
	4	21.0	21.6
MW6	1	11.9	15.5
	2	15.8	16.7
	3	18.0	18.6
	4	20.1	20.7
MW7	1	11.9	12.5
	2	14.9	15.5
	3	17.1	17.7
	4	20.1	20.7
MW8	1	12.0	12.6
	2	16.0	16.6
	3	18.0	18.6
	4	20.0	20.6
MW9	3	18.0	18.6
	4	20.0	20.6
MW10	1	12.0	12.6
	2	16.0	16.6
	3	18.0	18.6
	4	20.0	20.6
MW11	1	12.0	12.6
	3	18.0	18.6
	4	20.0	20.6
MW12	1	12.0	12.6
	2	16.0	16.6
	3	18.0	18.6
	4	20.0	20.6
MW13	1	12.0	12.6
	3	18.0	18.6
	4	20.0	20.6

2019 wells			
Well ID	Sampling port	Completion intervals	
		from (m)	to (m)
MW14	1	8.5	9.1
	2	11.3	11.9
	3	16.8	18.3
MW15	1	14.3	14.9
	2	17.4	18.9
MW16	1	11.3	11.9
	2	15.8	16.5
	3	18.3	18.9
MW17	1	11.3	11.9
	2	18.6	19.2
MW18	1	11.3	11.9
	2	16.8	17.4
MW19	1	11.3	11.9
	2	15.5	16.2
	3	17.7	18.3

elements were analyzed at the Water Quality Centre at Trent University (Peterborough, ON) using inductively coupled plasma–mass spectrometry. Anion concentrations in groundwater samples were determined by ion chromatography and automated colourimetry at the Applied Geochemistry group (AGg) Chemistry Lab at the University of Calgary (Calgary, AB). Dissolved gas composition for N$_2$, O$_2$, CO$_2$ and C$_1$ to C$_3$ (methane to propane) was analyzed using a Bruker 450 gas chromatograph at the AGg Chemistry Lab.

During the injection period, two wells (MW2, MW5) showed elevated dissolved methane concentrations compared to background levels (Table 2). Well MW2 exhibited particularly high dissolved methane concentrations (12.27 and 15.78 mg/L at ports 2 and 3, respectively), whereas MW5 showed more modest increases to 0.25 and 0.1 mg/L at ports 3 and 4, respectively. As can be seen in Figure 3, MW2 and MW5 are not the most proximal wells to the injection point, nor to each other, indicating that gas migration is largely controlled by small-scale geology and discrete preferential pathways. Approximately 44 days after the active injection of natural gas stopped (day 110), evidence of injected gas was detected in the dissolved phase in an additional two wells (MW11, MW12) and an additional shallower port in MW2. In the most recent results from September 2019 (day 460), two more wells (MW9, MW13) showed elevated dissolved methane in multiple ports, whereas MW5 decreased back down to background levels. In general, the highest methane concentrations have been observed in the shallower sample ports. Overall, preliminary mass balance calculations indicate that the majority of the injected gas has remained in the free-phase gas form, with a small proportion dissolving into the groundwater. Over a year since the start of the injection, it is clear the groundwater chemistry is still evolving.

Since June 6, 2018, hydraulic heads have been recorded by pressure transducers at MW6 at 12 and 20 m depth, MW13 at 15 m depth and MW10 at 16 m depth. These data will be

Table 2. Dissolved methane (CH_4) gas concentrations for wells and sampling ports that showed elevated concentrations at some point during the experiment. Dissolved methane concentrations are shown for days –6, 60, 110 and 460, with day 0 being the day the injection began. The active injection lasted for 66 days. Elevated concentrations from background are highlighted in bold. Abbreviation: N/d, no data, due to low or nonexistent flow.

Well ID	Sampling port	Depth (top of interval) (m)	Before injection (day -6) CH_4 (mg/L)	During injection (day 60) CH_4 (mg/L)	Post injection (day 110) CH_4 (mg/L)	Post injection (day 460) CH_4 (mg/L)
MW2	1	11.6	0.0019	ND	**9.75**	**7.09**
	2	14.6	0.0017	**12.27**	**13.18**	N//d
	3	18.9	0.0021	**15.78**	**14.15**	**14.30**
MW5	3	19.2	0.0021	**0.25**	**0.100**	0.0028
	4	21.0	0.0037	**0.1000**	**0.111**	N/d
MW9	3	18.0	0.0039	0.0065	0.0058	**10.60**
	4	20.0	0.0250	0.0159	0.0093	**0.47**
MW11	1	12.0	0.0030	0.0088	**0.1114**	**0.253**
	3	18.0	0.0230	0.0050	0.0131	**0.11**
	4	20.0	0.0168	0.0123	0.0127	**0.82**
MW12	2	16.0	0.0017	0.0181	0.0166	**10.032**
	4	20.0	0.0056	0.0091	**0.0231**(1)	**0.598**
MW13	3	18.0	0.0035	0.0110	0.0032	**0.370**

(1) Highlighted because even though the CH_4 level is low, other dissolved constituents showed evidence of injection gas.

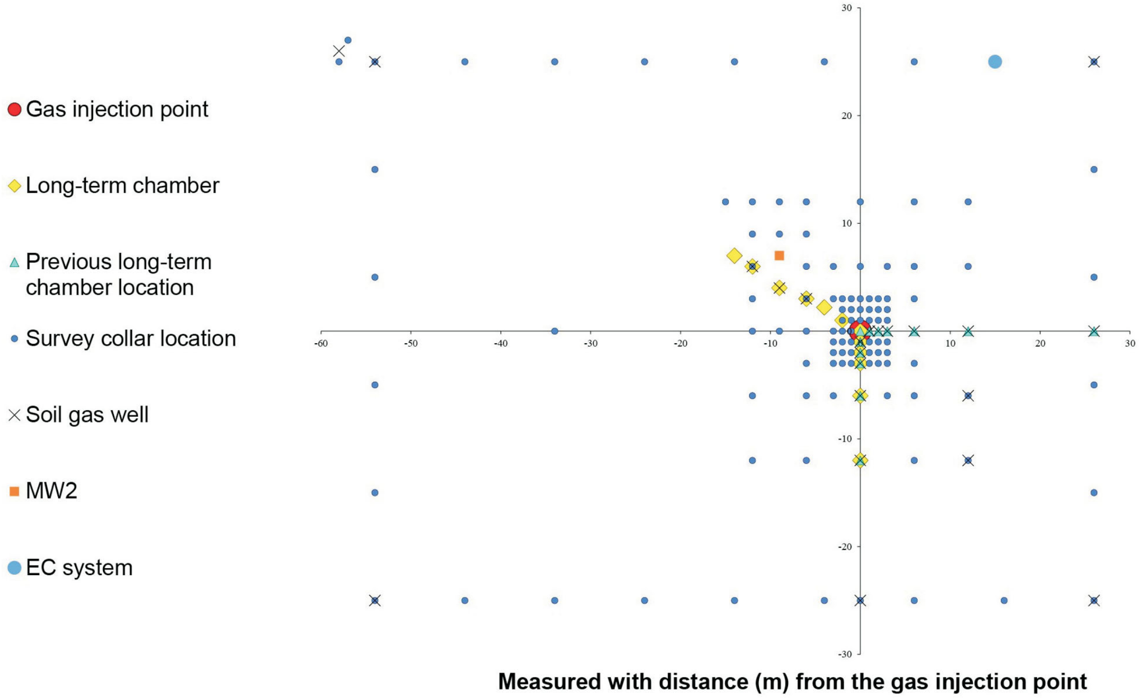

Figure 4. Illustration of the experimental setup and monitoring network for the vadose zone and surface efflux measurements at the Hudson's Hope Field Research Station. Abbreviations: EC, eddy covariance; MW, monitoring well.

compared to data from air-sparging studies (Johnson et al., 2001) where subtle transient pressure responses have been observed in groundwater levels and used to interpret groundwater flow directions and to infer gas movement.

Soil Gas and Surface Efflux

To monitor soil-gas concentrations and surface effluxes, 12 dynamic long-term chambers (8100-104, LI-COR, Inc.) were deployed and 22 soil-gas sampling ports were installed at HHFRS, primarily along two transects radiating from the injection point (Figure 4). The 12 long-term dynamic chambers sequentially measured carbon dioxide and methane concentrations at their designated locations. This allowed for the calculation of fluxes at the surface and provided high-resolution time series data for methane fluxes. The 22 soil-gas sampling locations were manually augured with sampling ports at 0.45 and 1.15 m below ground surface, allowing for the collection of soil-gas samples for compositional and isotope analyses. Additionally, 105 survey collars (green rings in Figure 5) were set up and an additional set of analyzers allowed for carbon dioxide and methane concentrations to be obtained across the site, providing discrete, detailed, spatially distributed, flux data. Survey flux measurements and soil-gas samples for isoto-

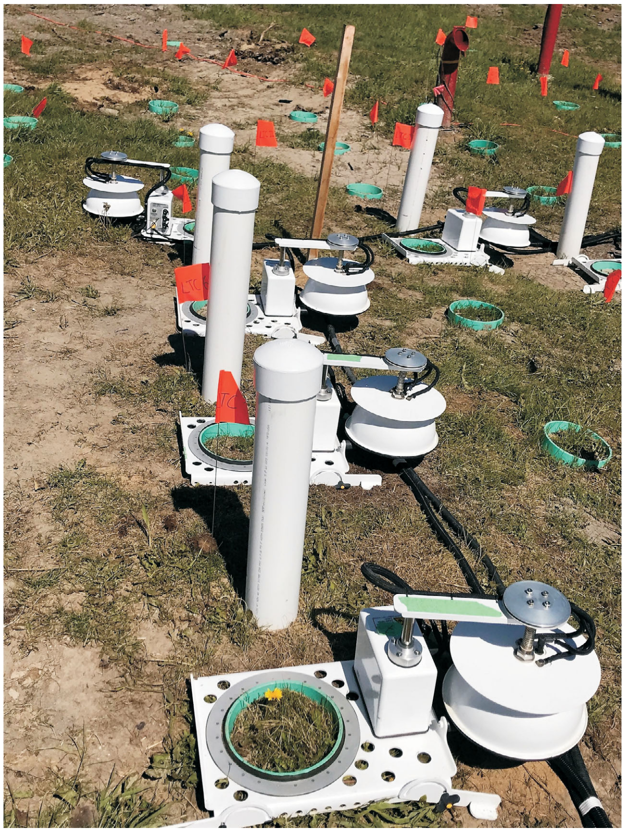

Figure 5. Dynamic long-term chambers sitting on green collars and co-located with soil-gas wells with white polyvinyl chloride (PVC) protective casings.

Figure 6. Operation of the miniRUEDI at Hudson's Hope Field Research Station.

pic and compositional analysis were collected every 2–4 weeks starting on May 28, 2018, ending on October 1, 2018, at the onset of winter conditions. Additionally, soil-gas samples were collected once in June 2019. The results illustrate that the injected gas moved upgradient against groundwater flow and broke through at the surface a month after the injection. Once the gas was detected, elevated methane (CH_4) fluxes were continuously detected at the surface and began to decrease exponentially after the injection was stopped. Soil-gas composition and isotopic data further show evidence that the injected gas moved through the near subsurface to surface and that CH_4 was microbially oxidized to CO_2.

Application of the miniRUEDI Portable Mass Spectrometer at HHFRS

During the HHFRS injection experiment, instruments were installed that provided continuous real-time measurements of surface emissions of the injected gas (soil efflux chamber and an eddy covariance flux tower, the latter discussed in the following section). While planning for the HHFRS injection experiment, novel field-portable methods were investigated for real-time detection of the injected gas in the subsurface, as the soil-gas and groundwater samples collected in vials take approximately one month to analyze. The portable mass spectrometer system selected was Gasometrix GmbH's miniRUEDI (Brennwald et al., 2016), developed by scientists at the Swiss Federal Institute for Aquatic Science and Technology (Figure 6).

It was decided to use the miniRUEDI during and following the controlled release experiment to achieve two scientific goals: 1) to provide real-time detection of the injected gas in the subsurface and 2) to provide measurements of He concentration. The miniRUEDI has the ability to detect a wide range of gases (including He, Ar, Kr, N_2, O_2, CO_2, CH_4, C_3H_8). The injected gas contained 5000 ppm He (1000 times higher than the atmospheric concentration of 5 ppm), but this gas could not be measured by the instrument used for the discrete soil-gas and groundwater samples. Helium is a particularly useful tracer because it is not produced or consumed by any biological or chemical process. Therefore, changes in the ratio of helium to hydrocarbons can provide insights into the subsurface consumption of the injected hydrocarbons.

The miniRUEDI was used at the HHFRS prior to, during and following the injection (in June, July and August 2018). In late July 2018, approximately five weeks after the injection began, the miniRUEDI detected elevated levels of tracer gases (methane, propane, helium) at MW2 (Figure 2). At MW2, groundwater was sampled and it was found that the peak heights for CH_4 and He were approximately 1000 times higher than the levels in air or air-equilibrated water. Subsequent measurements of soil efflux adjacent to MW2 also showed elevated levels of CH_4. As a result, the location of one of the soil efflux chamber long-term monitoring lines was moved so that it was close to MW2. The chambers closest to MW2 displayed much higher CH_4 levels than anywhere else on the site, and these data were necessary to accurately estimate the CH_4 emissions.

Following soil-gas composition measurements in the laboratory, the miniRUEDI was used to measure selected samples. All soil-gas samples that contained detectable levels of tracer gas also contained elevated levels of He. Further interpretation of the miniRUEDI data will be presented in upcoming peer-reviewed publications.

Overall, the miniRUEDI was a highly successful component of the experiment. The real-time detection of the injected gas at MW2 enabled the modification of the monitoring strategy during the experiment, improving estimates of the surface efflux. Additionally, a collaboration with European researchers was developed that will expand the international visibility of this research.

Eddy Covariance and Micrometeorology

The eddy covariance (EC) system was re-installed in March 2019, after the 2018–2019 winter decommissioning, with two main objectives:

1) to monitor any residual effluxes during and after the thaw,
2) to carry out controlled release experiments to evaluate flux footprints.

The system was set up similar to 2018 (Cahill et al., 2019b), however, the height of the tower was raised to 1.9 m to expand the flux footprint (Figure 7). All instruments as used in the previous year were re-installed, i.e., a 3-D sonic anemometer (CSAT3B, Campbell Scientific, Inc.), which measures wind direction and speed in three dimensions; a gas analyzer (LI-7700, LI-COR, Inc.) for methane, which is an open path system; and a gas analyzer (LI-7200, LI-COR, Inc.) for carbon dioxide and water vapour, which is an enclosed unit with a flow module. There is also a flow module (7200-101) with the LI-7200, which is responsible for maintaining a precise and controllable flow of air. An LI-7550 analyzer interface unit (AIU) was set up, which integrates data from the sonic anemometer and the LI-7200 and LI-7700 analyzers. The SmartFlux 2 system by LI-COR, powered by their EddyPro® software, was also installed. It computes covariances from the 20 Hz high frequency raw values (mixing ratios, wind velocity, etc.) obtained from the gas analyzers and provides half hourly averages for this data.

Figure 7. Eddy covariance system configuration at Hudson's Hope Field Research Station.

The climate system was also re-installed, including a net radiometer (CNR4, Kipp & Zonen B.V.); a 2-D anemometer (Windsonic, Gill Instruments Limited); CSI sensors (manufactured by Vaisala Corporation) for barometric pressure (CS106), temperature and relative humidity (HMP155A); three Decagon Devices, Inc. GS3 sensors (each measuring soil moisture, soil conductivity, soil temperature); two soil heat flux plates (HFP01-L, HFP01SC-L, Hukseflux Thermal Sensors B.V.) at a depth of 5 cm each, the latter being self-calibrating; and a tipping bucket rain gauge (TE525WS, Texas Electronics, Inc.).

A datalogger (CR1000, Campbell Scientific, Inc.) at the site collected all the climate data from the various components, and compiled it giving the averages, maximum and minimum values of each parameter every half hour. This climate data, after being collected onto the datalogger, and along with the computed EC measurements (by the Smartflux 2) were remotely sent to the UBC Biometeorology Soil and Physics Group lab daily at 6 a.m. via a modem (RV50, Sierra Wireless S.A.). The high-frequency data was collected onto a USB at the site and sent back and forth between the site and UBC.

Controlled atmospheric-release experiments were carried out in the summer of 2019 (Table 3), to study the response of EC measurements to factors like release rate, release location, release height and distance with respect to the tower. The objective was to fill in knowledge gaps about the footprint, i.e., the relationship between surface effluxes and EC measurements made at the EC tower. Based on this theory, relationships between EC fluxes and chamber measurements can be drawn (analysis in progress). Various footprint models (e.g., Kormann and Meixner, 2001; Kljun et al., 2015) can be used to do this analysis, depending on experimental conditions such as release height, stability parameters of the atmosphere, etc. The decision of which footprint model to use will be made by using data from these release experiments.

Table 3. Timeline of fieldwork in 2019 at Hudson's Hope Field Research Station.

Date of trip	Purpose
March 19 to 22	Re-installation of eddy covariance system
May 13 to 17	Surface release experiment
July 15 to 22	Surface release experiment
August 12 to 15	Surface release experiment (repeated some July experiments to have more confidence in measurements)

Various approaches were determined to compare flux data from the EC system with that from the chambers (including data from 2017 and 2018). In order to test this theory, EC fluxes were estimated using the release rate of the source and the footprint value at the location of the source, and these estimates were compared with actual measured EC fluxes. This was done for a release experiment conducted in 2017, and the results were very promising (Figure 8; C. Chopra, work in progress).

Similar analysis is in progress for the releases from this summer (2019) and this information will further be utilized to 1) make direct comparison with the data from chambers by combining chamber effluxes with the flux footprint, and 2) obtain the surface distribution of effluxes using EC fluxes and the flux footprint by carrying out a matrix inversion.

Geophysics

The geophysics team visited the site in late June 2019 to conduct a final post-injection electrical resistivity survey (Figure 9). The data collection employed the same configuration used in the previous surveys, which were designed to map the migration of the gas through time-lapse analysis

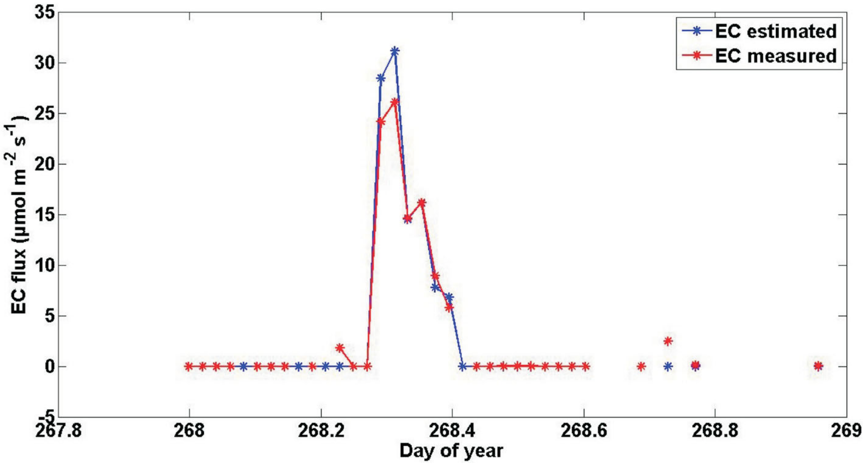

Figure 8. Estimated versus measured values of eddy covariance (EC) flux from the 2017 surface release experiment.

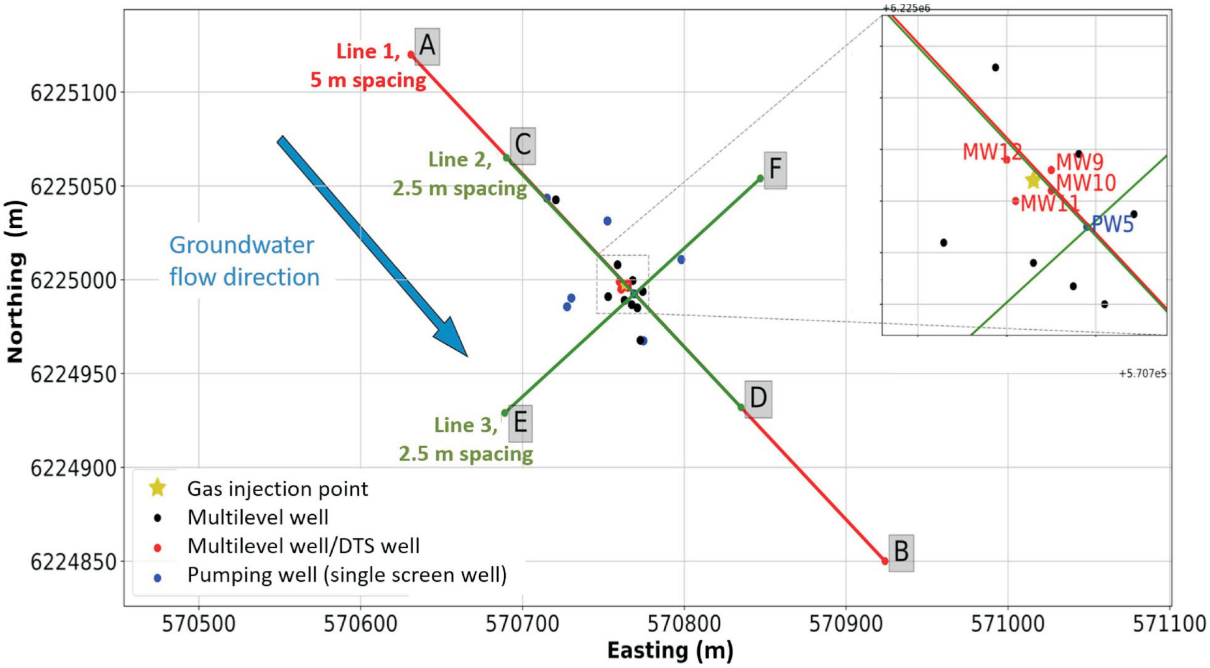

Figure 9. Site map showing the orientation of three electrical resistivity profiles measured across two line transects: line 1 consists of two survey lines, AB (5 m spacing of electrodes) and CD (2.5 m spacing of electrodes), and line 3 consists of one survey line, EF (2.5 m spacing of electrodes). The injection point is located at the centre of line CD. Wells MW9, MW10, MW11 and MW12 contain optical fibre for distributed temperature sensing (DTS) measurements, which were used to calculate temperature corrections for resistivity measurements.

(Cahill et al., 2019b). Two additional resistivity lines were collected around MW2 in an effort to identify potential sites of leakage, or gaps in the confining layer, which represent pathways for gas migration (Figure 10). Analysis of the time-lapse data is complete, and a manuscript is being prepared for submission to a peer-reviewed journal. The preliminary results were presented at the annual American Geophysical Union (AGU) Fall Meeting in Washington, DC, in December 2018 (Cary et al., 2018).

Microbiology

Sampling

Just prior to the start of the injection on June 12, 2018, all wells were sampled for H_2S, microbial diversity, cell counts, single cell amplified genomes, methane oxidation, methanogenesis and sulphate reduction (Tables 4, 5). Wells MW2, MW7 and MW10 were chosen for microbial rate determinations, with MW2 being upstream of the well (potentially a control) and MW7 and MW10 being downstream at varying distances. Following the injection, sampling was focused on the wells surrounding the injection point, collected about every two weeks. Low temperatures in late September 2018 prevented sampling during that month. After September 2018, the number of samples increased to cover the wells where methane had been discovered as well as the two inner circles of wells surrounding the injection well as to not miss wells where the gas may have been migrating (Table 4).

In September 2019, an additional drilling campaign was performed to get a better understanding of the gas plume in three dimensions as well as to obtain contamination control samples, soil samples for rates of microbial transformation of methane and sulphate reduction, and microbial diversity data from groundwater samples to compare with in situ microbial community determined from core samples. Six additional cores (MW14–MW19) were drilled and 15 sampling ports were installed. Soil samples were taken from four to seven horizons from each core (Table 6). Due to time constraints and late development of the new wells, no water samples from the new wells were taken during that trip. These will be sampled during the final sampling campaign in mid-October 2019. Results were not available for this publication.

Analysis

Incubation rates are determined by either radio tracer (sulphate reduction rate [SRR], methanogenesis [Met], dark carbon fixation [DCF]) or time course incubations (aerobic methane oxidation [MOX]) just after returning from the field site. First samples were analyzed for SRR, MOX and DCF rates. Following the September drilling campaign, soil rates were determined in MW15 at 12.2 m (40 ft.), 15.2 m (50 ft.) and 18.6 m (61 ft.), MW16 at 15.2 m (50 ft.) and MW19 at 12.2 m (40 ft.) and 18.3 m (60 ft.). Well MW15 at 18.6 m (61 ft.) showed the highest methane reading of 10% lower explosive limit (LEL) in the pumped water. Using an RKI Instruments, Inc. Eagle 2 gas monitor, testing for methane revealed methane was not detected at the other depths in MW15 and MW16. Wells MW17, MW18 and MW19 were not tested on site for methane.

Samples from the injection well and the monitoring and pumping wells collected prior to injection have been analyzed for total microbial community composition (Figure 11).

The new sampling method to determine in situ microbial diversity of an aquifer from water samples is based on analyzing the extracellular DNA (eDNA) in the water. To validate the method, the eDNA in the water samples must be analyzed along with the eDNA and intracellular DNA (iDNA) of the soil samples. For this project, a method has been developed to separate the eDNA and iDNA in both the water samples and the soil samples. This work is currently underway.

Preliminary Results

The microbial diversity in the water samples collected prior to injection show a clear difference in microbial composition and abundance between the pumping wells and the monitoring wells. This is most likely due to the longer screens in the pumping wells and thus mixing of water from different horizons. The pumping wells, however, also show a bigger variation in the abundance of microbes than in the

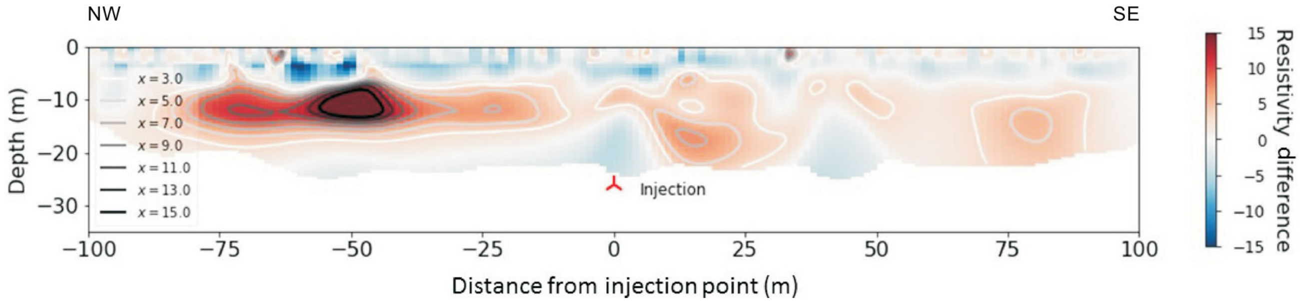

Figure 10. Images of percentage difference in resistivity for the time-lapse inversions of line 1 (survey line CD; 2.5 m electrode spacing), relative to pre-injection conditions. Grayscale contour lines (x-values on left axis) emphasize the resistivity difference gradient (red–blue colours) along transect CD. Line 1 is oriented parallel to the groundwater flow direction (see Figure 9). Abbreviations: NW, northwest; SE, southeast.

Table 4. Samples taken for microbial diversity, cell counts and single amplified genomes. The “s” denotes that S-isotope samples were also taken. Abbreviation: Inj, injection point.

Well ID - sampling port	October 17, 2017	June 6–12, 2018	June 27–28, 2018	July 12, 2018	July 27, 2018	July 30, 2018	August 15, 2018	August 27, 2018	September 18–19, 2018	October 5, 2018	October 29–31, 2018	May 5, 2019	July 19–20, 2019	September 9–12, 2019
PW1	x	s										x		
PW2	x	s										x		
PW3	x	s										x		
PW4	x	s										x		
PW5	x	s												
PW6	x	s										x		
Inj		x												
MW1-2		s	x	x		x	x	x	x			x	s	
MW2-1		s									x	x	s	
MW2-2		s				x	x	x	x	x				
MW2-3		s				x		x	x	x	x	x	s	s
MW3-2		s			x	x		x	x			x	s	x
MW4-1		s								x	x	x	s	s
MW4-2		s								x	x	x	s	s
MW4-3		s								x	x	x	s	s
MW4-4		s								x	x	x	s	
MW5-2												x		
MW5-3										x	x	x	s	
MW5-4										x				
MW6-1		s								x	x	x	s	s
MW6-2		s								x	x	x	s	s
MW6-3												x	s	s
MW6-4		s								x	x	x	s	s
MW7-1		s									x	x	s	s
MW7-2		s									x	x	s	s
MW7-3		s									x	x	s	s
MW7-4		s									x	x	s	s
MW8-1		s									x	x	s	x
MW8-3												x	s	s
MW8-4		s									x	x	s	s
MW9-3		s	x	x		x	x	x	x		x	x	s	s
MW9-4		s	x	x		x	x	x	x		x	x	s	s
MW10-1											x			
MW10-3		s		x		x	x	x	x					
MW10-4		s		x		x	x	x	x	x	x	x	s	s
MW11-1		s									x	x	s	s
MW11-3		s	x	x		x	x	x	x		x	x	s	s
MW11-4		s									x	x	s	x
MW12-1											x			
MW12-2											x			
MW12-3				x			x	x						
MW12-4		s							x		x	x	s	s
MW13-1											x			
MW13-3											x			
MW13-4		s									x	x	s	

Table 5. Samples taken for sulphate reduction, methanogenesis, methane oxidation and dark carbon fixation rates.

Well ID - sampling port	June 2018	July 2018	August 2018	May 2019	July 2019	September 2019
MW2-1	SRR, Met-H, Met-Ac, MOX	SRR, Met-H, Met-Ac, MOX	SRR, Met-H, Met-Ac, MOX	SRR, Met-H, Met-Ac, MOX, DCF		
MW2-2	SRR, Met-H, Met-Ac, MOX	SRR, Met-H, Met-Ac, MOX	SRR, Met-H, Met-Ac, MOX			
MW2-3	SRR, Met-H, Met-Ac, MOX	SRR, Met-H, Met-Ac, MOX	SRR, Met-H, Met-Ac, MOX	SRR, Met-H, Met-Ac, MOX, DCF	SRR, Met-H, Met-Ac, MOX, DCF	SRR, Met-H, Met-Ac, MOX
MW7-1	SRR, Met-H, Met-Ac, MOX	SRR, Met-H, Met-Ac, MOX	SRR, Met-H, Met-Ac, MOX	SRR, Met-H, Met-Ac, MOX, DCF	SRR, Met-H, Met-Ac, MOX, DCF	
MW7-2	SRR, Met-H, Met-Ac, MOX	SRR, Met-H, Met-Ac, MOX	SRR, Met-H, Met-Ac, MOX	SRR, Met-H, Met-Ac, MOX, DCF	SRR, Met-H, Met-Ac, MOX, DCF	SRR, Met-H, Met-Ac, MOX, DCF
MW7-3	SRR, Met-H, Met-Ac, MOX	SRR, Met-H, Met-Ac, MOX	SRR, Met-H, Met-Ac, MOX	SRR, Met-H, Met-Ac, MOX, DCF	SRR, Met-H, Met-Ac, MOX, DCF	SRR, Met-H, Met-Ac, MOX
MW7-4	SRR, Met-H, Met-Ac, MOX	SRR, Met-H, Met-Ac, MOX	SRR, Met-H, Met-Ac, MOX	SRR, Met-H, Met-Ac, MOX, DCF	SRR, Met-H, Met-Ac, MOX, DCF	SRR, Met-H, Met-Ac, MOX, DCF
MW10-3	SRR, Met-H, Met-Ac, MOX	SRR, Met-H, Met-Ac, MOX	SRR, Met-H, Met-Ac, MOX			
MW10-4	SRR, Met-H, Met-Ac, MOX	SRR, Met-H, Met-Ac, MOX	SRR, Met-H, Met-Ac, MOX	SRR, Met-H, Met-Ac, MOX, DCF	SRR, Met-H, Met-Ac, MOX, DCF	SRR, Met-H, Met-Ac, MOX

Abbreviations: DCF, dark carbon fixation; Met-Ac, acetoclastic methanogenesis; Met-H, hydrogenotrophic methanogenesis; MOX, aerobic methane oxidation; SRR, sulphate reduction rate

Table 6. Soil samples taken during drilling in September 2019.

Well ID	Depth (m)	Depth (ft)	Cell counts	e/iDNA	Total DNA	Rate samples	Contamination control
MW14	9.1	30	x	x	x		
	12.2	40	x	x	x		
	15.2	50	x	x	x		
	18.6	61	x	x	x		
	20.1	66	x	x	x		
MW15	3.0	10	x	x	x		x
	6.1	20	x	x	x		x
	9.1	30	x	x	x	x	x
	12.2	40	x	x	x	x	x
	15.2	50	x	x	x	x	x
	18.6	61	x	x	x	x	x
	20.1	66	x	x	x		x
MW16	9.1	30	x	x	x	x	x
	12.2	40	x	x	x	x	x
	15.2	50	x	x	x	x	x
	18.3	60	x	x	x	x	x
MW17	9.1	30	x	x	x		x
	12.2	40	x	x	x		x
	15.2	50	x	x	x		x
	18.3	60	x	x	x		x
MW18	9.1	30	x	x	x		
	12.2	40	x	x	x	x	
	15.2	50	x	x	x	x	
	18.6	61	x	x	x		
MW19	9.1	30	x	x	x	x	x
	12.2	40	x	x	x	x	x
	15.2	50	x	x	x	x	x
	15.8	52	x	x	x		
	18.3	60	x	x	x	x	x

monitoring wells. This again could be due to the longer screen, which might be sampling horizons that are not covered in the monitoring wells. Additionally, the pumping wells are more prone to contamination and the initial sampling showed a high abundance of cow hair in the samples, indicating surface contamination (HHFRS is located within a grazing lease and, though protected by an electric fence, is susceptible to cow intrusion). Overall, most of the pumping wells cluster away from most of the monitoring wells in a hierarchical cluster analysis.

There was no consistent pattern of microbial diversity found in samples from the monitoring wells, either in terms of sampling depth or well location.

Unsaturated Zone Injection Experiment

As reported in Cahill et al. (2019b), a second injection experiment was carried out at a separate but nearby site to HHFRS where unsaturated conditions exist. This experiment concluded at the end of 2017, with an additional round of soil samples collected in the summer of 2018. The past year saw the completion of analysis and interpretation of data from this site, and the publication of a peer-reviewed manuscript describing the effects of barometric fluctuations on surface effluxes (Forde et al., 2019a). A second manuscript is in preparation, examining the quantification of attenuation capacity of FG in unsaturated soils.

Conclusions and Ongoing Work

The following forms a summary of the progress made to date with respect to The University of British Columbia Energy and Environment Research Initiative's controlled methane release investigation project:

- completion of field activities at the unsaturated-zone site and publication of peer-reviewed manuscript entitled *Barometric-pumping controls fugitive gas emissions from a vadose zone natural gas release* (Forde et al., 2019a);
- continued monitoring, sample collection, geophysical surveying and microbial experiments at the Hudson's Hope Field Research Station;
- installation of 15 additional monitoring wells in six boreholes in September 2019;
- dissemination of work through conferences including GeoConvention, the American Geophysical Union Fall Meeting and The Geological Society of America Annual Meeting.

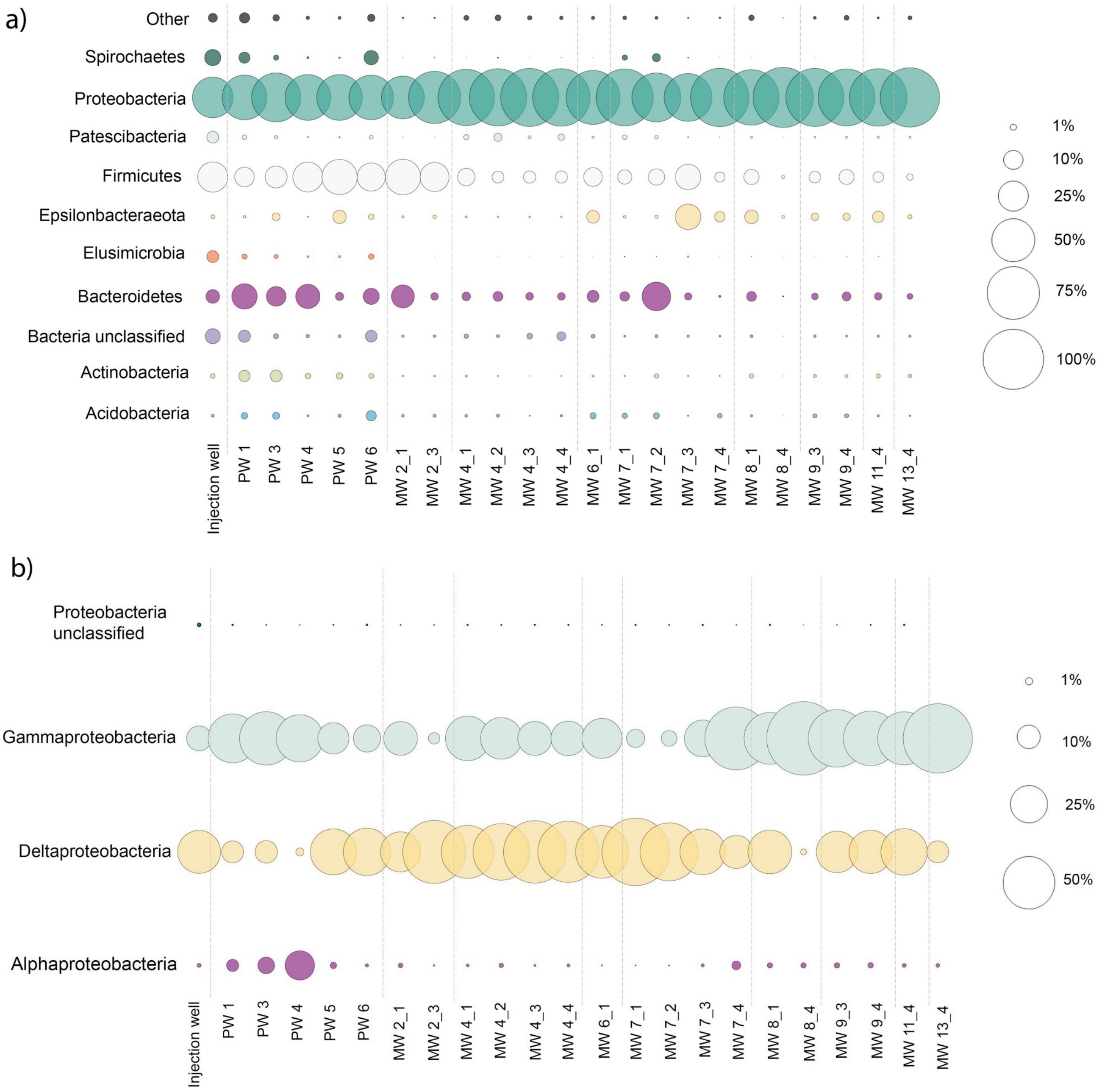

Figure 11. Bubble plot showing **a)** the microbial diversity on a phylum level and **b)** the diversity of proteobacteria in the pre-injection samples. The monitoring well number is followed by the sampling port number.

The bulk of future work on this project will be directed at data interpretation and analysis with mechanistic models. Final data collection will comprise several more rounds of groundwater sampling in order to capture the evolution of groundwater quality and gas dynamics through time at Hudson's Hope Field Research Station.

Acknowledgments

This manuscript was peer reviewed by C. Steelman. The authors gratefully acknowledge C. and E. Weder for allowing this work to take place on their grazing lease. This work was funded by Geoscience BC, Natural Resources Canada Clean Energy Innovation Program, the BC Oil and Gas Commission and the BC Oil and Gas Research and Innovation Society.

References

Appelo, C.A.J. and Postma, D. (2005): Geochemistry, groundwater and pollution, 2nd edition; A.A. Balkema Publishers, Amsterdam, The Netherlands, 649 p.

Berg, R.R. (1975): Capillary pressures in stratigraphic traps; AAPG Bulletin, v. 59, no. 6, p. 939–956.

Brennwald, M.S., Schmidt, M., Oser, J. and Kipfer, R. (2016): A portable and autonomous mass spectrometric system for on-site environmental gas analysis; Environmental Science & Technology, v. 50, issue 24, p. 13455–13463, URL <https://doi.org/10.1021/acs.est.6b03669> [March 2018].

Cahill, A.G., Beckie, R., Ladd, B., Sandl, E., Goetz, M., Chao, J., Soares, J., Manning, C., Chopra, C., Finke, N., Hawthorne, I., Black, A., Mayer, K.U., Crowe, S., Cary, T., Lauer, R., Mayer, B., Allen, A., Kirste, D. and Welch, L. (2019a): Advancing knowledge of gas migration and fugitive gas from energy wells in northeast British Columbia, Canada; Greenhouse Gases: Science and Technology, v. 9, issue 2, p. 134–151, URL <https://doi.org/10.1002/ghg.1856> [November 2019].

Cahill, A.G., Ladd, B., Chao, J., Soares, J., Cary, T., Finke, N., Manning, C., Chopra, C., Hawthorne, I., Forde, O.N., Mayer, K.U., Black, A., Croew, S., Mayer, B., Lauer, R., van Geloven, C., Welch, L. and Beckie, R.D. (2019b): Implementation and operation of a multidisciplinary field investigation involving a subsurface controlled natural gas release, northeastern British Columbia; *in* Geoscience BC Summary of Activities 2018: Energy and Water, Geoscience BC, Report 2019-02, p. 95–103, URL <http://cdn.geosciencebc.com/pdf/SummaryofActivities2018/EW/2016-043_SoA2018_EW_Cahill_ControlledGasRelease.pdf> [October 2019].

Cahill, A.G., Steelman, C.M., Forde, O., Kuloyo, O., Emil Ruff, S., Mayer, B., Mayer, K.U., Strous, M., Ryan, M.C., Cherry, J.A. and Parker, B.L. (2017): Mobility and persistence of methane in groundwater in a controlled-release field experiment; Nature Geoscience, v. 10, no. 4, p. 289–294, URL <https://doi.org/10.1038/ngeo2919> [April 2017].

Cary, T., Lauer, R.M., Innanen, K.A., Beckie, R.D., Cahill, A.G., Chao, J., Soares, J. and Sola, D. (2018): Monitoring methane gas migration in a near surface partially confined aquifer using geophysical methods; American Geophysical Union Fall Meeting, December 10–14, 2018, Washington, DC, Abstract H21I-1743, URL <http://adsabs.harvard.edu/abs/2018AGUFM.H21I1743C> [January 2019].

Chafin, D.T. (1994): Sources and migration pathways of natural gas in near-surface ground water beneath the Animas River valley, Colorado and New Mexico; United States Geological Survey, Water-Resources Investigations Report 94–4006, 56 p., URL <http://pubs.er.usgs.gov/publication/wri944006> [November 2019].

Christensen, T.H., Kjeldsen, P., Bjerg, P.L., Jensen, D.L., Christensen, J.B., Baun, A., Albrechtsen, H. and Heron, G. (2001): Biogeochemistry of landfill leachate plumes; Applied Geochemistry, v. 16, issues 7–8, p. 659–718.

Council of Canadian Academies (2014): Environmental impacts of shale gas extraction in Canada: the expert panel on harnessing science and technology to understand the environmental impacts of shale gas extraction; Council of Canadian Academies, Ottawa, Ontario, 262 p.

DataBC (2019a): Atlas of Canada 1,000,000 national frameworks data – hydrology rivers; BC Ministry of Forests, Lands, Natural Resource Operations and Rural Development and GeoBC, database, URL <https://catalogue.data.gov.bc.ca/dataset/atlas-of-canada-1-000-000-national-frameworks-data-hydrology-rivers> [January 2018].

DataBC (2019b): Digital road atlas (DRA) - master partially-attributed roads; BC Ministry of Forests, Lands, Natural Resource Operations and Rural Development and GeoBC, database, URL <https://catalogue.data.gov.bc.ca/dataset/digital-road-atlas-dra-master-partially-attributed-roads> [January 2018].

DataBC (2019c): Municipalities – Legally defined administrative areas of BC; BC Ministry of Municipal Affairs and Housing, database, URL <https://catalogue.data.gov.bc.ca/dataset/municipalities-legally-defined-administrative-areas-of-bc> [January 2018].

DataBC (2019d): OGC oil and gas regional fields; BC Oil and Gas Commission, database, URL <https://catalogue.data.gov.bc.ca/dataset/9010f337-3a82-4ca0-b2ac-44d72e13ac48> [January 2018].

Dusseault, M., Gray, M. and Nawrocki, P. (2000): Why oilwells leak: cement behavior and long-term consequences; Society of Petroleum Engineers, International Oil and Gas Conference and Exhibition in China, November 7–10, 2000, Beijing, China, conference paper, URL <https://doi.org/10.2118/64733-MS> [May 2018].

Forde, O.N., Cahill, A.G., Beckie, R.D. and Mayer, K.U. (2019a): Barometric-pumping controls fugitive gas emissions from a vadose zone natural gas release; Scientific Reports, v. 9, article no. 14080, 9 p., URL <https://doi.org/10.1038/s41598-019-50426-3> [October 2019].

Forde, O.N., Mayer, K.U. and Hunkeler, D. (2019b): Identification, spatial extent and distribution of fugitive gas migration on the well pad scale; Science of the Total Environment, v. 652, p. 356–366, URL <https://doi.org/10.1016/j.scitotenv.2018.10.217> [February 2019].

IHS Markit (2019): AccuMap™; IHS Markit, mapping, data management and analysis software, URL <https://ihsmarkit.com/products/oil-gas-tools-accumap.html> [January 2018].

Ji, W., Dahmani, A., Ahlfeld, D.P., Lin, J.D. and Hill, E. (1993): Laboratory study of air sparging: air flow visualization; Ground Water Monitoring & Remediation, v. 13, issue 4, p. 115–126, URL <https://doi.org/10.1111/j.1745-6592.1993.tb00455.x> [January 2019].

Johnson, R.L., Johnson, P.C., Amerson, I.L., Johnson, T.L., Bruce, C.L., Leeson, A. and Vogel, C.M. (2001): Diagnostic tools for integrated in situ air sparging pilot tests; Bioremediation Journal, v. 5, issue 4, p. 283–298, URL <https://doi.org/10.1080/20018891079339> [January 2019].

Kljun, N., Calanca, P., Rotach, M.W. and Schmid, H.P. (2015): A simple two-dimensional parameterisation for Flux Footprint Prediction (FFP); Geoscientific Model Development, v. 8, p. 3695–3713, URL <https://doi.org/10.5194/gmd-8-3695-2015> [November 2018].

Kormann, R. and Meixner, F.X. (2001): An analytical footprint model for non-neutral stratification; Boundary-Layer Meteorology, v. 99, issue 2, p. 207–224, URL <https://doi.org/10.1023/A:1018991015119> [November 2018].

Lovley, D.R. and Chapelle, F.H. (1995): Deep subsurface microbial processes; Reviews of Geophysics, v. 33, issue 3, p. 365–381.

Mercer, J.W. and Cohen, R.M. (1990): A review of immiscible fluids in the subsurface: properties, models, characterization and remediation; Journal of Contaminant Hydrology, v. 6, issue 2, p. 107–163, URL <https://doi.org/10.1016/0169-7722(90)90043-G> [September 2019].

Parker, J.C. (1989): Multiphase flow and transport in porous-media; Reviews of Geophysics, v. 27, issue 3, p. 311–328.

Geoscience BC

t: 604 662 4147
e: info@geosciencebc.com

SUITE 1101–750 WEST PENDER ST
VANCOUVER, BC V6C 2T7

www.geosciencebc.com